3D Printed Alkali-Activated Sensors for Civil Infrastructure

Christos Vlachakis

Civil and Environmental Engineering
University of Strathclyde
Glasgow, United Kingdom

Thesis submitted in fulfillment for requirements of the degree of
Doctor of Philosophy

June 2021

Declaration of Authenticity and Author's Rights

This thesis is the result of the author's original research. It has been composed by the author and has not been previously submitted for examination which has led to the award of a degree.

Signed: 

Date: 24 May, 2021

To my family for their everlasting love and support.

‘Man - a being in search of meaning.’

Plato

Abstract

Multifunctional cement-based materials have seen increasing interest in structural health monitoring due to their high sensing performance. While these materials typically involve the fabrication of large construction elements, smaller sensing patches can be deployed onto existing surfaces as an alternative means of monitoring.

This thesis presents the development of 3D printed self-sensing alkali-activated material patches for monitoring the strain and temperature of concrete substrates. Changes in the inherent ionic conductivity of metakaolin-based alkali-activated material patches are used to demonstrate sensing and monitoring of infrastructure without the need to use electrically conductive fillers. The additive manufacturing, meanwhile, presents a convenient method of improving the repeatability and economic viability of deploying self-sensing materials in construction contexts.

The work in this thesis includes first time demonstration of 3D printed alkali-activated sensors for temperature and strain monitoring and outlines the current state of the art on self-sensing alkali activated materials. The fabrication, development, automated deployment, and sensing performance in strain and temperature of these novel materials are investigated throughout this thesis and the final printing design requirements are compared to applications that use additive manufacturing to produce construction elements.

By combining a monitoring and maintenance technology with an automated approach to deployment, the work carried out as part of this thesis addresses important barriers to the implementation of civil structural health monitoring & maintenance technologies. It is the author's hope that the work outlined here eventually leads to an enhanced uptake of structural health monitoring by the construction sector. This will allow for prioritised maintenance of the ageing and degrading civil assets that currently underpin infrastructures across Europe and the US.

Acknowledgments

A PhD is an amazing adventure, maybe not exactly like the ones you read in books or you see in movies but it sure has its steep and rocky roads and, at least from personal experience, feels like you are lost the majority of the time just to reach the end when you least expect it.

Just like all journeys, this thesis would not have been possible without the help of many individuals whether that was technical support when experiments did not work or moral support in low spirits.

First and foremost massive, particular, special thanks to my supervisor Dr. Marcus Perry for providing me with this opportunity and for his continuous support and guidance throughout my PhD. His help was invaluable and cannot be described in words alone. I would like to thank Marcus for always coming up with a solution to any sort of research or non-research related problem, for pulling me out my endless thoughts and doubts and for trusting in me when I did not.

I would like to particularly thank Dr. Lorena Biondi for her support over the years and being the guide I needed during my PhD. Her dedication and hard work were truly inspirational. While the hours working together in the lab felt endless at times, I believe it is something we can both happily look back on as a sign of great teamwork and friendship.

Many thanks to Dr. Jack McAlorum for his help and for sharing his knowledge and experience with me allowing me to overcome hurdles I would not have been able to do so alone and for cheering me up when I felt all hope was lost.

Thanks also to Dr. Andrea Hamilton for the time she devoted in supporting me in my lab work.

I would also like to acknowledge the support and assistance provided by the lab crew at the Civil and Environmental Engineering Department. Many thanks to Mara Knapp, for all her help and ensuring the labs ran properly despite the circumstances. I would also like to thank Gavin Gibson, Derek McNee and Jim Francis for their technical support in the

lab. No matter how wacky my requests seemed at times, they always found a way to pull it off.

A special thanks goes to all my friends for being there for me and letting me talk about something other than research. Particular thanks to all the people at the Civil and Environmental Engineering Department at the University of Strathclyde for all the fun times and laughs we've shared.

I would like to thank my parents, Kostas and Panagiota, my sister Sotiria and brother Apostolis for their unwavering support over the years.

Last but not least, I would also like to thank God and the universe for letting me roam around in this cosmos.

Thank you all.

Table of Contents

List of Figures

List of Tables

Abbreviations

AAM	Alkali activated materials
AC	Alternating current
ASTM	American Society for Testing and Materials
BET	Brunauer–Emmett–Teller
BS	British Standard
CAD	Computer-aided design
CF	Correction factor
DC	Direct current
DIW	Direct ink writing
EN	European Standard
GF	Gauge factor
GFRP	Glass fiber reinforced plastic
GGBFS	Ground granulated blast-furnace slag
LVDT	Linear variable differential transformer
OGTC	Oil & Gas Technology Centre
OPC	Ordinary Portland cement
PP	Polypropylene
PVA	Polyvinyl alcohol
RILEM	Réunion Internationale des Laboratoires et Experts des Matériaux, systèmes de construction et ouvrages

SSC	Stress sensitivity coefficient
STL	Stereolithography
UK	United Kingdom
US	United States
VDP	Van der Pauw
XRD	X-ray diffraction
XRF	X-ray fluorescence

Chapter 1 Introduction

1.1 Introduction

Structural health monitoring of ageing civil assets can inform timely maintenance and ensure ongoing infrastructure resilience. Structural heath monitoring data are obtained by the deployment of sensing devices such as transducers, strain gauges and fiber optic sensors onto civil infrastructure (Cawley, 2018). This allows frequent auditing and evaluation of civil infrastructure under external stimulants such as strain, temperature and moisture.

Recent approaches to acquiring the data for structural health monitoring have made use of self-sensing cementitious materials. These materials are considered ‘smart materials’ as they behave as structural elements (e.g. slabs and beams) and sensing elements at the same time. This multifunctional behavior is advantageous as it can to reduce the number of steps involved in the deployment of an instrumented asset (Chung, 2021; Ding et al., 2019a; Z. Tian et al., 2019). One of the drawbacks associated with self-sensing materials though is their reliance on conductive fillers. This significantly increases cost, particularly in large scale civil engineering applications.

An efficient means of approaching this problem would be to apply self-sensing cementitious overlays or coatings onto specific areas of interest for localized health monitoring. Such cementitious overlays could even act as a localized repair. This would

reduce the cost and volume of material required and avoid the added complexities of formulating self-sensing mix designs at large volumes.

Alkali activated materials (AAM) are ideal candidates for self-sensing overlays for concrete structures. Their chemical microstructure provides them with enhanced electrical properties when compared to conventional ordinary Portland cement (OPC) binders and they therefore do not require conductive fillers to be used in sensing applications (Lamuta et al., 2016; Saafi et al., 2018). This minimizes costs and improves the scaleability of these materials when compared to conductive filler-based self-sensing cements.

Self-sensing materials alone, however, will not lead to wider deployment of structural health monitoring. The construction sector has seen a decline in its available workforce (Juricic et al., 2021), as construction sites are harsh and hazardous working environments that pose significant risks to workers (Eaves et al., 2016; Peng and Chan, 2020). These factors are already impacting the construction sector's ability to deliver traditional work, let alone the deployment of new monitoring methods. Alternatives to manual labour need to be sought. Additive manufacturing of cementitious materials has seen great rise over the past years. Construction elements can be fabricated in a layer-by-layer process without relying on the use of additional formwork. This method is able to significantly increase consistency, minimize construction time, labor costs and waste material while at the same time providing greater accessibility and a safer means of construction (Hossain et al., 2020; Manuel et al., 2019; Mohammad et al., 2020; Wong et al., 2018). Moreover, additive manufacturing follows similar fabrication approaches for onsite and offsite applications when compared to existing in-situ and ex-situ castings methods.

The work described in this thesis aims to develop and deploy self-sensing AAM overlays using additive manufacturing methods. This will allow for the remote, automated deployment of an inherently multi-functional material. It is the author's hope that this will lead to the provision of a scaleable and sustainable alternative monitoring approach for existing and newly developed civil infrastructure, and lead to a greater uptake of structural health monitoring across the construction sector.

1.2 Research contribution

The research contributions of the work carried out in this thesis are briefly summarized as follows:

- Review of alkali activated materials and subsequent experimental investigation of printable metakaolin AAM binders. The experimental investigation demonstrates the successful fabrication of AAM. The procedures followed in this analysis will be used for the development of AAM sensors.
- Review of the reported sensing applications of alkali activated materials and an analysis of the current state-of-the-art in strain, temperature and moisture AAM sensing. The review provides the current understanding of AAM sensors and outlines common experimental methodologies that are followed. The extent and limitations of this technology are highlighted and recommendations for future applications are also made.
- Review of 3D printing cement-based materials and the experimental investigation of printing AAM overlays/patches onto concrete substrates. The review outlines standard experimental methodologies that are followed in cementitious printing. These methodologies are adjusted and assessed accordingly to meet the fabrication requirements of AAM sensing overlays.
- Experimental investigation of the temperature sensing response of AAM patches. This examines the feasibility of using AAM as temperature sensors. This also provides a greater understanding of the behaviour of AAM sensors which can allow for further monitoring investigations in the future.
- Exploring the potential of using AAM patches as strain sensors. The behaviour under common strain conditions is examined and additional factors that may affect sensing performance are also addressed. Assessing the strain behavior of AAM sensors paves the way for future field and industrial applications.

1.3 Thesis outline

The outline of this thesis follows:

Chapter 2 reviews the literature on AAM, self-sensing AAM and 3D printing cementitious materials. An overview of these scientific fields is presented. The extents and current limitations are highlighted and recommendations are also provided. The experimental investigation in subsequent chapters of this thesis will be based on the theory provided in this chapter.

Chapter 3 presents the experimental investigation of AAM. This chapter focuses on the fabrication of these materials and their mechanical properties. This ensures the proper performance of AAM and allows for further investigations in the following chapters.

Chapter 4 focuses on 3D printing AAM overlays that aim to be used in sensing applications. The design process is based on existing guidelines that have been reported for cementitious printing applications. These design requirements were tailored and expanded accordingly to fit the mix design requirements for this application.

Chapter 5 outlines the temperature sensing behavior of printed AAM patches. The temperature sensing relationship and mechanical bond strength of the overlays to the concrete substrate are described. Factors affecting the integrity of the patches are also explored in this chapter.

Chapter 6 investigates the potential of using printed AAM overlays as strain sensors under compression, tension and 4-point bending. Considerations that must be made in sensing overlays are mentioned and potential avenues for future work are described.

Chapter 7 discusses potential applications and deployment methods for printed self-sensing AAM patches. Potential means of upscaling this technology are also presented.

Chapter 8 presents the conclusions and future work for this thesis. Recommendations on improving the technology are made, and pathways for future research and applications are outlined.

1.4 Research output

The research output derived from this thesis and related scientific work the author of this thesis has taken part in is depicted below.

1.5 Journal articles

Biondi, L.; Perry, M.; Vlachakis, C.; Wu, Z.; Hamilton, A.; McAlorum, J. Ambient Cured Fly Ash Geopolymer Coatings for Concrete. *Materials (Basel).* 2019, *12*, 923, doi:10.3390/ma12060923.

Biondi, L.; Perry, M.; McAlorum, J.; Vlachakis, C.; Hamilton, A. Geopolymer-based moisture sensors for reinforced concrete health monitoring. *Sensors Actuators, B Chem.* 2020, *309*, 127775, doi:10.1016/j.snb.2020.127775.

Vlachakis, C.; Perry, M.; Biondi, L.; Mcalorum, J. 3D printed temperature-sensing repairs for concrete structures. *Addit. Manuf.* 2020, *34*, 101238, doi:10.1016/j.addma.2020.101238.

Vlachakis, C.; Perry, M.; Biondi, L. Self-Sensing Alkali-Activated Materials : A Review. *Minerals* 2020, *10*, 885, doi:10.3390/min10100885.

McAlorum, J.; Perry, M.; Vlachakis, C.; Biondi, L.; Lavoie, B. Robotic spray coating of self sensing metakaolin geopolymer for concrete monitoring. *Autom. Constr.* 2021, *121*, 103415, doi:10.1016/j.autcon.2020.103415.

Biondi, L.; Perry, M.; McAlorum, J.; Vlachakis, C.; Hamilton, A., Lo. H, Alkali-activated cement sensors for sodium chloride monitoring. *IEEE Sensors.* 2021, i*n review for minor revisions.*

1.6 Conference papers

Biondi, L.; Perry, M.; Vlachakis, C.; Hamilton, A. Smart cements: repairs and sensors for concrete assets, *Proceedings SPIE 10598, Sensors and Smart Structures Technologies for Civil, Mechanical, and Aerospace Systems 2018, Denver, Colorado, USA.*

Vlachakis, C.; Biondi, L.; Perry, M. 3D printed smart repairs for civil infrastructure, *9th European Workshop on Structural Health Monitoring Series (EWSHM) 2018, Manchester, UK.*

McAlorum, J.; Perry, M.; Vlachakis, C.; Biondi, L. Autonomous Application of Smart Cement Sensor-repairs, *12th International Workshop on Structural Health Monitoring (IWSHM) 2019, Stanford, California, USA.*

Vlachakis, C.; Biondi, L.; McAlorum J.; Perry, M. Self-Sensing 3D Printed Repair for Concrete Substrates, *12th International Workshop on Structural Health Monitoring 2019 (IWSHM), Stanford, California, USA.*

McAlorum, J.; Vlachakis, C.; Perry, M. A Low-Cost Electrical Impedance Analyser for Interrogating Self-Sensing Cement Repairs, *IEEE International Instrumentation and Measurement Technology Conference (I2MTC) 2021, Glasgow UK.*

Tshimbombo, T.; Perry, M.; Hoy, C., Tzoura, E.; Vlachakis, C.; McAlorum, J. "Robotic Installation of Wireless Strain Gauges into Precast Concrete Elements, *IEEE International Instrumentation and Measurement Technology Conference (I2MTC) 2021, Glasgow UK.*

Perry, M.; Biondi, L.; McAlorum, J.; Vlachakis, C. Self-Sensing Concrete Repairs Based on Alkali-Activated Materials: Recent Progress, *IEEE International Instrumentation and Measurement Technology Conference (I2MTC) 2021, Glasgow UK.*

Vlachakis, C.; Perry, M.; McAlorum, J. 3D Printed Self-Sensing Alkali-Activated Coatings for Civil Infrastructure, *IEEE International Instrumentation and Measurement Technology Conference (I2MTC) 2021, Glasgow UK.*

1.7 Funding

This work was supported in part by the Royal Society (grant number RG160748) and the Oil & Gas Technology Centre (OGTC).

Chapter 2 Literature review

In this chapter a literature review on alkali activated materials, self-sensing alkali activated materials[1] and 3D printing cementitious materials is presented. The theory covered in this chapter will be used for the development of 3D printed AAM sensors for concrete structures in Chapters 3, 4, 5 & 6.

2.1 Introduction

3D printing AAM sensors for concrete structures is a multidisciplinary field that consists of alkali activated materials, self-sensing alkali activated materials and 3D printing cementitious materials. Adequate understanding in each of these fields is required to ensure the proper development of this technology. In this chapter literature on alkali activated materials, self-sensing alkali activated materials and 3D printing cementitious materials is presented. The purpose of this chapter is to cover the necessary theory behind each respective area to allow for the successful experimental investigation of 3D printed AAM sensors in the upcoming chapters.

2.2 Alkali activated materials

2.2.1 Introduction

Alkali activated materials (AAM) are an emerging alternative to ordinary Portland cements which have gained intensive interest over the past decades. AAM concretes attain

[1] The section on self-sensing alkali activated materials was published in the Special Issue Alkali Activated Materials: Advances, Innovations, Future Trends Vlachakis, C.; Perry, M.; Biondi, L. Self-Sensing Alkali-Activated Materials: A Review. *Minerals* **2020**, *10*, 885. https://doi.org/10.3390/min10100885. Minor changes have been made to follow the updated literature in this field.

similar mechanical properties to ordinary Portland cement (OPC) concretes, but are thought to be more sustainable due to their lower embodied carbon (Habert and Ouellet-Plamondon, 2016). While these materials have already seen use in industrial applications, the widespread use of these materials is somewhat hindered by the specialist knowledge required for fabrication, high alkalinity of the materials used and workability issues particularly at large volumes. Nevertheless, extensive research on AAM has been conducted in recent years. A considerable number of reviews on AAM are available at the time of writing (Assi et al., 2020; Bernal and Provis, 2014; Farhan et al., 2020; Mabroum et al., 2020; Mendes et al., 2021; Provis, 2018, 2014a; Provis and Bernal, 2014; A. Wang et al., 2020). Research in this field is ongoing and reviews are being published at a high pace to keep up with the current state of the art. Therefore, the purpose of this section is to not provide a full in-depth review of AAM but rather present a general overview on what AAM are and how they are formulated, so that the steps in designing printed AAM sensors are clear.

2.2.2 Alkali activated materials and geopolymers

The use of alkali-activated materials within construction is not a new concept. Multiple studies on the formation of binders with the use of alkaline solutions were carried out throughout the 20th century (Krivenko, 2017). Claims have also been made that a primal form of this technology was present in historical monuments dating back to 600 A.D (Davidovits et al., 2019). Prominent research in this field was carried out by Davidovits in the 1970s in which calcined clay (metakaolin) was mixed with alkaline solutions to develop heat resistant inorganic materials (Davidovits, 1991). Davidovits coined the term ‘geopolymer’ which was then regarded as a material with an amorphous to semi-crystalline three-dimensional silico-aluminate structure of the following types:

Poly(sialate) (Si-O-Al-O-)

Poly(sialate-sixolo) (Si-O-Al-O-Si-O)

Poly(sialate-disixolo) (Si-O-Al-O-Si-O-)

The composition of geopolymers was represented by the empirical formula equation (2.1):

$$M_n\{(SiO_2)_z - AlO_2\}_n \cdot wH_2O \quad (2.1)$$

Where M is the alkali metal cation, usually Na^+ or K^+; 'n' is the degree of polycondenstation; z is the oligomeric building unit (Si/Al ratio):1,2,3; and w is the molar ratio of water and the alkali cation.

The term geopolymer derived from the word polymer as the material was able to transform, polycondense and adopt a shape at temperatures below 100 ^oC. At the same time it is a mineral material which is hard, weather resistant and can withstand high temperature, thus it was named a 'geo' - polymer (Davidovits, 1991, 1989). The term geopolymer was quite popular and is still used today, albeit in a rather more generic manner than its initial meaning.

Following the research carried out by Davidovits (1991), research in geopolymers progressed quite rapidly. Extensive research was carried out by van Deventer, Duxson, Provis and colleagues at the University of Melbourne, Australia (Duxson et al., 2005b, 2007a; Provis et al., 2005a; Provis et al., 2005b). As research in geopolymers expanded, confusion and disagreements started to arise as to what should be regarded as a geopolymer and what should not. Various names have been used, and are still used today, to characterize the mixture of a materials high in silicate and aluminium content with an alkaline solution. Such names include inorganic binders, green cements, alkali activated cements, aluminosilicate binders, alkali activated binders, alkali activated materials etc. In recent years, geopolymers have been considered to represent a small category of materials in a larger group of materials called 'alkali activated materials' and in particular 'low calcium alkali activated materials'. Figure 2.1 portrays the characterization of alkali-activated materials, geopolymers and various types of cements in regards to calcium, aluminium and alkali content.

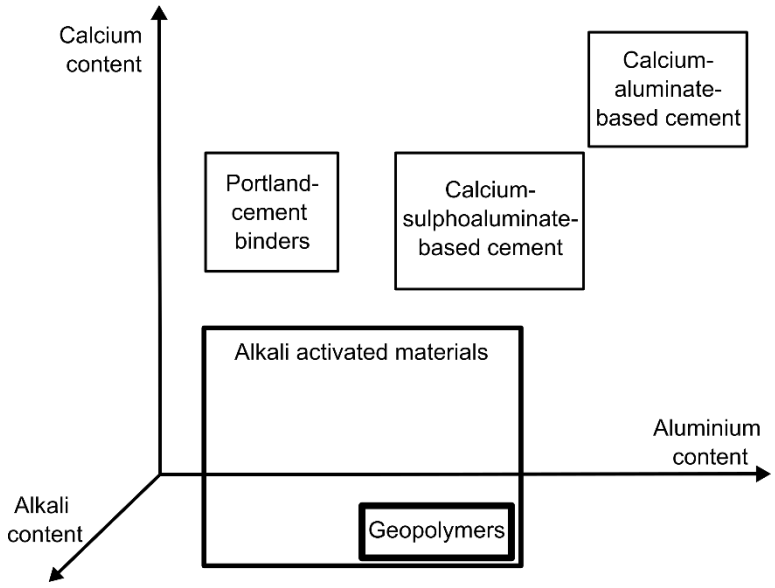

Figure 2.1 – Classification of geopolymers and alkali activated materials in comparison to other types of cement binders according to their chemical composition. Thicker borders indicate higher alkali content. Adapted from Provis (2014b).

Nomenclature aside, AAM and geopolymers have greatly progressed in research and industrial applications over the years. They are comprised of a broad range of materials that are constantly expanding. The naming conventions that the scientific community eventually settle on for the materials described in this thesis are of little importance to the outcomes. For this chapter and for the remainder of this thesis the mixture of a material high in silicate and aluminium content with an alkaline solution will be denoted as an alkali-activated material (AAM). The terms AAM and geopolymer may be used interchangeably and will ultimately refer to the same product.

2.2.3 AAM Production

Contrary to OPC binders AAM are formulated by mixing a precursor with high silicate and aluminium content and an alkaline solution which is typically a mixture of an alkali metal silicate and an alkali metal oxide. This method is also commonly known as the two-part method (Provis, 2018). AAM can also be formulated via the one-part method in which water is simply added to a dry powder which is a blend of aluminosilicate powder and solid activators. This method resembles the mixing procedure followed in OPC

binders in which water is added to cement. While the two-part approach has seen most study over the years, extensive focus has been given on the one-part method which is expected to be the prominent method for future, particularly onsite, applications.

When designing two-part AAM the following factors need to be considered:

- Precursor
- Calcination if kaolin is used
- Alkaline solution
- Molecular composition
- Mixing sequence
- Curing

These aspects will be explored in the following chapters to allow for the development of a functional AAM binder that will be used for sensing and printing purposes in the following chapters.

2.2.3.1 Precursor

The main precursors that have been used in the production of AAM are metakaolin (calcined clay), fly ash and ground granulated blast-furnace slag (GGBFS) (Provis, 2018). They have seen arguably the most research out of all the potential AAM precursors. They are also the prime materials used in the round robin tests conducted by the RILEM technical committee in durability testing of AAM (Gluth et al., 2020; Provis et al., 2019; Winnefeld et al., 2020).

Over the years the precursors used in AAM production have considerably expanded. Examples of more recently used precursors are glass powder (Khan et al., 2021), construction demolition waste (Komnitsas et al., 2015), volcanic ash (Zhou et al., 2021), palm oil fuel ash (Ranjbar et al., 2014) and rice husk ash (Nuaklong et al., 2020). Furthermore, blends of precursors are also common in AAM formulation (Alanazi et al., 2019; Bernal et al., 2012; Vogt et al., 2019). Broadly, literature has mostly focused on AAM formulated from:

- **Fly ash:** an industrial by-product of the combustion of pulverized coal (Amran et al., 2021). According to American Standard ASTM C618 (ASTM C618-19, 2015) fly ash can be classified as type C and type F. Class F consists a minimum of 70% SiO_2+Al_2O_3+Fe_2O_3 and up to 18% CaO (lower calcium content) whereas class C fly ash consists of at least 50% SiO_2+Al_2O_3+Fe_2O_3 and over 18% of CaO (high calcium content). Both Class F and Class C can be used in AAM formulation (Guo et al., 2010; Luan et al., 2020). The composition of fly ash displays high variability as it depends on the source of the coal, degree of pulverization, combustion conditions, collection of ash, handling and disposal methods. All these aspects vary from plant to plant and show high variability (Amran et al., 2021).
- **Slag:** a waste product of the production of different types of metals comprising of mainly silicate, alumina, calcium and magnesium. Depending on the cooling method used slag can be air-cooled, expanded or granulated. The cooling method that will be used will ultimately affect the chemical and mineral composition of the slag produced. Blast-furnace slag is typically used in OPC and AAM production. Typical chemical compositions that can be found in blast-furnace slag are the following: 27-45% SiO_2, 7-24% Al_2O_3, 31-50% CaO and 1-18% MgO (Awoyera and Adesina, 2019; Wang, 2016).
- **Metakaolin:** derived from naturally available clay (as opposed to fly ash and slag which are by-products). Metakaolin is pozzolanic material that is produced through the calcination of kaolin clay. Metakaolin contains high aluminosilicate content about 50–55% SiO_2 and 40–45% Al_2O_3 (Rashad, 2013). According to ASTM 618-19 (ASTM C618-19, 2015) metakaolin complies with the requirements as Class N, natural pozzolan (SiO_2 + Al_2O_3+Fe_2O_3 $\geqslant$ 70%). Metakaolin was selected as the precursor for AAM formulation in the work described in this thesis. It is considered a favorable precursor as its composition contains low amounts of impurities allowing a more predictable design (Duxson et al., 2007a). It is also obtained from a raw material that does not rely on additional industrial processes thus making it more accessible to use.

2.2.3.2 Kaolin calcination

Metakaolin is attained from the dehydroxylation of kaolin clay, a material with high content of kaolinite ($Al_2O_3 \cdot SiO_2 \cdot 2H_2O$) in the temperature range of 450 ^oC-850 ^oC. Calcining at lower temperatures results into an incomplete dehydroxylation of kaolin whereas calcining at temperatures over 900 ^oC may result into the recrystallization of kaolin into mullite. During the transformation phase the weight of the powder is reduced by about 14% due to the removal of hydroxyl ions. The weight reduction is due to the following reaction equation (2.2) (Rashad, 2013):

$$2SiO_2 \cdot Al_2O_3 \cdot 2H_2O \rightarrow 2SiO_2 \cdot Al_2O_3 + 2H_2O \uparrow \quad (2.2)$$

Kaolin calcination is normally carried out with the use of an electric muffle furnace, a rotary kiln or flash calcination in which clay passes through a flame for a few seconds (Rashad, 2013). While flash calcination and rotary kilns present a robust methodology, the results from using a muffle furnace are less repeatable. The basic approach when using a furnace is quite straightforward, the furnace is set at peak temperature for a specific amount of time. However, a universal standard does not exist due to the variety of material compositions. Key factors that need to be taken into account when calcining kaolin are the following:

- The conversion from kaolin to metakaolin is considered complete when all the traces of kaolinite have been removed from the substance. This can be validated through X-ray diffraction (XRD) analysis (Tironi et al., 2012).
- Calcination processes are frequently based on previous literature and typically range between 650-800 ^oC for 2-24 hours (Rashad, 2013; Zhang et al., 2016).
- Different chemical compositions of the source kaolin can lead to different temperatures and calcination durations (Badogiannis et al., 2005; Moodi et al., 2011; Tironi et al., 2012).
- Factors such as rate of calcination can assist in better decomposition of kaolin resulting into a higher quality metakaolin (Kenne Diffo et al., 2015).

- The means of calcination- furnace, rotary kiln or flash calcination- may also impact the reactivity (Autef et al., 2013) and the workability of the resulting metakaolin (Pouhet and Cyr, 2016).

Calcination methods are assessed via reactivity tests on the calcined clay. Such tests include the Chapelle test[2], Frattini test[3], strength activity index[4], isothermal calorimetry and mechanical properties of binders. In most cases a combination of these tests is practical as single tests may provide limited results (Alujas et al., 2015; Avet et al., 2016; Tironi et al., 2013). It is important to point out thought that the Chappelle, Frattini and strength activity index tests evaluate metakaolin's ability to react with calcium with the intention of serving as a supplementary material for OPC concrete. These tests though may not provide an accurate representation of the effects of calcination on alkaline activation. Wan et al. (2017a) stated dehydroxylation and recrystallization (and thus the formation of mullite-an undesired effect) of metakaolin should be considered when calcining clay for AAM formulation. It was also mentioned by the authors that similar compressive strength was observed for metakaolin AAM for calcination temperatures between 650-850 ^{o}C. In the current study assessing kaolin calcination was conducted through XRD analysis in which the dehydroxylation of the source material and any presence of mullite was investigated. If both these parameters were met, the calcination process was deemed sufficient.

2.2.3.3 Alkaline solution

As mentioned in Section 2.2.3 the alkaline solution is a mixture of an alkali oxide-MOH-and an alkali silicate-$M_2O{\cdot}rSiO_2$ where M is either Na^+ or K^+ (Provis, 2009). While most applications involve a mixture of these two constituents, solutions using only silicate

[2] 1 g of metakaolin is mixed with 1 g of $Ca(OH)_2$ and 100ml of water. The suspension is boiled for 16 h and the free $Ca(OH)_2$ is determined by means of sucrose extraction and titration with a HCl solution.

[3] A blend of Portland cement and metakaolin is mixed with water. The sample is placed in an oven at 40 ^{o}C for a givn time period. Samples are then vacuum filtered and allowed to cool down. The filtrate is then analysed for [OH^-] and [Ca^{2+}]. The [Ca^{2+}] and [OH^-] contained in an aqueous solution that covers the hydrated sample at 40 °C for a given time is compared with the solubility curve for calcium hydroxide in an alkaline solution at the same temperature. Test results below this curve indicate removal of Ca^{2+} from solution which is attributed to pozzolanic activity.

[4] Control Portland cement and blended Portland cement and metakaolin samples for compression testing are prepared. Strength activity ratio is the ratio of strength of the control samples by the strength of the blended samples at the same day. SAI>0.75 indicates high pozzolanic activity.

(Sun and Vollpracht, 2019) or hydroxide (Billong et al., 2018) have also been explored. In general, an alkaline solution must have a suitable pH to initiate the alkaline activation process (Duxson et al., 2007a). A high pH is required for the activation of metakaolin and fly ash. Blast furnace slag requires a solution with a more moderate pH and can therefore be activated with a larger variety of solutions (Provis, 2014a). Such solutions include sodium carbonate (Bernal et al., 2014b) and sodium sulfate (Mobasher et al., 2016). Other potential alkaline solutions include mixtures of sodium and potassium solutions (Palmero et al., 2015) and phosphate activators (Y. S. Wang et al., 2018).

The activator plays a vital role in the production of AAM. Contrary to the precursor, it can be tailored to meet the required molecular composition of the binder to achieve desired performance.

2.2.3.4 Alkaline activation

Mixing the solid precursor with the alkaline solution initiates a series of reactions. These reactions fall under the term alkaline activation[5].

Multiple studies have been carried out focusing on the kinetics of alkaline activation (Provis et al., 2008; Provis and van Deventer, 2007a,b; Zhang et al., 2012, 2013). The initial models focused primarily on metakaolin and fly ash AAM (Provis and van Deventer, 2007a,b). Later models that were developed expanded and incorporated slag based AAM as well (Provis and Bernal, 2014). Alkaline activation is a complex reaction that can be broken down into smaller phases namely dissolution, gelation, reorganization and hardening-strength development (Duxson et al., 2007a). Depending on the composition and potential contaminants in AAM additional reactions may also occur (Duxson et al., 2007a). In general, alkaline activation starts with the dissolution of the solid aluminosilicate source by alkaline hydrolysis which in turn produces aluminate and silicate species. Dissolution then results to the formation of a gel depending on the type of AAM, sodium aluminosilicate hydrate (N-A-S-H), calcium aluminosilicate hydrate (C-

[5] The reaction was initially labelled as ‘geopolymerisation’ deriving from the term geopolymer. Similar to how alkali activated materials became the more prominent term to characterize these materials, alkaline activation has been adapted as the more generic term.

A-S-H) etc. The product continues to rearrange and reorganize after gelation reaching a hardened state and commences strength development (Duxson et al., 2007a; Provis et al., 2008; Provis and van Deventer, 2007a). Alkali activation is affected by numerous factors such as the silica-aluminium content, alkali cation, temperature, salts present (Provis et al., 2008; Provis and van Deventer, 2007a,b; White et al., 2012; Zhang et al., 2012, 2013). Figure 2.2 portrays the reaction products of alkali activation for both low calcium and high calcium AAM.

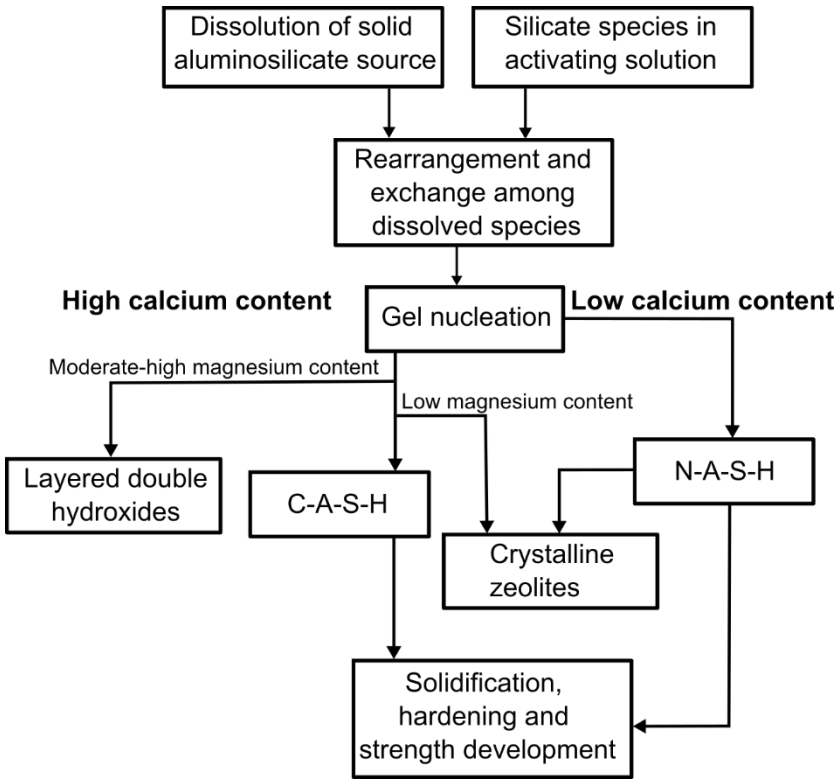

Figure 2.2 – Alkali activation and reaction products for low calcium and high calcium binders. Adapted from (Provis and Bernal, 2014).

2.2.3.5 Classifying AAM

AAM consist of an expanding group of materials which are difficult to classify. In general, AAM are classified according to their calcium content and subsequently by the notation introduced by Engelhardt (1989), $Q^n(mAl)$, where $0 \leq m \leq n \leq 4$, species. Q refers to the silicon atom, n = 0–4 refers to the bridging oxygen atoms, and m the number of Al neighbors. The notation $Q^n(mAl)$ is used to describe the connectivity of a silicon

tetrahedron bridged through oxygen to aluminum and to other silicon centers (Bernal and Provis, 2014; Duxson et al., 2005b).

The two main groups are 'low-calcium' AAM and 'high-calcium' AAM. The former group includes AAM made with metakaolin (which is almost if not entirely calcium free) and fly ash (small amounts of calcium). In the latter group lies BFS and high calcium fly ash AAM. High calcium AAM binders can be classified when the Ca/(Si + Al) ratio is roughly 1 (Provis and Bernal, 2014). Low calcium AAM leads to N-A-S-H or potassium aluminosilicate hydrates-K-A-S-H gels. This type of gel is structurally disordered and has a highly cross-linked Q^4-structure (Provis et al., 2005c), whereas high calcium-slag AAM results in C-A-S-H gels similar to the calcium-silicate-hydrate (C-S-H) gels in OPC. The gel contains silicate chains comprising Q^1 and Q^2 environments and low concentration of Q^3 sites in chain-bridging roles. In the cases of high calcium fly ash, certain types of slag or blended precursors (e.g. metakaolin-slag, metakaolin-fly ash etc.) the resulting gel is more complex. The nature of the gel is calcium-sodium-aluminosilicate-hydrate (C–N–A–S–H) but can lead to the formation of C–A–S–H gel with secondary products (Bernal and Provis, 2014; Ismail et al., 2014). The AAM used in this work is low-calcium AAM, therefore the gel is expected to result in a N-A-S-H gel with structurally disordered and a cross-linked Q^4-structure. This allows for a more straightforward reaction avoiding any potential secondary reactions in the binder.

2.2.4 Molecular composition

One of the most important differences between OPC and AAM binders is that the former is a mixture of cement and water whereas the latter requires a precursor that is rich in silica and aluminium and an alkaline solution. OPC mix designs are relatively simple when compared to AAM as the mixing constituents have been well defined and investigated over centuries. This has led to a strong understanding of the material allowing users to reliably predict the performance of various mix designs. As a result, mass ratios are almost exclusively used in OPC. The same cannot be said about AAM. While mass ratios are easier to use and can provide, to a certain extent, adequate results, the available source materials (precursor and solution) for the fabrication of AAM are quite broad.

Solely relying on mass ratios may not provide the entire picture of the AAM binder and this will affect repeatability and reproducibility. As a result, molar ratios are an additional consideration for AAM, as this provides more context on the composition of the binder (Provis, 2014a). To date a standard mix design for AAM binders does not exist. Mix designs are based on previous literature, RILEM recommendations and trial and error with the available resources at hand.

2.2.4.1 Common molar ratios

The most common molar ratios that have been investigated in AAM are SiO_2/Na_2O primarily in solution but also in binder, H_2O/Na_2O in solution, Na_2O/Al_2O_3 in binder and SiO_2/Al_2O_3 in binder. Frequently Na/Al and Si/Al are also used in place of the Na_2O/Al_2O_3 and SiO_2/Al_2O_3 respectively. If a potassium-based solution is used, then Na_2O and Na are substituted with K_2O and K respectively. Other ratios such as Ca/Si, CaO/SiO_2, CaO/Al_2O_3, MgO/Al_2O_3 may also be examined depending on the composition of the binder.

Various studies have been conducted that examined the effects of molar ratios on the performance and microstructure of AAM. This has allowed the progression and better understanding of the materials. In general, the chemical composition of the alkaline solution is what will ultimately influence the outcome of the binder. Over the years there have been multiple studies to identify which ratios play the most important role in AAM fabrication.

Table 2.1 displays the molar ratios that have been identified as the most impactful on metakaolin AAM binders as reported in existing studies. For example, Lahoti et al. (2017) conducted a comprehensive study on various molar ratios of metakaolin AAM. The results showed that the Si/Al ratio is the most significant parameter in determining compressive strength of AAM followed by the Al/Na ratio. It was also stated that unlike OPC, the water/solids ratio is not a significant factor governing the compressive strength of the binders. Riahi et al. (2020) stated that the Na_2O/Al_2O_3 could be considered the most important ratio in terms of mass loss and drying shrinkage. Similarly, Zhang et al. (2013, 2012) stated that the Na/Al has a more pronounced influence on the extent of alkaline

activation in metakaolin AAM than the curing temperature and Si/Al ratio. Yuan et al. (2016) stated that the SiO_2/K_2O molar ratio impacts the dissolution of Si and Al atoms to form an aluminosilicate gel in metakaolin AAM. High alkalinity can accelerate the dissolution rate of the Si and Al phases from metakaolin. Very high alkalinity though may result in early precipitation which leads to lower mechanical properties[6] (De Vargas et al., 2011). Pouhet et al. (2019) investigated the effects of water in flash calcined metakaolin AAM concrete. It was found that as the overall water content in the binder increased, the mechanical properties decreased. Furthermore apart from mechanical properties the H_2O/Na_2O ratio has proven to impact other properties of AAM binders such as workability and setting time (Yusuf et al., 2014). In general, under a constant H_2O/Na_2O ratio, it can be accepted that increasing the Si/Al ratio up to a certain point is beneficial. However, over-increasing the silica content can result in unreacted particles which could then lead to a decrease in strength. Ratios beyond the optimal values of Si/Al have been considered to lead to chemical instability (He et al., 2016).

Table 2.1 – Effect of molar ratio and impact on metakaolin AAM binders.

Molar ratio	Affecting Parameter	Reference
Si/Al	Compressive strength	Lahoti et al. (2017)
Na_2O/Al_2O_3	Mass loss and drying shrinkage	Riahi et al. (2020)
Na/Al	Alkaline activation	Zhang et al. (2013, 2012)
SiO_2/K_2O	Dissolution of Si/Al	Yuan et al. (2016)
Water content in binder	Compressive and flexural strength	Pouhet et al. (2019)
H_2O/Na_2O	Workability and setting time	Yusuf et al. (2014)

Judging by the above it is not exactly clear as to which ratio should be regarded as 'most important'. It can be accepted, however, that all ratios impact the binder to a certain extent. Focusing solely on one ratio is also rather difficult, as altering one ratio can simultaneously impact other ratios as well. This is more evident in liquid alkali silicates

[6] When potassium is used in AAM formulation, all ratios with sodium are replaced with potassium. The 'optimal' values and importance of each ratio remains the same. A similar finding was made by Vargas et al. (2011) for fly ash AAM for SiO_2/Na_2O. Higher sodium content was reported to lead to greater fly ash particle solubilization.

and hydroxides. Certain ratios may unachievable due to the composition of the liquids. For example, in order to increase the silica content of the solution, more liquid silicate will be required to be added to the alkaline solution. By doing so, apart from the Na_2O/SiO_2 ratio this will affect the H_2O/Na_2O ratio of the solution as well as the silicate itself contains high content of water. For this reason, studies that focus on the chemical composition of AAM typically use both solid and liquid activators as this approach allows more freedom in achieving the desired molar ratios (Bernal et al., 2012; Duxson et al., 2005a; Lahoti et al., 2017). However, silicates and hydroxides both in liquid form are simpler and more convenient to use. It is also important to point out that different molar ratios apply to different precursors. In continuation, different ratios may also apply to the same precursor depending on its chemical composition e.g. low calcium fly ash and high calcium fly ash, Mg content in blast furnace slag etc. The work outlined in this thesis aims to develop a simple yet consistent binder that will be used in sensing and printing applications. As a result metakaolin AAM was used for this investigation. A combination of both molar and mass ratios will be used to assess the performance of the binder.

2.2.4.1.1 Metakaolin AAM

In the case of metakaolin AAM, the desired molecular composition is rather clearer when compared to fly ash and slag AAM[7]. Metakaolin based binders have seen optimal performance for molar ratios around Si/Al=2 (SiO_2/Al_2O_3=3.0-3.6), Na/Al=1 (Na_2O/Al_2O_3=1), SiO_2/Na_2O (in solution)=1.5-2, SiO_2/Na_2O (in binder)=4.0, H_2O/Na_2O=11-12 (Batista et al., 2019; Bernal et al., 2012; Borges et al., 2017; Duxson et al., 2007b; He et al., 2016; Kamseu et al., 2017; Liu et al., 2020; Ozer and Soyer-Uzun, 2015; Pouhet and Cyr, 2016; Riahi et al., 2020; Rocha et al., 2018; Sarkar and Dana, 2021;

[7] Different ratios apply for other types of precursors. Molar ratios that have been used for Class F fly ash are Si/Al=2.40-3.0, SiO_2/Na_2O (in solution)=1.5-2.3 (Bocullo et al., 2021; Fan et al., 2018; Provis et al., 2019; Zhou et al., 2016). Molar ratios for GGBFS are not as clear. Several studies have focused on the modulus of the solution (Jiao et al., 2018; Mobasher et al., 2016; Sisol et al., 2019). Slag AAM is also influenced by the Mg and TiO_2 content (Bernal et al., 2014d; Haha et al., 2011; Park et al., 2020) and the type of alkali activation e.g. sulphate and carbonate activation (Bernal et al., 2016, 2014a). In red clay brick waste AAM applications the $SiO_2/Al2O_3$ ratios have exceeded 7 (Mahmoodi et al., 2020; Robayo et al., 2016). For AAM with blends of red clay brick and tungsten mining waste with Si/Al ratios between 1.36-2.16, the highest compressive strength was viewed at Si/Al=1.36 (Sedira et al., 2018).

Silva et al., 2007; Wan et al., 2017b; Zhang et al., 2017) . Common liquid-solid ratios range between 0.8-1.2 (Batista et al., 2019; Bature et al., 2021; Cai et al., 2020a).

2.2.5 Mixing sequence

Studies investigating the mixing sequence of AAM are few and far between. The difficulty in selecting an optimal mix sequence primarily derives from the point of introduction of the alkaline solution. As mentioned in Section 2.2.3.3 the alkaline solution consists of a silicate and a hydroxide. These can be both in liquid or solid form or a combination of the two. In most studies it is common for the alkaline solution to be prepared beforehand. However, these two solutions can also be added to the binder separately as well. Ways of assessing the mixing sequence involve assessing the mechanical properties of the binder, workability and cost (Junaid et al., 2015). Table 2.2 displays various sequences that have been explored in mixing sequence investigations[8].

[8] Mixes with multiple precursors or filler were not covered in the studies in Table 2.2. When multiple precursors are employed, they are first dry mixed for a few minutes to ensure a homogeneous distribution. The solids and liquids are then added together and mixed accordingly (Luan et al., 2020; Xu et al., 2017; Zaheer et al., 2016). Depending on the type of filler, it can be added in water or the solution and sonicated to achieve uniform dispersion (Candamano et al., 2019; Deng et al., 2019) or added directly to the mix (Batista et al., 2019).

Table 2.2 – Reported studies on mixing sequence of AAM.

Mixing sequence	No.	Ref
Alkaline solution->precursor+aggregates (if required)-> Mix liquids and solids	1	(Junaid et al., 2015), (Suwan and Fan, 2017) (Dassekpo et al., 2017)
Alkaline solution (no cooldown)-> precursor+aggregates (if required)-> Mix liquids and solids	2	(Dassekpo et al., 2017)
Precursor+hydroxide->silicate->aggregates (if present)->water if needed	3	(Junaid et al., 2015), (Suwan and Fan, 2017)
Aggregates+precursor+silicate->hydroxide->water	4	(Dassekpo et al., 2017)
Aggregates+precursor->silicate->hydroxide->water	5	(Junaid et al., 2015)
Aggregates+precursor+hydroxide -> silicate ->water	6	(Dassekpo et al., 2017)
Silicate+hydroxide (solid)-> precursor->water	7	(Kobera et al., 2011)
Hydroxide solution->silicate->precursor	8	(Kobera et al., 2011)
Precursor+silicate (solid) + hydroxide (solid)->water	9	(Suwan and Fan, 2017)

According to the studies presented in Table 2.2, the mixing method did not have a major impact on the strength of the binder when the alkaline solution was added in liquid form (sequences 1, 3, 4 & 5) (Dassekpo et al., 2017; Junaid et al., 2015; Suwan and Fan, 2017). The only time it did have an adverse effect was in Dassekpo et al. (2017), who investigated adding the alkaline solution to the binder without allowing the solution to cool down (sequence 2). When the silicate and hydroxide are mixed together, heat is generated. It was found that the increased temperature resulted in lower strength compared to the other mixing methods of that study. Cooling the alkaline solution prior to mixing is important for consistency: it affects reaction rates, but the viscosity of solutions can also decrease at higher temperatures (Yang et al., 2008). The viscosity of the solution has an immediate effect on the workability of the resulting binder (Favier et al., 2014), and using solutions at elevated temperatures may also present solubility issues (Provis, 2009).

Junaid et al. (2015) stated that sequence 5 (aggregates + precursor -> silicate -> hydroxide -> water) was preferred as it did not involve any preparation prior to mixing, while it also resembled the procedure followed in OPC binders. Incorporating silicates first, however, may lead to early workability issues as they tend to have higher viscosity than hydroxides (Provis and Bernal, 2014). This could be a particular problem for metakaolin based AAM, which possess inherent low workability and greater liquid demand (Favier et al., 2014; Provis et al., 2010).

Kobera et al. (2011) found that mixing sequence 7 (silicate + hydroxide (solid) -> precursor -> water) resulted in a binder with double the compressive strength compared to sequence 8. The difference in strength was attributed to the point of introduction of water, as it was stated to affect the hydration and in turn the structural stability and strength of the binder. It has been posited that the rate of the condensation/polymerisation increases in the presence of additional water under low water conditions during alkaline activation. While water is required for the hydration of the alkali metal cations, it was hypothesized that the cations will instead bind strongly to dissolved anionic species to account for the lack of water in the system. When water is eventually provided the binding between the alkali metal cations and the small anions is weakened as a result accelerating the condensation reactions (Provis and van Deventer, 2007a).

While several combinations of the sequence of the materials can be concocted the primary aim of the mixing order should be to ensure a homogenous slurry leading to a binder with consistent performance. Due to the different workability properties of the available precursors not all mixing approaches may be applicable in every application. In construction based applications, a mixing procedure similar to OPC is favorable as it allows transferring previous practice into newer technology and thus an easier transition from OPC to AAM binders. The work described in this thesis though focuses on a more niche application in which following an OPC-based mixing procedure is not currently required. The aim of the mixing sequence for this application focuses on ensuring a homogenous mix with a repeatable performance while satisfying other requirements that

will be explored in the following chapters. Mixing sequence 1 presents a more generic procedure that meets these criteria in this regard.

2.2.5.1 One-part mixes

One-part AAM mixes are presented for completeness. This method of formulation has been promoted as a more applicable approach for onsite applications. The main concept behind this method is to reduce handling of hazardous chemical compounds and adapt the 'just add water' mentality, resembling the methodology followed in OPC binders. While studies in two-part AAM have been conducted for decades, research in one-part mixes has seen rapid growth within just the last few years (Abdollahnejad et al., 2020a; Coppola et al., 2020).

One-part AAM mixes consist of solid precursors and activators which are first dry-mixed and then water is added to formulate the binder. In some cases, the solids may be present in raw form (Hajimohammadi and van Deventer, 2017; Nematollahi et al., 2015). In other instances, the solids may contain pulverized AAM. In this case AAM are premade with the two-part mix, crushed and pulverized for reuse in the one part method (Liew et al., 2017). The mixing order for one-part mixes is fairly straightforward compared to two-part mixes. The solids are first dry mixed, then water is added. Lastly additives and filler are usually added after a slurry has been formed (Abdollahnejad et al., 2020a; Shah et al., 2020a). One-part mixes may result to larger heat generation compared to two-part mixes, however studies have shown that the intensity and duration of the heat liberation is not able to be sustained to such a degree for it to beneficially impact alkaline activation (Suwan and Fan, 2017). Lastly, similar to two-part AAM, one-part AAM are also influenced by the molecular composition of the binder (Hajimohammadi and van Deventer, 2017), source material (Choo et al., 2016; Nematollahi et al., 2015; Yousefi Oderji et al., 2019), the curing regime (Shah et al., 2020b), fiber content (Abdollahnejad et al., 2020b; Shah et al., 2020a) etc. The application in this thesis is primarily aimed at precast elements rather than onsite applications considering the printing process that is followed. As a result, the need for one-part mixes is not currently necessary and does not provide any essential advantages to the formulation of AAM.

2.2.6 Curing

Similar to all other aspects of AAM, a definitive curing regime does not exist. In most cases, curing follows accepted methodologies based on existing literature. The approach to curing followed in AAM is slightly different than that for OPC binders. AAM binders are required to be kept under sealed conditions to avoid liquid loss due to excessive drying. Curing AAM in water tanks is also not favorable as this could cause leaching of the alkaline solution and negatively impact the properties of the binder (Chi, 2012; Provis, 2018). While not that common, AAM binders can also be cured in alkaline solutions (Bernal and Provis, 2014), and the mechanical properties of the binder can be enhanced depending on the solution employed (Xia and Sanjayan, 2018). Furthermore, curing at an elevated temperature is also quite common to accelerate alkaline activation (Bernal and Provis, 2014).

Various studies have been conducted investigating the optimal temperature and duration for AAM curing. The typical temperature range for curing is between 40 ^{o}C and 80 ^{o}C. Higher temperatures have been mentioned to lead to moisture loss which then negatively impact the mechanical properties of the binder (Chen et al., 2016; Duxson et al., 2007b; Mahmoodi et al., 2020; Mo et al., 2014; Yuan et al., 2016). In most cases the samples are heat cured for about 24-48h (Bernal et al., 2012; Borges et al., 2017; Cheng et al., 2015; Duxson et al., 2007b; Gao et al., 2014). However, extended periods (up to 7 days) of continuous heat curing (Chen et al., 2016; Yuan et al., 2016) and short periods (up to 8 hours) (Aydin and Baradan, 2012; Rovnaník, 2010) have also been investigated. It has been mentioned that prolonged heat curing could be detrimental for the binder and lead to decreased mechanical properties over time (Ozer and Soyer-Uzun, 2015; Zhang et al., 2009).

After heat curing, the samples are then removed from their current conditions and stored under ambient conditions to continue curing. Heat curing essentially allows the acceleration of alkaline activation, which in turn leads to high strength in AAM samples at early ages.

Heat curing does not, however, have the same effect across all AAM. In regards to metakaolin AAM, studies have shown ambient cured binders are able to reach strength values close to their 28 day strength after 7 days of ambient curing (Provis et al., 2019; Rocha et al., 2018; Rovnaník, 2010). This signifies that heat curing is not essential for metakaolin AAM, which was considered standard practice in earlier stages of AAM research[9].

Furthermore, there has been a debate in the AAM community if the curing duration of 28-days for OPC should be applied for AAM as well (Provis et al., 2019). As previously mentioned, the compressive strength ambient cured metakaolin AAM at 7 days was fairy comparable to the strength reached at 28 days (Provis et al., 2019; Rocha et al., 2018). On the other hand, ambient cured fly ash has a slower reaction rate and thus sees strength increase past 28 days (Ma et al., 2016; Sun and Vollpracht, 2019). Therefore, it can be accepted that the 28-day target may not be as applicable to all AAM binders as cases could be made that this duration should be shorter for some binders and longer for others.

2.2.7 Overview and caveats of AAM formulation

While extensive research in AAM formulation has been carried out outliers and alternative approaches exist. Even though a consensus around the optimal molar composition of metakaolin AAM exists serviceable performance can be achieved outside the molar ratios stated in Section 2.2.4.1 (Bature et al., 2021) or by simply focusing on the mass ratios of the constituents (Albidah et al., 2021; Mohseni, 2018; Vogt et al., 2019; Zulkifly et al., 2021). Furthermore, reproducibility also appears to pose an issue in AAM. Variability in results of the same mix design and methodology is quite common. This has been also pointed out in the round robin tests carried out by the RILEM technical committee 'Durability Testing of Alkali-Activated Materials' (Provis et al., 2019). These differences have been speculated to occur due to variances in source materials, the

[9] The same does not apply though to binders with slower reaction rates, such as fly ash AAM (Alanazi et al., 2019). Fly ash AAM have slower reaction rates and thus slower strength development. Therefore, heat curing is beneficial in this aspect (Sun and Vollpracht, 2019). In situations in which fly ash is activated only with a hydroxide, the reaction rates in that situation are very slow in which at that point heat curing is necessary to achieving a hardened binder (Criado et al., 2005). Moreover, heat curing may negatively impact slag AAM as well. High temperature may interfere with the development of the C-A-S-H gel therefore leading to a porous matrix (Huseien et al., 2016; Kubba et al., 2018).

compatibility of the aggregates with the binders and with minor differences in curing techniques. The source (whether in liquid or solid form) of key components such as of silica (Hajimohammadi et al., 2011) and alumina (Hajimohammadi et al., 2010) can also influence the performance of the binder. It is also important to point out that the molar ratios presented in studies are primarily based on calculated ratios. The actual composition of the binder may vary due to unreacted particles (Tian et al., 2019).

On another note, comparisons between mix designs may also not be that straightforward. AAM have been investigated as paste, mortar and concrete in which a direct comparison between the three cannot always be made. For example, while the addition of fine aggregate sand is beneficial in terms of drying shrinkage (Koutník et al., 2020; Kuenzel et al., 2014; Wang et al., 2020) it is rather unclear if it can lead to higher compressive strength. Cases have been made for it having a positive (Kuenzel et al., 2014; Riahi et al., 2020) and negative (Li et al., 2018; Sarkar and Dana, 2021; Wang et al., 2020) impact on the binder. Part of this disagreement can originate from the manner sand is added to the binder or depending on the additional filler present. Sand may be substituted into the binder at the expense of the precursor (precursor is removed to add sand), rather than it being added as a direct proportion to the precursor (precursor content remains the same irrespective of the amount of sand added).

2.2.8 Summary of alkali activated materials

Overall AAM are a diverse group of construction materials with numerous fabrication techniques that are able provide a sustainable approach for future construction applications. Alkali activated materials though require a different means of design and fabrication compared to the conventional ordinary Portland cement binders: much of the knowledge associated with OPC is not easily transferable to AAM. Taking into account the literature presented in this section fabricating AAM is possible as the approach and procedures to key parameters in AAM formulation outlined below have been identified:

- Fabrication process and mixing sequence for two-part AAM.
- Calcination approaches and evaluation of kaolin to produce metakaolin.

- Expected molar composition and solid-liquid ratios for fabricating metakaolin AAM binders.
- Curing regimes for metakaolin AAM binders.

These methods will be followed to fabricate AAM binders in the experimental investigation of this thesis

2.3 Self-sensing alkali-activated materials

2.3.1 Introduction

Monitoring and surveillance of civil infrastructure is required to ensure structural health and resilience in the face of degradation. While sensors can provide adequate localized measurements, self-sensing 'smart' materials have gained popularity over the years. In a civil engineering context, self-sensing materials are components that can simultaneously detect measurands without the need of additional sensing instruments. Such materials include self-sensing cementitious materials (Ding et al., 2019a; Z. Tian et al., 2019), bricks (Downey et al., 2018; Meoni et al., 2020), aggregates (Kong et al., 2017; Zhao et al., 2019) and pavements (Arabzadeh et al., 2018; Han et al., 2013). In terms of self-sensing cementitious materials, extensive research has been carried out in both ordinary Portland cement (OPC) and alkali activated materials (AAM).

AAM are multifunctional materials that have gained extensive interest over that past decades, predominantly as an emerging, low-carbon alternative to OPC in concrete production (Zhang et al., 2020). AAM display similar mechanical properties to OPC, and have been reported to attain high early age strength under both heat curing (Assi et al., 2016) and ambient curing (Provis et al., 2019) regimes. They also present higher thermal (Khan and Sarker, 2020) and chemical resistances (Aguirre-Guerrero et al., 2021) when compared to conventional OPC systems. AAM applications have been demonstrated in waste immobilization (Komljenović et al., 2020), repairs (Nunes et al., 2019), coatings (Biondi et al., 2019) and in additive manufacturing (Panda and Tan, 2018), and they have also been shown to demonstrate self-healing (Kan et al., 2019) and self-compacting (Huseien and Shah, 2020) properties.

In the realm of smart materials, AAM were initially used as bonding agents (He et al., 2011) and as encapsulants (Suweni Muntini and Ahmadi, 2018) for conventional sensors. However, as the understanding and the technology of AAM progresses, the need for these additional sensing devices has diminished: interrogation of changes in the electrolytic conductivity of AAM allow them to be directly used as a sensing tool in their own right (Lamuta et al., 2016). As a result AAM have increased the number of supporting roles in structural health monitoring and maintenance, being used as both structural self-sensing elements (e.g. AAM concrete cubes and beams) (Bi et al., 2017; Saafi et al., 2016; Vilaplana et al., 2013), and as self-sensing coatings for OPC concrete substrates (Perry et al., 2015; Vlachakis et al., 2020).

There are already numerous reviews on self-sensing cementitious materials in general (Ding et al., 2019a; Dong et al., 2019; Tian et al., 2019), and on multifunctional AAM (Tang et al., 2019), but there are currently no reviews that detail the self-sensing aspects of AAM. This review covers the sensing applications reported for AAM, specifically strain, temperature and moisture sensing. Materials denoted as 'alkali activated materials', 'geopolymers' and any other derivatives originating from these terms will be considered for this review, without focusing on debates over their terminology. Our hope is that this review will shed light on areas where further work on self-sensing AAM is required.

2.3.2 Alkali activated material sensors

2.3.2.1 Fabrication, fillers and additives

AAM sensors follow the same fabrication procedure as conventional AAM binders components as outlined in Section 2.2.3. As with OPC systems, AAMs can be mixed with sand and aggregates to produce:

a) Pastes / binders: precursor + alkaline solution
b) Mortars: precursor + alkaline solution + fine aggregate (typically sand)
c) Concretes: precursor + alkaline solution + fine aggregate + coarse aggregate

Although it is not required to produce a self-sensing material, electrically conductive additives can also be added to an AAM binder to improve electrical conductivity. Fillers

must be properly dispersed to achieve a homogenous mix and avoid agglomeration (Kim et al., 2017). For two-part mixes the main ways of achieving this are:

A. **Filler in aqueous solution:** The conductive filler can be added to an aqueous solution and sonicated. Following this, the filler is added to the alkaline solution which is again mixed and/or sonicated. The precursor is subsequently added and mixed (Candamano et al., 2019; Deng et al., 2019; Rovnaník et al., 2019a,b; Vilaplana et al., 2013).
B. **Filler in sodium hydroxide:** The conductive filler is added only to the sodium hydroxide solution, which is subsequently mixed and sonicated. The silicate-based solution and the precursor are added from there on (Lamuta et al., 2017; Payakaniti et al., 2017; Saafi et al., 2015, 2014).

Cases have also been reported in which the filler is sonicated but added to the mix at a later stage, particularly after the alkaline solution and the precursor have been mixed together (Behera et al., 2018; Saafi et al., 2013). However, the recommended process is to disperse the fillers in the alkaline solution (prior to mixing with the solid precursor), as this has been reported to lead to greater dispersion and uniform density in the matrix and therefore leading to increased electrical performance (Candamano et al., 2019; Hanjitsuwan et al., 2014; Saafi et al., 2013). Fillers can also be chemically manipulated to enhance their dispersion, for example, carbon nanotubes coated with SiO_2 demonstrated enhanced dispersion, owing to a chemical reaction between the coated filler and the alkaline solution (Bi et al., 2017).

Reported one-part self-sensing filler AAM applications are quite limited. The fabrication of such binders though is rather straightforward. In a study by D'Alessandro et al., (2020) the following mixing process was employed: The solid material (precursor and activator) were first dry mixed together. Water was then added to the solids and mixed until a homogenous mix was achieved. Conductive filler was sonicated in the water for greater dispersion prior to the addition to the solids.

2.3.2.1.1 Sensor fabrication

Regardless of whether a conductive filler is used, electrodes can be prearranged within the binder, either in a mold or on the surface of a substrate. The AAM can then be cured. During curing, temperature and humidity may need to be adjusted to control reaction rates and water transport within the system. Alternatively, electrodes can be attached to cured specimens using conductive paint. Examples of AAM components and coatings are shown in Figure 2.3.

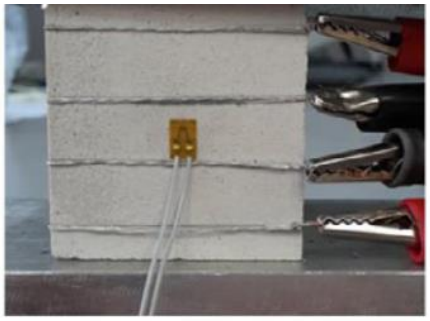

(a)

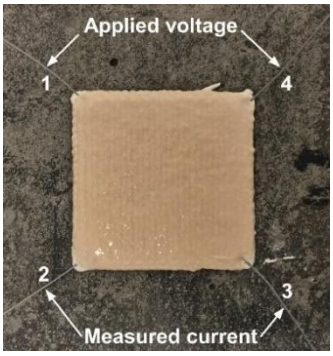

(b)

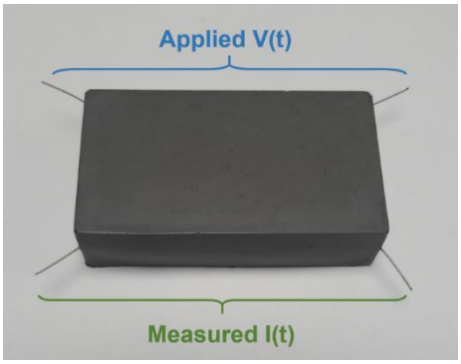

(c)

Figure 2.3 – Self-sensing AAM substrates a) metakaolin AAM with wound wires (Lamuta et al., 2017) b) metakaolin AAM printed coating with stainless steel wires (Vlachakis et al., 2020) c) fly ash AAM with stainless steel wires (Biondi et al., 2020).

AAM sensing essentially relies on measuring changes in electrical conductivity in response to environmental variables. To interrogate conductivity, an electrical current (or voltage) is applied across the specimen, and the voltage (or current) response is measured. This allows the electrical conductivity, σ, to be calculated via equation (2.3):

$$\sigma = \frac{I}{V} \cdot \frac{L}{A} \tag{2.3}$$

where V is the voltage, I is the current, L is the distance between the electrodes, and A is the shared cross-sectional area of sample between the electrodes. Studies will sometimes quote the resistivity of AAM samples, $\rho = 1/\sigma$.

2.3.2.2 Electrical (ionic) conductivity: mechanisms

2.3.2.2.1 Overview of mechanisms

Ionic conduction of AAM and OPC materials is associated with the mobility of free ions in the pore solution, primarily Ca^{2+}, K^{+}, Na^{+}, Si^{4+}, Fe^{2+}, Al^{3+} and OH^{-} (Hansson and Hansson, 1985). In OPC, ionic conductivity is attributed to the mobility of the Ca^{2+} and OH^{-} ions in the pore solution. This form of ionic conduction is highly dependent on the amount of free water in the matrix, and usually results in an electrical conductivity that is too low to be of use for deploying a sensing solution. OPC substrates are effectively electrical insulators unless they are wet (Xu et al., 2010).

Ionic conductivity is stronger in AAM. Ionic conductivity originates from the structure of AAM, as the alkali cations (Na^{+} or K^{+}) in the matrix charge balance the aluminium (III) in the tetrahedral AlO_4^{-} group (Duxson et al., 2007a; Provis, 2014a). Cations are either bonded to the matrix via Al-O or Si-O bonds, or are present in the framework cavities to maintain electrical charge balance. Ions that are not bound to the structure are "free ions" that are able to move through the pore network to enhance electrical conductivity (Cui et al., 2008).

2.3.2.2.2 Equivalent circuits

The current best understanding of AAM electrical conductivity states that it is mainly a function of three components, the resistance of the electrolyte, ion transport of the connected and unconnected pores, and the effect of the electrodes on the matrix. In fact, these three components can be modeled as a circuit, made up of serial and parallel combinations of standard electronic components (e.g. resistors, inductors, capacitors) (Biondi et al., 2020; Dong et al., 2015; Ravikumar and Neithalath, 2013). There are several of these so-called "equivalent circuits" that can be used to model the electrical response of AAM. One of the most common equivalent circuits used in electrochemistry is the Randles circuit, as displayed in Figure 2.4. The Randles circuits leads to ideal Nyquist and Bode plots illustrated in Figure 2.5. The components that are used to model the Randles circuit are the following (Bard and Faulkner, 2001):

i. *Solution resistance R_Ω*: refers to the series element in which all the current (faradaic process and double-layer charging) passes through.

ii. *Faradic impedance Z_f*: refers to the faradaic process which can also be expressed as a series combination comprising the series resistance, Rs (also treated as polarization resistance) and the pseudocapacitance, Cs whose values are independent of frequency.

iii. *Double capacitance C_d*: refers to the nearly pure capacitive behavior of the circuit.

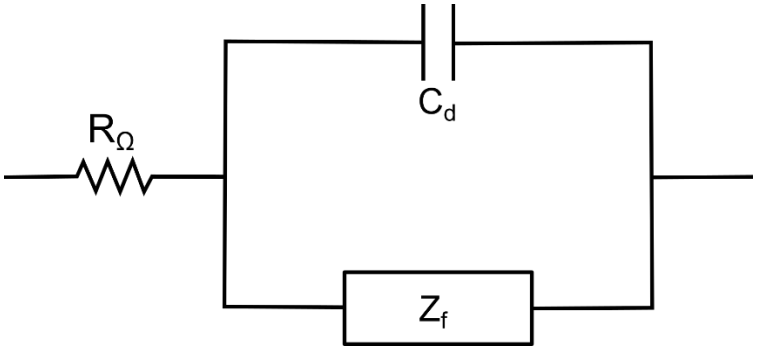

Figure 2.4 – Equivalent Randles circuit. Adapted from Bard and Faulkner (2001).

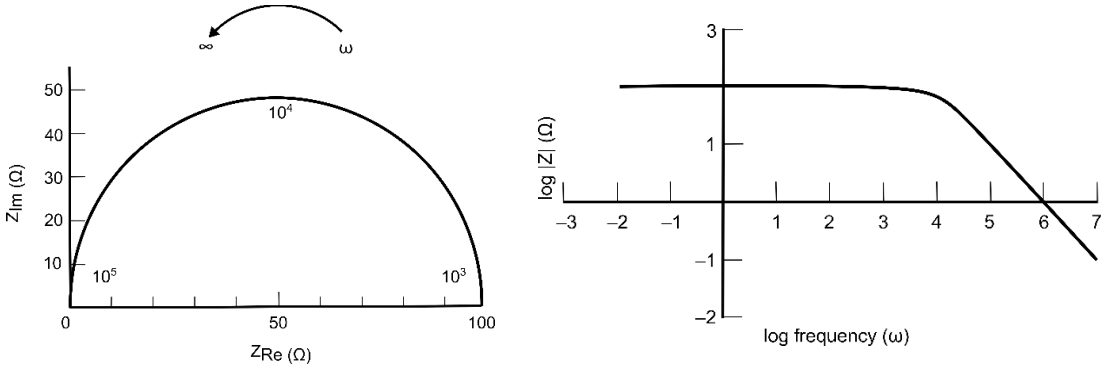

(a) (b)

Figure 2.5 – Typical Nyquist plot (left) and Bode plot (right). Adapted from Bard and Faulkner (2001).

Conventional circuits though such as the Randles circuit cannot encompass the complexity of AAM systems. AAM can have partial or fully saturated pore solution and double phase regions. Furthermore, potential chemical reactions can alter the charge transfer and diffusion in the sample (Dong et al., 2015). As such more complex circuits are considered

more suitable. Figure 2.6 displays one such equivalent circuit that contains components to model:

i. *The resistance of the electrolyte, Re*: refers to the liquid electrolyte in the AAM pores and is dependent on the number of ions (which is based on the concentration of the volume of the AAM) and ion mobility (which is a function of ion concentration, alkali metal and temperature).
ii. *The connected pore resistance, Rc, and unconnected pore resistance, Ruc:* are the resistance of the ion conducting pathways between the connected (percolating) and unconnected pores in the AAM matrix.
iii. *An interface resistance, Ri*: refers to the specimen- electrode interface in which a single layer of Na+ ions in the AAM will adhere to the negatively charged surface of the metal electrode. This layer acts as a dielectric, separating the electrons in the metal electrode from the Na+ in the AAM (Gu et al., 1992; McCarter and Brousseau, 1990).
iv. *Qi and Qp are double-layer capacitances:* this is an imperfect capacitor, or "constant phase element" used to describe the net result of ion dynamics in electrochemical systems.
v. *L refers to inductance effects*: that are observed at high frequencies due to factors such as electrode cross-talk, particularly when measured currents are small and due to relaxation of adsorbates on the electrodes.

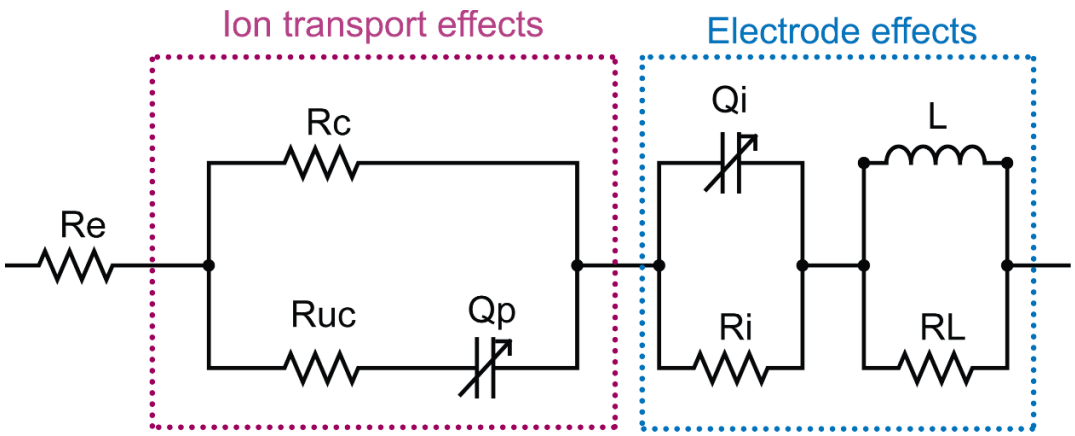

Figure 2.6 – Equivalent circuit of AAM (Biondi et al., 2020).

2.3.2.2.3 The impact of conductive fillers

In the case of cementitious materials with conductive fillers, the sensing mechanism may include additional electronic conduction: in fact, it may be the dominant conduction mechanism. The type of electronic conduction depends on whether there are a large number of locations where adjacent filler particles (or fibers) are in direct physical contact. This can be seen as the conductivity of the binder significantly decreases which is known as the percolation threshold. This is also used to determine the 'optimal' amount of filler to add to the sample. Adding filler beyond the percolation threshold does not provide great conductivity gains in the sample.

If there is a continuous, long-range conductive network of filler / fibers inside the material (i.e. the system is above the percolation threshold), then electronic conduction is the result of the straightforward movement of electrons. If the filler / fibers are not in direct contact but are close enough, then conductivity is still possible, as electrons can hop (via tunneling) between fibers. Changes to the distance between fibers affect the dominant conduction mechanism, and overall conductivity (Chen et al., 2004; Han et al., 2010a; Li et al., 2006; Sun et al., 2017b; Wen and Chung, 2006, 2001a).

In AAM, it is common (though sometimes unnecessary) to add conductive fillers to further improve conductivity (Fiala et al., 2017; Payakaniti et al., 2017; Rovnaník et al., 2017a). The volume of filler added is usually high, so that the percolation threshold can be overcome, and so the conductive filler can form a continuous electrical path in the material

(Al-Dahawi et al., 2016; Chung, 2002). It has been reported that conduction is a combination of both ionic and electronic conduction, as ions are still mobile while the filler allows the shortening of the conduction path in the matrix (Payakaniti et al., 2017), but there have not yet been many in-depth studies on this topic within AAM.

2.3.2.3 Electrical impedance

Direct current (DC) and alternating current (AC) have been both been used to interrogate AAM conductivity. If DC is used, the electrical resistance, R, of the sample is calculated via equation (2.4):

$$R=\frac{V}{I} \tag{2.4}$$

This equation assumes the material obeys Ohm's Law, but AAM are electrolytic cells, and so the use of DC has significant drawbacks. Similar to salt water solutions, applying DC will result in electrolysis. Ions within the AAM cannot travel within the electrodes (which conduct via electrons), and so the conducting cations within the AAM migrate towards and react with the cathode. This results in a so-called "polarization resistance", that gradually increases in magnitude over time. The effect is likely less pronounced when conductive fillers are used to set up an electronic conduction path, but issues with electrolysis may still arise in the long-term if even a small part of the conduction is ionic (Pour-Ghaz et al., 2009; Song, 2000; Wen and Chung, 2001b).

To prevent electrolysis, AC is preferred (the direction, or polarity, of the applied current is frequently switched) (Han et al., 2012; Rovnaník et al., 2019a). Using AC allows one to determine the electrical *impedance* of a sample, *Z*. In this case, a sinusoidal voltage of magnitude *V* and frequency *f,* is applied to the sample and the current response, *I* is measured. This allows the impedance to be calculated by using equation (2.5) (Lasia, 2014):

$$\vec{Z}=\frac{V}{I}e^{i(\phi_V-\phi_I)} \tag{2.5}$$

where $\Phi_V - \Phi_I$ is the phase difference between the applied voltage and measured current and the impedance is a complex number of the form in equation (2.6) (Lasia, 2014):

$$\vec{Z}=Ze^{i\arg(Z)} \quad (2.6)$$

where Z and arg(Z) are the impedance's magnitude and argument. In AAM, the phase difference between the current and voltage results from capacitive effects in the material.

Electrical impedance is frequency dependent, and so sweeping the frequency can lead to a rich dataset for sensor characterization. The AC frequency can be selected to minimize or maximize the measurement of capacitive or resistive effects in the sample, depending on the application (Perry et al., 2015; Saafi et al., 2016, 2014) and allows for the elimination of polarization if desired (Perry et al., 2015; Rovnaník et al., 2019c; Rovnaník et al., 2019a). Overall, however, frequency tends to be selected to produce the highest sensitivity to measurands during characterization (Lamuta et al., 2017; Saafi et al., 2016).

2.3.2.4 Electrical (ionic) conductivity: reported magnitudes

AAM possess a higher conductivity than OPC at room temperature due to the alkali metal ions in their matrix. The electrical properties of AAM tend to vary as they are influenced by mix ratios, chemical composition, and environment. Table 2.3 summarizes reported conductivities for AAM composites with and without conductive fillers.

Table 2.3 – Reported conductivity for AAM under ambient-near ambient conditions. Notations- sodium silicate (Na_2SiO_3), sodium hydroxide (NaOH), potassium silicate (K_2SiO_3), potassium hydroxide (KOH), silicon (Si), aluminium (Al), sodium (Na), potassium (K), Phosphorus (P).

Matrix	Precursor	Activator	Liquid-binder ratio	Molar ratios	Filler content	Filler concentration	Order of magnitude for conductivity (S/m)	AC or DC?	Reference
Paste	GGBFS	K_2SiO_3+ KOH	Unreported	Si/Al=1.64* K/Al=1.56*	Single wall carbon nanotubes	0.2wt%	10^{-3}	DC	(MacKenzie and Bolton, 2009)
Mortar	Fly ash Class C +GGBFS	Na_2SiO_3+ NaOH	0.4	Cannot calculate	Carbon fiber	0.5%volume	1	DC	(Deng et al., 2019)
Paste	Fly ash Class F	Na_2SiO_3+ KOH	0.51	Si/Al=3.10* Na+K/Al=2.23*	Graphene	1wt%	10^{-1}	DC	(Zhang et al., 2018)
Paste	Metakaolin	Na_2SiO_3+ NaOH	1.2	Si/Al=2	Carbon microfiber	15wt%	10^{-2}	DC	(Behera et al., 2018)
Paste	Unreported	Unreported	0.53	Cannot calculate	Graphene oxide	20wt%	10^{2}	Unreported	(Zhong et al., 2017)

Mortar	GGBFS	Na_2SiO_3	0.84	Cannot calculate	Carbon black	2.25wt%	10^{-1}	DC	(Fiala et al., 2019)
Paste	GGBFS	Na_2SiO_3+ NaOH	0.43	Si/Al=3.20* Na/Al=1.19*	Carbon fiber	0.76wt%	10^{1}	Unreported	(Vilaplana et al., 2013)
Paste	Fly ash Class F	Na_2SiO_3+ NaOH	0.39	Cannot calculate	Graphene oxide	0.35wt%	1	AC	(Saafi et al., 2014)
Mortar	Fly ash Class F	Na_2SiO_3+ NaOH	0.36	Si/Al=1.57* Na/Al=0.27*	Multiwall carbon nanotubes	1wt%	1	AC	(Saafi et al., 2013)
Paste	Fly ash Class C	Na_2SiO_3+ NaOH	0.5	Si/Al=2.05* Na/Al=0.85*	Carbon fiber	0.5wt%	10^{1}	AC	(Payakaniti et al., 2017)
Paste	Fly ash Class C	Na_2SiO_3+ NaOH	0.4	Si/Al=1.93* Na/Al=0.51*	No filler	-	10^{-1}	AC	(Hanjitsuwan et al., 2011)
Paste	Fly ash Class F	Na_2SiO_3+ NaOH	0.37	Si/Al=near 2	No filler	-	10^{-2}	AC	(Saafi et al., 2016)
Paste	Fly ash Class F	K_2SiO_3	0.6	Si/Al=1.17	No filler	-	10^{-1}	AC	(Saafi et al., 2018)
Paste	Fly ash Class F	Na_2SiO_3+	0.4	Si/Al=2.15* Na/Al=1.18*	No filler	-	1	AC	(Hanjitsuwan et al., 2014)

		NaOH							
Mortar	GGBFS	Na_2SiO_3+ NaOH	0.61	Cannot calculate	Carbon nanotubes	2.5wt%	10^{-6}	AC	(Kusak and Lunak, 2017)
Mortar	GGBFS	Na_2SiO_3	0.36	Si/Al=6.71* Na/Al=1.11*	Graphite powder	30wt%	10^{-4}	AC	(Rovnaník et al., 2019a), (Rovnaník et al., 2019c)
Mortar	GGBFS	Na_2SiO_3	0.61	Si/Al=6.71* Na/Al=1.11*	No filler	-	10^{-6}	AC	(Rovnaník et al., 2019c), (Rovnaník et al., 2019a)
Paste	Metakaolin	Na_2SiO_3	Unreported	Si/Al=1.04* Na/Al=0.17*	No filler	-	10^{-4}	AC	(Cui et al., 2008)
Paste	Metakaolin	Phosphoric acid	Unreported	Si/P=1	No filler	-	10^{-7}	AC	(Sellami et al., 2019)

*Not provided by authors, calculated from data available in cited paper (s)

2.3.2.4.1 Without conductive fillers

The conductivity of AAM without conductive fillers has been reported to range from 10^{-4} S/m (Cui et al., 2008) to 1 S/m (Hanjitsuwan et al., 2014). In general, the conductivity of AAM increases with increasing alkali metal concentration (Cai et al., 2020b; Hanjitsuwan et al., 2014), and with higher liquid-to-binder ratios (Payakaniti et al., 2017). Too much liquid in an AAM can, however, lead to highly porous binders which in turn can affect conductivity. While increased porosity has been reportedly linked to higher conductivity (Liang et al., 2017; Liu et al., 2019; Salem and Ragai, 2001), it has also been linked to reduced conductivity (Hanjitsuwan et al., 2011; Kultayeva et al., 2020). Having reviewed this literature, the authors of the present review believe that increasing porosity likely leads to higher conductivities, up until a point: the dominant conduction mechanism in AAM is, after all, accepted to be via pore solution, the volume of which would be higher with more pore space. This hypothesis is also supported by the fact that when interrogating at moderate-to-low AC frequencies, maximum conductivity tends to coincide with high liquid-to-solid ratios: at moderate-to-low AC frequencies, the conduction mechanism that dominates is related to bulk pore solution conductivity. It should be pointed out though that at low AC frequencies, the conduction mechanism of the binder is influenced by the electrodes rather than the bulk pore solution (Gu et al., 1993; McCarter and Brousseau, 1990). As a result careful consideration is required to distinguish between the two regions to ensure proper data interpretation. This also makes it clear that the dominant conduction mechanisms that occur at different AC frequencies could be better used to probe and make sense of behavior.

Results from Cai et al. (2020b) show that metakaolin AAM have a higher conductivity than fly ash AAM. It was again speculated that the difference in conductivities was due to the higher liquid-to-solid ratio used for metakolin AAM. The same authors also reported that incorporating different types of precursors in the same mix can create a denser matrix, which subsequently leads to decreased conductivity (Cai et al., 2020b). This is all further evidence for our hypothesis. Comparisons are, however, still often challenging, because

precursors of the same type, but from different sources, can also present variable behavior due to their dissimilar chemical composition (Zeng et al., 2016).

For samples with low to no conductive filler content, the resistance of the matrix continues to increase over time due to the progress of the geopolymerization process (Payakaniti et al., 2017; Zeng et al., 2016). Under the same curing and alkaline conditions, it has been reported that the resistance of metakaolin-based AAM stabilizes over a quicker period of time due to their quicker geopolymerization and higher chemical activity when compared to low calcium fly ash AAM (Cai et al., 2020b).

While not as common, high water contents in the binder during fabrication have been reported to have a negative impact on the conductivity of AAM. In a study carried out by Cui et al. (2008) it was mentioned that even when increasing Na_2O/Al_2O_3 ratios the conductivity did not increase as expected. It was explained by Cui et al. that the excess water was overriding the effect of the free ions in the matrix. By removing the water through drying, the conductivity of AAM was reported to increase with increasing sodium content. That said, it can be observed that for the same Na_2O/Al_2O_3 ratios, drying led to decreased conductivity. Moreover, based on the molecular composition of this study, the highest Na/Al ratio is approximately 0.55-0.60. The sodium ions in this situation are not enough to charge balance the aluminium ions (Provis et al., 2005c). Therefore, increasing sodium content will have a direct impact on the overall chemistry and structure of the binder. Subsequently, this will also influence ion mobility. Bearing all this in mind, additional factors need to be taken into account before a definitive claim on the impact of water in this investigation could be made.

2.3.2.4.2 With conductive fillers

Conductive fillers can increase electrical conductivity of the composite by several orders of magnitude. Comparing conductivity of AAM is somewhat difficult due to the broad nature of available materials, the conductive fillers employed and the type of current (AC or DC) used.

From the data available in Table 2.3, it can be seen that the addition of graphene-based filler and carbon fiber has led to high conductivities between 10^{-1} – 10^{2} S/m and

10^{-2} – 10^{1} S/m respectively. However it can be easily observed that the range of reported conductivities is quite vast and varies significantly. For example:

- By adding 0.5% by volume carbon fibers to fly ash AAM, Deng et al. (2019) reported an increase in conductivity from 10^{-2} S/m to 1 S/m. Payakaniti et al. (2017) found similar results.
- On the contrary, Behera et al. (2018) added over 10% by volume carbon microfiber to metakaolin AAM, and found conductivity only increased from 10^{-3} S/m to 10^{-2} S/m.

While we do wish to posit a mechanism, these are seemingly contradictory results that might suggest there is some turning point in the conductivity gains produced by fiber addition. The difference could, on the other hand, stem from the fact that Deng et al. and Payakaniti et al. dispersed their carbon fibers in the alkaline solution, whereas Behera et al. dispersed the carbon microfiber in deionized water.

The literature underpinning Table 2.3 also shows that fiber size impacts conductivity, with longer fibers able to form conductive paths more easily than short fibers. This suggests the percolation threshold is an important consideration when adding fibers (Chen et al., 2004; Chuang et al., 2017; Wang et al., 2002). If this is the case, it means that the difference in dispersion techniques could potentially be the primary source of the differences in reported conductivities.

Graphite powders are an alternative to carbon fibers. By adding 10wt% graphite powder to slag AAM Rovnanik et al. (2019a) reported conductivities of order 10^{-5}-10^{-4} S/m. Conductive filler in powder form (carbon black, or graphite powder) has been speculated to result in lower conductivity gains compared to fiber fillers due to the formation of shorter conductive pathways (Ding et al., 2019a). This is indeed supported by the results presented in Table 2.3.

While the information in Table 2.3 is relevant to sensor design, binder conductivity does not alone determine how the material will perform as a sensor. Powder fillers may not generally present the highest conductivity gains, but they have proven highly beneficial

for strain sensing applications (Han et al., 2010b, 2009). The interrogating electronics, the spacing between electrodes, the volume of the sample, and even the requirements of the application: these are all just examples of variables that can be tuned to deliver adequate sensing performance with almost any AAM formulation.

The addition of conductive filler does however, provide other important benefits: when added in appropriate quantities they can significantly enhance the mechanical properties of the composites (Abbasi et al., 2016; Behera et al., 2018; Khater and Abd El Gawaad, 2016; Saafi et al., 2015; Vilaplana et al., 2016). One of their only major downsides is that they increase cost, and the additional costs can be significant when scaled to the volumes of material required in a civil engineering context.

2.3.2.5 Electrode layout

The electrode layout used to apply electrical excitation and measure the response of an AAM plays an important role in the behavior of the electrical system, and hence the sensing capabilities. AAM follow a similar principal to OPC in this regard. Table 2.4 summarizes the electrode configuration of reported AAM sensing applications.

Table 2.4 – Electrode configuration for AAM sensing applications.

Matrix	Precursor	Number of probes	Material of probe	Attachment method	Reference
Paste	Fly ash	2-probe	Graphene	Embedded	(Saafi et al., 2016)
Paste	Fly ash	4-probe	Copper	Embedded	(Saafi et al., 2014), (Saafi et al., 2013)
Paste	Fly ash	2-probe	Steel mesh	Embedded	(Saafi et al., 2018)
Paste	Fly ash	4-probe	Copper fibers	Embedded	(Perry et al., 2015)

Paste	Fly ash	4-probe	Stainless steel wires	Embedded	(Biondi et al., 2020)
Paste	Fly ash	4-probe	Brass plates	Embedded	(Payakaniti et al., 2017)
Paste	Metakaolin	2-probe	Copper wires	Embedded	(Bi et al., 2017)
Paste	Metakaolin	4-probe	Stainless steel wires	Embedded	(Vlachakis et al., 2020)
Paste	GGBFS	4-probe	Copper wires	Wound around substrate with conductive silver paint	(Vilaplana et al., 2013)
Mortar	Metakaolin	2-probe	Copper foils	Attached	(Lamuta et al., 2016), (Candamano et al., 2019)
Mortar	Metakaolin	4-probe	Copper wires	Wound around substrate with conductive paste	(Lamuta et al., 2017)
Mortar	GGBFS	2-probe	Copper mesh	Embedded	(Rovnaník et al., 2019a), (Rovnaník et al., 2019c)
Mortar	GGBFS	4-probe	Self-adhesive copper tape	Attached with graphite conductive paste	(Rovnaník et al., 2019b)
Mortar	GGBFS+ fly ash	4-probe	Titanium mesh	Embedded	(Deng et al., 2019)

Concrete	Fly ash	2-probe	Copper wires	Wound around substrate with conductive silver paste	(Vaidya and Allouche, 2011)

As shown in Figure 2.3 interrogation can be achieved with two-probe or four-probe electrode layouts. While two-probe sensing provides a simpler setup, this method means that the contact resistances and lead resistances of the electrodes contribute to the resistance measurement. Four-probe sensing, on the other hand, significantly reduces the contribution of lead and contact resistances, allowing only the AAM specimen itself to be measured.

Four probe sensing can either be in a serial arrangement (i.e. a linear configuration, as shown in Figure 2.3a & Figure 2.7a or in a rectangular arrangement with the electrodes placed at the corners of the specimen, also known as the Van der Pauw (VDP) configuration (Figure 2.3c, Figure 2.3d & Figure 2.7b). Both these applications have merits and can be advantageous in various situations when used accordingly.

2.3.2.5.1 Serial arrangement

Linear layouts, shown in Figure 2.7a, are the most commonly used electrode configuration in AAM and OPC sensing. This layout is applicable to the majority of cementitious sensing applications. The electrodes are usually equally spaced or in proportionate distances and are symmetrical in reference to the center of the substrate. The electrodes are divided as ‘inner’ electrodes and ‘outer’ electrodes, as depicted in Figure 2.7a, in which voltage or current are applied and measured respectively.

Careful consideration must be given primarily in strain sensing as the response of the substrate is dependent on the direction of the applied load. In uniaxial compression and tension the load is typically parallel to the electrodes. Under flexural tests, the load is primarily perpendicular to the electrodes. Altering the measuring configuration can ultimately impact the response of the specimen (Liu et al., 2018). Furthermore, in a linear setup the current density is concentrated between the electrodes, this essentially provides a more localized sensing capability for the entire substrate.

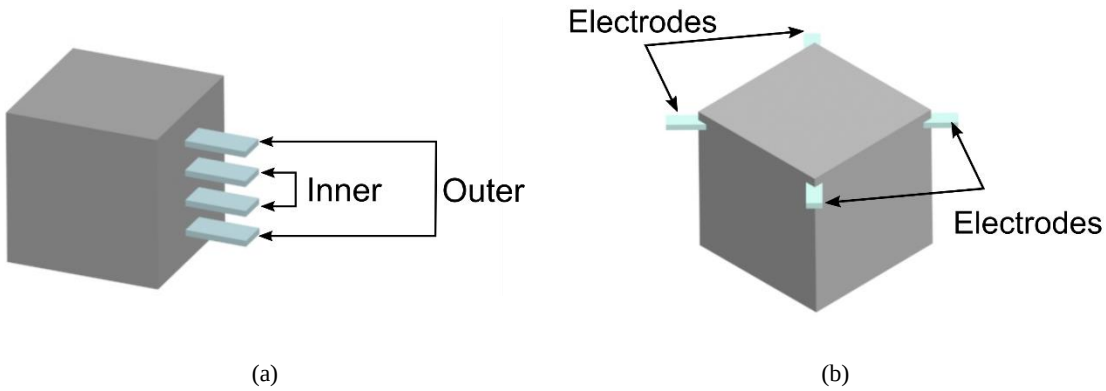

(a) (b)

Figure 2.7 – Electrode array for AAM sensing a) serial arrangement b) Van der Pauw arrangement.

2.3.2.5.2 Van der Pauw arrangement

In the Van der Pauw configuration, shown in Figure 2.7b, the electrodes are placed at the corners of the specimen (van der Pauw, 1958). This approach measures the overall average resistance of the sample as the voltage and current are applied / measured over the entire span of the sample's surface. The layout is also beneficial as it minimizes the concentrated stresses that can be developed near the electrodes during curing (Yao et al., 2017). This occurs as shrinkage during curing creates stresses at the electrode-material interface that can cause cracking and delamination, particularly in thin samples. The use of VDP is thought to reduce and spread stress, and it is what allows electrodes to be embedded successfully in these thin samples, rather than attached onto the substrate with conductive paint.

While the VDP method is typically employed in samples with low thickness, it can also be used in larger specimens as well (Biondi et al., 2020). The distances between electrodes are essentially predefined by the geometry of the sample. The application and measurement of the electrical properties are carried out over a larger area allowing for an average measurement of substrate resistance (not local as with the linear layout) (Yao et al., 2017). This method provides multiple options in terms of the direction of voltage application. As a result, consistency in probe connections is required for repeatability and proper interpretation of the sensor's response.

Under strain sensing, in order to mirror the performance of the linear configuration, for uniaxial compression and tension, the voltage and current should be measured and applied

parallel to the applied load. Similarly, these two measurands should be perpendicular to the applied load under flexure.

2.3.2.5.3 Embed or surface mount

Embedding electrodes has shown more consistent and reliable results than surface-mounting electrodes with conductive paint (Chiarello and Zinno, 2005; Han et al., 2007). However, embedding can result in additional stresses to the AAM matrix, resulting in cracking during curing (Han et al., 2007; Tang et al., 2016). Embedding thin wires (rather than large electrodes) can reduce stress concentration and minimize the mechanical impact of the electrodes on the AAM during curing (Biondi et al., 2020; Vlachakis et al., 2020).

2.3.2.5.4 Electrode-less measurement

In a recent study, Zhuang et al. (2021) used an electrodeless system to monitor the early age reactions of slag AAM. The authors employed a coil-transformer system that was able to generate an electric and magnetic field inducing voltage and current. The current setup of this system though limits its application particularly in strain-sensing but has the potential to pave the road for newer electrode configurations in future applications.

2.3.2.6 Sensor interrogation

In general sensor interrogation of self-sensing systems is based on measuring the change of electrical properties of the sample (in this case AAM) in response to an applied external factor e.g. strain, temperature, water content.

A general sensor characterization equation for AAM has the form of equation (2.7):

$$\frac{\Delta M}{M_0} = f(\varepsilon) + g(\Delta T) + h(\Delta w) \tag{2.7}$$

where M is the electrical response variable measured (e.g. conductivity, resistivity, resistance, impedance, or capacitance), M_0 is the response variable with no applied strain, temperature change or moisture change, $\Delta M = M - M_0$, and f, g and h are functions that parameterize the response to changes in strain, ε, temperature, ΔT, and moisture, Δw. The functions f, g, h, and their constants are what need to be parameterized. The methods and results of this parameterization are outlined in detail in the following sections.

2.3.3 Strain sensing

2.3.3.1 Loading schemes

Strain sensing is the most prominent application for AAM sensors. The electrical response of AAM components to strain is similar to OPC components. When the applied load is colinear to the serial electrode configuration of the substrate, under compression the resistance (and impedance) of the sample decreases. Likewise, under tension the resistance of the specimen increases. This behavior has been widely reported in both AAM (Perry et al., 2015; Rovnaník et al., 2019a; Saafi et al., 2018, 2016, 2014; Vilaplana et al., 2013) and OPC (Azhari and Banthia, 2012; Han et al., 2017, 2009; Xiao et al., 2011; Yoo et al., 2018a) strain sensing. Figure 2.8a and b display a typical sensing response for AAM under compression and tension under constant temperature and humidity for ambient working conditions. The effects of temperature and humidity on the strain response of AAM have not been studied. Based on previous OPC studies it can be inferred that a similar response will occur under different conditions however further study is required to investigate the behavior in greater depth. The loading schemes for the strain characterization of cementitious materials typically employ monotonic or cyclic loading.

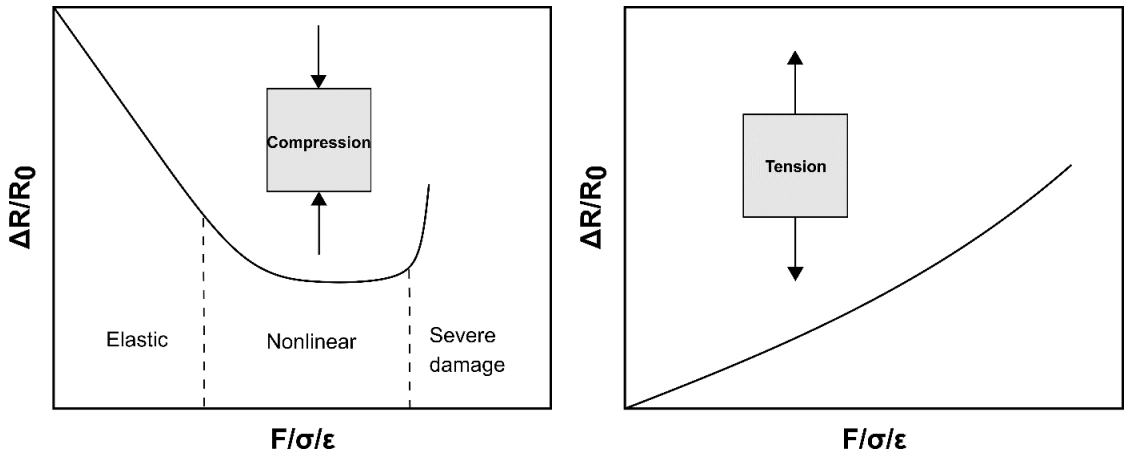

(a) (b)

Figure 2.8 – Diagram of typical response of AAM under a) compression b) tension; The x-axis represents the force, stress, or strain applied to the binder. The y-axis displays the fractional change in resistance (or impedance) in relation to the external factors applied.

2.3.3.1.1 Monotonic loading

Under monotonic loading, a load is applied at a constant rate to the AAM and is removed once the test has terminated. The sensing response is different for tension and compression: not just in its sign. Under tension, resistance tends to increase in a quasi-linear manner (Yoo et al., 2018a). In compression, however, the response of the substrate differs and can be typically broken down into three regions depending on the loading amplitude, as illustrated in Figure 2.8a and Figure 2.9:

1) **Elastic:** The first region of monotonic loading coincides with the elastic region of the substrate. In this zone, the relationship between change in resistance and applied strain is considered to be linear (Li et al., 2006; Sun et al., 2014) or of a linear-like function (Ding et al., 2019c; Han and Ou, 2007). The sensor's performance is usually at its peak within this region. In various cases, a nonlinear segment with low sensitivity at the very early stages of loading has been detected (Lamuta et al., 2017; Rovnaník et al., 2019c) which has also been regarded as a separate region in monotonic compression altogether (Galao et al., 2014). This has led to applications commencing above zero (Lamuta et al., 2017; Rovnaník et al., 2019c; Saafi et al., 2016). While this has been attributed to contact resistance between the substrate and electrodes in two-probe sensing (Rovnaník et al., 2019c),

this behavior has also been observed in four-probe sensing applications as well (Lamuta et al., 2017).

2) **Non-linear:** In the second region of monotonic loading, the resistance of the materials continues to change, however the sensing performance is generally lower and the response at this stage is nonlinear which eventually plateaus (small-no change for load applied) (Azhari and Banthia, 2012; Yoo et al., 2018b). At this stage damage to the matrix has begun in the form of cracks and defects. This leads to the destruction and reconstruction of the conductive network and ultimately reaching a state of balance (Tian et al., 2019; Wang et al., 2008).
3) **Severe damage:** Lastly, the third region of monotonic compression is associated with severe damage to the matrix as the cracks continue to expand and the performance is being compromised. At this juncture an abrupt increase in resistance is typically expected with increasing load (Wang et al., 2008). The substrate in this instance essentially loses its sensing capabilities, and resistance may not even begin to return to its original baseline value once load is removed (Han et al., 2015; Wang et al., 2008).

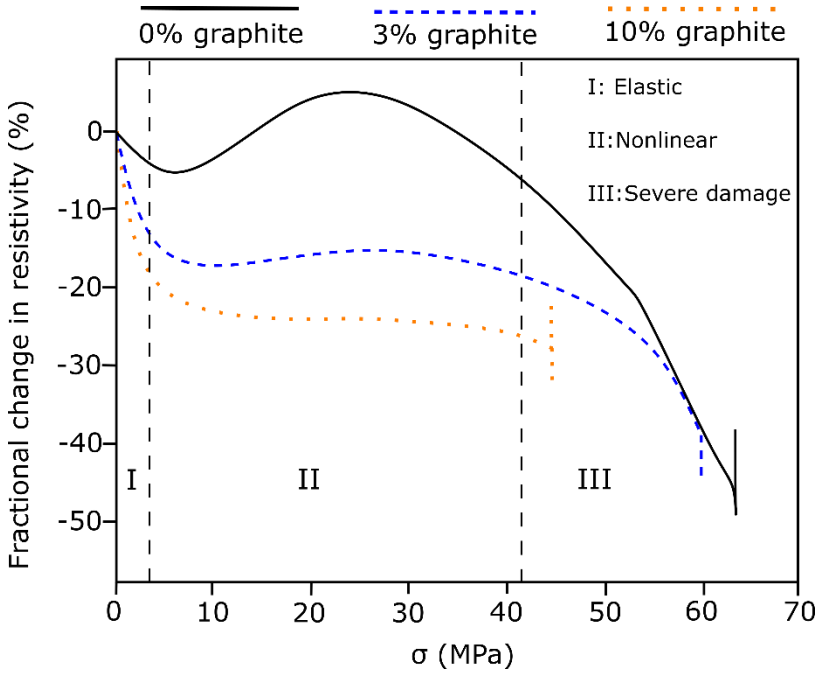

Figure 2.9 – Fractional change in resistivity of slag AAM under monotonic compression for three filler contents, example adapted from Rovnaník et al. (2019a).

2.3.3.1.2 Cyclic loading

Cyclic loading refers to the loading and unloading of a substrate multiple times under a certain magnitude. This loading scheme typically takes place within the elastic region of the material (Ding et al., 2019c; Konsta-Gdoutos and Aza, 2014): the load applied is normally below 30% of the ultimate failure load (Han and Ou, 2007). As such the sensor response of the AAM is linear in both tension and compression (Yoo et al., 2018c). Figure 2.10 provides an example of the response of slag AAM under repeated loading.

When referring to cyclic loading, the terms reversible and repeatable are often used to characterize the performance of the sensor. The term reversible indicates that the resistance of the substrate can start reverting towards its initial value once the applied load has been removed: this is often the case regardless of the magnitude of load applied. By repeatable, it is meant that the sensing performance of the sample (e.g. the change in resistance in regards to the applied load) remains fairly constant after multiple loading cycles.

The resistance of the material at the beginning of the sensing test is usually referred to as the 'baseline resistance' or 'initial resistance', and is denoted as R_o. Since the test is taking place within the elastic region, according to Hooke's Law the sample behaves elastically and reverts to its initial state (Beer et al., 2009). Subsequently, the resistance is also expected to change reversibly close to its initial value (Konsta-Gdoutos and Aza, 2014; Sun et al., 2017a). That said, AAM like OPC is only ever *quasi*-linear: due to the internal changes inside the matrix upon every load cycle, repeatable strain sensing can be difficult to achieve (Fu and Chung, 1996; Sun et al., 2014), even in the linear region (if the material enters the plastic region, repeatable sensing is not achievable, as there is a reconstruction of the conductive network inside the matrix upon load removal (Han et al., 2017).

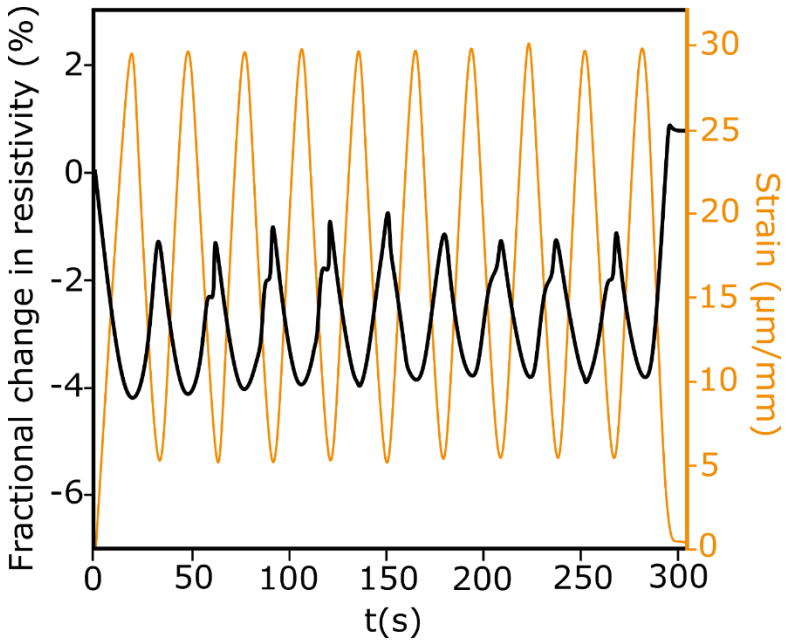

Figure 2.10 – Fractional change in resistivity of slag AAM under cyclic flexural loading, example adapted from Rovnaník et al. (2019b).

2.3.3.1.3 Other strain responses in AAM samples

While most sensing applications follow the above behaviors, self-sensing cementitious materials are comprised of a diverse and broad range of available materials and system layouts, and therefore exceptions to the rules above are actually rather common.

To provide a few examples, in a monotonic compression AAM application by Bi et al. (2017) it was reported that upon load the change in resistance in the sample continuously increased rather than decreased. It was posited that the formation of cracks in the matrix hindered ion migration. While this is a justifiable explanation, it was also mentioned by the authors that the binders were fabricated with the electrodes perpendicular to the applied load and on different planes. This approach differs from the conventional orientation employed in these circumstances (Han et al., 2007) and could have ultimately influenced the sensing response of the sample (Liu et al., 2018; Wen and Chung, 2000).

In a similar application for AAM under monotonic compression, as can be seen in Figure 2.9, Rovnanik et al. (2019) mentioned that upon loading the resistance of the matrix initially decreased as expected in the elastic zone, however as the load increased, the resistance began increasing until it started decreasing again up until failure. This behavior was explained due to the initial formation of cracks and the destruction of the conductive network and the subsequent reconstruction of the conductive network due to the healing of the defects.

Finally, Vaidya and Allouche (2011) reported a fluctuation in the electrical response of carbon fiber AAM cylinders under compression. It was mentioned that this behavior could be attributed to the simultaneous densification of the AAM paste and the development of micro-cracks as both these occurrences have opposite effects on the resistance of the sample.

2.3.3.2 Gauge factors

The performance of a strain sensing material is generally evaluated by the change in resistance compared to the applied strain. The most common approach used in these applications is the strain sensitivity coefficient, otherwise known as the gauge factor (GF) which is also used in commercial strain gauges. The GF is calculated by the fractional change in resistance divided by the applied strain, equation (2.8).

$$GF = (R_i - R_0)/R_0/\varepsilon \quad (2.8)$$

where R_0=resistance at start of the test, R_i=resistance at given strain, ε=applied strain. Alternative methods of assessing strain capability similar to the gauge factor include

expressing the change in resistance per unit of stress, equation (2.9), e.g. 100Ω/MPa or by displaying the resolution of the sensor in terms of strain sensitivity e.g. 1000με.

$$(R_i\text{-}R_0)/\sigma \quad (2.9)$$

Where σ=applied stress. The strain response may differ between loading cycles due to repeatability issues resulting from microcracks and deformations in the matrix (Yoo et al., 2019) or due to polarization effects (Deng et al., 2019).

Table 2.5 below displays the reported strain sensing performances and GFs of AAM. AAM showcase similar strain sensitivity to OPC exhibiting GFs within similar orders of magnitude in respective applications (Baeza et al., 2013; D'Alessandro et al., 2016; Han et al., 2017; Liu et al., 2018; Materazzi et al., 2013; Sun et al., 2017b). The highest reported GF for AAM is 2610 in a GGBFS+fly ash ceramsite-carbon fiber application (Ma et al., 2020). In the same study the report GF for binders without ceramiste remained high, 2027, albeit with a different mix design. This sensing performance is comparable with a study on OPC with nickel powder that reported GF = 1930 (Han et al., 2009). Table 2.5 also presents strain sensing values such as resistance per unit stress (Ω/MPa), electric charge per unit force (pC/N) and the fractional change in resistance ($\Delta R/R_0$). While these values provide important information in their own respect, a comparison with other applications is difficult to make with these values alone. Therefore it is recommended that the GF is used in these instances to allow for simpler comparisons with other strain sensing applications. If other strain sensing values are used then information such as strain, modulus of elasticity of binder and conversion into common electrical units should be provided to allow for the calculation of the GF.

Note that AAM strain performance presented in Table 2.5 is based on 'standard' testing conditions i.e. at room temperature and once the substrate has reached moisture equilibrium. The influence of additional factors such as moisture and temperature on strain performance have not yet been accounted for in AAM apart from certain niche applications (Lamuta et al., 2016). In comparison, the effects of moisture (Demircilioğlu et al., 2019; Zhang et al., 2019) and temperature (Hong et al., 2018) on OPC strain sensing have already been reported. While the literature available is fairly limited, it can be viewed

that metakaolin and ground granulated blast furnace slag based AAM have the potential of showcasing high sensing capabilities compared to fly ash AAM. Lastly, as can be seen in Table 2.5, compared to OPC, AAM also exhibit sensing capabilities without the use of conductive filler.

Table 2.5 – Strain sensing performance of AAM. Notations-sodium silicate (Na_2SiO_3), sodium hydroxide (NaOH), sodium carbonate (Na_2CO_3), potassium silicate (K_2SiO_3), potassium hydroxide (KOH).

Matrix	Precursor	Activator	Conductive filler	Filler concentration	Application	Loading amplitude	Gauge factor or reported response	Reference
Paste	Fly ash	Na_2SiO_3+NaOH	No filler	-	Tension	10N-40N	358	(Saafi et al., 2016)
Paste	Fly ash	Na_2SiO_3+NaOH	Graphene oxide sheet	0.35 wt%	Compression Tension	0.6-12MPa 200-1000με	43.87 20.7	(Saafi et al., 2014)
Paste	Fly ash	Na_2SiO_3+NaOH	No filler	-	Compression	0-100kN	47*	(Perry et al., 2015)
Paste	Metakaolin	Na_2SiO_3+NaOH	Carbon nanotubes	0.25% volume	Compression Bending	7-9% 0.05%-0.08%	663 724.6	(Bi et al., 2017)
Paste	Metakaolin	Na_2SiO_3+NaOH	PEDOT: PSS solution	-	Compression	Up to 200 N	loading: 376.9 unloading: 513.3	(Chen et al., 2019)
Paste	GGBFS	Na_2SiO_3+NaOH	Carbon fiber	0.58% volume	Compression	0-8kN	662	(Vilaplana et al., 2013)
Mortar	Metakaolin	Na_2SiO_3+NaOH	Graphene	1wt%	Compression	1kN-5kN	1986	(Lamuta et al., 2017)

Mortar	GGBFS	Na_2SiO_3	No filler	-	Compression	5-50kN	97.13 Ω /MPa; 35*	(Rovnaník et al., 2019c)
Mortar	GGBFS	Na_2SiO_3	Graphite powder	30wt%	Compression	5-50kN	292*	(Rovnaník et al., 2019a), (Rovnaník et al., 2017b)
Mortar	GGBFS	Na_2SiO_3	Carbon black	4%wt	Flexure	0.07-0.50kN	≈1300*	(Rovnaník et al., 2019b)
Mortar	GGBFS	Na_2SiO_3+KOH+Na_2CO_3 (solid)	Carbon nanofibers /Carbon black/graphene nanoplatelets	1%wt	Compression	1-3kN	62/65/39	(D'Alessandro et al., 2020)
Mortar	Fly ash+GGBFS	Na_2SiO_3+NaOH	Carbon fiber+ ceramsite	0.3wt%-35%	Compression	6.25-18.75 MPa	2610	(Ma et al., 2020)
Paste	Fly ash	K_2SiO_3	No filler	-	Compression	0-15kN	11 Ω/MPa	(Saafi et al., 2018)
Mortar	Metakaolin	Na_2SiO_3+NaOH	No filler	-	Compression	0-2500 N	4.02 ± 0.49 pC/N	(Lamuta et al., 2016)
Mortar	Metakaolin	Na_2SiO_3+NaOH	Graphene	1wt%	Compression	0-2500 N	11.99 pC/N	(Candamano et al., 2019)
Mortar	GGBFS+ fly ash	Na_2SiO_3+NaOH	Carbon fiber	0.1% volume	Compression	6.25-18.75 MPa	$\Delta R/R_0$=0.11	(Deng et al., 2019)

Concrete	Fly ash	Na_2SiO_3+NaOH	Carbon fiber	0.4wt%	Compression Bending	0-9.34kN	6-7.5 Ω/MPa	(Vaidya and Allouche, 2011)

*Not provided by authors, calculated from data available in cited paper (s)

2.3.3.3 Conductive filler applications

As mentioned in Section 2.3.2.1, conductive filler is added to cementitious materials to increase their conductivity thus making them more suitable for large area/volume sensing applications. When AAM are loaded with conductive fillers, the sensing mechanism is attributed to both ionic and electronic conduction (Payakaniti et al., 2017). Under strain tests, the response is dominated by conduction within the filler, and the change of the conductive network inside the matrix. In situations in which the applied load generates cracks in the sample, the resistance is expected to abruptly increase due to the destruction of the conductive network (Deng et al., 2019; Rovnaník et al., 2019a, 2019b; Saafi et al., 2013).

The types of conductive filler that have been used in AAM strain sensing include carbon fiber (Deng et al., 2019; Vaidya and Allouche, 2011; Vilaplana et al., 2013), graphene (Lamuta et al., 2017; Saafi et al., 2016), graphite powder (Rovnaník et al., 2019a), carbon nanotubes (Bi et al., 2017; Saafi et al., 2013) and carbon black (Rovnaník et al., 2019b):

- With respect to carbon fiber, the change in resistance has been attributed to the reduction in the conduction length due to physical shortening of the compression surface (Vaidya and Allouche, 2011), and the change of the proximity between fibers (Deng et al., 2019).
- For a graphene-based application, Saafi et al. (2014) reported that the electrical response of graphene composites is attributed to the contact resistance of the overlapped graphene filler. When the contact area between the graphene sheets increased under compression, the resistance of the material would decrease. Similar behavior was also reported by Lamuta et al. (2017) in a graphene metakaolin-based application under compression.
- Similar to carbon fibers, in carbon nanotube applications the resistance of the matrix is influenced by the distances between the filler under mechanical load (Bi et al., 2017; Saafi et al., 2013). Coating carbon nanotubes with SiO_2 was reported to result into a better conductive network, due to greater dispersion, allowing for the greater detection of cracks (Bi et al., 2017).

- For graphite powder and carbon black the changes in resistance have been attributed to changes in the conductive path the current follows in the matrix (Rovnaník et al., 2019a,b). Chen et al. (2019) coated metakaolin AAM with a conductive polymer PEDOT: PSS solution. The sample was subjected to natural and artificial cracking and tested under uniaxial compression. The conducting mechanism proposed by Chen et al. was coupled-mechanical-conductive contact mechanism based on the Hertizan contact model between cracks.

2.3.3.4 Filler free applications

As mentioned in Section 2.3.3.2, AAM have seen multiple applications without the use of conductive filler due to ionic conductivity of the alkali metals in the matrix. In simple terms, most researchers accept that strain affects the mechanisms responsible for hopping of the Na^+ or K^+ ions in the matrix (Bi et al., 2017; Padma Kumar and Yashonath, 2006; Saafi et al., 2018, 2016). The exact mechanisms are not completely understood, however. For strain-sensing applications the following more elaborate mechanisms have been provided by authors to explain the change in electrical properties of AAM:

I. Lamuta et al. (2016) proposed a chemical-physical model to explain the piezoelectric effect of AAM based on ionic mobility due to the presence of water. This effect is promoted by the migration of mobile hydrated cations under loading in the pores of the AAM matrix, thus creating a charge imbalance and local dipoles. The Na^+ ions balance the single negative charge associated with aluminium (III) in tetrahedral coordination. In completely dry samples, the AAM did not exhibit any piezoelectric effect due to the absence of water. Hydration reduces the cation–lattice electrostatic interaction through cation–water interaction, thus resulting in a weaker bond that promotes the Na^+ migration away from the framework wall during mechanical loading and therefore creates the charge imbalance. Figure 2.11 presents a schematic representation of this model.

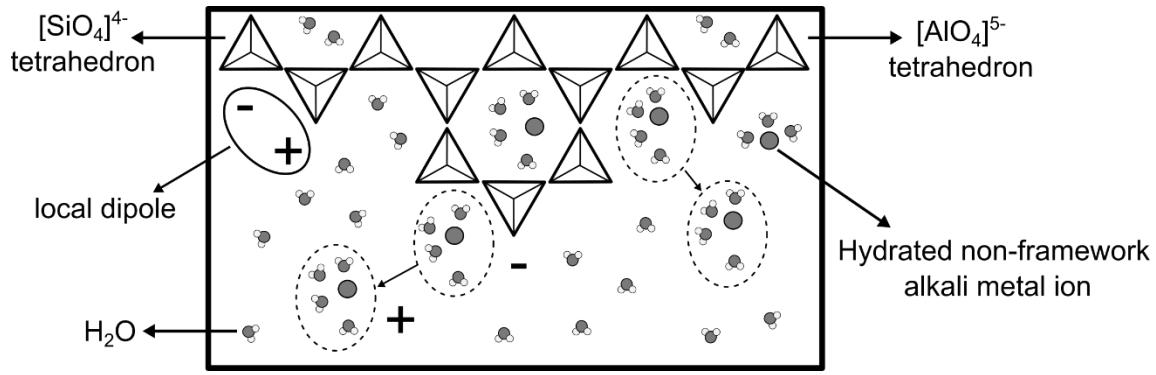

Figure 2.11 – Schematic representation of model proposed for the direct piezoelectric effect in AAM. The amorphous network is built from SiO_4 and AlO_4 tetrahedrons, which are joined at the corners with oxygen. The distancing between the cations and the framework (indicated by dashed lines) causes charge imbalance and the formation of local dipoles. Adapted from Lamuta et al. (2016).

II. Saafi et al. (2018, 2016) stated that the alkali ions diffuse in the structure by hopping through vacancy sites to balance the negative charge on the AlO_4^- tetrahedral. It was hypothesized that the induced load to the substrate changes the lattice structure and alters the ion diffusion paths (essentially the distances between electron holes) in the matrix. As a result, it has been speculated that this changes the activation energy barrier the ion is required to overcome to accommodate a vacant site. As the hopping distance changes this subsequently affects the ion movement inside the AAM and as a result the resistance of the substrate changes accordingly. Figure 2.12 presents a schematic drawing of the ion hopping mechanism that can be found in AAM and Figure 2.13 explains the ion diffusion paths in AAM under applied stress.

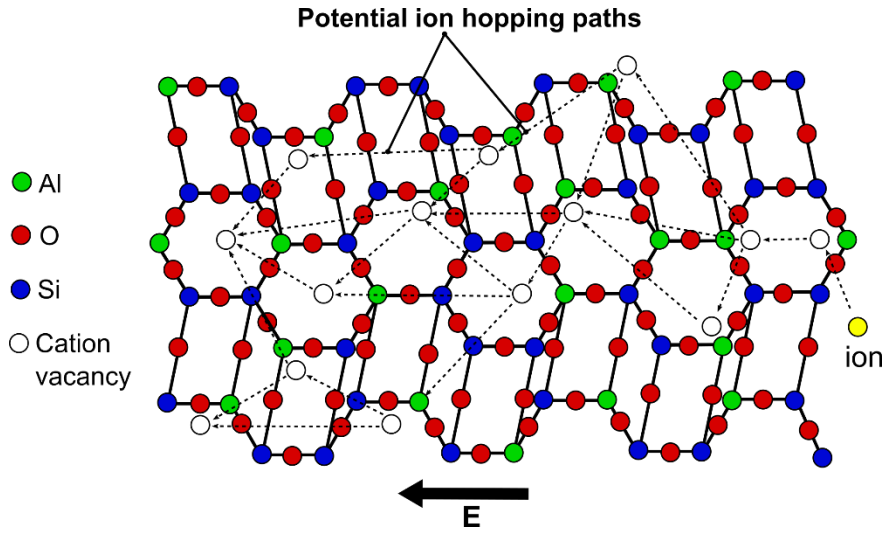

Figure 2.12 – 3D crystal structure of AAM and ion hopping of alkali metal under electric field, adapted from Saafi et al. (2016).

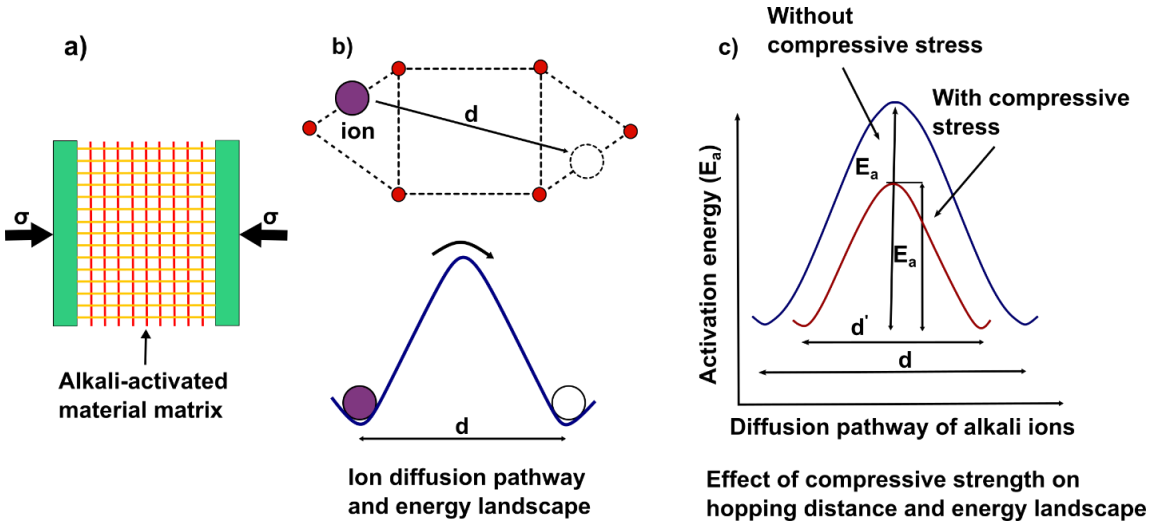

Figure 2.13 – Self-sensing mechanism in AAM a) AAM sensor under stress, b) ion diffusion pathway in the matrix and energy landscape, c) effect of the compressive stress on the activation energy and hopping distance d; adapted from Saafi et al. (2018).

III. Bi et al. (2017) mentioned that the water in the matrix facilitates the migration of Na^+ ions within the framework during mechanical loading which leads into ionic conduction. As ionic conduction is associated with the movement of hydrated Na^+ ions, the formation of the cracks in the substrate during loading potentially hindered the migration process.

IV. Moreover, in the case of slag-based AAM it was reported by Rovanik et al. (2019) that apart from the alkali metals ions in the matrix, the Fe ions found in the precursor also have a positive effect on the sensing capability of the substrate. This ultimately led to a combination of ionic, contact and tunneling conduction. This was explained due to the fact that the Fe content in the slag precursor does not always contribute to the overall chemistry of the binder and is passivated in the pore solution (Bernal et al., 2014c). However, that is not to say that all Fe does not contribute to alkaline activation. Slag with high Fe content has seen successful applications in the formulation of AAM (Machiels et al., 2014; Peys et al., 2019, 2018). As a result, this conduction mechanism remains unproven.

While AAM have been effectively used in sensing applications without conductive filler, situations exist in which filler free samples did not present similar performance. In particular, cases have been reported where AAM failed to showcase any sensing response (Deng et al., 2019) and in which AAM have been rendered unsuitable for certain types of applications due to repeatability and reversibility issues (Rovnaník et al., 2019b). As a result, conductive filler was required in both cases to allow for more reliable sensing performances. Furthermore, even in the cases in which substrates absent of filler saw successful applications, the sensing performance of the substrate undoubtedly benefited from the addition of conductive filler (Bi et al., 2017; D'Alessandro et al., 2020; Rovnaník et al., 2019a; Saafi et al., 2014). Table 2.6 showcases filler free applications of AAM and their respective performances.

Table 2.6 – Strain sensing performance of AAM with no conductive filler. Notations- sodium silicate (Na_2SiO_3), sodium hydroxide (NaOH), potassium silicate (K_2SiO_3), potassium hydroxide (KOH).

Matrix	Precursor	Activator	Application	Loading amplitude	Gauge factor or reported response	Reference
Paste	Fly ash	Na_2SiO_3+NaOH	Tension	10N-40N	358	(Saafi et al., 2016)
Paste	Fly ash	Na_2SiO_3+NaOH	Compression Tension	0.6-12MPa 200με - 1000με	21.6 9.76	(Saafi et al., 2014)
Paste	Fly ash	Na_2SiO_3+NaOH	Compression	0-100kN	47*	(Perry et al., 2015)
Paste	Metakaolin	Na_2SiO_3+NaOH	Compression Bending	7-9% 0.05%-0.08%	62.7 189.8	(Bi et al., 2017)
Mortar	Metakaolin	Na_2SiO_3+NaOH	Compression	1kN-5kN	1662	(Lamuta et al., 2017)
Mortar	GGBFS	Na_2SiO_3	Compression	5-50kN	97.13Ω/MPa 35*	(Rovnaník et al., 2019c)
Mortar	GGBFS	Na_2SiO_3	Flexure	0.07-0.50kN	≈1150*	(Rovnaník et al., 2019b)
Mortar	GGBFS	Na_2SiO_3+KOH+ Na_2CO_3 (solid)	Compression	1-3kN	64	(D'Alessandro et al., 2020)
Mortar	GGBFS+ fly ash	Na_2SiO_3+NaOH	Compression	6.25 - 18.75 MPa	Close to 0	(Deng et al., 2019)
Paste	Fly ash	K_2SiO_3	Compression	0-15kN	11 Ω/MPa	(Saafi et al., 2018)
Mortar	Metakaolin	Na_2SiO_3+NaOH	Compression	0-2500 N	4.02 ± 0.49 pC/N	(Lamuta et al., 2016)

*Not provided by authors, calculated from data available in cited paper.

2.3.4 Temperature sensing

2.3.4.1 Overview

Temperature sensing using AAM is less frequently explored, but is critical: without knowledge of the sensor's response to thermal effects, its strain behavior cannot be decoupled.

The response of cementitious materials to temperature tends to be more complicated when compared to strain sensing. This is because elevated temperatures tend to cause evaporation, and so changes to environmental humidity and AAM matrix moisture (effects which are discussed separately in Section 2.3.5 of this chapter). The result is that temperature characterization must be conducted in a sealed environment with controlled or monitored moisture and humidity conditions.

For the most part the behavior of AAM and OPC under temperature change is fairly similar. As a rule of thumb, as the temperature increases, the resistance of the sample decreases due to increased ion mobility at high temperatures (Biondi et al., 2020). Figure 2.14 displays the fractional change in impedance of AAM for various temperatures. Based on the existing literature in both OPC and AAM, the behavior of cementitious materials under temperature change can be divided into three primary regions. Compared to strain sensing though, these regions are not as distinctly defined and overlapping among regions is quite common.

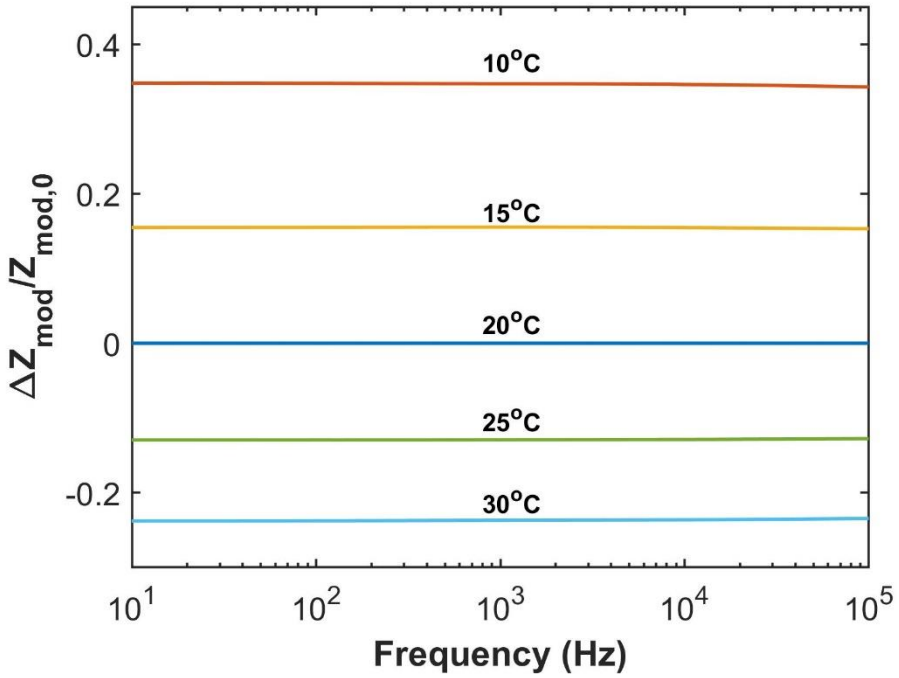

Figure 2.14 – Fractional change in impedance-frequency response for 3D printed metakaolin AAM between 10°C-30°C, adapted from Vlachakis et al. (2020).

2.3.4.2 Sensing behavior at different temperatures

The first region of temperature sensing of reported applications is situated approximately between -30°C up to around 50°C. This section encapsulates most of the temperature sensing tests that have been carried out, and corresponds to the majority of field and civil engineering applications. The behavior for this temperature range is fairly straightforward as when the temperature increases, the resistance of the material decreases (Biondi et al., 2020; Chang et al., 2013; Dehghanpour and Yilmaz, 2020; Demircilioğlu et al., 2019; Lee et al., 2019; MacKenzie and Bolton, 2009; Perry et al., 2015; Saafi et al., 2016; Sun et al., 2017a; Vlachakis et al., 2020).

The second region typically lies between 50°C – 110°C. In this region, the response of the materials begins to showcase somewhat irregular behavior depending on the testing conditions. For metakaolin AAM, it was reported by MacKenzie and Bolton (2009) that as the temperature increased up to 80°C the resistance of the sample started to increase as well due to the depletion of water in the matrix. On the contrary though, in an OPC based investigation conducted by Demircilioglu et al. (2019) under sealed conditions the

resistance of the sample between 50^{o}C – 115^{o}C remained fairly constant due to the equilibrium of water vapor as a result of the sealed environment. Similarly, in another OPC based application under sealed conditions Teomete (2016) reported small changes in resistance between 50 ^{o}C up until 200 ^{o}C.

The third region has so far been loosely defined as “the temperature at which the behavior of the sample begins to change once again”. This point is usually found to lie between 80^{o}C - 200^{o}C. In AAM, MacKenzie and Bolton (2009) pointed out that beyond 80^{o}C the mobile charge-carrying hydrous species were depleted and other charge carrying mechanisms were more significant at this point. Up until 290^{o}C after the water has been removed, the resistance of the material decreased as a function of the added conductive filler content and temperature. Similarly, Gulicovski et al. (2020) noted that at greatly elevated temperatures (500 ^{o}C – 700 ^{o}C) the impedance of AAM decreased as the temperature increased. This was explained due dehydration and dehydroxylation of the AAM, introducing new conduction pathways in the matrix. In addition, Sellami et al. (2019) mentioned that for temperatures beyond 575 ^{o}C the AAM underwent structure rearrangement which ultimately led to the improved alkali metal ion transfer rate and electrical conductivity (decrease in resistance). Under sealed conditions in OPC applications by Teomete (2016) and Demircilioglu et al. (2019) it was reported that beyond a certain point the resistance of the sample started to increase significantly. It was explained by the authors that this rapid increase in resistance was due to the mismatch in behaviors between the cement paste and the aggregates and conductive fiber at elevated temperatures. The cement paste contracted while the aggregates and conductive fiber elongated causing tensile stresses to develop and thus damage inside the matrix. In general, the third region of temperature sensing is highly complex due to the simultaneous occurrence of multiple phenomena. The increased temperature can cause depletion of moisture in the pores of the binder (Lo Monte et al., 2019). Moreover, as previously mentioned, the increased temperature can also cause the expansion of aggregates. Both can lead to cracks in the binder and thus an increase in resistance. At the same time though, elevated temperature increases ion mobility which leads to decreased resistance. In this region applications only for AAM pastes have been reported, in which a decrease in

resistance was observed. It can be inferred that AAM with aggregates will showcase a different response. This region requires greater in-depth analysis to determine the dominant factor affecting resistance for each type of AAM binder.

2.3.4.3 Temperature sensing: characterization equation

Most temperature applications of AAM are conducted at around ambient temperatures, in the first region of temperature sensing. Similar to strain tests, a material's temperature behavior is normally examined by investigating the change in resistance/impedance against the applied temperature. The relationship in this case is not as clearly defined as it is in strain sensing applications as the reported responses tend to vary.

In a fly ash AAM study by Saafi et al. (2016) conducted between -10^{o}C – 35^{o}C, a linear relationship between the change in impedance and temperature was presented, although with a low coefficient of determination (0.802-0.904). Moreover Perry et al. (2016) also reported a linear response between change in impedance and temperature change for fly ash AAM, albeit under a small temperature range ($\Delta T=3^{o}C$) where a linear approximation can be made. A linear change in resistance has also been identified in OPC for temperatures between 25^{o}C – 50^{o}C (Demircilioğlu et al., 2019).

In contrast, Perry et al. (2015) reported a polynomial relationship between change in impedance and temperature change between 10^{o}C – 30^{o}C in a fly ash AAM investigation. More recent and in-depth work on filler free AAM applications between 5 ^{o}C – 30^{o}C and 10 ^{o}C – 30^{o}C conducted by Biondi et al. (2020) and Vlachakis et al. (2020) respectively showcased that the change in impedance in relation to temperature follows an exponential trend, equation (2.10), expressed by Van Meurs (1958) such that:

$$Z_i/Z_0=e^{\left(\frac{A}{T}+BT+C\right)} \tag{2.10}$$

where Z_0=impedance at start of the test, Z_i=impedance at given temperature, T=temperature and A, B and C are constants. Figure 2.15 illustrates the temperature response of printed metakaolin AAM following equation (2.10). Similarly, in OPC based studies carried out by Lee et al. (2019) between 5 °C to 40 °C, Chang et al. (2013)

between -15ºC – 20ºC and Sun et al. (2017a) between -30 ºC – 60ºC, while the response was not characterized, it can be easily observed by the graphs provided that the relationship between resistance and temperature was nonlinear in both instances.

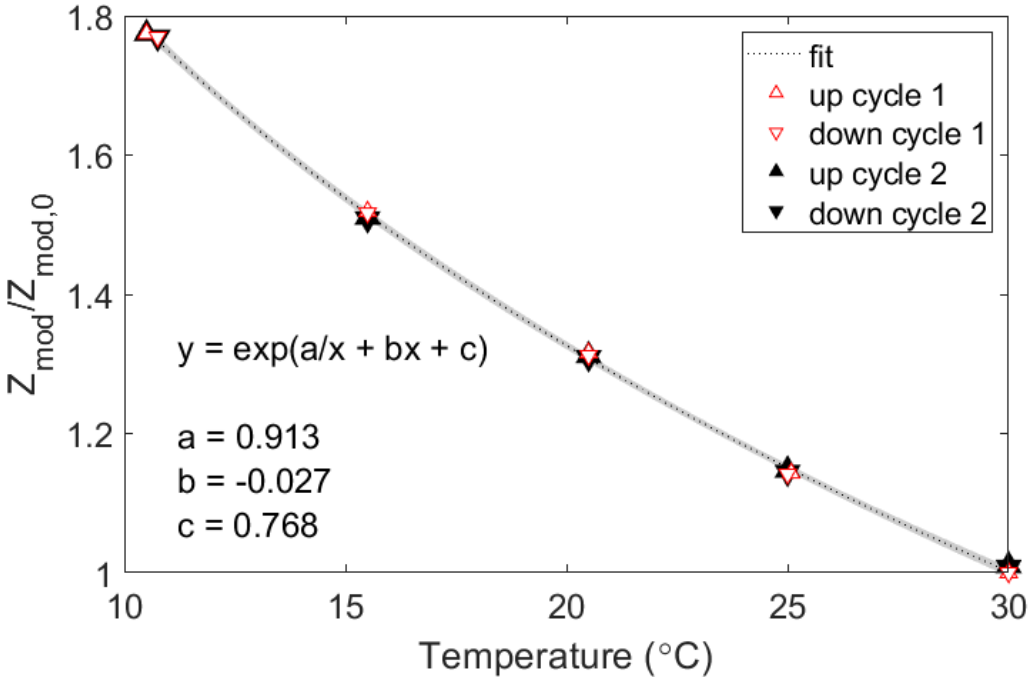

Figure 2.15 – Normalized impedance response of metakaolin 3D printed AAM patch to temperature during four temperature cycles. Z_{mod} is the modulus impedance at a given temperature and $Z_{mod,0}$ the initial modulus impedance at 10ºC (Vlachakis et al., 2020).

Crucially, equation (2.10) is underpinned by accepted physical explanations of the mechanisms responsible for changes in cementitious material conductivity. The temperature response of AAM can be described using the time-temperature superposition principle (Funke and Banhatti, 2006). While this is described in detail by Biondi et al. (2020), the time-temperature superposition principle states that increasing the temperature of an AAM is completely equivalent to speeding up the motion of its ions and conduction mechanisms. In order to produce an electrical current, an ion within the AAM must hop from its existing site to an adjacent site, and that site must relax to accommodate the ion. The longer it takes for an ion to be accommodated, the greater the probability of a backwards hop. Increasing temperature speeds up relaxation, and essentially accelerates ion hopping.

2.3.4.4 Temperature sensitivity values

The temperature response of various AAM applications is presented in Table 2.7. As the characterization equation describing the relationship between temperature and impedance/resistance has historically been poorly defined, the sensitivity values of AAM during temperature characterization has varied.

Saafi et al. (2016) reported a linear temperature sensitivity of k_T = 0.02 $^oC^{-1}$ (21.5kΩ/C) for AAM with graphene-based electrodes. Perry et al. (2016, 2015) in a fly ash-based coating applications showcased a sensor with a sensitivities ranging from k_T = of 0.08 $^oC^{-1}$ to 0.5 $^oC^{-1}$. Cai et al. (2020c) also investigated the Seebeck effect for both fly ash and metakaolin AAM, and quoted their sensitivities as -6.31 μV/^{o}C for fly ash AAM, and -15.12 μV/^{o}C for metakaolin AAM. The Seebeck effect for metakaolin AAM was also investigated by Li et al. (2021). The sensitivity values in that study ranged between 1736–2170 μV/^{o}C, several orders of magnitude higher than what was presented in Cai et al. (2020c). Both studies attributed the response of the samples to AAM microstructure and alkali ions in the matrix. Potential reasons for this vast difference could originate from the fact that Cai et al. (2020c) tested samples after 28 days of curing whereas Li et al. (2021) cured the samples for 7 days. The different moisture content in the samples at the age of testing could lead to different response. Studies have shown that moisture content can heavily impact the sensing response of the AAM (Biondi et al., 2020). Further considerations could include sample sizes and the different alkaline solutions used.

Biondi et al. (2020) explored the temperature response for fly ash AAM for various water content ratios. The temperature sensitivity ranged between 0.06 $^oC^{-1}$ to 0.18 $^oC^{-1}$ and with a repeatability of 1-2% deviation. Additionally, in a 3D printed AAM coating application Vlachakis et al. (2020) reported a temperature sensitivity of 0.1 $^oC^{-1}$ and a repeatability of 0.3 ^{o}C. In a robotic sprayable AAM application. McAlorum et al. (2021) reported the temperature sensing precision of sprayed patches as δT = 0.2 ^{o}C.

Table 2.7 – Temperature sensing response of AAM.

Matrix	Precursor	Conductive filler	Temperature range	Reported response	Reference
Paste	Fly ash	No filler	-10°C - 35°C	21.5kΩ $^{o}C^{-1}$	(Saafi et al., 2016)
Paste	Fly ash	No filler	10°C - 30°C	0.5$^{o}C^{-1}$	(Perry et al., 2015)
Paste	Fly ash	No filler	5°C - 30°C	0.1$^{o}C^{-1}$	(Biondi et al., 2020)
Paste	Fly ash	Magnetite	ΔT=3°C	0.0781$^{o}C^{-1}$*	(Perry et al., 2016)
Paste	Metakaolin	Graphite, single wall carbon nanotube	Up to 340°C	Conductivity function of temperature	(MacKenzie and Bolton, 2009)
Paste	Metakaolin	No filler	10°C - 30°C	0.1$^{o}C^{-1}$	(Vlachakis et al., 2020)
Paste	Metakaolin	No filler	10°C - 30°C	0.2$^{o}C^{-1}$	(McAlorum et al., 2021a)
Paste	Metakaolin Fly ash	No filler	ΔT=45°C	-15.12μV/°C -6.31 μV/°C	(Cai et al., 2020c)
Paste	Metakaolin	No Filler	ΔT=16°C	1736-2170 μV/°C	(Li et al., 2021)

*Not provided by authors, calculated from data available in cited paper

Making a clear comparison between AAM and OPC binders is challenging. While the resistance for OPC binders has been reported for various temperatures, the sensing response has not been characterized as it has for AAMs. Figure 2.16 provides temperature characterization curves for conductive-fiber laced OPC composites reported in (Chang et al., 2013; Demircilioğlu et al., 2019; Lee et al., 2019; Sun et al., 2017a). These data were not explicitly included in the original references, but were determined based on the reported dependencies of electrical resistance, resistivity, or impedance, on temperature. In Figure 2.16, M is the reported electrical quantity measured (e.g. resistance, resistivity, or impedance), and M_0 is the value of that measurand at 20 °C. Normalization using M/M_0 is performed to make fractional shifts in resistance and resistivity comparable, as the

normalization reduces the impact of geometric effects. The fits shown all use an equation of the form, equation (2.11):

$$\ln M/M_0 = -ax + b \tag{2.11}$$

Where the parametric constants, a and b, for each study are listed in Table 2.8.

Table 2.8 – Parametric constants for the fits for temperature characterization of OPC and AAM binders.

Application	a	b	Reference
OPC	0.054	1.01	(Chang et al., 2013)
OPC	0.050	1.00	(Lee et al., 2019)
OPC	0.040	0.86	(Sun et al., 2017a)
OPC	0.030	0.68	(Demircilioğlu et al., 2019)
AAM	0.028	0.58	(Vlachakis et al., 2020)

An AAM study by Vlachakis et al. (2020) is also included in Figure 2.16 for comparison. As shown, the temperature response of OPC and AAM binders is comparable. However, temperature sensing is affected by numerous factors such as saturation of the binder (Biondi et al., 2020) and therefore a definitive claim cannot be made with these data alone.

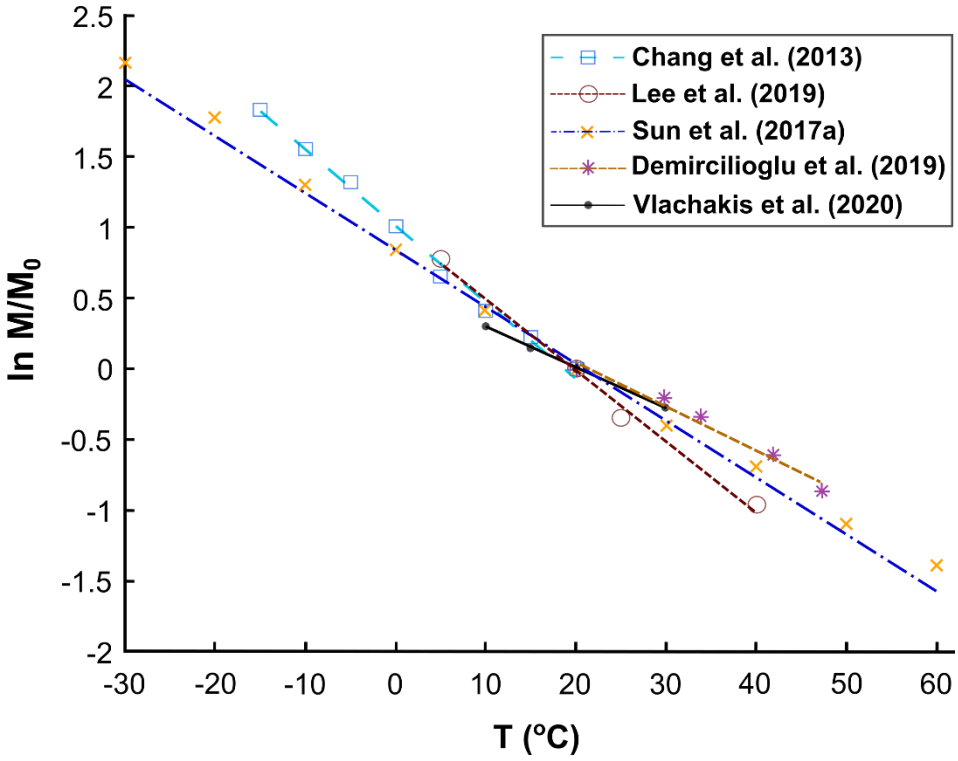

Figure 2.16 – Characterization of temperature sensing response for OPC and AAM binders. M refers to the reported electrical measurand (resistance, resistivity or impedance) and M_0 the value at 20 °C.

2.3.5 Moisture sensing

Moisture sensing is infrequently explored in AAM, but is important even in strain sensing applications due to moisture's significant impact on AAM electrical conductivity.

Moisture is here defined as the water content inside the matrix: this is something which can be impacted by environmental humidity condensing in AAM pores or existing in a vapor phase. It is universally acknowledged that increasing the water content, whether AAM or OPC, increases the sample's conductivity (Brantervik et al., 1990). The relationship between resistance and moisture content is typically expressed as an exponential (Saleem et al., 1996) or by a power law correlation (Brantervik et al., 1990; Nguyen et al., 2017).

A study was carried out by Biondi et al. (2020) in fly ash based AAM for water content ranging between 25.5–87.7%. It was shown that similar to temperature, increasing water content in the matrix increases the ion hopping mechanism described in Section 2.3.3.4. Water was explained to increase the connectivity of the pore network and the volume of

the pore network filled with electrolyte solution. It was also posited by the authors that higher frequencies may present a more sensitive region in moisture sensing, which would allow differentiating the sensing response in simultaneous occurrences e.g. temperature and moisture sensing. The relationship between impedance, water content and temperature was defined by equation (2.12):

$$\ln\left(Z_{mod}/Z_{mod,0}\right) = G_1/T + G_2T + G_3/T + G_4T/W + G_5 \quad (2.12)$$

In which $G_{1\text{-}5}$ = constants, T=temperature, W=water content, $Z_{mod,0}$ = impedance at ambient conditions, Z_{mod} = impedance at given temperature and water content. Figure 2.17 displays the moisture response of AAM for different temperatures. Similarly, in cement-based moisture sensing applications the resistance of the specimens increased as the moisture content decreased as the water which acts as an electrolyte in the micro-voids was removed (Demircilioğlu et al., 2019; Teomete, 2016) and due to ionic and moisture conductivity (Saleem et al., 1996).

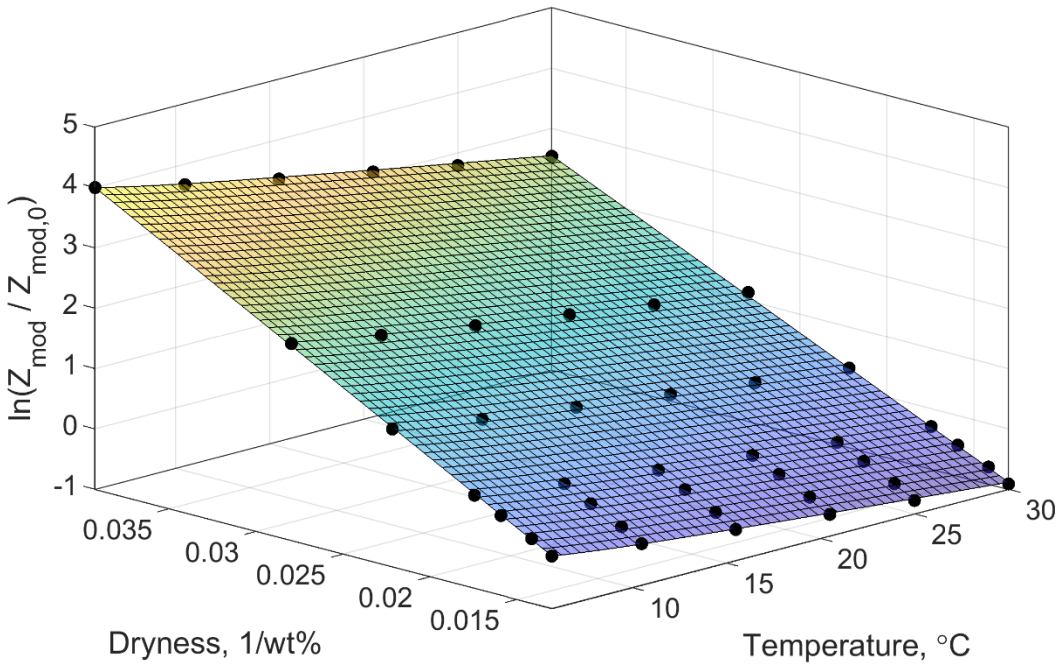

Figure 2.17 – A 3D calibration curve for a fly ash AAM, showing sensor response to both moisture and temperature (Biondi et al., 2020).

2.3.6 Future work and recommendations

While extensive research has been carried out in self-sensing AAM, Table 2.9 highlights that the extent of study is very limited compared to the body of work for OPC. This is simply because AAM are relatively new, and OPC concretes are still the most widely used construction material today. This will change as civil engineers strive to meet climate targets, and it will be important to bear in mind that the work from OPC will not always be translatable to AAM.

Table 2.9 reveals the gaps in knowledge that need to be filled in future work:

- AAM sensor response to humidity *has* not been investigated
- while strain applications exist, they have primarily focused on uniaxial loading: multiaxial applications are quite limited.
- the combined effects of multiple phenomena on the sensing performance of AAM have not been looked into apart from combined moisture and temperature. The impact of both moisture and temperature on strain sensitivity have not yet been explored.

AAM sensing is also currently limited in its applications: most papers are focused on concrete structural health monitoring. Broader applications such as traffic detection would be feasible but are currently absent in AAM literature.

AAM sensing is also limited in the number of techniques it employs. OPC sensing, for example, has already explored small-sized self-sensing composites embedded in larger substrates (Baeza et al., 2013; Liu et al., 2018; Sun et al., 2014). While applications with a similar purpose have been explored in AAM in the form of coatings (McAlorum et al., 2021a; Perry et al., 2016, 2015; Vlachakis et al., 2020), the number of applications and available literature is still quite limited.

Table 2.9 – Could literature be found that demonstrated sensing techniques in OPC and AAM?

Material	Strain	Temperature	Moisture	Humidity	Strain-Temperature	Strain-Moisture	Temperature-Moisture
AAM	Uniaxial, multiaxial limited	Yes	Yes	No	No	No	Yes
OPC	Yes	Yes	Yes	Yes	Yes	Yes	No

As mentioned in Section 2.3.3.4 the sensing mechanism for filler-free AAM is not fully understood but various explanations have been given. A more in-depth explanation of this mechanism is required to further progress in AAM sensing applications.

It has been acknowledged that the performance of AAM is governed by molar ratios rather than the mass ratios that are typically used in OPC (Provis, 2014a). While studies have focused on the effect of the chemical composition and mix design on the conductivity of AAM (Cai et al., 2020b; Cui et al., 2008; Hanjitsuwan et al., 2014, 2011; Payakaniti et al., 2017) a direct translation between molar ratios and sensing capability, apart from very specific applications (Cai et al., 2020c), translation between molar ratios and sensing capability, apart from very specific applications (Li et al., 2021), is currently absent. As can been seen in Table 2.5 and Table 2.6 the reported sensing performances of AAM are quite vast and broad. Correlating the molecular composition with the sensing performance may potentially pave the road for more repeatable and consistent results. With that in mind,

it can be accepted that altering the chemistry of AAM to fit research requirements and performing a proper analysis may be associated with more challenges compared to an OPC mix design.

AAM can be fabricated with different types of precursors, each with a different molar composition. While the reported applications have focused on using fly ash, metakaolin and ground granulated blast furnace slag, the range of available precursors for AAM keeps on increasing. Materials such as rice husk ash, palm fuel ash, red mud etc. have seen applications in AAM fabrication (Provis et al., 2015). This can open the path to new research and development possibilities and perspectives on AAM sensing. Sensing applications have primarily focused on the standard two-part mix of AAM. It has been posited that one-part mixes may provide a more approachable route in future applications of AAM (Provis, 2018). Therefore, exploring one-part AAM mixes may allow a more straightforward approach allowing the material to be more easily deployed in the field.

Finally, while standards for AAM fabrication and sensing applications do not currently exist, a unified approach or common sensing setup for general cementitious sensing is required to allow for more convenient and accurate comparison between applications. A universal methodology will be essential for laying the groundwork for industrial applications. Recommendations that can be considered in future applications follow:

- The chemical composition of all constituents should be reported where possible. A thorough mix design with both solid-liquid ratios and molar ratios of AAM should be included. The curing regime should also be clearly stated e.g., heated cured, sealed conditions etc.
- Gauge factors or common equivalent sensing performance units should be reported in all applications. For strain applications the applied strain and/or modulus of elasticity should also be provided where possible to allow for further analysis and comparisons in future applications.
- An average gauge factor/sensing performance with standard deviation and coefficient of determination should be provided instead of reporting the highest sensing performance values achieved.

- The surrounding conditions e.g., temperature and humidity should be monitored with an external sensing device to ensure a relatively constant testing environment. Strain sensing in particular can be impacted by fluctuations in temperature and humidity.
- The number of samples tested and number of measurements per sample should be reported.
- Proper insulation between the binder and the surrounding environment must be ensured throughout the entire duration of the experiment.
- The type of current, direct or alternating, should be explicitly mentioned. The frequency and sampling rate should also be reported if alternating current is used.
- The orientation of the electrodes should be consistent throughout subsequent tests. For strain sensing, the direction of the electrodes should reflect the anticipated behaviour of the sample e.g., current and voltage are parallel to the applied load for compression and perpendicular for tension.
- A period of stabilization should be allowed for samples prior to testing.
- The state of the binder e.g., dried, saturated, unsaturated etc. and the testing conditions, sealed or unsealed, should be stated.

2.3.7 Summary of self-sensing alkali activated materials.

This section provided an overview of the current state-of-the-art in sensing using alkali activated materials. As our understanding of these materials progresses, agreement between studies will hopefully begin to converge. As alkali-activated materials provide the benefits of being an economically viable and environmentally friendly alternative to OPC, we anticipate this field of research will grow as their use becomes more common. AAM have already seen some successful applications in strain, temperature and moisture sensing either as the main structural material or as a self-sensing coating applied to existing infrastructure. Drawing on the literature outlined in this section the following considerations for the upcoming sensing investigations in this thesis are made:

- AAM can be used in self-sensing applications without relying on the use of electrically conductive filler. This is a key parameter to consider as the presence of filler can pose limitations in 3D printing applications.
- The AAM sensor fabrication, testing and evaluation methods outlined in this chapter will be followed for the temperature and strain characterization of AAM sensors.
- The expected response of AAM under strain, temperature and moisture sensing is established and will be considered in the experimental phase of this thesis.

2.4 3D printing cementitious materials

2.4.1 Introduction

Additive manufacturing, otherwise known as 3D printing, is a layer-by-layer process that enables deposition of a material through a nozzle. 3D printing has seen numerous applications in biomedical engineering (Ghilan et al., 2020), electronics (Espera et al., 2019), and the food industry (Baiano, 2020). Over the past decade, 3D printing has seen rapid growth in the construction sector as well (Buswell et al., 2018; Li et al., 2020; Lim et al., 2012; Salet et al., 2018). This means of fabrication has gained interest as it allows construction without the use of additional formwork allowing for greater construction efficiency, reduced labor costs and less waste production (El-Sayegh et al., 2020; Weng et al., 2020).

Over the years printing methodologies have been proposed for cementitious materials. In this chapter, existing practices are investigated and additional methods are examined to successfully carry out the requirements of this thesis.

2.4.2 Cementitious printing

Common names for the extrusion of cement-based materials include digital concrete construction (Mechtcherine et al., 2019) and concrete printing (Lim et al., 2012). For this chapter we will use the term cementitious printing to refer to the extrusion of ordinary Portland cement (OPC) and alkali activated materials (AAM) paste, mortar and concrete. The first step in 3D printing is data preparation. This involves the drawing of the intended design with the use of computer-aided design (CAD) software and the

conversion of that drawing to stereolithography (STL) format. Following that, the STL file is required to be inserted into slicer software and converted into G-code (a programming language used in manufacturing). Through the slicer software the print path is generated and printing settings, such as print speed and layer height can be modified. The file is then inserted into the 3D printer to initiate the printing process. A flowchart of the data preparation sequence is presented in Figure 2.18.

Figure 2.18 – Data preparation sequence for 3D printing.

Various printing setups have been devised for cementitious printing. The most common printing setups involve an XYZ gantry system with a four or six-axis coordinated motion control system and six-axis autonomous robotic systems. A dispensing unit is mounted onto the gantry or the robot with a pumping delivering system or a syringe feeding material into the extruder. The sizes of these printing systems (gantry and robots) can range from small scale (a few meters) to large scale applications (the size of a lab). Figure 2.19 depicts an example of a syringe-based dispenser mounted onto an x-y gantry system. Large scale gantry printing systems such as those presented by Bos et al.(2016) and Lim et al. (2012), resemble contour crafting (Khoshnevis, 2004). Smaller scale gantry systems that employ to use of syringes rather than pumps are called direct ink writing (DIW). Despite the size of the gantry systems, they are normally situated at fixed locations. Robot printing provides greater flexibility as it can be used mobile and in concurrent applications (Zhang et al., 2018).

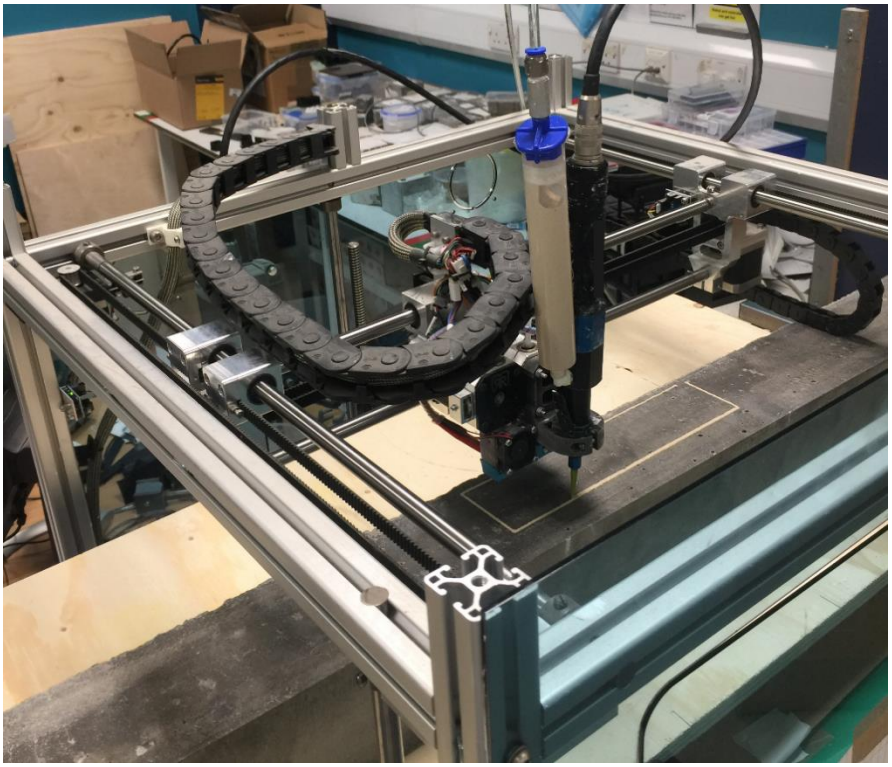

Figure 2.19 – Dispenser mounted onto x-y gantry system of commercial 3D printer.

The uniqueness and intricacies of printing systems reported in existing literature makes it challenging to directly compare them. Analyzing additive manufacturing with the printing system alone does not provide a complete picture on the method followed. Nerella et al. (2020) classified cementitious printing as full width printing and filament printing. In full width printing the nozzle opening is normally the size of the width of the object. As such a single ‘filament’ would be extruded for each layer. Common printing features such as infill and perimeters are absent in this printing method. In filament printing, the size of the nozzle is multiple times smaller than the intended width of the object. Therefore, one layer would require multiple ‘filaments’ to be completed, along with perimeters and infill. The printing method selected will be based on the intended application. For example, beams or panels are most likely to be extruded using full width printing. It is more common for larger printing setups to employ full width printing due to the larger volume of material and equipment. Filament printing is more likely to be encountered in DIW systems due to the small nozzle openings.

The size of the printing system affects the efficacy of the printing method. For instance, two gantry systems with different nozzle openings (e.g. 1 mm and 10 mm) that employ the same printing method may not be able to produce the same quality (refer to Table 2.10 for definition) objects. Furthermore, filament printing of larger scale systems may only require a few 'filaments' compared to DIW systems where filament printing may require tens or hundreds of filaments per layer. The interactions and drying effect between filaments will impact the final result. As such while defining the printing method is useful to provide more context in printing, it is more beneficial when used to compare applications of similar printing setups.

2.4.3 Printing terminology

Cementitious printing employs similar printing terminology to that found in plastic printing. Slight adjustments to the definition of certain terms have been made to account for the nuances of cementitious printing. Common printing terms used in research studies (Bos et al., 2016; Buswell et al., 2018; Labonnote et al., 2016; Panda et al., 2018; Wangler et al., 2019; Zhang et al., 2018) are presented in Table 2.10:

Table 2.10 – Common terminology used in printing applications

Term	Definition
Object	The printed specimen.
Filament/ink	The extrudable cementitious mix
Print bed	The surface in which the filament is printed on.
Print head	The dispensing unit including the nozzle
Layer height	The distance the print bed (primarily in 4-axis applications) or print head (in six-axis applications) moves once a layer has been deposited. The layer height is typically equal to or less than the size of the nozzle
Standoff distance/head distance/print head/nozzle distance	The distance between the nozzle and the previous layer (or print bed for first layer). This distance is typically equal to or less than the size of the nozzle.
Print/tool path	The path the nozzle follows during printing.
Print speed	The speed in which the layer is printed. Common units are mm/s.
Quality	Refers to the combined effects of voids, surface texture and ability to meet intended shape. High quality objects have no voids, smooth surface texture and are able to meet their intended shape.
Perimeter	The outer printed filament of the object. In cement-printing this may be omitted depending on the application

Infill pattern	The print path the nozzle follows inside the perimeters. If perimeters are not used, then the infill pattern normally starts where the conceivable perimeter would have been deposited. Common infill patterns are rectilinear, honeycomb, triangular.
Infill density	The density percentage of the infill pattern.
Time gap/delay time	The time that lapses between two subsequent layers. Time gap has a default value in the time it takes to complete one layer. Additional time gap may be considered in cementitious printing to allow the material to develop sufficient strength to allow for greater structural stability before depositing the next layer.

Cementitious printing usually occurs on flat surfaces, though recent research has explored the possibility of printing on curved surfaces (Borg Costanzi et al., 2018). Similar to plastic printing, print speed impacts the outcome of the printed object. Faster speeds increase the likelihood of more voids and improper filament deposition (Panda et al., 2018; Tay et al., 2019a). As a result, low and constant speed is advised during cementitious printing as this will allow a consistent result across the entire printed specimen. Similarly, a constant layer height should also be employed to ensure the same head distance throughout the print. Changing this distance can lead to objects with a heterogenous structure (Ma et al., 2018) that may compress the object or lead to incorrect deposition of the material at different heights[10] (Bos et al., 2016; Panda et al., 2018).

2.4.4 Printing requirements

In most cases a conventional cementitious mix cannot be successfully used in printing applications (Rahul et al., 2019). Additional factors must be considered to accommodate the needs of this fabrication method. Standards for preparing printable mixes are currently not available. Mix designs are primarily based on trial-and-error and on previous research studies depending on the available printing setup (Marchment and

[10] In plastic printing filament is fed into a heated nozzle (between 190-230 ºC) and is extruded onto a heated surface (60-90 ºC). There is more freedom in layer height selection as it determines the fineness of the object. Smaller layer heights lead to higher quality objects at the expense of printing time. Larger layer height objects lead to quicker but lower quality prints. Printing speed is determined by the desired quality of the respective printed surface. Outer surfaces are printed at a slower speed to achieve a higher quality finish. Other features such as brims are not that advisable in cementitious printing as they will generate large amounts of additional material that will not be easily removeable and can potentially disrupt the structural integrity of the print. Skirts comprised of a few filaments can be beneficial as this can be viewed as a short 'trial run' before the actual object is printed. Minor adjustments to the standoff distance and print speed can be made in this time frame without affecting the integrity of the object.

Sanjayan, 2020; Panda and Tan, 2018; Wangler et al., 2019). A strong foundation on 3D printing was laid out by Le et al. (2012) that outlined the properties a mix design must attain in order to be used in 3D printing. Namely, these properties were extrudability/printability, buildability, workability/pumpability and open time. Extrudability and buildability were new terms that were introduced to cementitious fabrication. A short description of each of these parameters is presented below.

- Extrudability/printability: The ability of a mix to be continuously extruded as a continuous filament from a dispensing unit.
- Buildability: The number of layers that can be 'stacked' without any noticeable deformation, or the ability of a material to maintain its self-weight and the weight of subsequent layers.
- Workability/pumpability: The ease with which the mix can move through a pumping system or be deposited into the dosing system.
- Open time: The time window in which the mix attains the above features and remains useable for printing.

A more detailed description of the printing parameters introduced by Le et al. (2012) and methods of assessments follows.

2.4.4.1 Buildability

Buildability is considered one of the two most important factors of 3D printing as this property essentially eliminates the use of formwork (Paul et al., 2018). In simple terms buildability refers to a mix's ability to meet its design shape with minimal deformation. In order for a material to be considered buildable it should be able to maintain its self-weight (green strength), and possess high enough strength to withstand the deposition of additional layers (shape stability or retention) (Kazemian et al., 2017).

Buildability can be achieved when a mix is in a pseudo-solid state (Roussel, 2018) and attains a high material stiffness (Bos et al., 2016). Printable mixes are usually associated with high solid content (Romagnoli et al., 2012). In most cases though, high solid content alone is not enough to meet this requirement. Employing additives such as nanoclay

(Panda et al., 2020, 2019d), silica fume (Kondepudi and Subramaniam, 2021; Panda and Tan, 2018), nanosilica (Mendoza Reales et al., 2019), attapulgite clay (Panda et al., 2019b) and filler such as polyvinyl alcohol (PVA) fibers (Chougan et al., 2021), polypropylene (PP) fibers (Nematollahi et al., 2018), glass fibers (Archez et al., 2021) and nanographite (Chougan et al., 2020) have been reported to substantially improve buildability. Buildability can also be achieved with the use of plasticizers (Valentini et al., 2020) and viscosity modifiers (Guo et al., 2020; Kondepudi and Subramaniam, 2021; Sun et al., 2020). Keeping the mix at rest can also result in high buildability (Perrot et al., 2015), however this increases the risk of adding voids to the object at prolonged times (Tay et al., 2018).

Common tests of assessing buildability involve the conventional slump-cone or mini slump-cone tests. In most cases low slump values have been stated to be required for printable mixes (Alghamdi and Neithalath, 2019; Archez et al., 2021; Nematollahi et al., 2018). Slump cone tests though provide limited information on a material's buildability. Buildability can also be assessed using a more practical approach. In particular a mix's buildability can be defined by the number of layers that can be extruded or 'stacked' without major deformation or collapse of the printed object (Albar et al., 2020; Mechtcherine et al., 2019; Panda and Tan, 2018; Sun et al., 2020). This ultimately leads to cases in which mixes are defined by a number of layers, such as mix A being able to print X amount of layers while mix B is capable of printing Y amount of layers. An effective way of increasing the buildability of a mix by using this method is by increasing the time gap between layers (Sanjayan et al., 2018; Tay et al., 2018). This essentially allows the mix to sufficiently harden and thus be able to support the weight of the subsequent deposited layers. This is similar to the structural buildup of a mix in which the building rate (print speed) should be equal to the amount of time a mix requires to harden such that it is able to sustain the weight of the subsequent layer while still achieving an optimal bond with the previous layer (Perrot et al., 2016). Irrespective of the type of test small deformations may be allowable (Chen et al., 2020; Nair et al., 2019; Tay et al., 2019b).

While quantifying the number of layers is convenient in providing a numerical value to buildability, comparisons between other mixes cannot be easily made. In most cases comparisons are only valid when referring to the same or a very similar printing system. The mix designs and the number of 'stacked' layers used in larger printing systems cannot be replicated by smaller sized syringe-based printers. Large printers have a larger variety of additives, filler and aggregates to select from to include in the mix design, whereas syringed based printers are limited to lower percentages of filler or exclusion of certain materials due to potential blockage in the smaller nozzle size and delivery system. Furthermore, the maximum printable height an object can achieve is also confined by equipment limitations. Indeed, what is considered 'buildable' is quite a subjective term. To give an example, in a fly ash AAM printing application, Panda and Tan. (2018) deemed a mix buildable when it was able to achieve a height of 600 mm. In a syringe-based application, Sun et al. (2019) stated their mix was able to attain high buildability for a total height of 10 mm. Both these studies considered their mix 'buildable' for two vastly different values. A point that is not often mentioned though is that buildability is not always put into proper context. In this situation, the former application was aimed at construction purposes whereas the latter was intended for electronic packaging. In certain cases, an extreme number of stacked layers does not provide any essential advantage as it does not fit the intended application of the printed object. This would inevitability lead to overdesigning and waste of material (Nerella et al., 2020). Therefore, while the number of layers may provide some insight on the buildability of the mix, the printing system and the intended application is something that must always be considered when comparing the buildability of materials.

More recent studies have also focused on defining buildability through the development of rheology models (Kruger et al., 2020; Perrot et al., 2016; Sun et al., 2020; Sun et al., 2020). While this may provide a more universal approach to assessing buildability, one of the issues with these models is that they rely heavily on the rheology of mixes which can present large variability between batches and within the same batch over time.

2.4.4.2 Extrudability

Extrudability can be defined as the ability of a cementitious filament to be continuously extruded through a nozzle without any defects (Lim et al., 2012; Rahul et al., 2019) Extrudability and printability were initially used as interchangeable terms (Lim et al., 2012) however over time these two terms started to diverge. Printability has been regarded as the combination of extrudability and buildability/shape retention (Alghamdi and Neithalath, 2019; Moeini et al., 2020; Nerella et al., 2019). In essence it provides a more rounded evaluation on how well the two key parameters of 3D printing interact with each other. In some cases printability may be assessed separately or simply considered as an extension of extrudability or buildability.

Extrudability is the second key parameter of 3D printing applications. It can be easily accepted that if a mix cannot be extruded, then it cannot be 3D printed. The most common approach to assess extrudability is to extrude a few single layers of filament and assess the printed object either by measuring the filaments or via visual inspection. If the layer is free from voids and does not have any dimensional variations it 'passes' the extrudability test and is deemed acceptable for printing. If discontinuities are formed or if the layer presents a large spread and does not meet the intended shape and size, then this would mean the mix 'failed' the extrudability test. Similar to buildability, satisfying extrudability requirements essentially requires a series of trial-and-error investigations by taking into account the printing limitations imposed by the equipment available.

Extrudability assessments can be considered rather generic as they only take into account the state of the mix at a specific time. As time progresses cementitious materials stiffen and thus extrudability can be compromised. As a result, extrudability tests have been developed that expand beyond the conventional 'extrudable' or 'not extrudable' investigations[11].

[11] The standard test can be viewed as the first step in extrusion investigation as this ensures the mix design meets equipment limitations. There is no meaning in conducting an in-depth extrudability analysis if the filament cannot be extruded at all.

Such tests include the following: Long et al. (2019) defined extrudability as a combination of rheology tests and shape stability. Tay et al. (2019b) defined printable regions in terms of buildability and pumpability. Chen et al. (2019) investigated the extrusion pressure required to maintain extrudability over time. Weng et al. (2019) investigated extrudability in combination with rheology tests concluding that low torque values resulted into extrudable filaments. Nair et al. (2019) investigated extrudability in regards to rheology and extruder geometry. Tay et al. (2019a) identified extrudable regions in regards to flow rate and printing speed. Mechtcherine et al. (2019) defined extrudability by printing a mix at different time intervals (up to 90 minutes). Nerella et al. (2019) defined extrudability in terms of energy consumption and flowrate.

Overall, extrudability can be investigated individually or in combination with other printing factors. Combining extrudability with other parameters can be more beneficial as it provides more meaningful insight on the mix.

2.4.4.3 Workability-flowability-pumpability

The terms workability and pumpability/flowability are grouped in one category as they are dependent on the printing setup. In some cases, these properties may be assessed separately or not examined at all. As their names suggest, these properties focus on the workability and the rheological properties of a mix. The assessment of these requirements is rather straightforward as their testing methods are based on existing national standards such as slump tests and flow table tests (Nematollahi et al., 2018; Tay et al., 2019b) and rheology models (Bingham plastic and Herschel-Bulkley) (Guo et al., 2020; Moeini et al., 2020). Extrudable mixes favor high workability whereas buildable mixes are associated with low workability (Panda et al., 2019a). Therefore, as previously mentioned, the rheological properties of a mix can be examined in conjunction with extrudability or buildability (Panda et al., 2019d; Panda and Tan, 2019; Zhang et al., 2019). Workability assesses the ease of material can move in a delivery system which ultimately determines a mix's suitability for printing.

Flowability and pumpability are relevant parameters in printing setups that use pumps to feed the material into the dispenser. In syringe-based setups these parameters are not

considered as the air pressure feeds the material into the dispensing unit. Overall workability is not a substantial factor on its own but provides more context when used properly. In certain cases, this parameter can be omitted and considered in tandem with other factors such as extrudability and buildability.

2.4.4.4 Open time

Open time was initially defined as the period in which a mix maintained sufficient workability such that it was still useable for printing. Open time is commonly associated with the Vicat needle apparatus (British Standards Institution, 2016). The information provided by this test though is limited to the initial and final setting time of the mix. This time frame alone cannot determine if and how a mix can be useable for printing. As a result additional tests are conducted such as:

- Thixotropic open time, in which the thixotropy (rheology) of the mix is measured over time (Panda and Tan, 2018);
- Extrudability over a set time frame/printability window, in which the time a mix meets extrusion/printability requirements is investigated (Alghamdi et al., 2019; Kazemian et al., 2017; Ma et al., 2018; Mechtcherine et al., 2019; Rahul et al., 2019)

Open time can also be affected by equipment limitations such as heating up of equipment or gradual material clogging in the dispenser (Diggs-McGee et al., 2019). As a result, the setting time observed by the Vicat needle test and the actual printing time may differ (Chougan et al., 2020). Therefore, examining the open time as an extension of extrudability over the course of time can provide a more accurate representation of the actual extrudability time of a mix.

2.4.4.5 Additional parameters

The printing requirements provided by Le et al (2012) are able to provide a good starting point for cementitious 3D printing. One of the issues with these requirements, however, is their reliance on testing methods that were not developed for 3D printing and their limited uses outside of construction purposes. Over the years, additional printing considerations have been suggested by other authors to encapsulate the 3D printing

requirements for cementitious mixes. For example, Kazemian et al. (2017) stated that a cementitious filament should attain the following properties:

- Print quality: Layer free of defects, visible layer edges and dimension consistency and conformity.
- Shape stability: Zero deformation whether that may occur from self-weight, weight of subsequent layers or extrusion pressure.
- Printability window: time limit in which the mix is printable and no blockage occurs.

In essence these considerations refer to the same concept as mentioned by Le et al (2012). The main difference is that these requirements are based on a more empirical approach that focus more on the printing process. The limitations of printing setups may differ and this cannot be realized by standard testing methods alone. That said, solely relying on empirical methods can also make comparisons difficult and can be viewed as a roadblock to standardization. As both these approaches have their merits a combination of both can allow mix designs to be tailored to specific printing setups while also enabling comparisons with other applications[12].

Over the years additional factors have been considered in 3D printing. A key property that is often investigated is the interlayer adhesion of the printed object. It has been well studied that the layer-by-layer fabrication technique leads to anisotropic behavior which affects the structural integrity of the objects (Nerella et al., 2019; Panda et al., 2017; Sanjayan et al., 2018). Interlayer adhesion can be directly influenced by factors such as buildability and workability. As mentioned in Section 2.4.4.1, buildability can be improved by increasing the time delay between layers, but this may have an inverse effect on interlayer adhesion (Panda et al., 2019a; Wolfs et al., 2019). Furthermore, mixes with poor workability also result in poor interlayer adhesion strength. One way to avoid weak bonds between layers is to avoid overdesigning, and to instead tailor the mix design to just

[12] In fact, 3D printing can be carried out without relying on *either* set of printing requirements. Printing optimization studies have been conducted that do not refer to any of the parameters above and mainly focus on investigating the rheology of the mix designs (Franchin et al., 2017; Zhou et al., 2020).

meet its required needs. For example, if the buildability requirements of an object are low employing a more workable mix or a mix with less solid content can improve the bond between layers (Nerella et al., 2020) while fulfilling its intended use. Interlayer adhesion can also be improved by incorporating bonding agents (Marchment et al., 2019) or adding layers of mortar (Ma et al., 2020) or aggregates (Yu et al., 2020) between layers to improve surface contact. These methods though are not always effective as they may interfere with the stability or with the homogeneity of the printed object. In general interlayer adhesion is primarily investigated in full-with printing systems rather than in filament printing.

Further considerations that have been made in printing outside of mix properties include economic viability (Nerella et al., 2020) and energy consumption (Nerella et al., 2019). As research in the preparation of printable mixes matures, incorporating such elements can bring about new perspectives in cementitious 3D printing. Overall how the printed objects will be used will influence which parameters will be investigated in the end. As a result, while some requirements may remain the same from a generic 3D printing point of view, different applications may see different requirements.

2.4.5 Printing alkali activated materials

Similar to OPC mixes, AAM have seen multiple applications in additive manufacturing in both the two-part and one-part formulation methods (Archez et al., 2021; Franchin et al., 2017; Muthukrishnan et al., 2021; Nematollahi et al., 2018; Panda et al., 2019c; Paul et al., 2018; Zhong et al., 2017). The printing requirements for OPC and AAM mixes are essentially same. As mentioned in Section 2.2.3 and 2.2.6 binder formulation and curing regimes differ in AAM than in OPC binders. This has led to authors investigating alternative methods in 3D printing to make use of the uniqueness of AAM in this aspect.

2.4.5.1 Printing AAM at elevated temperatures

A common theme in recent AAM printing applications is introducing a source of heat to the overall system as heat can accelerate alkali activation and solidification. For example, Sun et al. (2020) printed AAM directly into a heat box to increase solidification of the printed filament. This allowed the deposited layers to harden and develop sufficient

strength to bear the weight of subsequent layers. While this method can bypass buildability barriers, it also induces quicker moisture evaporation in the printed object which inevitably results in higher shrinkage. In a similar study Souza et al. (2021) printed metakaolin AAM while using a heated nozzle. This allowed greater control of the rheology of the mixes investigated. This approach essentially was able to convert mixes with low buildability and high workability to mixes with high buildability. One of the drawbacks of this method is that it may induce a shorter printing window and cause extrudability issues if the mix is overheated and starts to solidify.

In another AAM printing application, Muthukrishnan et al. (2020) microwaved AAM filament as a means of quick heat application. This concept is similar to the printed box employed by Sun et al. (2020). It can also be viewed as a means of circumventing prolonged time delays between layers. Microwaving the filament was stated by the authors to allow the mix design to achieve greater buildability and interlayer adhesion. Excessive microwave heating though can result in moisture loss that can cause a negative effect on the properties of printed object. While microwave heating is not a new concept in AAM (Kastiukas et al., 2020; Tan et al., 2020), this technique limits the scalability of printing applications and may affect the dimensional integrity of an object if it is constantly transferred in the middle of printing. Moreover, the concept of microwaving AAM may be associated with unknown behavior that has not yet become evident.

2.4.5.2 Molecular composition effect on printing parameters

Printing applications are primarily based on mass ratios (Archez et al., 2021; Panda and Tan, 2018). As mentioned in Section 2.2.3 it is well known that the alkali solution greatly influences the workability of AAM binders. Few studies have focused on the impact of the molecular composition of AAM on printing properties. Dai et al. (2020) studied the impacts of the solution modulus (SiO_2/Na_2O) and the fly ash and slag content in regards to structural buildup and setting times. Increasing the solution modulus and decreasing fly ash content led to decreased setting times. This is quite expected as the silicate content in the solution affects reactivity of the mix (Bernal et al., 2012) and fly ash is a precursor will lower reactivity compared to metakaolin and slag which leads to

longer setting times (Nedeljkovic et al., 2018). In regards to the precursor, increasing slag content led to increased structural buildup. Likewise this is expected as slag is associated with lower slump values and quicker setting than fly ash (Nedeljkovic et al., 2018). The solution's influence on structural buildup though was not as clear as it resulted in delayed and then increased structural buildup. While this study provides useful information on considerations in AAM printing, it did not involve actual extrusion. Therefore, a conclusion on the overall impact these factors have on printing cannot be made. For example, solutions with high silicate content can lead to sticky pastes. This could pose an issue in extrusion if filament cannot be deposited properly and 'drags' previously deposited layers. In a study conducted by Bong et al. (2019) the effects of the alkaline solution on AAM printing were examined. In this study it was found that sodium-based solutions were more suitable for printing as they were able to attain a higher shape retention compared to potassium-based solutions. Furthermore, among the sodium-based solutions examined sodium silicate with a modulus of 3.22 was deemed optimal when compared to sodium silicate solutions with a modulus of 2.00. It is important to mention that mixes employing the latter solution resulted in higher compressive strength. This requires further consideration as it may limit a mix's useability in future construction applications. In a similar study, Panda et al. (2019d) investigated the effects of two different potassium-based solutions with a modulus of 2 and 1.8. A higher shape retention was observed in printed objects that employed a solution with a modulus of 2. This was attributed to the higher viscosity linked with the solution. Zhang et al. (2018) investigated the Si/Na ratio of the alkaline solution for AAM formulation in regards to buildability and rebuilding behavior (ability to regain viscosity after mixing). It was found that employing solutions with lower Si/Na ratios were more suitable for printing applications. Similar to Bong et al. (2019), the 'printable' mixes in this investigation were also those that attained lower mechanical properties.

Judging by the studies at hand a definitive claim on the activator's impact cannot be made. It can be inferred that a correct balance between the alkali metal and the silicate must be found prior to printing. Furthermore, the above applications focused on fly ash and slag precursors. The findings in these studies will most likely not be applicable to metakaolin

AAM due to the workability issues of metakaolin AAM (Favier et al., 2014; Provis et al., 2010).

2.4.5.3 Additional parameters to be addressed

Overall, other factors that are studied in conventional AAM formulation should be considered in additive manufacturing as well. For instance, due to the high solid ratios used in printing mix designs, binders may experience efflorescence and subflorescence (Zhang et al., 2018). While not reported, it can be inferred that the presence of subflorescence can have a severe impact on the object due to the weakened interfaces between layers as this occurs under the surface of the binder. Furthermore, curing and proper sealing of printed AAM objects should be considered as well. Heat curing is more crucial in binders with slower strength development such as fly ash AAM. Sealing is important where high shrinkage is anticipated such in metakaolin AAM.

2.4.6 Summary of 3D printing

This section provides a general overview on 3D printing cementitious materials. The extrusion of OPC and AAM binders has seen increasing interest over the years alike. In this segment, typical printing setups are presented and common terminology used in this field is introduced. In most instances mixes used in such applications must comply to certain printing requirements in order to successfully fabricate printed binders. While framework for 3D printing has been proposed, each investigation should be tailored accordingly to meet the intricacies and requirements of its intended application. Bearing this in mind, 3D printing in this thesis will be based on existing guidelines, however, practice will be adjusted where necessary to satisfy the requirements for 3D printing AAM sensors.

2.5 Conclusions

In this chapter a comprehensive literature review on AAM, self-sensing AAM and 3D printing was presented. Each of these fields require a certain level of understanding in order to conduct the experimental investigation of this thesis. The theory covered in this chapter allows fabrication of AAM in Chapter 3, 3D printing of AAM sensors in Chapter

4 and assessment of the temperature and strain sensing capabilities of printed AAM in Chapters 5 & 6 respectively.

Chapter 3 Alkali activated materials

In this chapter alkali activated materials will be explored. The mechanical properties of these materials are investigated in support for the development of sensors that will be investigated in Chapters 4, 5 and 6.

3.1 Introduction

When developing AAM sensors, the material is required to simultaneously behave as a sensor and an AAM binder. To ensure the standard performance of an AAM binder the proper formulation process needs to be followed. Formulation alone though does not guarantee satisfactory sensing results. For example, sensing applications involve monitoring structures under various strain conditions. This requires the sensors to possess adequate strength to endure the strain that is applied. Therefore the mechanical properties of AAM need to be investigated as well.

In this chapter AAM are investigated. As mentioned in Section 2.2 AAM comprise of a broad range of materials with various design approaches. The performance of AAM is influenced by numerous factors such as molar ratios, solid-liquid ratios and curing regimes. As such these parameters will be investigated in order to establish a suitable design approach for AAM formulation that will be followed for the remainder of this thesis. Therefore, drawing on the literature on AAM presented in Section 2.2, the following investigation was carried out:

i. Calcined kaolin was analyzed through X-ray diffraction analysis to assess its suitability as a precursor for AAM formulation.

ii. The compressive strength of two mix designs was examined. The first was based on ‘optimal’ fabrication following AAM theory and the second was tailored for printing AAM overlays.

iii. In order to explore potential means of deployment for AAM sensors (in-situ and ex-situ fabrication) the compressive strength of AAM for two heat treatments, ambient curing and heat curing, were investigated.

iv. To demonstrate the suitability of the material in strain sensing tests, apart from compressive strength, the flexural strength of AAM for ambient cured samples was also assessed.

v. The kinetic reactions of the AAM mix were verified via isothermal calorimetry tests to ensure the expected reactions transpire in the mix.

vi. Avenues for further research in terms of AAM formulation are presented. The impact of the alkaline solution on the compressive strength is examined and its drawbacks in printing are addressed.

By assessing the parameters above the successful fabrication of AAM binders can be confirmed. The methodology employed in this chapter will thereafter be used in Chapter 4 for 3D printing AAM overlays and in Chapters 5 and 6 for the development of AAM sensors.

3.2 Experimental procedure

The following sections outline original experimental work conducted as part of this thesis, drawing on the scientific literature outlined in Section 2.2.

3.2.1 Raw materials

In the work outlined in this thesis, commercially supplied kaolin originating from Southwest England was calcined at 800 ^{o}C for 2h at peak temperature in an electric furnace. The calcined clay (metakaolin) was left inside the furnace to cool down before being taken out and stored in sealed containers. Densified silica fume 90% was added to the mix as a high source of silica content. This allows the increase of the silica content in the matrix allowing a higher molecular composition to be achieved as outlined in Section 2.2.4. Polyvinyl alcohol (PVA) fibers (3mm) were also added to the matrix due to their

positive effect on adhesion and shape stability: these are important requirements for printing that will be further explored in subsequent chapters.

The mass ratios of the solid materials in this mix are as follows: metakaolin 95% w/w, silica fume 5%w/w and PVA fibers 0.5% w/w. The chemical composition of kaolin, metakaolin and silica fume are presented in Table 3.1. The chemical composition of kaolin and silica fume is provided by the supplier, while the amorphous content of metakaolin was distinguished from the author's own X-ray diffraction analysis. The exact SiO_2 and Al_2O_3 content could not be calculated with the XRD analysis alone: this would require access to quantitative X-ray fluorescence (XRF).

Table 3.1 – Chemical composition of kaolin and silica fume is as provided by suppliers and metakaolin through XRD analysis.

Material	SiO_2 (%)	Al_2O_3 (%)
Kaolin	47	38
Metakaolin	87%	
Silica fume	92.85	0.27

Sodium silicate with a chemical composition of 27.8% SiO_2, 8.5% Na_2O and 63.7% H_2O and sodium hydroxide (10M solution) were used to make the alkaline activator. The modulus of the silicate (SiO_2/Na_2O) is 3.3 and is therefore too high to be used in AAM fabrication alone. As a result, sodium hydroxide (10M) was added to the solution to allow for a more suitable modulus to be reached. The mass ratio of sodium silicate with sodium hydroxide was set at 2. The resulting solution had a modulus of 1.42 and H_2O/Na_2O=17.4. The alkaline solution was left to cool down for at least 24 hours prior to use. The mass ratios are presented in Table 3.2.

Table 3.2 – Mass ratios of mixing constituents.

	Metakaolin	Silica fume	PVA (3mm)	Sodium silicate: Sodium hydroxide
w/w (%)	95	5	0.5	2

3.2.2 Mix design

In this study, two mix designs were investigated denoted as 'Mix 1' and 'Mix 2'. Mix 1 had a solid-liquid ratio of 0.55 and Mix 2 had a solid-liquid ratio of 0.9. The ratio for Mix 1 was selected as it was able to achieve an Si/Al and Na/Al ratio closer to the

optimal range reported for metakaolin AAM as depicted in Section 2.2.4. Mix 2 was selected as this mix design was within the range of solid-liquid ratios than have been employed in AAM formulation as mentioned in Section 2.2.4.1.1. Mix 2 can also be used in printing applications owing to its higher solid-liquid ratio. The solid content includes the mass of metakaolin and silica fume as they are able to react with the alkaline solution and take part in alkaline activation. The liquid content is referred as the mass of the alkaline solution (sodium silicate and sodium hydroxide once mixed and cooled down). The mass percentages of the solid and liquid content were kept constant. Irrespective of the mix, the total solid content of each mix consisted of metakaolin 95% w/w, silica fume 5%w/w and PVA fibers 0.5% w/w. The molecular composition and mass ratio of each mix are presented in Table 3.3. As mentioned the SiO_2 and Al_2O_3 content of the metakaolin was not able to be exactly quantified. The amorphous content was 85% and 87% in kaolin and metakaolin respectively. The additional 2% of amorphous content in the metakaolin was equally divided among SiO_2 and Al_2O_3. Therefore for the calculations of the binder the SiO_2 content was regarded as 48% and the Al_2O_3 content as 39%.

Table 3.3 – Molecular composition of Mix design 1 and Mix design 2

Mix	Solid-liquid	Si/Al	Na/Al	SiO_2/Na_2O (solution)	SiO_2/Na_2O (paste)	H_2O/Na_2O (solution)
Mix 1	0.55	2.00	0.92	1.42	3.54	17.42
Mix 2	0.90	1.69	0.56	1.42	4.89	17.42

3.2.3 Mix procedure and curing

The mixing procedure followed in this study resembled mixing sequence 1 mentioned in Table 3.1. Metakaolin, silica fume and PVA fibers were dry mixed for 2 minutes. The alkaline solution was then poured into the dry materials and mixing was continued for another 10 minutes. Figure 3.1 displays the mixing sequence followed in this study.

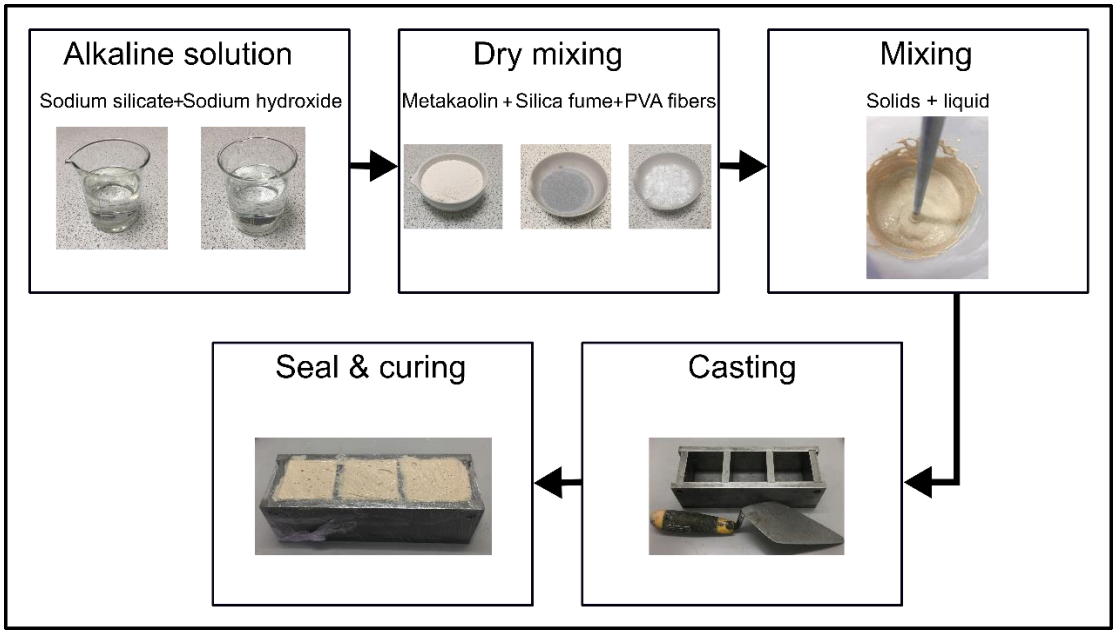

Figure 3.1 – Mixing sequence of AAM formulation.

AAM was deposited in 30 mm × 30 mm × 25 mm silicon moulds for compression tests and in 40 mm × 40 mm × 200 mm formwork for flexural beam tests. The moulds were vibrated to remove the entrapped air. Following that, the moulds were wrapped in plastic film and stored in plastic containers to avoid water loss. For heat cured samples, the moulds were stored at a controlled temperature chamber at 40 ^{o}C for 24h. The samples were demoulded and stored in plastic containers in another controlled temperature and humidity chamber at 17 ^{o}C. For ambient cured specimens, the samples were stored in plastic containers and placed directly into the controlled temperature and humidity chamber. Depending on the degree of hardening the samples were demoulded after 24h or 72h of casting.

3.3 Experimental testing

In this section, macroscopic properties of Mix designs 1 & 2 and the calcined clay are explored using the following techniques: XRD analysis, compressive & flexural testing, isothermal calorimetry. The experimental procedure of each is described in the following sections.

3.3.1 X-Ray Diffraction Analysis

X-ray diffraction (XRD) analysis was carried out on the calcined clay. XRD data was collected using a Bruker D8 Advance instrument. Data for Rietveld refinement was collected in Bragg-Brentano geometry from 12◦–75◦ 2theta with an increment of 0.02 ◦/s and a step time of 0.8 s. using a divergence slit of 0.23◦. A Ni β filter was placed in the incident beam path. The sample was rotating at 30 rpm and a knife edge collimator was used to reduce air scattering.

3.3.2 Compression testing

Compression tests were carried out on 30 mm × 30 mm × 25 mm samples using a universal loading cell with a maximum loading capacity of 50 kN. The load was applied on the 30 mm × 25 mm face of the specimens at a displacement rate of 0.5 mm/s. The compressive strength was calculated as the force divided by the area it was applied on. The ultimate strength was the average of at least five samples.

3.3.3 Flexural testing

3-point bending tests were carried out on 40 mm × 40 mm × 200 mm samples using a universal loading cell with a maximum loading capacity of 25 kN. The flexural stress was calculated using equation (3.1):

$$\sigma = \frac{3PL}{2bd^2} \tag{3.1}$$

Where σ=stress, P=force at failure, L=distance of beam between supports, b=width of beam and d=depth of beam. The distance from the edge of the beam to the support was 40 mm. A total of three specimens were tested for each day.

3.3.4 Isothermal calorimetry

A thermal analysis was conducted using an isothermal calorimeter (Calmetrix, I-CAL 4000 HPC) to measure the heat release of AAM pastes produced by the exothermic reactions occurring during alkaline activation. The raw materials and the alkaline solution were mixed outside the calorimeter. Shortly after mixing, 20 g of AAM was inserted into sealed plastic containers and then placed in the calorimeter for testing. The test was conducted at 20 ^{o}C. All materials were at room temperature to keep consistent with the

testing temperature. Measurements were conducted every 60 seconds for 72 hours. Four samples for each batch were tested, for a total of two batches. The heat release was normalized by the total amount of paste. The average heat curve and average cumulative heat release is presented in the results.

3.4 Results and Discussion

3.4.1 XRD analysis

XRD shows that the starting material is composed of kaolinite and muscovite mica (layered phyllosilicate) with quartz (SiO_2), halloysite (aluminosilicate clay), feldspar (sodium aluminium silicate) and minor rutile (TiO_2). The composition is detailed in Table 3.4.

Table 3.4 – wt% mineral phase assemblage for kaolin powder

Mineral	kaolin (wt%)	metakaolin (wt%)
Kaolinite (kaolin)/amorphous content (metakaolin)	83.9	87
muscovite mica	11.9	9.5
rutile	0.65	0.9
halloysite	1.52	–
quartz	2.07	2.6

The main secondary minerals are mica and quartz which are also present in the dehydroxylated (metakaolin) sample. Metakaolin is usually produced by heating at 600 – 800 ^{o}C and it appears that the sample has been heated enough to remove all of the kaolin with a detection limit of 1 wt% but the diffractogram in Figure 3.2b shows that several of the secondary minerals are still present (quartz, mica, rutile). The influence of secondary minerals in the metakaolin sample is notable as they do not fully participate in the alkaline activation process. It was noted by Zibouche et al. (2009) that AAM made from impure metakaolin may result in more cracks at the surface. That said, it was also stated that impure metakaolin was still able to produce an AAM binder, with the advantage of using a readily available resource.

Referring to Figure 3.2b, the broad ‘hump’ at 15 – 35 degrees 2theta is characteristic of metakaolin, and the Bragg peaks represent the secondary minerals which remain present after kaolinite dehydroxylation. As displayed in Table 3.4, the wt% content of secondary

minerals of kaolin and metakaolin is about 15.5% and 13% respectively. The content of the secondary materials was slightly reduced. Further decomposition of these secondary materials can be possible if a lower calcination rate (i.e. longer calcination period) method is employed (Kenne Diffo et al., 2015). Taking into account what was mentioned in Section 2.2.3.2, as dehydroxylation was complete and mullite was not present in the composition of metakaolin, calcining kaolin at 800 ^{o}C for 2 hours was sufficient to produce metakaolin for AAM formulation.

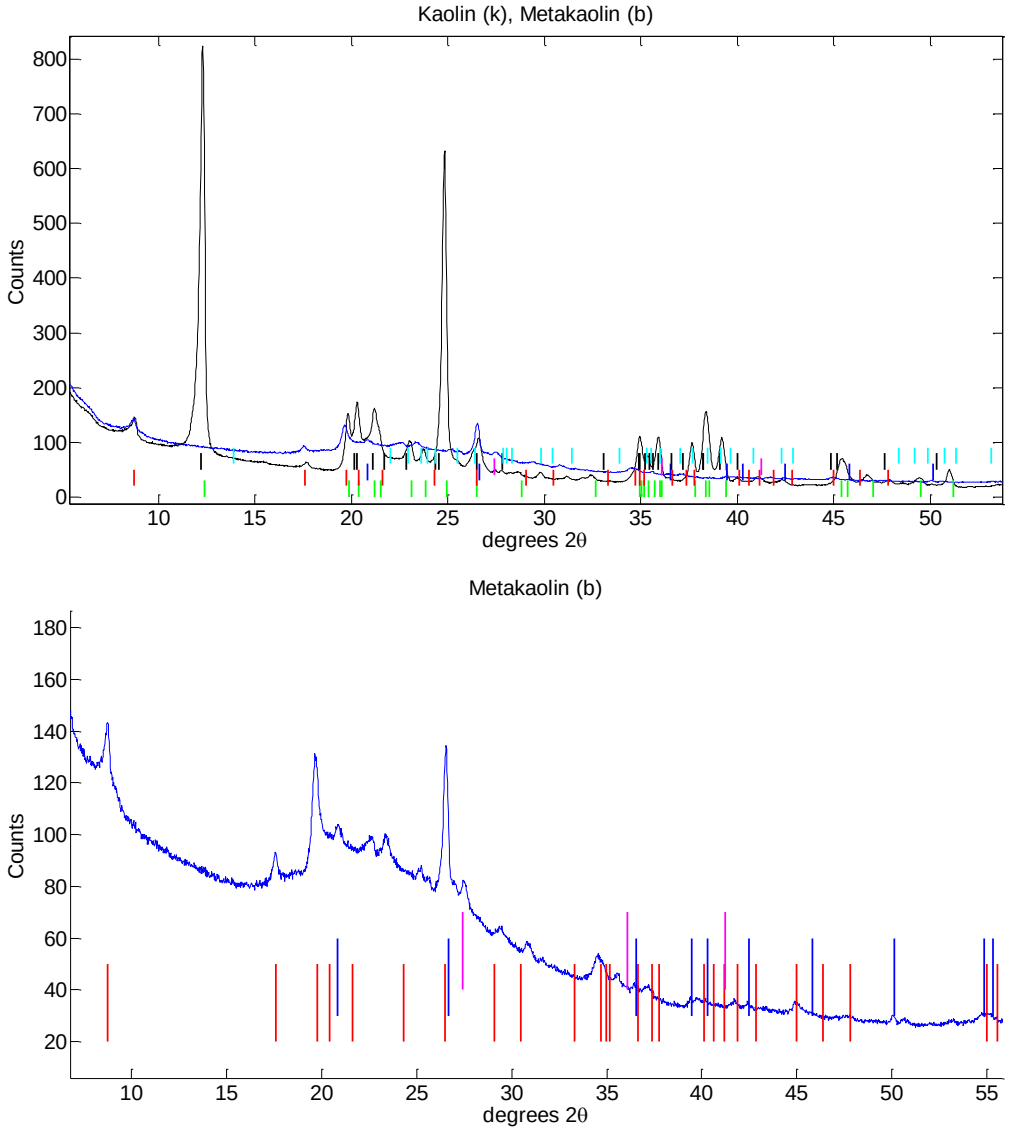

Figure 3.2 – a) Top - X-ray diffractogram of kaolin. b) Bottom X-ray diffractogram of metakaolin. Stick plots - Green is kaolinite, red is muscovite mica, blue is quartz, black is halloysite, magenta is rutile, cyan is feldspar (albite).

3.4.2 The effect of solid to liquid ratio

Figure 3.3 displays the compressive strength for ambient cured samples for Mix 1 (low solid-liquid ratio) and Mix 2 (high solid-liquid ratio) for days 1,7 and 28 of curing. Mix 1 had not completely hardened in 24h and therefore this test could not be conducted. The compressive strength after 28 days for Mixes 1 and 2 are 22.5 MPa and 34 MPa respectively. Mix 2 achieved higher compressive strength for both 7 and 28 days. On one hand this is expected as higher solid content can lead to improved mechanical properties for metakaolin AAM (Bature et al., 2021; Vogt et al., 2019; Zulkifly et al., 2021). On the

other hand this outcome can be regarded as somewhat contradictory despite Mix 1 meeting some of the stated "important molar requirements" of AAM (see Section 2.2.4) better than Mix 2.

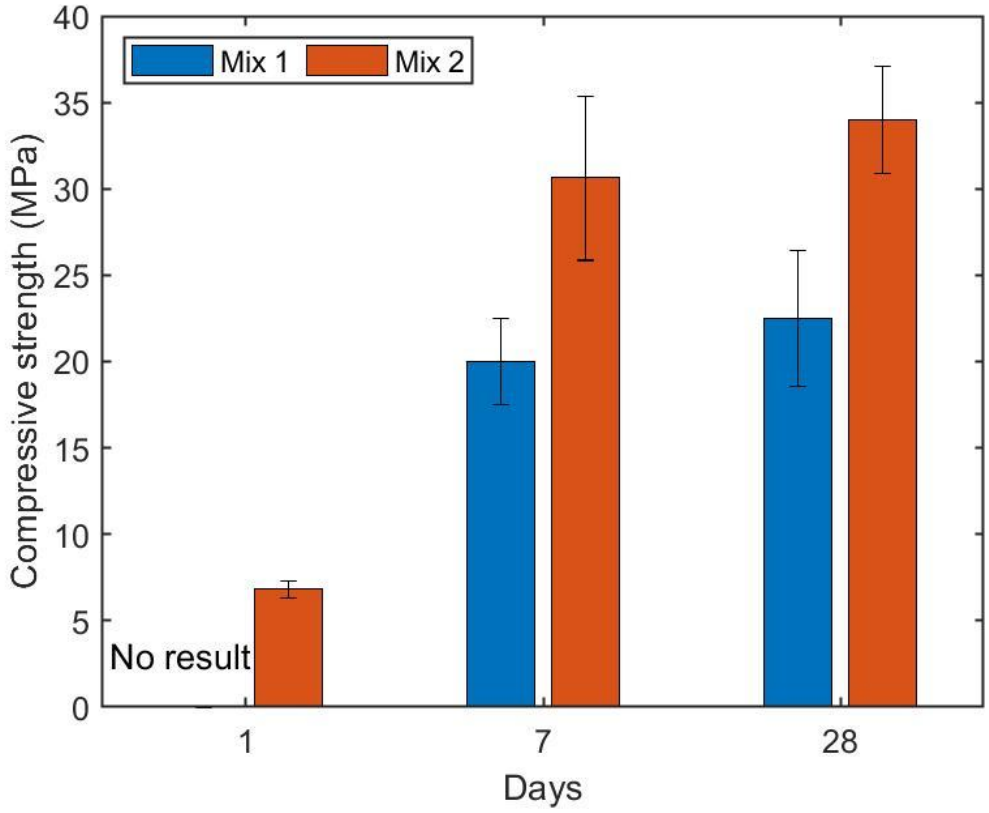

Figure 3.3 – Compressive strength for Mix 1 and Mix 2 for days 1, 7 and 28. Errors bars represent standard deviation of compression tests for 5 samples.

One of the main drawbacks when utilizing molar ratios is that the overall water content in the binder is not always clear. High liquid contents can affect the polycondensation rate of the gel by hindering the diffusion of dissolved species (Bature et al., 2021) and can lead to binders with high porosity (Borges et al., 2017). This initial work conducted as part of this thesis aimed to establish a robust mix design based on existing scientific literature. The difficulty in achieving this with the information available has allowed the author to propose recommendations about how results in the literature could be better reported to improve mix reproducibility:

In most cases, the H_2O/Na_2O ratio (which note, is the same in both mixes tested here) quoted in scientific literature refers exclusively to the alkaline solution[13]. The total amount of water in the binder should be examined as well. To illustrate this, Table 3.5 displays for Mix 1 and Mix 2, the mass ratio of water compared to the other constituents in the AAM paste (SiO_2, Al_2O_3 and Na_2O) and the mass percentage of water in relation to the total mass of all constituents (SiO_2, Al_2O_3, Na_2O and H_2O). As expected, there is overall more water in Mix 1 than Mix 2 in relation to the other parts of the binder. Higher water content in the matrix results in lower compressive strength (Albidah et al., 2021). Furthermore, Mix 2 is closer to the requirement for producing a "high strength metakaolin AAM", which can be formulated with water percentages between 26-34% (Pouhet et al., 2019).

Table 3.5 – Mass ratio and percentage of water content in Mix 1 and Mix 2.

Mix	$H_2O/(SiO_2+Al_2O_3+Na_2O)$	$H_2O/(SiO_2+Al_2O_3+Na_2O+H_2O)$ %
Mix 1	0.84	46%
Mix 2	0.59	37%

In summary, this work demonstrates that more molar ratios should be considered, not just the small subset that are currently considered as the most important. Moreover, additional factors such as the overall water content in the binder need to be taken into account. A combination of both molar ratios and mass ratios can be beneficial in providing a generic overview of the binder in this regard. It can be inferred that water may have a greater impact on mechanical properties compared to other elements in the matrix. As water is not a main structural part of the N-A-S-H gel in metakaolin AAM (Provis and Bernal, 2014), incorporating it in large quantities does not contribute to strength development. That said, a sufficient amount of water is required to be present in the binder. If chemically bound water is removed the binder would experience drying shrinkage (Kuenzel et al., 2012). This can be an important parameter to consider for applications where water evaporation is anticipated.

[13] Metakaolin does not contain any sodium and therefore does not impact this ratio. Fly ash and slag AAM contain small Na_2O content. In addition, they are added in higher doses to the binder compared to metakaolin and thus can have a greater impact on the H_2O/Na_2O ratio.

3.4.3 Heat curing

Figure 3.4 presents the compressive strength for ambient cured (17 ^{o}C) and heat cured samples for Mix 2 for days 1, 7 & 28. From what can be seen, a high degree of strength development was achieved within 1 day for heat cured samples and 7 days for ambient cured samples. These results are in line with the expected behavior of the respective curing regimes.

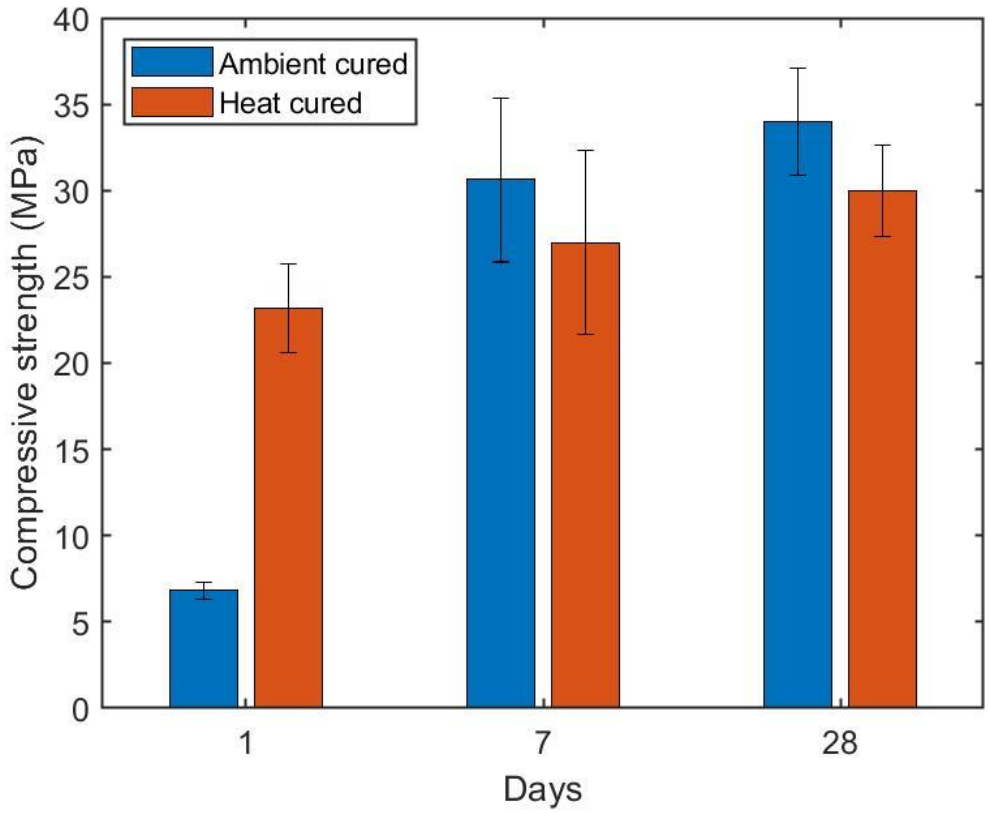

Figure 3.4 – Compressive strength for Mix 2 for ambient cured and heat cured binders at days 1, 7 and 28. Errors bars represent standard deviation of compression tests for 5 samples.

In regards to ambient curing, the samples presented low strength 24 hours after casting (6.8 MPa). Following that, the binder was able to achieve high strength after 7 days of casting (29 MPa) with a slight increase thereafter at 28 days (33 MPa). This demonstrates that metakaolin is a highly reactive material with a high rate of strength development even in ambient conditions. It is able to achieve 88% of its 28-day-strength within the first 7 days of curing. This is in line with the expected outcome of ambient cured metakaolin

AAM (Provis et al., 2019; Rocha et al., 2018). It shows that metakaolin AAM can be used in applications that are incompatible with heat curing.

When it pertains to heat curing, however, the compressive strength at day 1 was 22 MPa, and the strength of the binder slightly increased thereafter to 30 MPa at day 28. Heat curing allows the acceleration of alkaline activation. In the current study, curing at 40 ^{o}C is able to achieve a substantial degree of strength very rapidly: within 1 day, 73% of the 28-day-strength is achieved[14].

As can be seen in Figure 3.4, the strength at 7 and 28 days was higher for ambient cured samples than in heat cured samples. This is somewhat of an unexpected outcome for metakaolin AAM as the consensus is that heat curing is beneficial for the binder (Chen et al., 2016): usually, binders see an increase in strength even after being thermally cured. In a study conducted by Rovnanik (2010) it was found that the mechanical properties of ambient cured metakaolin AAM at 28 days were similar or higher in some cases compared to heat cured samples. It was stated that the binders cured at lower temperatures were able to develop higher quality reaction products and result in lower porosity compared to heat cured samples. can cause water in the binder to evaporate and therefore resulting in a weaker matrix. Secondly, the source of silica (solid or liquid form) plays an important role in reactions that will follow in the binder. Solid silica will first have to dissolve in order to react with the aluminium content in the precursor to generate a stable nucleus for further gel growth. Higher extent of dissolution of silica particles is expected in areas where soluble silica is present-essentially in the activator and further from unreacted particles in solid form. The differences in silica source can cause different concentration gradients of silicon and therefore impact silica dissolution in terms of silica availability (Hajimohammadi et al., 2011). In this mix design, silica fume was added as a dry component to the mix to increase the silica content in the binder. Silica fume though can also be added directly to the activator for greater dissolution (Batista et al., 2019). Considering the above, it can be hypothesized that the slower reactions associated with

[14] It should be considered though that as the strength of the binder was relatively low, the impact of curing at 40 ^{o}C may be different for higher strength metakaolin binders or for fly ash AAM that has a slower reaction rate.

ambient curing can allow more time for the silica fume to properly dissolve. Heat curing may prevent proper dissolution of the silica fume due to accelerated curing, leading to unreacted silica particles that do not take part in alkaline activation. The small difference in strength suggests that only a small portion of silica fume has not reacted, therefore not having a significant impact on the final result. Further investigation is, however, required to make a definitive claim. Considering all the above, heat curing allows the potential of high strength as soon as day 1. However, curing under ambient conditions results in high strength development within 7 days. Ambient curing allows for a simpler curing approach and avoids any inconsistent behavior in the matrix while achieving greater mechanical properties. Therefore, ambient cured samples will be explored in the remaining experiments of this chapter. The effects of heat curing on AAM overlays though will be explored in subsequent chapters.

3.4.4 Flexural strength

Figure 3.5 presents the flexural strength of Mix 2 for day 1, 7 and 28. From what can be seen, the mix attained a low flexural strength at day 1 of 0.41 MPa. Rapid strength increases were seen at day 7 in which strength reached 3.81 MPa. The flexural strength at 28 days was recorded as 3.38 MPa. Similar to compressive strength, the flexural strength was somewhat low compared to other studies (Uysal et al., 2018) which can be in most part due to the reasons mentioned in Section 3.4.2. Furthermore, higher doses of PVA fibers (closer to 2%) are required compared to those used in this experiment (0.5% w/w) to provide an impactful contribution to flexural strength (Borges et al., 2017). In addition long fibers (8 and 12 mm) are also able to contribute to higher flexural strength as well (Xu et al., 2017). Larger fibers and higher doses of fibers are favorable in manual applications. They can pose printing issues though that will be explored in the following chapters and can therefore not be employed in the work described in this thesis.

The flexural strength of this mix decreased from day 7 to day 28. In this investigation strength loss was not observed in the compression test conducted for the same curing duration. Considering the decrease in flexural strength was relatively low, 0.43 MPa and that low strength gains past 7 days have been reported in previous studies it could be

inferred that this apparent decrease is simply within error bars, or could be due to mixing heterogeneities in casting rather than any changes in the microstructure of the binder within this time period[15].

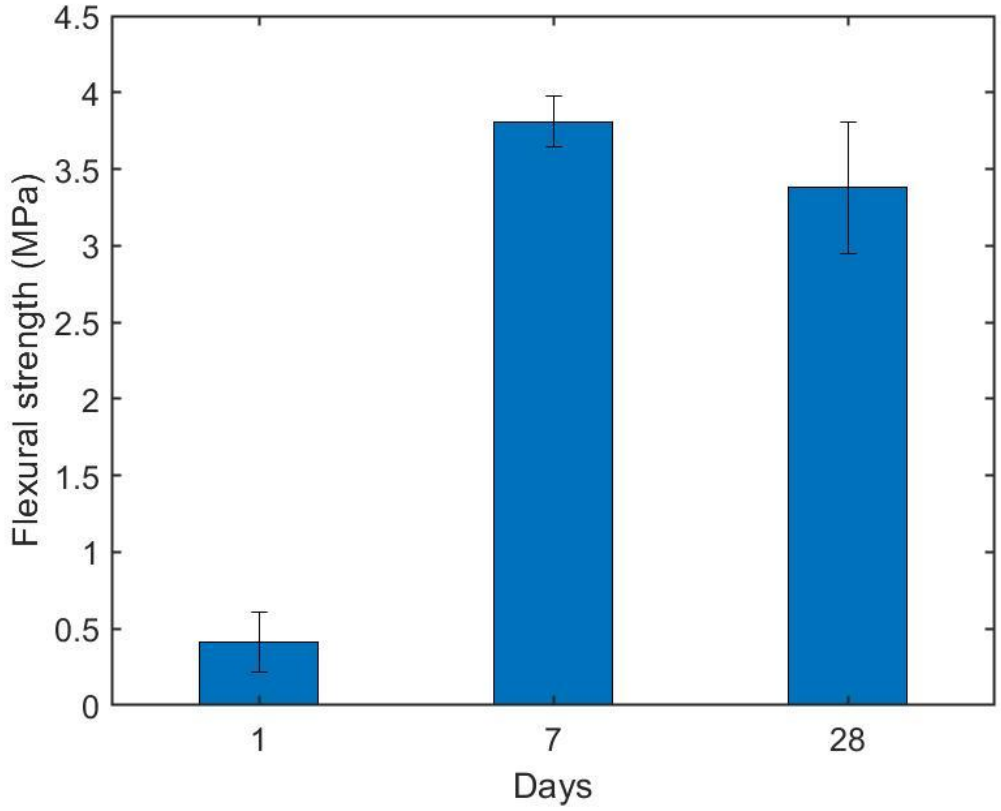

Figure 3.5 – Flexural strength for Mix 2 for ambient cured samples at days 1, 7 and 28. Errors bars represent standard deviation of flexural tests for 3 samples.

3.4.5 Heat release

The amorphous content in AAM is that which takes part in alkaline activation. The PVA fibers that were added to the mix do not take part in this reaction though. Isothermal calorimetry is an effective means of investigating AAM kinetics. Figure 3.6 and Figure 3.7 present the heat release for Mix 2 and the total energy consumption for 72 hours after

[15] Previous studies have indeed shown that there is low increase or even decrease in flexural strength between 7 days and 28 days for metakaolin AAM (Pacheco-Torgal et al., 2011; Rovnaník, 2010; Uysal et al., 2018). Decreases in strength over time have been associated with microstructural changes in the matrix which lead to the formation of large pores in chemically unstable binders (Lloyd, 2009). This strength loss though is usually observed in later stages of curing (56 days and onwards) and has been disputed in more recent studies (Provis et al., 2019).

mixing respectively. In Figure 3.6 it can be seen that a sharp peak is developed within the first 15 minutes which then immediately drops from that point forward. A smaller and much broader peak can be observed at around 10 hours and spans until 40 hours after mixing. The first sharp peak has been attributed to the dissolution of metakaolin and the release of Al and Si when in contact with the solution. The second peak involves the polymerization between the dissolved Al and Si and the silicate monomers present in the activator. When dissolution reaches a critical level and exceeds saturation conditions, polymerization becomes the dominant reaction and the second exothermic peak appears (Zhang et al., 2013). These steps of alkaline activation are also presented in Figure 2.2. As testing temperatures increase the extent of both peaks increases and the duration of the second peak shortens. In addition, as the modulus (SiO_2/Na_2O) of the solution decreases (therefore more alkaline species) the heat release of the second peak increases. In this study the second peak is quite small as a consequence of the testing temperature (20 ^oC) and the modulus of the solution (1.42). From the study conducted by Zhang et al. (2013), activating metakaolin with solutions with a modulus between 1.4-1.6 results in a relatively flat second peak.

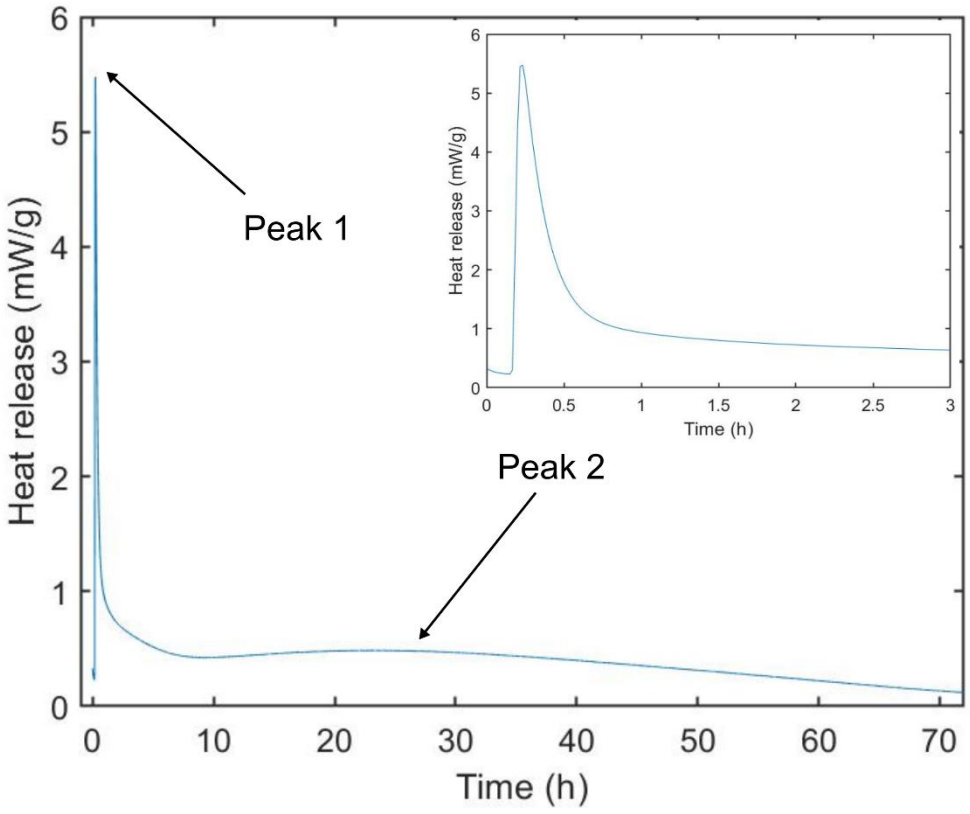

Figure 3.6 – The average rate of heat release of metakaolin AAM over 3 hours (inset) and over 72 hours.

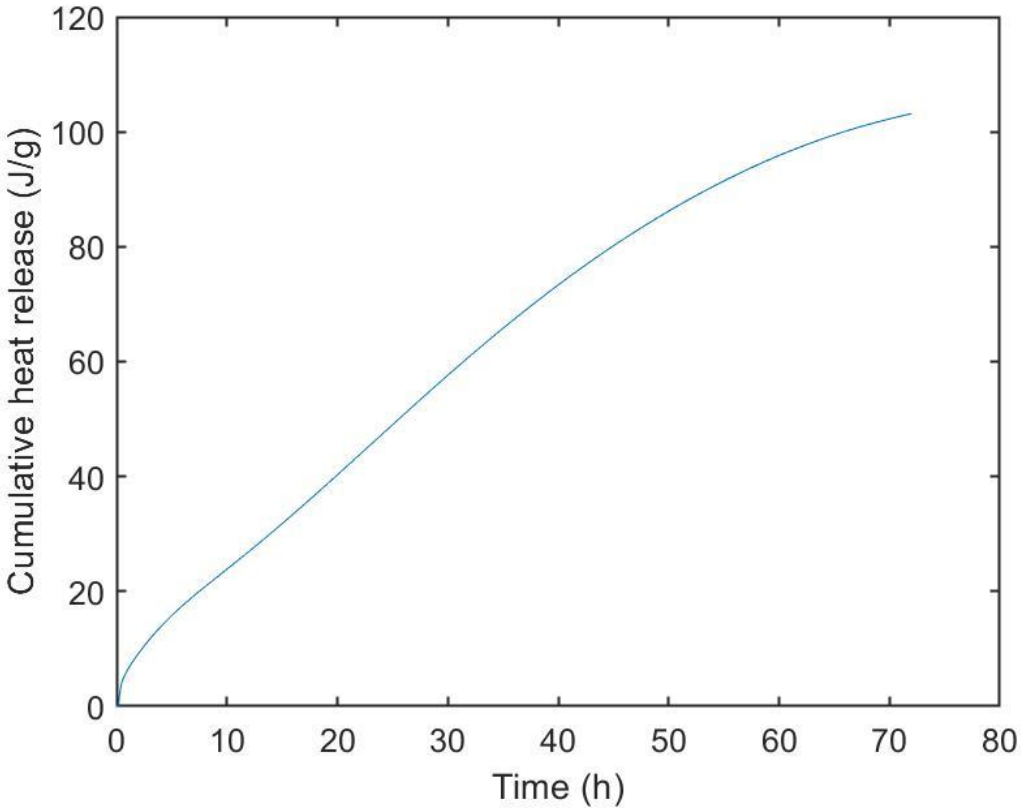

Figure 3.7 – Cumulative heat release of metakaolin AAM over 72 hours.

In regards to the cumulative energy released, cumulative energy release saw a constant increase with evidence of slight plateauing at around 60 hours of testing. This can also be seen in Figure 3.6 where the heat release at around the same period, while subtle, starts decreasing after the second peak. Similarly, this occurrence can be attributed to the testing temperature. Calorimetry tests conducted at ambient temperatures result in a slower energy release compared to higher temperatures (40-60 ^{o}C) due to the slower reactions that occur in the matrix (Elahi et al., 2020; Sun and Vollpracht, 2019).

In the current study initial peak heat release of the paste was calculated as 5.5 mW/g. The intensity of heat release is relatively lower than other reported metakaolin AAM pastes, common values typically range between 10-20 mW/g (Cai et al., 2020a; Sun and Vollpracht, 2019). The cumulative heat release at 72 h on the other hand was relatively high, 103 J/g compared to initial heat release. This indicates a continuous reaction in the

paste owing to the high reactivity of metakaolin. This is somewhat expected when considering the molecular composition of the binder. The modulus of the solution used in this study was 1.42, solutions with a lower modulus, thus high alkalinity lead to higher heat release (Elahi et al., 2020; Zhang et al., 2013). Moreover, the paste that was investigated in isothermal calorimetry contained PVA fibers which do not take part in alkaline activation and could therefore affect the heat release of the specimen. Judging by the calorimeter results, the binder follows the expected reactions of AAM even with the addition of fibers. It can therefore be effectively used in AAM applications.

3.4.6 Effect of alkaline solution

As mentioned in Section 3.4.3, the mechanical properties of Mix 2 are relatively low when compared to other applications. This was primarily attributed to the high water content in the alkaline solution. When it pertains to molecular composition, while the Si/Al ratio is within a reasonable range to the required value, 1.69, the matrix appears to be somewhat sodium deficient (low alkalinity). The Na/Al and SiO_2/Na_2O (in binder) ratios are 0.59 and 4.89 respectively. Ideally these ratios should be closer to 1 and 4. Small changes in the Na/Al ratio can lead to a high increase in mechanical properties (Liu et al., 2020).

With the current resources used in this study it is relatively difficult to increase sodium content without adding high amounts of water into the binder. The silicate solution contains 63.7 % water and the sodium hydroxide 10M solution is 77% water. In this situation options to increase the alkalinity of the binder are the following:

1. Use sodium silicate solution with lower water content, and subsequently higher SiO_2 and Na_2O content; Use sodium hydroxide with higher molarity.
2. Use sodium hydroxide pellets rather than solution and add them directly to the silicate solution as illustrated in (Pouhet et al., 2019).

In a preliminary study, option 2 was briefly investigated. This approach reduces the water content originating from the hydroxide while maintaining high degree of alkalinity. Sodium hydroxide pellets were added to the sodium silicate with some slight water to

assist in dissolution. The ratios added were sodium hydroxide: sodium silicate: additional water=1.0:9.8:0.13 by mass.

Metakaolin AAM samples were formulated for compression tests using Mix design 2 outlined in Section 3.2.2. The samples were cured at 40 ^{o}C. The compressive strength for day 1 was measured as 41.8 ±5.3 MPa. The strength is much higher than the previous specimens. Judging by the previous results in heat curing, it could be suggested that the strength would continue increasing by 28 days. The drawbacks when employing this solution were the large workability issues and the c presented compared to the previous solution which is a result of the overall low water content in the matrix and the high viscosity of the solution (Favier et al., 2014; Vitola et al., 2020). In summary, a stronger mix can be achieved, but there are sacrifices, some of which would make printing with this material impossible with the author's current printing set up.

3.5 Conclusions

In this chapter an investigation of alkali activated materials is presented. The experimental work conducted allows the successful fabrication of AAM and enables this methodology to be used in the subsequent chapters of the thesis. The findings of this chapter are the following:

- Calcining kaolin at 800 ^{o}C for 2 hours at peak temperature is able to produce metakaolin that can be used in the production of AAM.
- Mix design 2 achieved higher compressive strength than Mix design 1 due to higher solid content despite having lower molar ratios than those reported in AAM literature. As a result, adequate or high strength binders can be achieved without heavily relying on molar ratios.
- Ambient curing AAM has been found to result to adequate compressive stress, 34 MPa and flexural stress 3.38 MPa at 28 days. Heat curing, while still able to produce adequate AAM, was not found to be essential in the production of AAM.
- The reactions of the AAM paste followed the expected behavior reported in similar applications. This verifies the current mix design can be used in AAM applications.

- The compressive strength of AAM binders can be increased by reducing the water content in the alkaline solution. This however comes at the expense of workability and severely limits potential 3D printing applications.

Taking all this into consideration, the groundwork for AAM fabrication has been laid out, it has been displayed that AAM can be successfully formulated with the procedures outlined in this chapter. Mix design 2 presented in this chapter will be used in Chapters 4, 5 & 6 to develop printed AAM overlays.

Future work outside of the scope of this thesis should involve optimizing the binder for a designated application rather than arbitrarily formulating mix designs. The optimization method could involve the following: increase alkalinity of solution, identify ‘optimal’ ratios in terms of metakaolin.

Chapter 4 3D printing of alkali activated materials

In this chapter 3D printing of alkali activated materials is explored. A novel mix design verification process for printing is presented. The importance of the intended printing application and the additional factors that must be considered are also outlined.

4.1 Introduction

Over the years printing methodologies have been proposed for cementitious materials. Despite the extensive research that has been carried out in cementitious printing, applications such as 3D printed cementitious overlays and self-sensing materials have not been addressed. 3D printing technology has been used to develop plastic moulds to be filled with repairing mortar to replicate the shape of damaged or cracked surfaces (Yeon et al., 2018). This method though presents quite a few limitations as it requires a sufficiently large and damaged surface. It also cannot provide any preventive protection to the surface in advance. In regards to sensing materials, conductive AAM have been extruded in the past (Zhong et al., 2017; Zhou et al., 2020) however their sensing performance was not been tested.

In this chapter we aim to print AAM patches onto concrete substrates that can serve as a sensing mechanism (without relying on the use of additional electronics) while also acting as a protective coating to the substrate. This will require investigating the mix's printing properties as depicted by Le et al. (2012). The author of this thesis notes that existing

printing requirements though do not account for the additional requirements that sensors and coatings should obtain to be efficiently used in this application. As a result adhesion and conductivity/sensing will also added to the properties the mix design must attain to be successfully used as a self-sensing coating. Out of the referred printing parameters mentioned in Section 2.4.4, the ones that will be assessed in the work conducted in this thesis are the following:

- Extrudability
- Printability window
- Buildability
- Adhesion
- Conductivity
- Open time

Not all the printing requirements bear the same importance though. In this thesis printing parameters were categorized as ‘Essential’ and ‘Can be omitted’. A short definition of each follows:

- Essential – These parameters must be investigated and met to a certain degree to ensure printing is carried out properly. Not assessing these parameters properly will lead to experimental failure.
- Can omit – Printing can be conducted without considering these parameters and other parameters can be considered in their place.

The parameters classified as ‘Essential’ can be further divided into ‘Mix-based’ and ‘Application-based’. While both these parameters must be still considered, they are influenced by different factors:

- Mix-based – These parameters are met by focusing primarily on the mix design.
- Application-based – Apart from the mix design these parameters are also influenced by external factors that must be taken into account.

Table 4.1 depicts the overall significance of the referred requirements in this application. Extrudability, printability window and buildability are categorized as ‘Essential’ and are

‘Mix-based’ parameters. By buildability it is meant that the material can achieve the necessary degree of buildability (see Section 4.2.4.3) to meet its application’s requirements (not ‘high buildability’ as in an arbitrary number of stacked layers).

Adhesion and conductivity/sensing were categorized as ‘Essential’ and are ‘Application-based’ parameters. It must be ensured that these parameters are met but considerations outside the mix design must also be made. For example, adhesion could be increased by altering the surface preparation method or by including bonding agents; sensing responses can be adjusted with changes to interrogation systems and curing regimes. Meeting these requirements for adhesion and conductivity/sensing may require the addition of specific filler to the mix design which can directly impact the extrudability of the mix. For instance, if the conductivity of an overlay needs to be improved conductive filler can be added. A common filler such as carbon fiber though may present extrudability issues. As such alternative solutions can be sought out such as carbon nanofibers or graphene oxides which would then require the investigation of extrudability, printability window and buildability anew.

Workability and open time were classified as ‘Can be omitted’. Both these parameters can be substituted by the printability window which effectively provides the same information in a more empirical manner. Open time may be more relevant in certain applications as it can provide an allowable delay between mixing, filament loading and printing initiation.

Overall, while some parameters retain constant significance throughout additive manufacturing (i.e. extrudability), whether other or additional parameters should be assessed is rather application dependent. Figure 4.1 displays a flow chart on the mix design procedure followed.

Table 4.1 – Printing parameter relevance.

Printing property	Significance	Type of parameter
Extrudability	Essential	Mix-based
Printability window	Essential	Mix-based
Buildability	Essential	Mix-based
Adhesion	Essential	Application-based
Conductivity/Sensing	Essential	Application-based
Workability	Can be omitted	–
Open time	Can be omitted	–

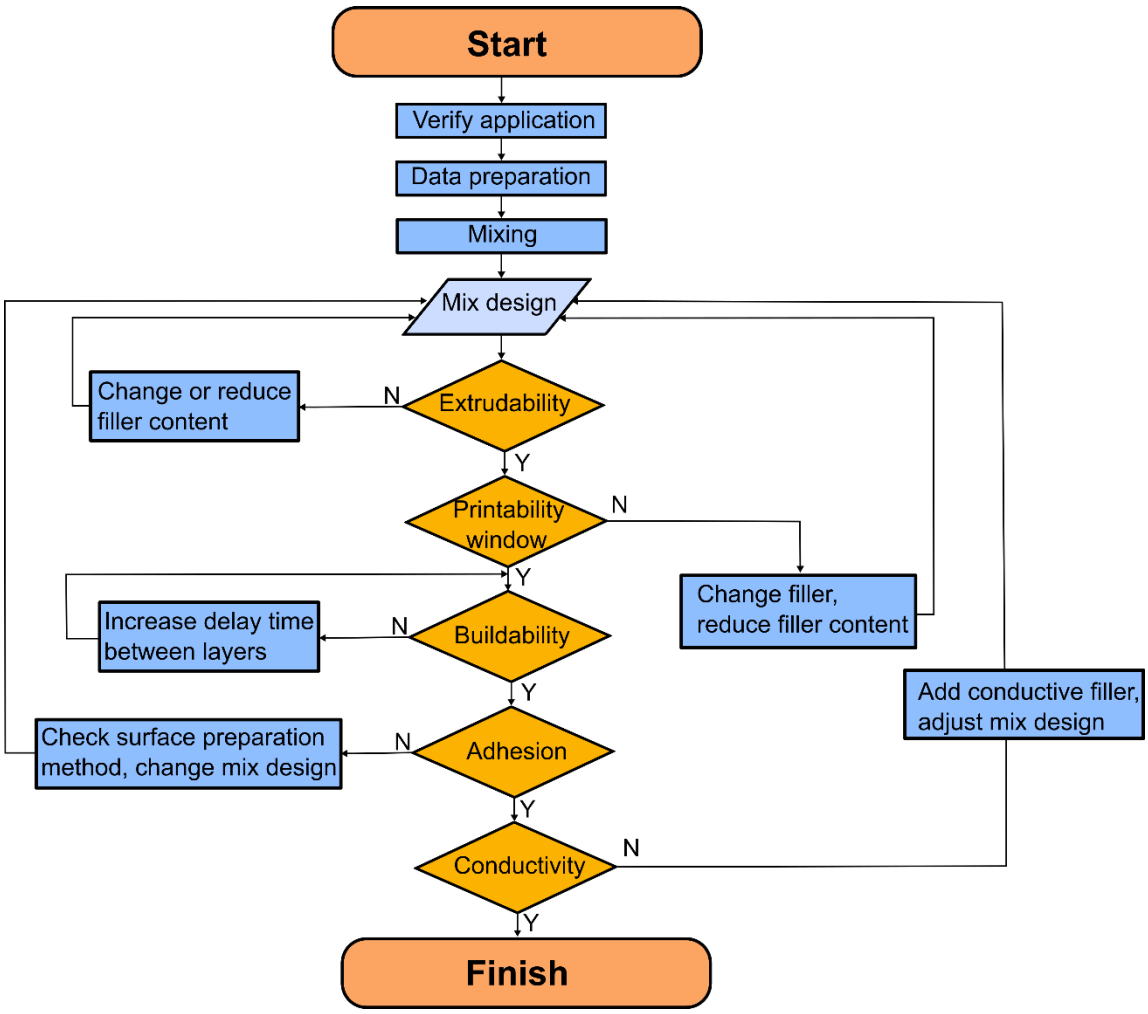

Figure 4.1 – Flow chart of printing procedure.

4.2 Experimental investigation

This section outlines experiments that were conducted by the author of this thesis to determine the suitable of mix designs for printing.

4.2.1 Materials and mixing

The materials and mixing procedure that will be followed are based on the procedures introduced in Chapter 3. Mix design 2 will be used for printing overlays in this chapter. The reader is referred to Section 3.2 for a detailed analysis on the procedure followed. Additional fibers will be investigated to assess their viability on printing in this chapter. The filler explored in this thesis aimed at simultaneously improving adhesion with the concrete substrate and buildability. This would limit the amount of filler

incorporated and avoid having a heavily heterogeneous mix. For this reason viscosity modifiers were not investigated as they would not provide additional adhesion capabilities. Fibers that meet these parameters are PVA (Chaves Figueiredo et al., 2019; Zanotti et al., 2017), PP (Nematollahi et al., 2018; Nunes et al., 2019) and carbon fibres[16] (Feng et al., 2020; Kosson et al., 2020). Therefore, apart from PVA (3mm) fibers, PVA (6 mm), PP and carbon fibers were also investigated in the mix design and their printability was assessed.

4.2.2 3D printing

A screw cavity extruder with a nozzle size of 18 G (0.84 mm) was mounted onto a commercial 3D printer with an x-y gantry axis. The AAM mix was added in the syringe barrel and air pressure of 2 bar was applied to syringe to force the material to flow into the dispensing unit. The print speed was set at 30 mm/s and the flowrate of the mix during printing was 2 mL/min. Printing was carried out either on the printing bed or on concrete cubes. A picture of the setup is presented in Figure 4.2.

[16] Carbon fibers are also able to increase the electrical conductivity but this is of secondary importance as AAM are innately electrically conductive. Therefore, they will be regarded in the same light as PVA and PP fibers. Graphene may present dispersion issues compared to fibers. It will also substantially increase the cost of the mix and was therefore not considered. Other conductive filler such as multi-wall nanotubes have been mentioned to not impact buildability (Sun et al., 2020) and were therefore not suitable for this application.

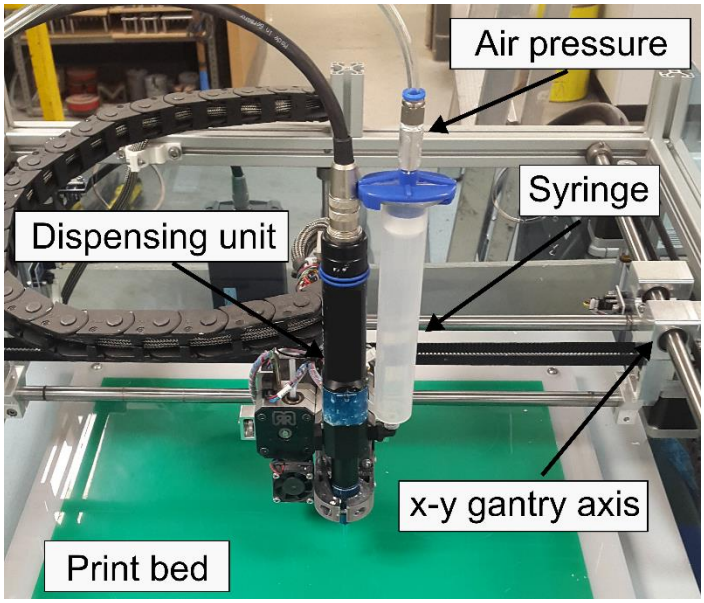

Figure 4.2 – Cavity dispenser installed onto x-y gantry of commercial 3D printer.

4.2.3 Data preparation

A 3D CAD file of the intended objects was exported in stereolithography (STL) file format. Slicer software (Slic3r) was used to generate the required G-Code from the STL file, which defines the print paths and extrusion rates. Adjustments to the G-Code to include time gaps were made by editing the code in NotePad++. A constant print speed was set at 30 mm/s. The buildability rings were single layers printed one on top of the other. The patches printed for adhesion consisted of multiple filaments with a rectilinear infill density of 100 % and a 90º crosshatched infill pattern. A single perimeter was also added to close potential gaps at the object's edges caused by the infill path. This also allowed greater interlocking between the infill and the outer shell (Zareiyan and Khoshnevis, 2017). Stepover between layers was not required as filament setting was expected to occur such that it will allow for sufficient overlap between the inner filaments. Each patch consisted of two layers with a layer height of 0.66 mm. The layer height was selected to be smaller than the nozzle size to allow for greater compaction between layers and with the substrate. The head distance of the nozzle was equal to the layer height. For the concrete cubes, the distance was measured from the highest point of the surface to avoid nozzle obstruction. Figure 4.3 presents a typical data file for a buildability ring and the overlay.

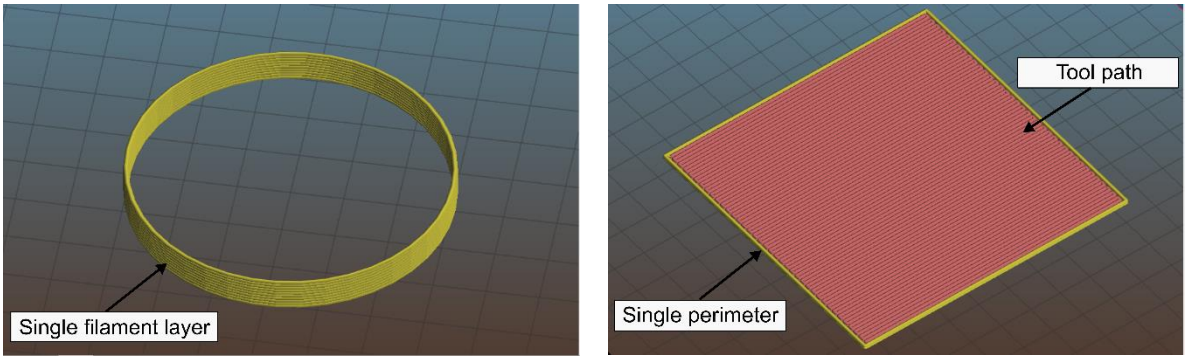

(a) (b)

Figure 4.3 – G-Code representation of a) buildability ring and b) overlay for concrete substrate.

4.2.4 Printing parameters

4.2.4.1 Extrudability

The author of this thesis broke down the investigation of extrudability into two parts, the 'preliminary investigation' and the actual investigation. The preliminary investigation involved examining if the mix design was compatible with the dispensing unit. Therefore, a small amount of filament was extruded for 10 seconds. If the filament was extruded continuously then the mix passed the preliminary test. The actual investigation involved printing three lines of filament with a length of 200 mm and 4 mm apart. If the lines were free from defects and had a consistent shape the mix was deemed extrudable.

4.2.4.2 Printability window

Once the mix was deemed as extrudable, the printability window was assessed. The printability window determines how long a particular mix can be extruded without any discontinuities or gaps. Three lines with a length of 200 mm and 4 mm apart were printed over the course of 120 minutes at a 10-minute interval.

4.2.4.3 Buildability

Buildability was assessed by extruding cylinders with a diameter of 60 mm denoted as 'buildability rings'. A preliminary assessment of 60 layers was conducted. Buildability was at first assessed by determining the amount of layers that could be 'stacked' prior to the collapse of the object. Initially 60-layer buildability rings were printed with a one-minute time gap between layers. A total of four rings were tested for

this investigation. This testing method led to poor results. Out of the four samples, two collapsed at the 42nd and 47th layer. When it pertains to the remaining two, as the layer height was kept constant throughout printing, the head distance continuously increased beyond a certain point which led to poor filament deposition. It was evident that neither objects were able to meet their intended shape. Following the above, the total height of the rings was reduced to 30 layers with the same time delay. In this occasion all four printed specimens remained intact, but similar to the 60-layer test, it could be visually accepted that the objects still maintained relatively poor quality.

Instead of changing the mix design, an effective means of increasing buildability is by increasing the time delay between layers to allow for greater strength development of the filament. Therefore, the gap between layers was increased to 3 minutes and the same investigation for 30 and 60 layer rings was carried out again. The effect of the increased delay between layers for both ring tests was evident. While all samples were able to maintain their shape without collapsing printing issues still persisted. Figure 4.4 presents 30 and 60 layer cylinders printed with a one minute and three minute time gap. Visually the 30-layer rings with a 3 minute time delay were able to achieve their intended shape to a greater extent compared to the rest of the samples. However, a different surface texture can be observed at the higher ends of this sample which signals poor filament deposition due to increasing head distance. In addition, even though the 60-layer samples did not collapse they resulted in uneven surfaces and gaps in the object which is a combined effect of extrudability issues due to the prolonged print run and head distance issues. Overall, it was evident that the objects were not able to meet their intended shape and therefore they were regarded as ‘failed’ trials.

(a)

(b)

Figure 4.4 – Buildability investigation a) 30 layer buildability rings with 1 minute (left) and 3 minute (right) time delay; b) 60 layer buildability rings with 1 minute (left) and 3 minute (right) time delay.

Taking everything into consideration, this means of assessing buildability was not deemed efficient and was not able to provide meaningful information on the buildability of the mix. As a result a different approach to buildability was followed[17].

Two sets of tests were conducted for rings between 2 and 10 layers. The two sets of tests employed different time gap between layers. The first test has a time gap of 1 minute and the second 3 minutes. Ten rings were printed for each layer test and 10 height measurements were made for each ring. The height of each ring was measured with a digital caliper. Following that the author of this thesis has defined a new metric to counter limitations of existing practice. The 'degree of buildability[18], was calculated for each ring using equation (4.1). In this case the extent in which a ring's actual height meets the design

[17] Another option to overcome buildability issues is with the use of 'adaptive slicing'. In this scenario a variable layer height is used which is proportional to the setting of the object. In order to use this method the structural buildup of the filament and the deformation upon each layer must be known. These factors were not investigated in this thesis as the height requirement of the patches were low. This approach can be considered in future printing applications particularly those with greater height requirements.

[18] This was implied by Nerella et al. (2020) but was not explicitly nor numerically stated.

height is assessed. This will allow to quantitatively determine the maximum allowable height an object can achieve within acceptable deformations.

$$\text{degree of buildability} = \frac{\text{Actual height}}{\text{Design height}} \times 100\% \quad (4.1)$$

When investigating the degree of buildability, it is important to keep a constant head distance between all objects. Different head distances can lead to different quality objects and ultimately different heights as well. Figure 4.5 presents 4 identical rings with different head distances. As can be seen, as the nozzle's distance from the bed increases the quality of the object decreases. As a result, the head distance was kept constant (equal to the layer height) for the investigation of degree of buildability to avoid inconsistencies between tests.

Figure 4.5 – Printed objects with different surface quality due head distance issues (head distance increases from left to right).

4.2.4.4 Open time

The open time of the AAM mix was measured using a Vicat needle apparatus as outlined in BS EN 196-3:2016 (British Standards Institution, 2016) in order to define the workable time a mix can be used. AAM paste was inserted in a conical mould with a height of 40 mm, bottom diameter of 70 mm and top diameter of 60 mm. The mould was placed underneath the needle with a thickness of 1 mm of the Vicat apparatus. The needle was dropped every 15 minutes and the penetration reading was acquired. The initial setting time is calculated from the point where the AAM constituents are mixed until the penetration reading reaches 25 mm. The final setting time is the time in which the needle does not leave a mark on the mix in the mould.

4.2.4.5 Adhesion

Double layered 90 mm × 90 mm patches were printed onto 100 mm concrete cubes. The mix design used for the concrete cubes is illustrated in Table 4.2. In order to

achieve adequate adhesion, proper surface preparation is required. While printing on a smooth concrete surface will simplify the printing process this will also lead to poor adhesion between the patch and the concrete cube. The patch will be in contact with the weak thin layer of cement on the surface of the cube which does not provide essential benefit in terms of adhesion. As a result the top layer of the concrete cube surface was removed with an electrical brush to expose the aggregates to improve adhesion between the patch and the substrate (Courard et al., 2014). The faces of the cube treated were the sides in contact with the formwork. The concrete substrate was also pre-wetted (Morgan, 1996) prior to printing to avoid liquid absorption from the concrete and thus excess liquid loss from the patch. The cubes were immersed in a water tank at least for twelve hours and were removed 30 minutes before printing. Excess water was removed with paper towels.

Table 4.2 – Concrete mix design for adhesion test.

Cement	7.5 kg
Sand	10.5 kg
10 mm aggregate	13.35 kg
Water	3.375 l

The bond strength of the printed AAM patches onto concrete was evaluated by using a pull-off adhesion tester in accordance with BS EN 1542-1999 (British Standards Institution, 1999). Once the patches were extruded the samples were stored in plastic containers and cured at 17 ^{o}C until testing. Three samples were tested at 6, 28 and 97 days after extrusion. Figure 4.6a and Figure 4.6b depict a schematic drawing and a picture of the cored samples The sample preparation for adhesion tests were as follows:

- The surface of the printed overlays was smoothened to remove any profile variations caused by printing.
- The samples were core drilled with a 50 mm diameter cylinder through the patch and into the concrete substrate for a total depth of 10 mm.
- An epoxy adhesive was used to attach an aluminium 50 mm dolly to the cored surface. The centre of the dolly was aligned with the centre of the core to limit eccentricity issues and assure proper load application.

- The epoxy was left to dry as per manufacturer requirements. The adhesion tester was then fastened onto the dolly for pull-off testing. The nut of the tester was tightened to evenly apply force to the dolly and subsequently stress to the coating. The nut was tightened until the dolly was detached from the substrate and a reading was taken for each sample.

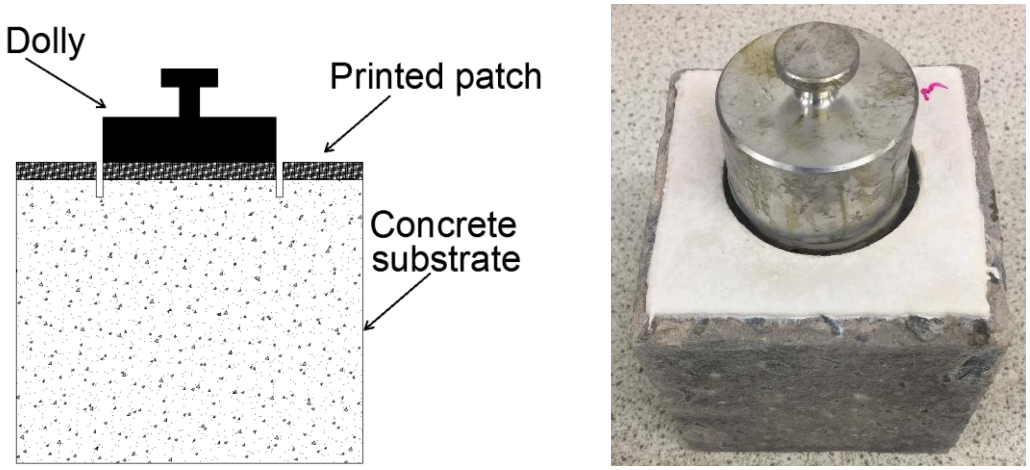

(a) (b)

Figure 4.6 – Printed overlay for adhesion test a) schematic drawing of sample b) picture of sample.

The surface roughness (R_a) of the concrete substrates was measured by 3D laser scanning (using a Micro Epsilon Scan Control 2700-100, an exposure time of 1 millisecond, 56 profiles per second, and 1600 buffered profiles). The values for surface roughness were determined by analysing the root mean square deviation of the point cloud from a mean plane, which represents the fitting plane of the cloud of points.

4.2.4.6 Conductivity

Four stainless steel electrodes were placed at the corners of double layered 90 mm × 90 mm patches employing the van der Pauw electrode configuration (van der Pauw, 1958). Voltage (V) 10 mV was applied with an impedance analyzer (Gamry Interface 1000) at an alternate current frequency between 1 kHz – 10 kHz and a current (I) was measured. Impedance was calculated via equation (4.2). The conductivity of the sample for this frequency range was measured using equation (4.3).

$$Z=\frac{V}{I} \tag{4.2}$$

Where: Z=Impedance; V=voltage and I=current.

$$\sigma=\frac{L}{Z\cdot A}CF \tag{4.3}$$

Where: σ=conductivity, L=length between applied voltage, Z=impedance measurement at a given frequency, A=the area of electrodes and CF=correction factor (between 0.5-1.0) applied to conductivity when employing the van der Pauw electrode configuration (Weiss, 2011). Figure 4.7 presents a printed patch with embedded electrodes. The conductivity and sensing performance of the printed patches will be assessed in greater detail in Chapters 5 & 6.

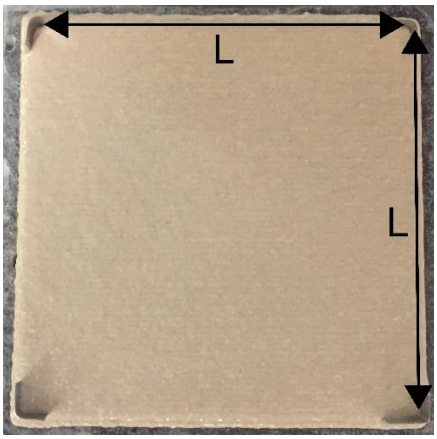

Figure 4.7 – Electrode configuration of printed coating.

4.3 Results and discussion

4.3.1 Extrudability

In order to formerly assess extrudability, a preliminary test was required which would determine the mix design that would be used going forward. This essentially investigates the compatibility of the various mix designs with the current printing setup. In order for fibers to have a strong impact on adhesion, a minimum content of 0.5 wt% is normally required (Albidah et al., 2020; Bhutta et al., 2019; Nunes et al., 2019; Zanotti et al., 2017). As a result, the initial mix designs included 0.5 wt% of PVA (3 mm), PP and carbon fibers of in the mix. Out of the three fillers only PVA fibers were extrudable at this

amount as they are more malleable due to their flexible nature. PP and carbon fibers are stiffer fibers and caused clogging in the nozzle and thus were unable to be continuously extruded. The solid content would have to be lowered to provide greater flowability of the paste in the dispensing unit and thus extrudability. However, this would come at the expense of buildability. While the mix does not require high extents of buildability (see Section 4.3.3) it still requires a certain degree of consistency to maintain its shape and prevent the mix from spreading onto the concrete surface. Bearing all this in mind PVA fibers will continue being investigated in extrudability.

Considering the nature of PVA fibers, two addition investigations were carried out. The first involved increasing the quantity of PVA fibers to 1 wt%. The second was to incorporate larger sized PVA fibers of 6 mm. Both these mixes though did not pass the preliminary extrudability investigation as they led to discontinuities in extrusion. As a result PVA (3 mm) fibers at 0.5 wt% were used as filler for the remainder of the thesis.

The preliminary investigation enabled us to narrow down the available mix design options for extrudability. Extrudability can now be formally assessed by printing three straight lines. Figure 4.8 depicts the outcome of this test for this mix design. As can be seen, the three lines maintained a fairly consistent shape and were free from defects. Slight variations in dimensions were due to slight leveling issues and entrapped air which caused less material to be extruded in certain areas and more in others. This however can be adjusted by calibrating the dispenser and print bed accordingly. The impact this had on the extrudability test though was minimal and did not affect the extrudability integrity of the mix. Taking all this into account the mix was deemed extrudable and can be assessed for further printing parameters.

Figure 4.8 – Extrudability assessment of mix design by printing three 200 mm lines.

4.3.2 Printability window

Although the mix was deemed extrudable this test provides limited information on the overall extrudability of the mix. In essence this demonstrates that the mix meets extrudability requirements for a particular point in time (e.g. t=0). Printability window assesses the mix's extrudability over a set period of time. Figure 4.9 presents the results of the printability window test for 120 minutes at 10-minute intervals. As can be seen, the filament is extrudable over the course of 120 minutes as the printed lines maintain a consistent shape and do not display discontinuities. Some small gaps that are visible in some lines are primarily due to residual air bubbles in the filament. Beyond this time frame, extrudability issues were experienced due to hardening and clogging of the mix at various points in the extruder. While this is more related to the equipment rather than the mix itself, it is still a factor that must considered in printing even if the material is still in an extrudable state. Under these conditions the dispenser would require maintenance which would involve cleaning or replacing parts for this print run. Moreover, it should be mentioned that as the material is dormant for 10 minutes more pressure is required to initiate extrusion. This may lead to small gaps at the toe of the lines. These gaps though do not affect the extrudability integrity of the mix.

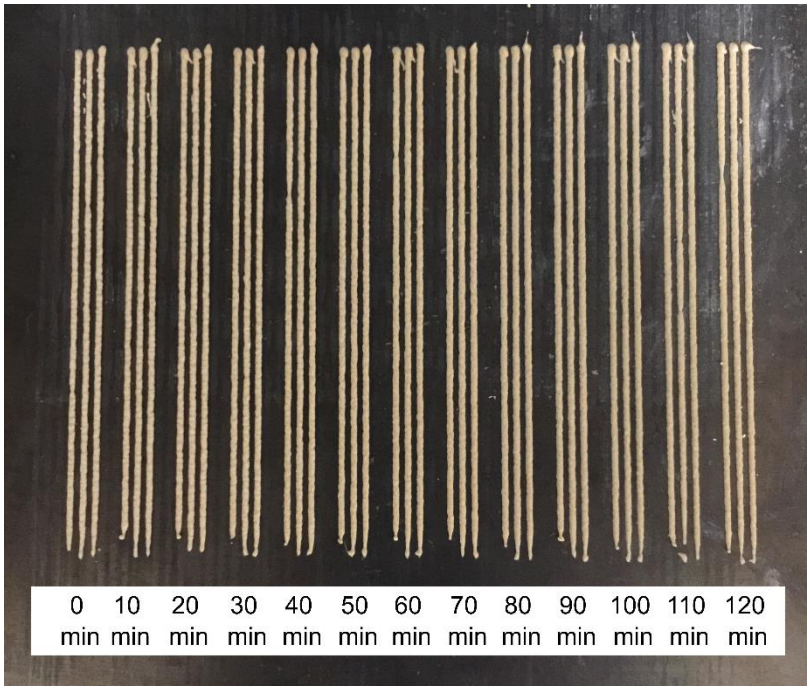

Figure 4.9 – Printability window test for 120 minutes at 10 minute intervals.

4.3.3 Buildability

For this thesis, 3D printing will be used to apply overlays onto concrete substrates. This will require relatively large spans in the x and y directions only a few layers in the z-direction. While this still includes the use of a gantry system and a dispensing unit extruding a cementitious filament in a layer-by-layer manner, it can also be viewed as 2.5D printing due to its low thickness[19] (Leech et al., 2020). Nonetheless, the mix must still undergo the verification process to ensure it meets printing requirements to be compatible for its intended use. Therefore while 2.5D printing can provide some insight on the shape and size of the printed objects, the name of the extrusion process is of secondary importance.

Following the methodology presented in Section 4.2.4.3 buildability rings were extruded between 2 to 10 layers with a time gap of 1 minute and the degree of buildability was

[19] Authors have also considered contour crafting as 2.5D printing as extrusion was described as a vertical extension of a plane shape and is essentially unable to print complex shapes (Gosselin et al., 2016). This is not considered as 2.5D printing in this study. Cementitious printing has been given various names over the course of time that attempt to define the uniqueness of each printing application. For example, cementitious printing has also been regarded as 4D printing to account for the fourth dimension of time (Franchin et al., 2017).

calculated for each ring using equation (4.1). Figure 4.10 depicts the degree of buildability for these specimens. The degree of buildability in this case ranged between 73% and 98% for rings between 10 to 2 layers respectively. The degree of buildability continuously decreased with the deposition of additional layers. This signals that the previous layers are unable to fully support the weight of the newly deposited layers. This results in deformation and subsequently incorrect filament deposition due to the increasing head distance. Maximum deformation allowed in buildability and shape retention tests ranges between 80-90% with structural applications being at the higher end of this spectrum (Chen et al., 2020; Nair et al., 2019; Tay et al., 2019). Considering the low thickness requirements of the coatings and in order to allow proper interlocking with the substrate, a maximum deformation of up to 80% was deemed acceptable irrespective of the number of layers object.

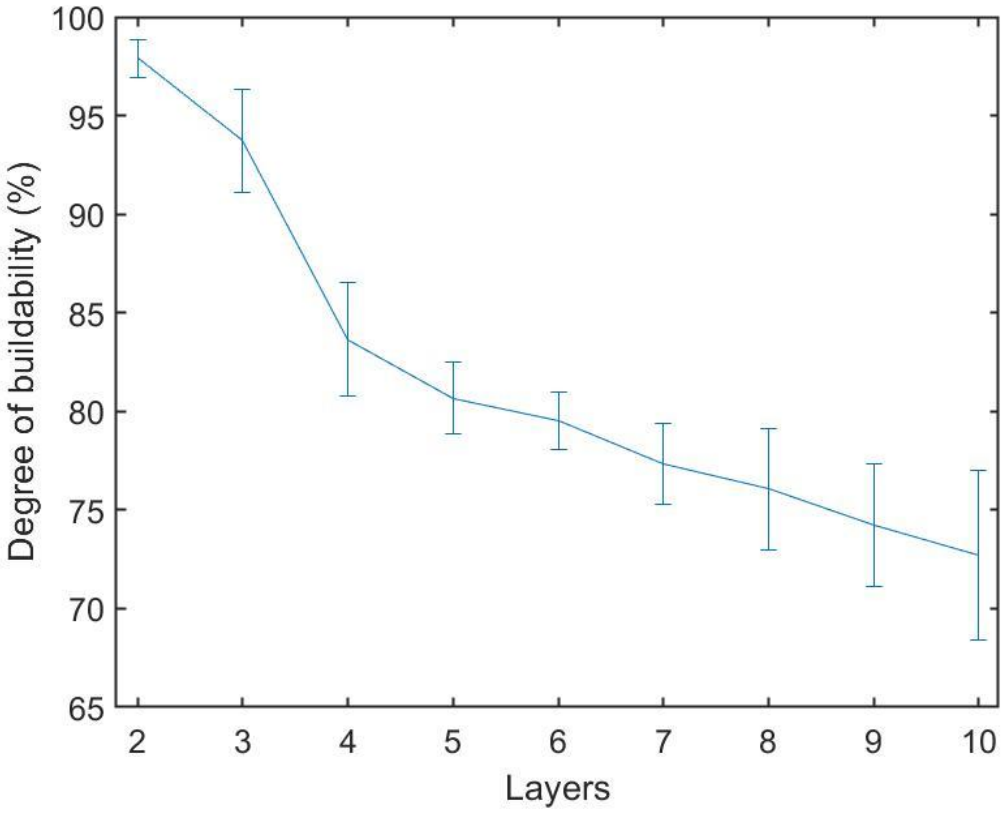

Figure 4.10 – Degree of buildability for buildability rings between 2-10 layers with a time delay between layers 1 minute. Errors bars represent standard deviation of 10 measurements per sample for 10 samples.

Considering the above, only rings with layers between 2-4 are able to securely meet the 80% deformation threshold. In order to allow the filament to withstand the weight of additional layers the time delay was increased to 3 minutes for buildability rings between 5 and 10 layers. Figure 4.11 presents a typical buildability ring with 10 layers. Figure 4.12 presents a comparison of the degree of buildability between the rings between 5 and 10 layers with a time gap of 1 and 3 minutes. Increasing the time gap was beneficial for the shape of these objects. The degree of buildability ranged from 85% to 92% for rings between 10 and 5 layers respectively. Under these conditions, the mix is able to be print objects up to 10 layers within deformation limits.

Figure 4.11 – Ten layer printed buildability ring.

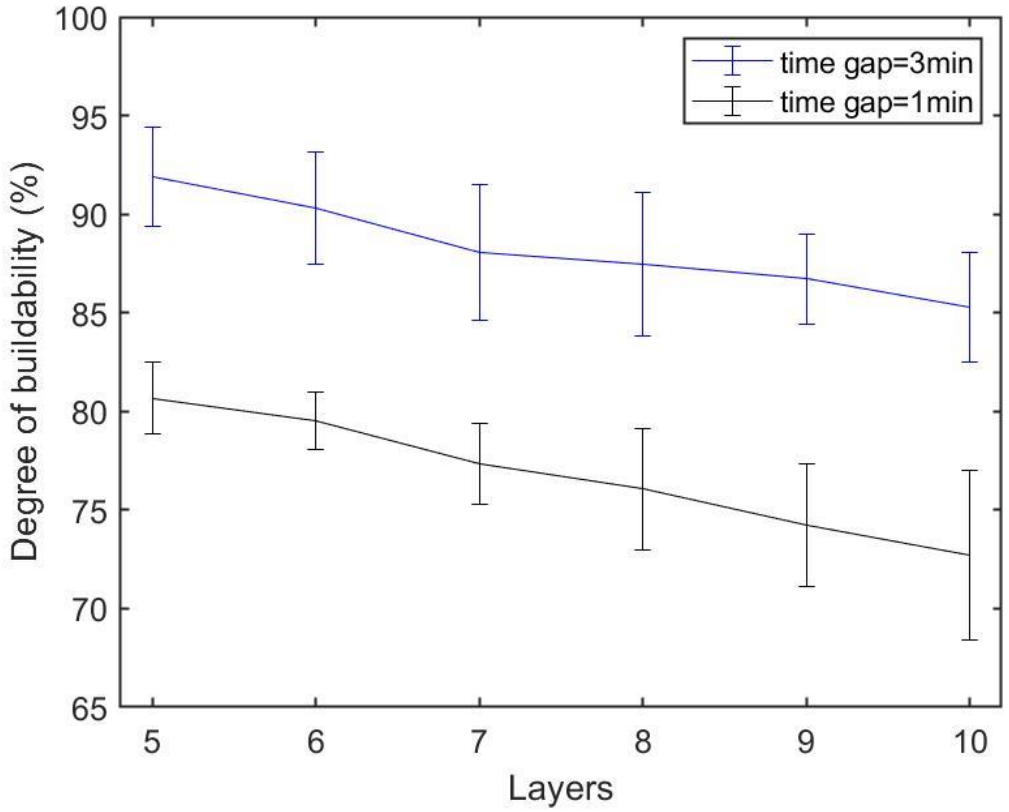

Figure 4.12 – Comparison of degree of buildability for buildability rings between 5-10 layers with time delays between layers 1 and 3 minutes. Errors bars represent standard deviation of 10 measurements per sample for 10 samples.

Buildability is a relatively abstract term to address due to the different printing setups and applications. As mentioned in Section 2.4.4.1, buildability is associated with low-deformation mixes. This however does not depict the entire picture of printing in the civil

engineering. The importance defining buildability in the proper context was pointed by Nerella et al. (2020). It was stated by the authors that deformations and tolerances should be allowed depending on the application to avoid the risk of overdesigning. In the current application, the intention is to produce coatings on substrates. Deformation is allowable in this application as coatings are required to spread onto the concrete surface and anchor into the concrete capillaries to achieve a greater bond (Courard and Degeimbre, 2004). In like manner, this mix will not be suitable for construction purposes with great height demands. Achieving a greater height or improving the degree of buildability of the existing rings is possible by extending the delay time even further. This however would be counterproductive as the delay time will significantly outweigh the printing time and thus altering the mix design would be a better option. Furthermore, developing objects with such capabilities lies beyond the scope of this thesis.

4.3.4 Open time

The initial setting of the mix was recorded as 16 hours and the final setting time as 20 hours. The setting time in this test was quite long compared to mixes used in most printing applications in the literature, but mixes with prolonged setting times (Chaves Figueiredo et al., 2019) are still usable. In general the setting time of mixes is short (less than an hour) in mixes with a high solid content, filler and thickening agents (Chougan et al., 2020; Panda et al., 2019). The current mix did not employ a large amount of filler nor did it involve any additional agents, therefore the long setting time is anticipated. While short setting times may be common for construction elements (short setting time can be associated with high viscosity which is a common trait in several printable mixes) having a long setting time is beneficial for coating applications due to the larger surface areas that are required to be covered. Moreover, it was shown in Section 4.2.4.3 and Section 4.3.3 that slight modifications in extrusion settings can increase a mix's printing potential if required. The setting time of the mix should be primarily used as an indication on the workability window of a mix.

Open time is the only printing parameter directly referring to time by provided by Le et al. (2012). However, it only covers a small aspect of time in 3D printing. Diggs-McGee

et al. (2019) conducted an extensive study to define the different categories of time in 3D printing. Time was classified as total construction time, print time of layer, delay time and elapsed time of layer. Most studies primarily focus on the total time to construct an object without considering potential faults and maintenance requirements in printing. For example, a material with a short setting time (below 30 minutes) may present issues in extended printing sessions as this may require constant maintenance of the equipment due to clogging. Overall the different aspects of time may impact printing systems differently. For instance in the current setup mixing and printer preparation time took about 30 minutes. The same process would most likely take longer in larger scaled applications due to manual handling of larger volume of material and equipment.

4.3.5 Adhesion

Figure 4.13a displays a typical concrete surface after surface preparation and Figure 4.14 presents a standard printed overlay onto a concrete cube. Figure 4.15 presents the adhesion strength of the printed overlays for days 6, 28 and 97. The bond strength was measured as 0.90 ± 0.36 MPa, 0.68 ± 0.2 MPa and 0.78 ± 0.06 MPa respectively[20]. The bond strength does not experience substantial change over the course of time, as changes are all within the error of the adhesion testing apparatus. All coatings tested exhibited adhesive failure – failure at the interface between the patch and the substrate. The mean surface roughness (R_a) ranged between 0.44-0.68 mm. Overall the bond strength was somewhat low compared to other AAM repair investigations (Nunes et al., 2019; Zanotti et al., 2017) but is still within a serviceable range. While it can be inferred that the layer-by-layer deposition may have affected the mechanical properties of the coatings (Bong et al., 2019), this could also be a result of the surface preparation technique. The roughness achieved from wire brushing was relatively low compared to that achieved in other studies (Santos and Julio, 2011). In certain cases, as can be seen in Figure 4.13b wire brushing led to a rather polished surface which does not provide much benefit in terms of adhesion[21]. This signals that a more aggressive treatment technique is required for the concrete

[20] The large variation of results is also due to the of the adhesion tester's variability of force measurement ±15%.
[21] The differences in polished layers could also indicate inconsistencies in the concrete mix designs between batches.

substrates used in this thesis. Employing a more suitable surface preparation technique such as sandblasting can increase the surface profile between the patch and the substrate and improve the adhesion through mechanical interlocking (Courard et al., 2014). This would require additional layers to be extruded to allow for proper levelling of the coating.

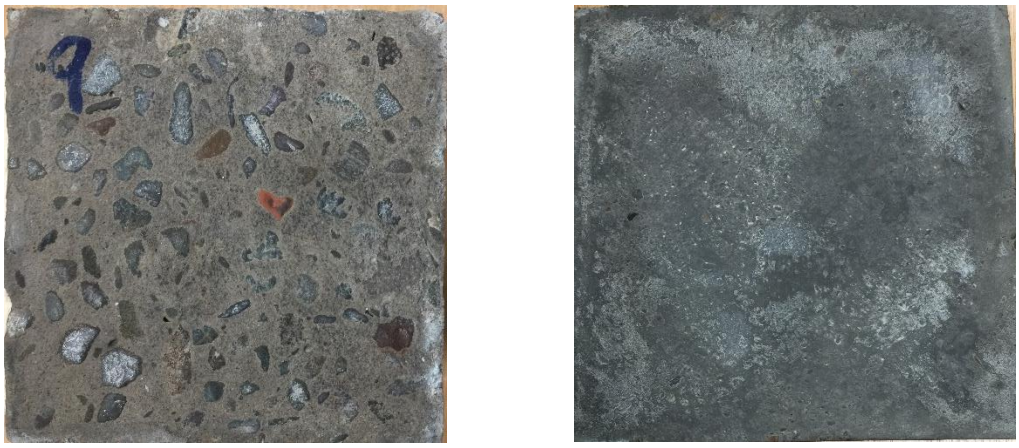

(a) (b)

Figure 4.13 – Variations in concrete surfaces after wire brushing a) rough surface with exposed aggregates b) polished surface.

Figure 4.14 – Typical printed coating deposited onto concrete cube.

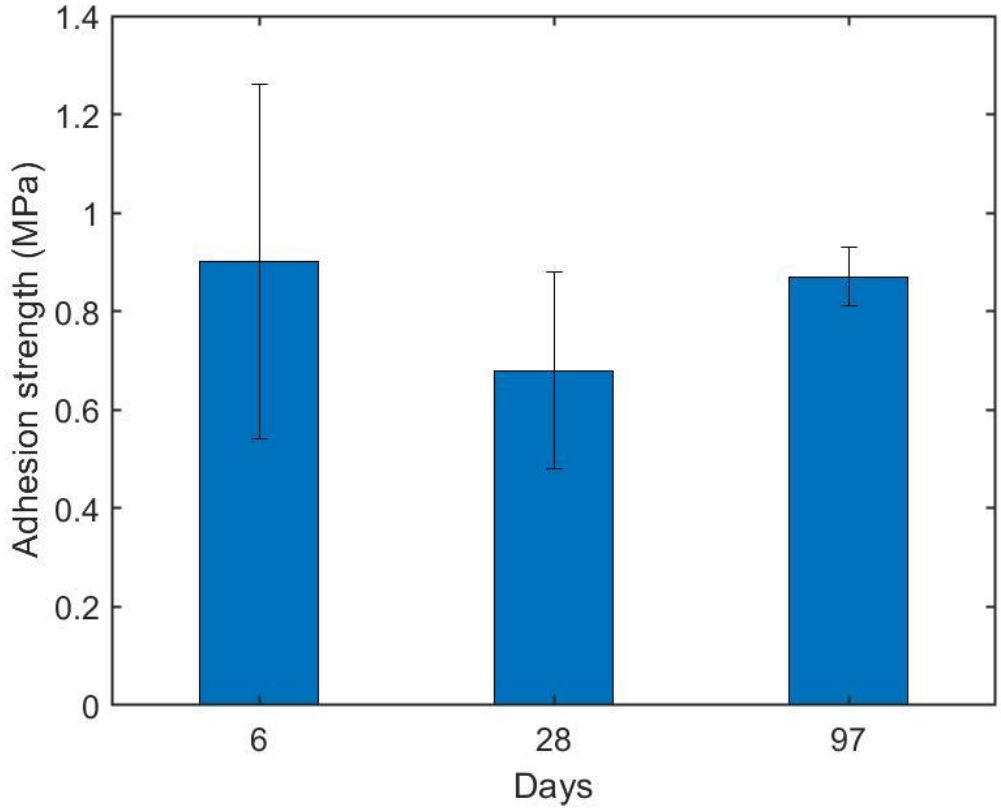

Figure 4.15 – Adhesion strength of printed overlays at days 6, 28 & 97. Errors bars represent standard deviation of measurements for 3 samples.

In this study interlayer adhesion is not assessed as this is normally examined in objects fabricated using the full width printing technique (Panda et al., 2018). While the

‘buildability rings’ are considered full width objects, their size is too small to be accurately tested. Furthermore, as the primary objective is to print coatings, adhesion between two single layers does not provide essential information for this application with the current setup. Additionally, considering adhesive failure occurred in all bond strength tests, this indicates that the tensile strength in the overlays was greater than the bond strength achieved.

Adhesion and interlayer adhesion have been mentioned to share some similarities (Wolfs et al., 2019). The author of this thesis considers that they should be regarded and dealt as two separate concepts in 3D printing. Adhesion involves a freshly deposited material onto an already cured surface of another material which has undergone proper treatment (surface preparation and prewetting) to promote greater adhesion between the two materials. Interlayer adhesion involves the bond strength of two layers of the same material within a relatively short time frame which is something that cannot always be achieved in adhesion.

4.3.6 Conductivity-sensing capacity

AAM possess inherent electrical properties due to the alkali ions in their matrix and thus can be used in sensing applications via ionic conduction. The reader is referred to Section 2.3 for a more in-depth review on conductivity and sensing performance of alkali activated materials. The impedance of the sample remained relatively stable for frequencies between 1 kHz - 10 kHz. The conductivity of a printed patch in this frequency range was measured in the range of 10^{-5} – 10^{-4} S/m. This value is within the range of conductivity of cementitious materials used in previous sensing applications. As mentioned in Section 2.3.2.4 though, while the binder must showcase some form of conductivity in order to be used in sensing applications, high conductivity does not always translate to high sensing capabilities. The following step in this requirement would be to characterize the sensing response of the material. Section 2.3 presents testing methods for strain, temperature and moisture sensing. The sensing characterization in terms of temperature and strain of the printed patches is presented in Chapters 5 & 6.

The conductivity and sensing requirement for sensing overlays is achieved by the source material being an alkali activated material. As mentioned in Section 2.3.3.2 AAM are able to be used in sensing applications without relying on the use of conductive filler (Biondi et al., 2020; Saafi et al., 2018). If an OPC mix was used, this requirement would require greater investigation as the main conduction mechanism in OPC binders is through electronic conduction which demands conductive filler.

Overall, conductivity and sensing should not be viewed in the same lens as other printing requirements, because they are not only influenced by the mix design and printing parameters. However, they are important as they are prerequisites for the intended application outlined in this thesis.

4.3.7 Workability

In this work, workability-flowability was not assessed. The material was manually inserted into the syringe barrel as shown in Figure 4.2. If the mix was not able to be inserted, then it would automatically be disregarded for printing. Furthermore, the material is required to flow through the syringe barrel and into the dispensing unit as illustrated in Figure 4.2. In the event where flowability was an issue, this would have a direct impact on extrudability. Therefore, extrudability and printability window can be used to indirectly provide information on the workability-flowability of the mix.

4.4 Conclusions

In this chapter the 3D printing of cementitious materials is presented. Sets of guidelines and requirements have been developed over the years to assess a mix's suitability for printing. These requirements have expanded and been modified by the author of this thesis to adapt to the requirements and the intended application of the printed object. In this chapter the printing requirements were tailored to allow the extrusion of self-sensing overlays for concrete substrates. This led to examining the following parameters: extrudability/printability window, buildability, open time, adhesion and conductivity/sensing. The testing method and results for each are presented and their significance in printing is also outlined. The key findings of this chapter are the following:

- PVA fibers present greater extrudability for syringe-based printing setups. PP and carbon fibers are not as effective as they cluster inside the dispensing unit causing extrudability issues.
- Printability window is an effective means of providing essential information on the extrudability, open time and workability of a mix in a single investigation. The printability window of the mix design was 120 minutes. This time frame allows the extrusion of multiple sensing patches. Extruding beyond the printability window could lead to printed objects with poor quality.
- Buildability and shape stability can be achieved to a greater degree by allowing the filament sufficient time to solidify and develop adequate strength before depositing additional layers. Increasing the time gap from 1 minute to 3 minutes between layers led to significantly increased print quality and degree of buildability.
- Adhesion and conductivity are added requirements that must be met to ensure proper functionality of self-sensing overlays. These parameters must be considered when developing AAM sensors as they may influence the mix design and preparation steps required for printing sensing patches. The conductivity of the patches was measured as 10^{-5} – 10^{-4} S/m. Adhesion between the printed patches and the substrate was determined between 0.68 MPa – 0.90 MPa.

The temperature sensing capabilities of the sensing coatings produced by following the methodology outlined in this chapter will be explored in Chapter 5.

Chapter 5 3D printed temperature-sensing coatings for concrete structures

In this chapter the temperature sensing response of printed coatings is investigated. The coatings are fabricated following the printing methodology presented in Chapter 4. Other factors such as adhesion and printing settings are also investigated[22].

5.1 Introduction

Following the literature on AAM sensing and the development of AAM patches, this chapter focuses on the temperature sensing response of printed metakaolin AAM patches onto concrete substrates. We discuss and test the adhesion of the patch, its temperature-sensing capability, and the challenges in development. As far as we are aware, this is the first time that 3D printable self-sensing repairs for concrete substrates have been demonstrated. In this chapter the following investigation is carried out:

- The impedance and repeatability of AAM for temperatures between 10 ^{o}C – 30 ^{o}C for two temperature cycles is examined.

[22] This chapter was published in the August 2020 issue of the Additive Manufacturing journal Vlachakis, C., Perry, M., Biondi, L., & Mcalorum, J. (2020). 3D printed temperature-sensing repairs for concrete structures. Additive Manufacturing, 34(August), 101238. https://doi.org/10.1016/j.addma.2020.101238 Minor changes have been made to this chapter to include data acquired after the publication of the manuscript and to update figures and literature.

- The temperature sensing behavior of the AAM patch is characterized.
- An equivalent circuit model for AAM patches on concrete substrates is presented.
- The effect of heat curing on the adhesion of printed patches is explored.
- Factors affecting the quality of the printed patches are also highlighted.

Applications for this technology include remotely-deployable, retrofitted repairs and continuous monitoring solutions for existing structures in hazardous construction, nuclear or oil and gas environments. Due to the fabrication steps involved, this technology is better positioned to be deployed onto precast elements for installation in structures in the aforementioned environments. In order for the AAM patch to function as a temperature sensor, both the substrate and the patch should be situated in an environment where relatively stable conditions are anticipated. This is necessary as AAM require a considerable amount of time to stabilize due to low thermal conductivity (Prałat et al., 2021). Having the concrete substrate and AAM patch exposed to different environments (e.g. AAM is indoor and part of the substrate is outdoor) can lead to simultaneous temperature effects on the system which can cause sensing interference and inaccurate readings.

It is important to point out that while simpler methods for temperature sensing exist (i.e. thermocouples) it remains essential that the temperature behavior of AAM is characterized. This will allow for the investigation of more complex testing conditions in future applications such as strain tests at various temperatures. The temperature behavior of AAM can also assist in distinguishing behaviors that may occur in prolonged monitoring applications such as creep or even electrolysis. Overall facilitating cheap, low-risk, continuous data acquisition could contribute to a clearer understanding of concrete structural health and design.

5.2 Methodology

The following sections outline the experimental procedure that is carried out to investigate the temperature sensing response of coatings. The sensing procedure was drawn on the scientific literature presented in Section 2.3. Material preparation was based on the methodology presented in Section 3.2 on alkali activated materials and the printing

process was based on the investigation carried out in Chapter 4. The reader is advised to revisit those chapters for more detailed explanations in each of the respective areas.

5.2.1 Materials and mixing

The AAM constituents and mixing procedure used in this chapter is based on Mix design 2 outlined in Section 3.2.

5.2.2 3D Printing overview

The 3D printing process followed in this chapter is based on the procedure introduced in Chapter 4. Figure 5.1 depicts the printing setup as a reminder to the reader. The steps in the 3D printing were extended from Le et al. (2012a) to encompass: 1) data preparation, 2) concrete surface preparation, 3) filament mixing and loading, 4) printing, 5) electrode insertion, and 6) curing. The printing process is outlined as a flowchart in Figure 5.2. It essentially explains the iterative process in 3D printing. Similar to other cement-printing flow charts, the data files are prepared by using a slicing software and the filament is prepared and printed (Panda and Tan, 2018). Compared to other flowcharts in 3D printing, the main differences are the addition of concrete surface preparation, electrode insertion and curing. In most cases these factors are absent, however in the current application these parameters must be investigated as they are paramount factors in ensuring proper function of sensing repairs. The printing process is explained in further detail in the Sections 5.2.2.1, 5.2.2.2 and 5.2.2.3.

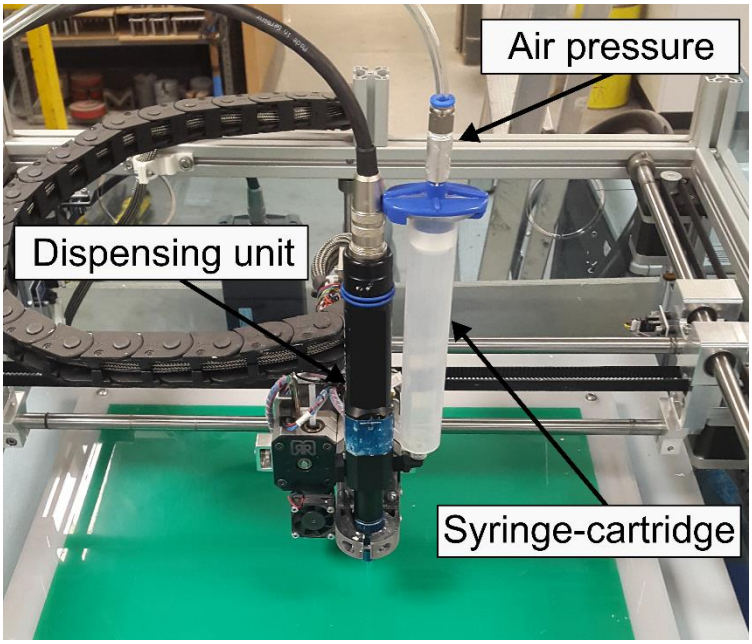

Figure 5.1 – 3D printing setup showing the dispensing unit and an empty pressurized feed cartridge.

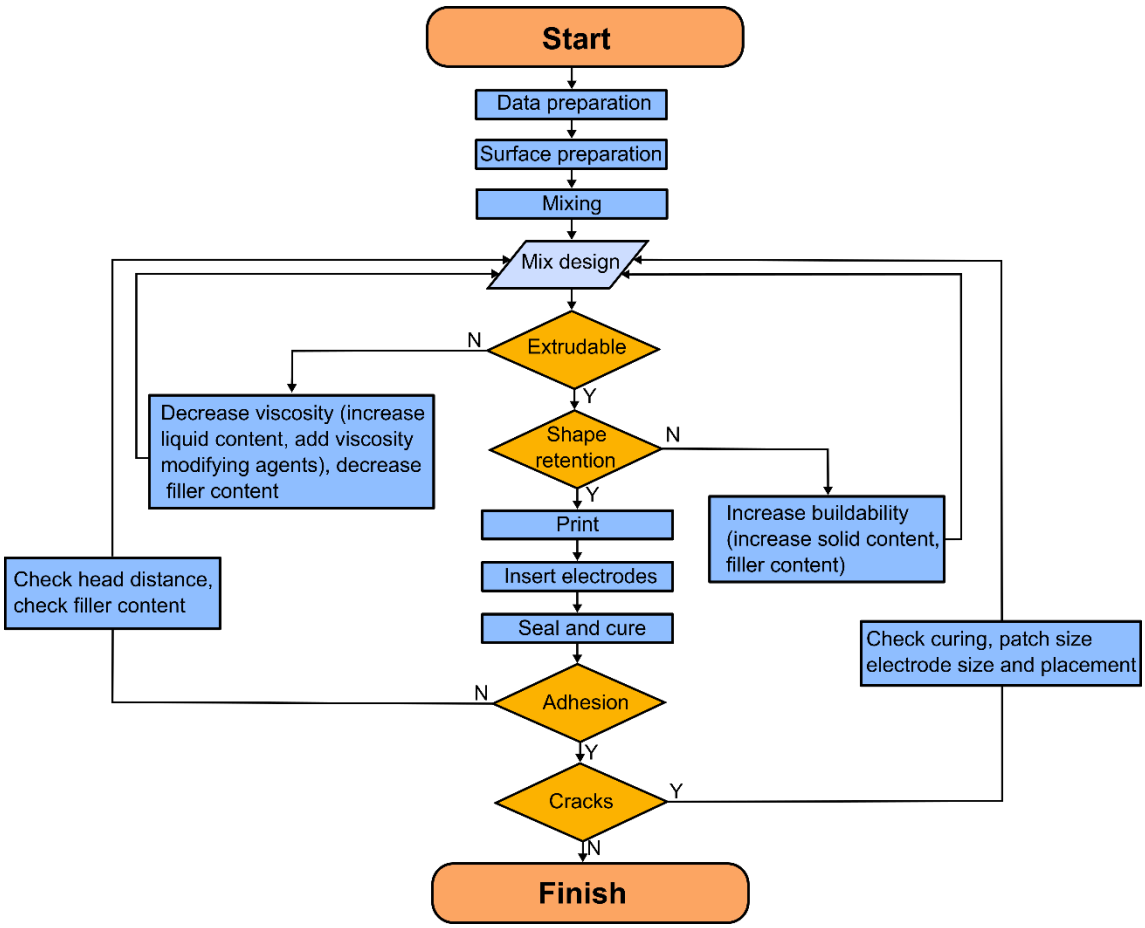

Figure 5.2 – Flow chart of printing and fine-tuning process.

5.2.2.1 Data preparation

Data preparation followed the same procedure as in Section 4.2.3. In this investigation double layered 90 mm × 90 mm patches were extruded at a print speed of 50 mm/s and a layer height of 0.66 mm. Figure 5.3 depicts the sliced model for a standard AAM patch.

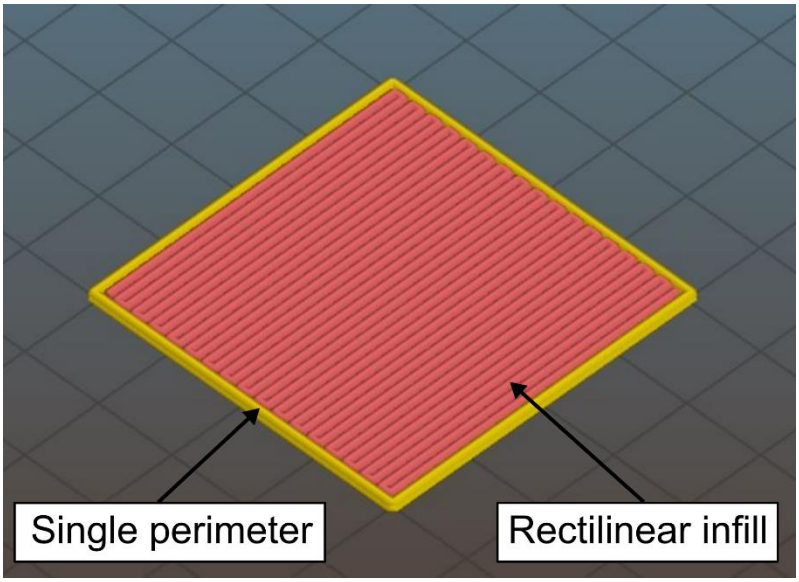

Figure 5.3 – G-Code representation of patch.

5.2.2.2 Concrete surface preparation

In this work, AAM patches were printed onto concrete slabs (70 mm × 20 mm × 20 mm) and cubes (side 100 mm). The former substrate was used for temperature sensing purposes and the latter for adhesion testing. Smaller substrates were selected for temperature sensing tests as larger concrete substrates exhibit high thermal inertia leading to longer stabilization periods for the AAM overlay. Both concrete substrates employed the same mix design presented in Table 4.2. Likewise, the surface preparation technique presented in Section 4.2.4.5 is followed in this chapter. As a recap, the top layer of the cube surface was removed with an electrical brush to expose the aggregates and improve adhesion between substrate and patch (Courard et al., 2014). This is standard practice when repairing a concrete structure. In order to avoid liquid absorption, the concrete substrate was then pre-wetted (Morgan, 1996) prior to printing to avoid excess liquid loss from the patch. The substrates were immersed in water at least for twelve hours and were removed shortly before printing. Excess water was removed with paper towels. Long print runs may lead to concrete surface drying and induce high levels of shrinkage in the patch. The longest printing duration lasted about 20 minutes for the 100 mm concrete cubes. This printing time was not deemed long enough to cause excessive drying in the concrete substrate. This was empirically confirmed as patches printed on prewetted substrates did

not display any cracks. As a result, any potential drying effects of the concrete substrate were disregarded. The reader is referred to Section 5.2.7 for greater analysis on shrinkage control.

5.2.2.3 Filament mixing and loading

The AAM mix was deposited into the barrel syringe (the cartridge labelled in Figure 5.1). As the material was, by design, not self-levelling, it was placed under an air pressure of 2 bar to force the material to flow into the screw extruder's dispensing cavity. Figure 5.4a presents a drawing of the dispensing unit printing and Figure 5.4b depicts a photograph of the printing procedure on a concrete slab that has undergone surface preparation. The density of the mix was 1.73 g/mL and the flowrate of the mix during printing was 2 mL/min.

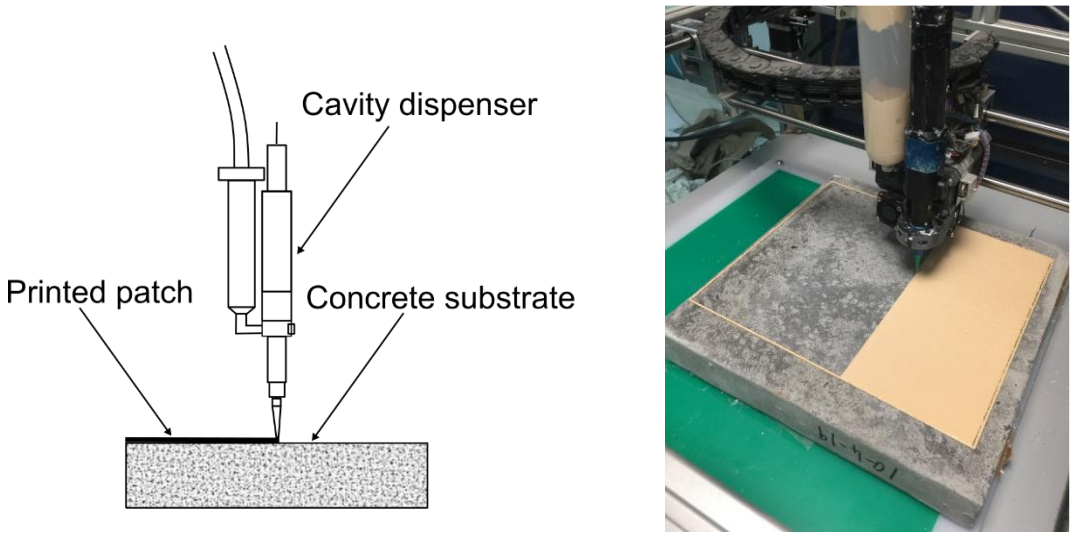

(a) (b)

Figure 5.4 – a) Schematic diagram and b) photograph of AAM being extruded onto concrete slab.

5.2.2.4 Electrode insertion

The probes for electrical sensing were stainless steel wires, attached according to the Van Der Pauw (VDP) configuration (van der Pauw, 1958). Thin wires were used as they are able to minimize the electrode effect on the patch and limit the generation of cracks considering the relatively small patch size that was employed. The VDP configuration further contributes to maintaining the integrity of the patch as sufficient

distance is maintained between the electrodes avoiding high levels of stresses being developed. By maintaining a sufficient distance between the electrodes, inductance due to electrode cross-talk can also be avoided to a certain degree. Moreover the VDP configuration also provides an average (rather than localised) measurement of the patch's overall impedance. Two methods of incorporating the electrodes were tested in this work:

- Method 1: was to pre-arrange the probes on the concrete substrate and print directly over them.
- Method 2: probes were inserted into the patch after the patch was printed.

5.2.2.5 Curing

The samples were then stored in sealed, plastic containers to maintain moisture and cured at 40 °C for 24 hours. The elevated temperature is not mandatory (Biondi et al., 2019) but accelerates the alkaline activation process. The samples were then kept under ambient conditions until testing.

5.2.3 Sensor testing

The electrical properties of the patch were analysed with an electrical impedance analyser (Gamry Interface 1000) running in potentiostatic mode. The impedance of the samples was measured by applying 10 mV voltage for frequencies between 10 Hz and 100 kHz and measuring the electrical current response. The impedance was then determined using equations (2.5) and (2.6) listed in Section 2.3.2.3. The electrical configuration is depicted in Figure 5.5. The voltage was applied across electrodes 1 and 4 and the current was measured across electrodes 2 and 3.

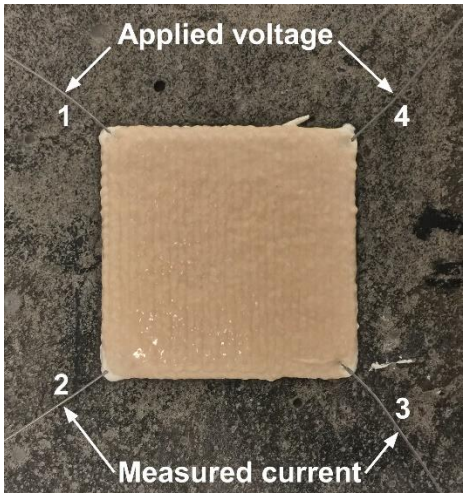

Figure 5.5 – Printed sensor on a concrete substrate.

In order to avoid humidity fluctuations during temperature experiments, samples were placed in a controlled environmental chamber. The chamber set the temperature at 30 °C and then reduced it to 10 °C in 5 °C steps: we denote this the "down cycle". It then performed an "up cycle", increasing temperatures from 10 °C to 30 °C in 5 °C steps. When target temperatures were reached, they were held for 135 minutes to ensure thermal stabilisation of the patch and the concrete substrate. Following this, temperatures were held for a further 15 minutes and measurements of impedance were taken. This allowed for extraction of average values of impedance components over this time period. Note that this long measurement period is not something that would be required during sensor operation, but it does improve measurement confidence during characterisation. The temperature steps as recorded by an external sensor are presented in Figure 5.6.

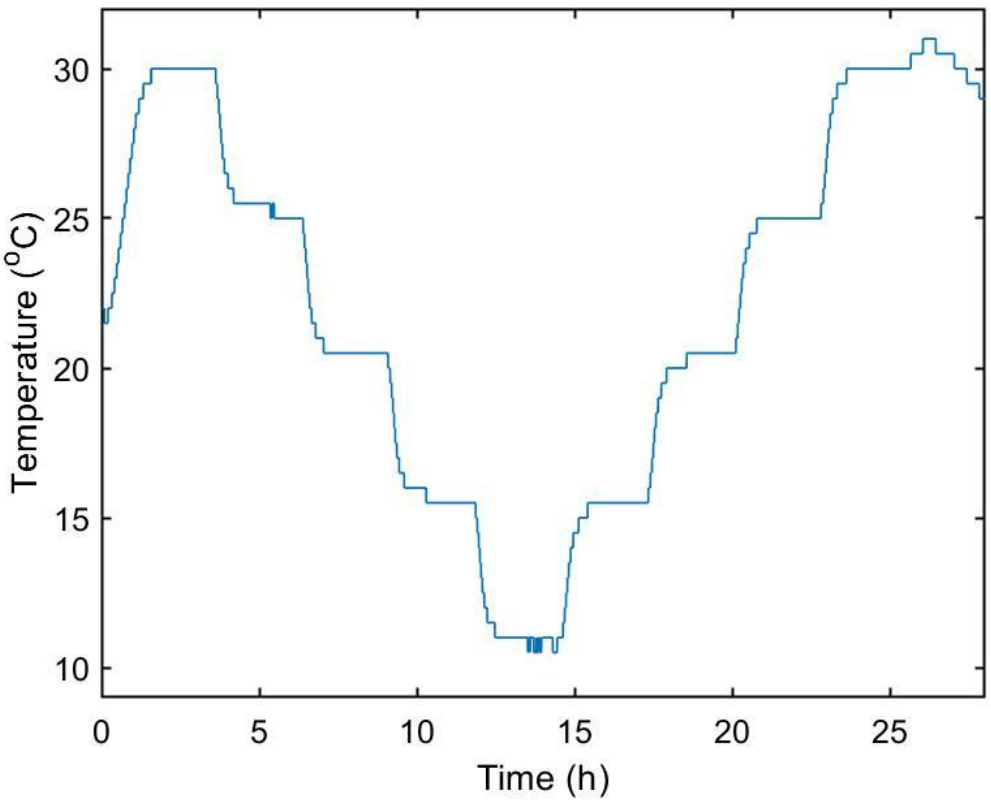

Figure 5.6 – Time-temperature series for temperature characterization.

5.2.4 Adhesion testing

In this chapter the effect of heat curing on printed patches was investigated. Double layered 90 mm × 90 mm patches were printed onto concrete substrates. The mix design for the substrates is depicted in Table 4.2. The surface of the substrates was prepared and adhesion was assessed following the methodologies and testing procedure outlined in Section 4.2.4.5.

5.2.5 3D printing: tuning and improvement

The mix design used in this chapter has been verified that it is suitable for printing AAM overlays for concrete substrates following the investigation conducted in Chapter 4. Out of the parameters requirements examined in Chapter 4, buildability adhesion and conductivity sensing are further analyzed in this chapter.

The final requirement, and the one that required the most mix design alterations was the trade-off between buildability and adhesion (and to a lesser extent, a trade-off with electrical conductivity). Unfortunately, in cementitious materials, a high buildability and high adhesion tend to be two contradictory requirements. Normally, buildability of a cementitious material (including AAM) would be increased by increasing its solid content (Roussel, 2018), but this comes at the expense of inter-layer and substrate adhesion (Courard, 2005; Courard and Degeimbre, 2004; Le et al., 2012b; Sanjayan et al., 2018), higher shrinkage due to greater stress development (Beushausen and Bester, 2016) and conductivity (Hanjitsuwan et al., 2011; Payakaniti et al., 2017), as shown in Table 5.1. In other words, opting to maximize the patch's printing potential would compromise the repair and sensing aspects of the patch. For this reason, a zero-slump mix was not suitable for this sort of application.

Table 5.1 – Functional requirements for 3D printed self-sensing materials.

	3D printing/extrusion	Repairs	Self-sensing materials
Solid content	High	Low (high liquid content)	High liquid content (greater conductivity)
Surface quality	Smooth flat surface	Rough surface better adhesion	–

This issue could be solved by using several mixes, such as a low viscosity primer layer followed by more viscous additional layers for printing. This would come at the cost of process complexity and cost. In this case, we were able to find an optimal mix by sacrificing some buildability (see Section 4.3.3). A solid-liquid ratio of 0.9 allowed the AAM to maintain shape stability and provide reasonable adhesion (see Section 5.3.3). For this application, sacrificing buildability for adhesion was worthwhile, as we only needed to print coatings which were a few layers thick. Any thicker, and we would risk debonding of the coating during curing due to shrinkage.

5.2.6 The concrete substrate

Another matter to consider is the 'printing bed' in these applications. Normally a flat surface is required to ensure proper structural integrity and avoid deformations in subsequent layers (Bos et al., 2016). The effective printing bed in this application is the concrete substrate.

For repairs a rough surface is preferred to ensure proper adhesion and interlocking between repair and substrate (Morgan, 1996). However, this could pose various issues in printing especially when small nozzle sizes are employed. Firstly, this could result to nozzle obstruction if proper head distance (distance between substrate and nozzle) is not considered. Secondly, if a large head distance is selected to avoid any potential interferences, the unevenly distributed surface can result in a printed object with ununiform quality. Figure 5.7a and Figure 5.7b present an example of such an effect. It could be viewed that the area with a higher head distance resulted in poorer quality and gaps in printing in comparison to the area with a shorter head distance. The higher distance prevented proper interlocking with the substrate, which led to dragging of the filament and inaccurate deposition creating a mismatch between previous and subsequent printing paths.

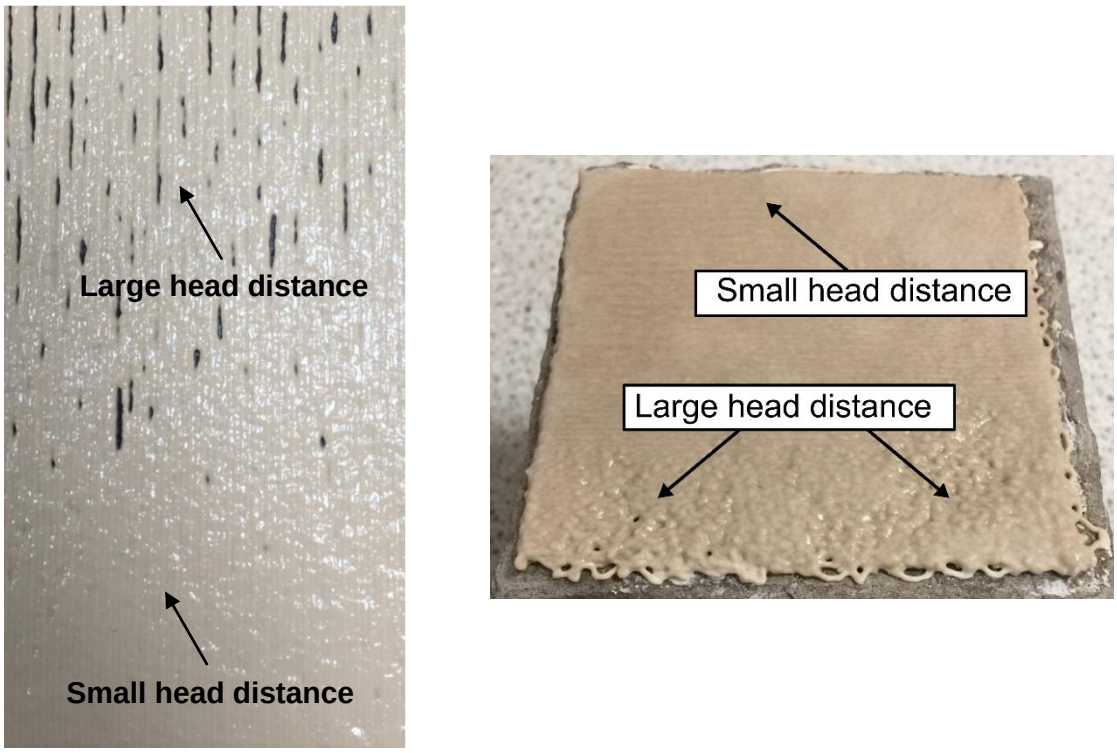

(a) (b)

Figure 5.7 – Examples of adverse print quality due to uneven concrete surface and head distance.

5.2.7 Shrinkage control

Shrinkage in this system is a vital point of consideration and thus proper shrinkage control is required to avoid the formation of cracks. Tensile stresses develop between the substrate and the repair which could result into cracks (Zhou et al., 2008). Moreover, metakaolin based repairs are prone to delamination (Nunes et al., 2019) and cracks (Vasconcelos et al., 2011) primarily due to high levels of shrinkage. For this reason, incorporating additives to deal with these issues is necessary. PP (Aguirre-Guerrero et al., 2017; Zhang et al., 2012) and PVA (Zanotti et al., 2017) fibres could provide a solution to high restrained shrinkage. Water loss in the system is also an issue to tackle. Figure 5.8 presents a square patch printed onto a dry substrate. As can be seen, depositing patches on dry surfaces led to crack generation, this is a result of liquid absorption from the concrete substrate. As such, pre-wetting the substrate is required as it prevents loss of liquid in the patch (Morgan, 1996). Furthermore, sealing the sample prevents water evaporation during

thermal curing (Zhang et al., 2009). It should be added that thermally curing also leads to reduced cracks and increased bond strength (Zanotti et al., 2017). In this thesis shrinkage was assessed via visual inspection. If cracks were visible the overall preparation process was deemed unsuitable for fabricating AAM patches and a new shrinkage control approach was required.

Figure 5.8 – Cracked patch printed onto dry concrete substrate.

In order to counter shrinkage issues, the use of fibre additives was employed. However, having tested PP fibres, extrudability was found to be poor even at 0.5-1% w/w, as the inflexible fibres would cluster near the nozzle and cause congestion. Short (3 mm) PVA fibres, being more flexible, did not cause extrudability issues at 0.5 % w/w (6 mm fibres compromised extrudability). The inclusion of PVA fibres enhances shape stability (Chaves Figueiredo et al., 2019). In addition, according to Zanotti et al. (2017), PVA fibres also increase the bond strength of repairs, as they decrease repair cracking and delamination due to restrained shrinkage, and enhance interfacial failure resistance with the patch and the concrete substrate. The fibres are able to bridge the gaps of cracks while carrying the induced tensile loads (Soltan and Li, 2018).

Another factor that may be overlooked for shrinkage control when printing overlays for repairing purposes is the total print time. Rapid drying can occur when large surface areas are being repaired with relatively thin overlays. This is relevant in 3D printing applications especially when the extrusion rate is low. This can subsequently prolong the total print run and delay proper curing leading to potential moisture loss. (Vaysburd et al., 2011). The repair application must be quick enough to avoid material hardening and developing

high viscosity. Low viscosity is desired as it would be able to spread on the surface and enable penetration into the capillaries (Courard and Degeimbre, 2004). In order to accomplish this in the current application, increasing the print speed was an option. However, as could be seen in Figure 5.9a and Figure 5.9b, increasing print speed from 50mm/s to 100mm/s had a negative impact on the quality of the print leading to multiple gaps and thus poor printing. This is mainly because the volume of material that can be extruded per second (and therefore per mm) is limited in our setup. In essence the same amount of filament is being extruded per second despite the faster movement of the extruder. This ultimately results in thinner filaments at higher print speeds. In order to have accurate deposition at higher speeds, the flowrate of the dispenser will be required to be increased as well. Based on the flowrate used for 50 mm/s (2 mL/min), it can be inferred that the flowrate should be increased to 3.5 – 4.5 mL/min to avoid gaps in printing.

Taking everything into account when extruding for repairing purposes the printing duration, speed and any delays, should be such that does not negatively impact the repair quality but at the same time is quick enough to maintain adequate viscosity and to allow proper sealing and curing to avoid moisture loss. In essence, the open time in repair applications can be viewed as not by the time a mix is printable but in which the time a mix can achieve adequate adhesion while avoiding excessive shrinkage. This, however, is closely linked to equipment limitations which can cause variations in the final time.

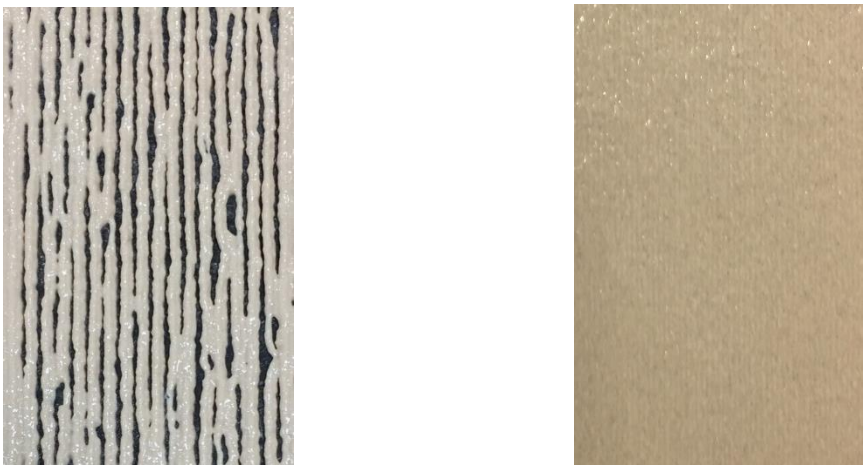

100 mm/s (a) 50 mm/s (b)

Figure 5.9 – Poor printing due to increased print speed: a) printing at 100 mm/s, and b) printing at 50 mm/s.

5.2.8 Electrode insertion

Electrode insertion is another parameter to take into account when 3D printing self-sensing materials. In conventional smart materials, embedded electrodes are often inserted into moulds prior to casting to ensure proper placement (Han et al., 2015). However, as 3D printing is a means of fabrication without the use of moulds, other routes must be considered. In general, electrodes alone are capable of generating cracks in cementitious materials (Tang et al., 2016). Therefore, a proper electrode insertion method is necessary to avoid any addition impairments to the patches. Figure 5.10a and Figure 5.10b present the two electrode insertion methods outlined in Section 5.2.2.4. Figure 5.10a refers to method I in which the electrodes are prearranged and printed directly over and Figure 5.10b depicts method II in which the electrodes were inserted into the object after it was printed.

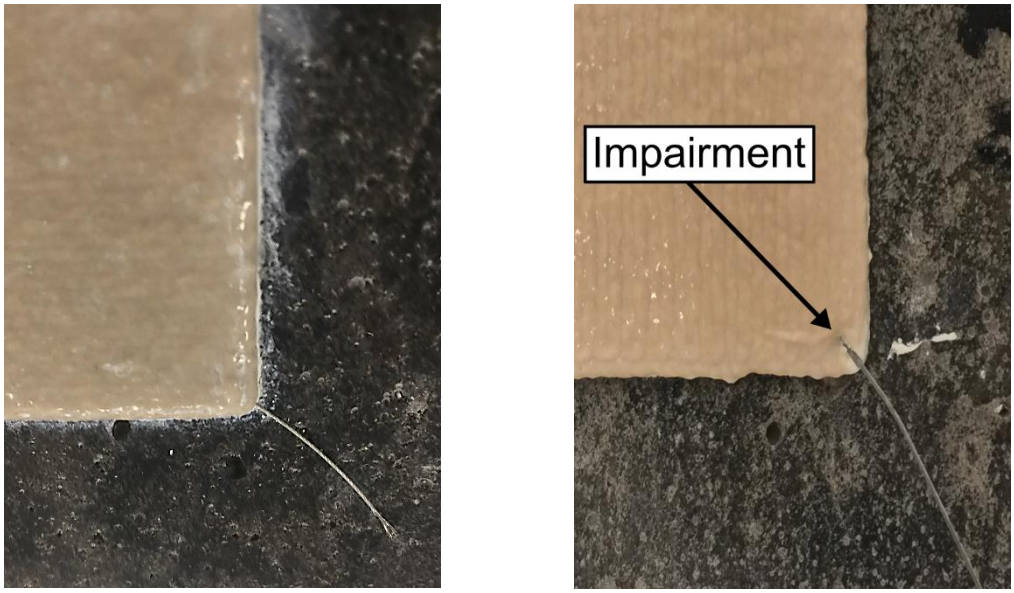

Method I Method II

(a) (b)

Figure 5.10 – Electrode insertion methods can be a) prearranged, or b) inserted after printing.

It is evident that inserting the electrodes after printing causes impairments to the printed object compared to printing directly onto them in a prearranged manner. When using method II the patch is still in a relatively fresh state and it is still susceptible to deformations. Any unaccounted interferences can impair the shape of the printed object, which in turn will carry over to the hardened state of the material. This could pose an issue as this practice could generate undesired cavities making it prone to water and chloride ingress. Furthermore, depending on the electrode size and impairment caused, the geometrical and mechanical properties of the patch could be affected, and this can have knock-on effects on sensor performance and reliability.

5.3 Results and discussion

5.3.1 Equivalent circuit modelling

Equivalent circuit modelling of self-sensing cementitious materials is an effective method of understanding, predicting and characterizing the electrical response of the binders. In this thesis, the equivalent circuit of AAM patches printed onto concrete substrates was based on previous applications in similar AAM-OPC systems (Biondi, 2020). Figure 5.11 depicts such an equivalent circuit.

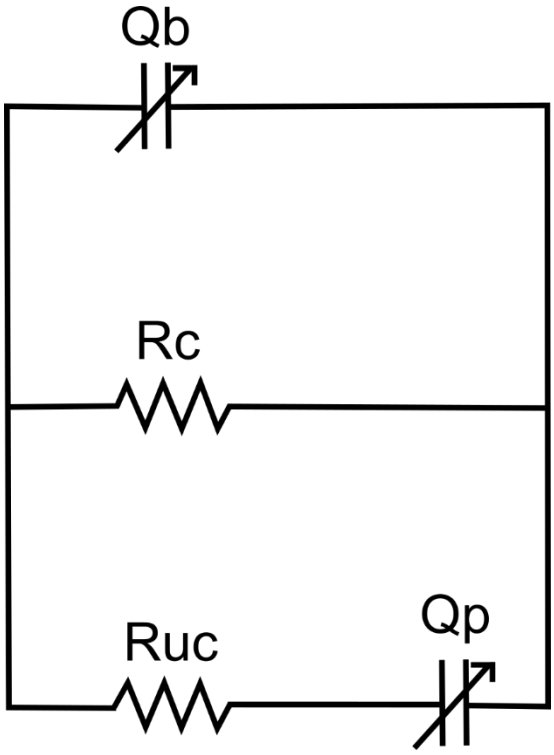

Figure 5.11 – Equivalent circuit for AAM patches on concrete substrates (Biondi, 2020).

The circuit elements portrayed in Figure 5.11 are the following:

i) *Qb* – the bulk capacitance or "constant phase element" of the concrete substrate.
ii) *Rc* – the connected pore resistance representing the ion conducting pathways in the AAM matrix.
iii) *Ruc* – the unconnected pore resistance of the concrete substrate.
iv) *Qp* – pore wall capacitance of the concrete substrate between the unconnected pores of the pore solution.

One of the drawbacks of using circuit modelling is that cementitious systems are relatively complex and can be represented by multiple equivalent models. Depending on the binder a separate circuit can be proposed. For instance, equivalent circuits with notable differences have been proposed for carbon black self-sensing concrete binders (Li and Li, 2019) and for reinforced concrete binders (Sobhani and Najimi, 2013). The model presented by Biondi (2020) is able to accurately depict the AAM patch-concrete configuration used in this thesis as effects from both the patch and the substrate are taken

into account. Additional circuit elements can be added though to incorporate cement hydration products at the interface between the patch and the substrate similar to concrete-steel models that have been proposed by Sobhani and Najimi (2013). Overall while equivalent circuits allow for better understanding of AAM patches, this could result in complex models with multiple circuit elements that may ultimately play a small role in the actual sensing performance of the patch.

5.3.2 Printed sensor: impedance response to temperature

Impedance measurements are affected by the frequency voltage is applied. Commercial impedance interrogators provide a large range of available frequencies (10 μHz – 1 MHz) that can be applied in electrochemical impedance spectroscopy. The frequency range that was selected in this thesis was based on the repeatability and consistency of the impedance readings between sensing cycles. The investigation for the 'optimal' frequency range was based on a series of trial and error. After multiple trials it was found that data contained noise at frequencies below 10 Hz. This can be explained by electrical interference by devices that are in same vicinity as the impedance interrogator. Low frequencies can also cause electrolysis promoting ion migration to one electrode thus causing corrosive chemical reactions. Moreover, it was observed that frequencies above 100 kHz often led to scattered results which can be explained due to inductance from electrode cross-talk. Taking all this into account the frequencies that were used for temperature sensing were between 10 Hz – 100 kHz.

Figure 5.12a and Figure 5.12b present a typical Nyquist plot for a printed patch and an AAM cube at room temperature (20 °C), for frequencies between 10 Hz and 100 kHz respectively. The Nyquist plot for the AAM cube is similar to the conventional Nyquist plot displayed in Figure 2.5. On the contrary, as can be seen the AAM patch does not exhibit the same behavior. In this case, a semi-circle is not present and the imaginary impedance of the sensor is almost negligible. Therefore, the patch displays low capacitance behavior and essentially act as a pure resistor in this frequency range. This signals that there is small difference in the phase between the applied voltage and measured current and that the material possess poor energy storage characteristics. This is

somewhat unexpected as AAM have been reported to attain high capacitance and have been used as supercapacitors (Xu and Zhang, 2017) and as energy storage units (Saafi et al., 2018). That said the aforementioned applications focused on standalone AAM binders rather than overlays applied onto concrete substrates. Capacitance has been mentioned to be affected by the moisture content in cementitious binders (Chung, 2021). As such low capacitance in this investigation could indicate high moisture content in the AAM patch (Biondi et al., 2020). This could be a result of excess water that remained on the concrete surface after pre-wetting. It could also be hypothesized that the capacitance and the Nyquist plot (e.g. no semi-circle) are influenced by hydration products that are developed at the interface between the patch and the concrete substrate, similar to what has been reported in concrete-steel interfaces (Sobhani and Najimi, 2013). These however, are speculations and additional research is required. Overall the capacitance of the AAM patch is of secondary importance as the main focus of this thesis is to analyze the AAM sensor using the real or modulus impedance. AC voltage has been selected to prevent electrolysis rather than exploring additional functions of AAM sensors. Even though it is not as ideal, DC voltage could also be used to conduct this experiment. While multifunctionality of AAM is within the realm of the work that is carried out, investigating the capacitance behavior of AAM sensors currently lies outside the scope of this thesis.

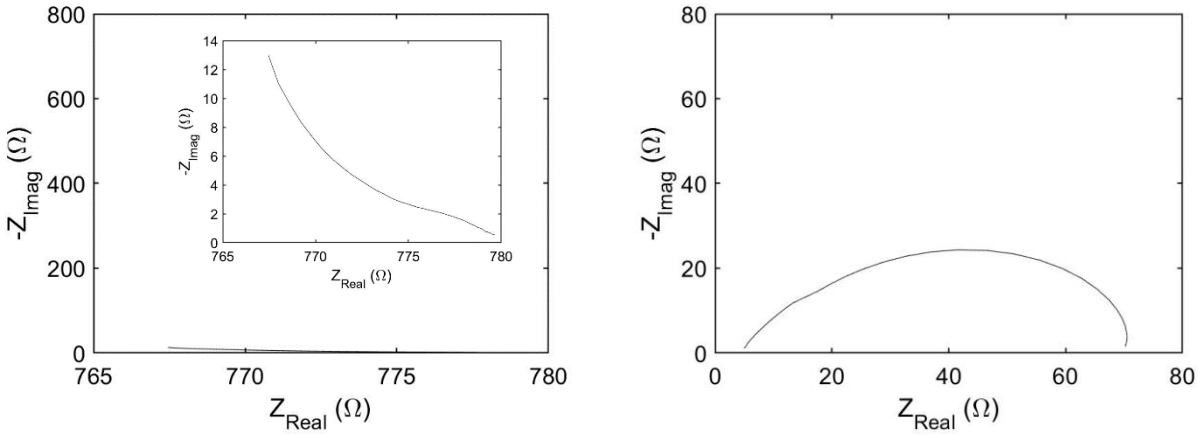

(a) (b)

Figure 5.12 – Typical Nyquist plot for the frequency range 10 Hz – 100 kHz of a) printed patch. Inset displays magnified version of plot b) metakaolin AAM cube.

Figure 5.13 and Figure 5.14 depict the Nyquist and Bode plot respectively for frequencies between 10 Hz – 10^5 Hz for the down cycle (see Section 5.2.3 for definition of down cycle). As shown, a clear shift in impedance can be observed for the different temperatures in both the Nyquist and Bode plot for each cycle. The sensor's response is in accordance to the expected behaviour of AAM under these circumstances. In specific, the impedance decreased with increasing temperature and increased when the temperature decreased. The change in impedance under these conditions can be attributed to ion mobility in the pores of the patch. This behaviour is in accordance to previous authors (MacKenzie and Bolton, 2009; Perry et al., 2015; Saafi et al., 2016).

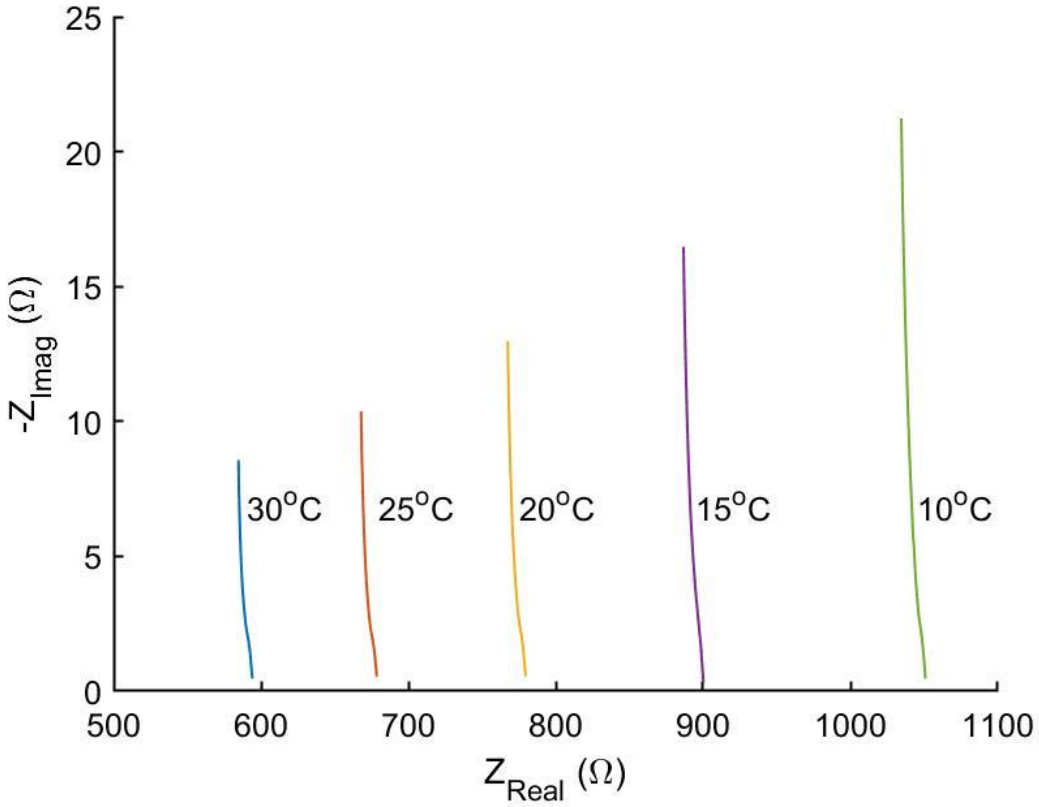

Figure 5.13 – Nyquist plot for each temperature during a down cycle.

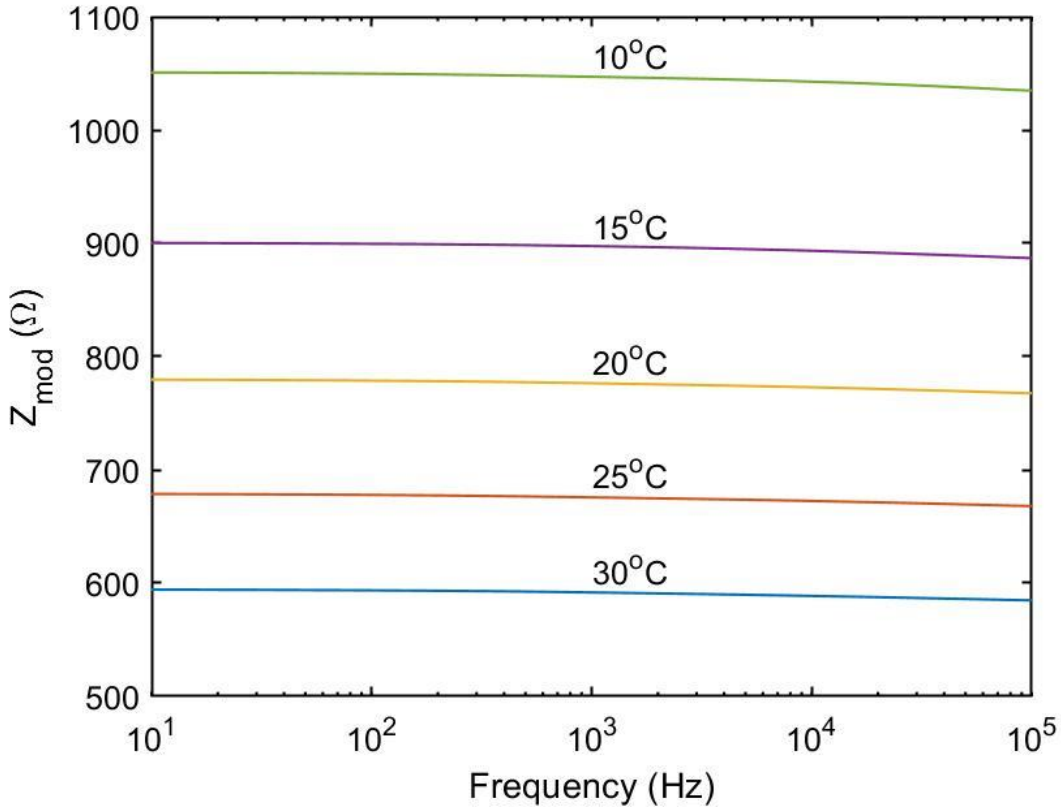

Figure 5.14 – Bode plot for each of temperature during a down cycle.

Figure 5.15 plots the sensor response (at 1 kHz) against temperature during two temperature cycles taken over two days. The fit to equation (2.10) is excellent, and the sensor response is repetable: the pooled repeatability was measured to be 0.3 °C. Under the current experimental conditions it has been assumed that the moisture content in the patch is relatively stable as moisture is controlled due to sealed conditions and under the assumption no liquid in the patch is lost due absorption from the concrete substrate. In practice, moisture conditions can be compensated for with a reference sensor.

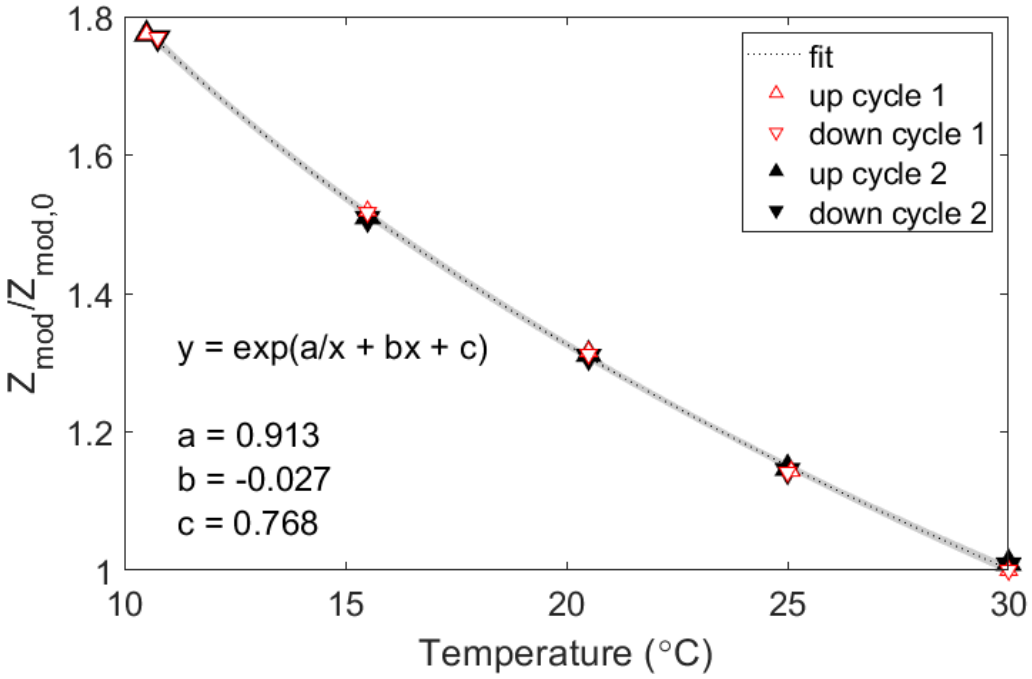

Figure 5.15 – Normalised impedance response of AAM patch to temperature during four temperature cycles. Shaded region shows the 95% confidence interval of the fit for 10 impedance measurements for one sample.

5.3.3 Adhesion results

The average bond strength between heat cured printed patches on concrete substrates for 5 samples was 0.6 ±0.16 MPa. The failure type in all AAM overlays was adhesion failure (failure at the interface between the substrate and the repair). The bond strength between heat cured samples and ambient cured samples investigated in Chapter 4 was relatively similar for 6 days of curing. Figure 5.16 presents the bond strength for heat cured and ambient cured overlays. Ambient cured samples presented slightly higher strength, which again could be due to the curing issues explained in Section 3.4.3. Considering that heat curing does not provide any additional benefits, it can be concluded both heat and ambient curing can be equally considered when deploying the patches. Overall though the strength was relatively low with high variability and therefore a definitive claim on the adhesion strength cannot be made.

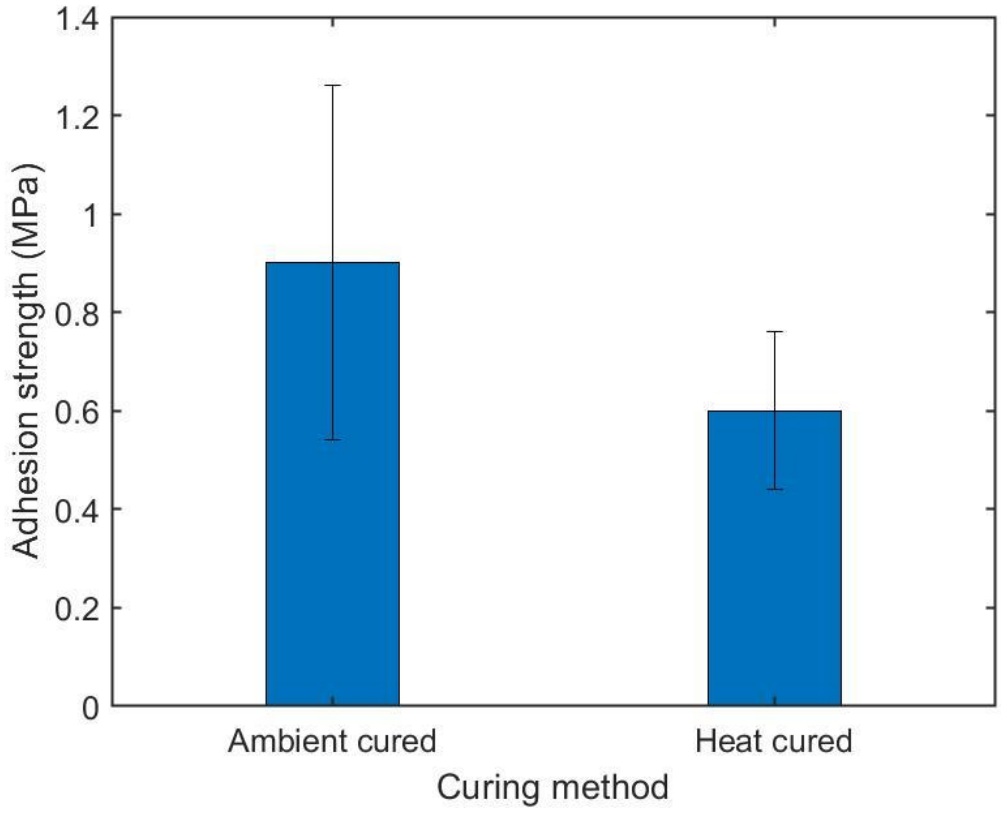

Figure 5.16 – Adhesion strength of ambient cured and heat cured coatings. Error bars represent standard deviation of measurements acquired from 3 ambient cured samples and 5 heat cured samples.

Conventionally applied metakaolin-based repairs with proper optimization can achieve adhesion strength within the range of 1 – 2 MPa with the pull-off test (Kramar et al., 2016; Nunes et al., 2019). The difference in strength can be attributed to numerous factors. Firstly, as shown by Vasconcelos et al. (2011), metakaolin based AAM repairs can achieve poor bonding performance if the mix design is not properly tailored. Metakaolin AAM have a high liquid demand, which leads to excessive water in the alkaline solution. This promotes drying shrinkage thus compromising the bond between the repair and the substrate at the interface (Nunes et al., 2019; Zanotti et al., 2017). Furthermore, the low adhesion strength can also be attributed to 3D printing fabrication process. It could be that the mix is not coming in to full contact with the substrate, thus compromising anchorage between the two materials (Courard and Degeimbre, 2004). While the AAM repair was tuned to achieve both adequate printability and adhesion in this experiment, the mix design

was not optimized for achieving maximum levels of bond strength, due to the trade-offs discussed in Section 5.2.5.

Another crucial factor that needs to be taken into account is the concrete substrate. In typical 3D printing applications, the printing bed should be level and smooth to ensure proper stability during printing. In the current application, the effective printing bed is the concrete substrate, which as previously mentioned in Section 5.2.6, was wired brushed to increase surface roughness to promote greater adhesion between the repair and the substrate. Even though wire brushing could lead to inconsistencies in surface profiles (see Figure 4.13), in samples where a rough surface was achieved, this practice could simultaneously compromise adhesion in extrusion applications. As the head distance is measured from the highest peak of the surface in order to avoid nozzle obstruction, apart from gaps in printing as mentioned in Section 5.2.7, the contact between the two materials will not be uniform. This issue is even more prevalent the rougher the surface is. As illustrated in Figure 5.17 the AAM filament may not come into full contact with the substrate when the material is deposited onto a valley (area between two peaks on the surface). This could result into air pockets in the repair and due to the lack of compaction in the extrusion process this could cause an adverse effect on its bonding performance (Silfwerbrand et al., 2011).

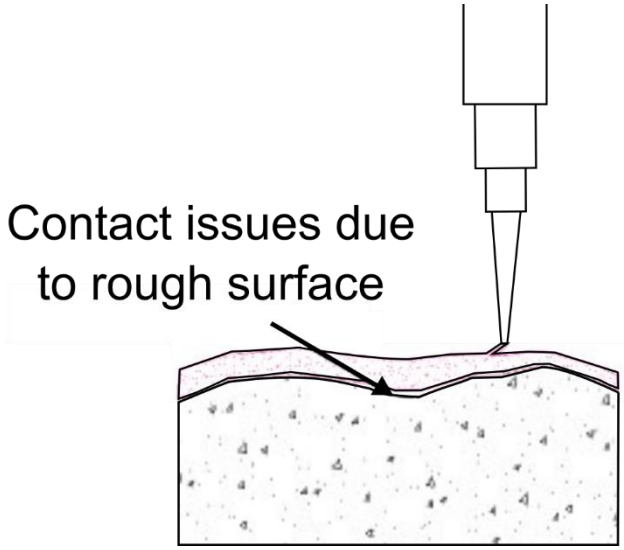

Figure 5.17 – Non-uniform contact due to the rough surface of the concrete substrate.

A potential solution to work around rough surfaces would be to employ a nozzle with a diameter larger than to the height difference between the highest and lowest peak of the surface to avoid the formation of air pockets. Moreover, this allows greater surface coverage which would minimize layers and print paths thus lessening the formation of gaps in the material formed due to printing and subsequently leading to a stronger object (Lim et al., 2016; Zareiyan and Khoshnevis, 2017). In addition, setting a smaller layer height than the nozzle diameter allows for greater compaction between layers (Bos et al., 2016) which could enable greater contact between the patch and the substrate. Finally, digitally scanning the surface profile and creating a respective G-code file could properly tailor the repair to the respective substrate. Further investigation is required to optimize the mix design and printing process to allow for a more suitable repair solution.

5.4 Conclusions

In this chapter a 3D printed, multifunctional AAM sensor-repair for concrete structures was presented. The temperature sensing response of the printed sensor was outlined and adhesion was investigated. The key findings of this chapter are the following:

- An equivalent circuit for the AAM sensor was proposed. The circuit contained resistors and capacitors to account for the AAM patch and concrete substrate in the system.

- Extruding objects onto uneven concrete surfaces and increasing print speed led to low print quality. The method of electrode installment could also impact the integrity of the AAM patch.
- The performance of the sensor was in accordance with the expected behaviour of AAM dependence to temperature. The impedance of the AAM patch decreases as temperature increases and the impedance increases as temperature decreases.
- The temperature sensing performance of the patch was characterized using an exponential fit. The resolution of the AAM sensor was 0.1 °C with a repeatability of 0.3 °C.
- The adhesion of the printed patch to the concrete substrate was 0.6 MPa. It was found that heat curing did not improve the bond strength when compared to ambient curing. Overall, the bond strength achieved was lower than a typical AAM repair due to low surface roughness and limitations in the 3D printing process itself.

Further investigation is required to optimize 3D printing for repair and sensing applications. Chapter 6 will explore the strain sensing capabilities of the printed coatings.

Chapter 6 3D printed strain-sensing coatings for concrete structures

In this chapter the strain sensing response of printed alkali activated coatings is investigated. Their sensing capability under compression, tension and 4-point bending are presented. The importance of adhesion and electrode effects are also discussed.

6.1 Introduction

Continuing from Chapter 5, this chapter expands on the author's research into self-sensing alkali activated materials (AAM). Historically, applications have primarily focused on the fabrication of new construction elements. Developing cementitious materials to monitor existing infrastructure is uncommon. Conventional sensing applications involve the fabrication of structural elements such as beams and cubes. Alternative types of cementitious sensing techniques such as embedded cement-based sensors (Azhari and Banthia, 2012; Ding et al., 2019a; Saldarriaga et al., 2021) and sensing overlays (Baeza et al., 2013; McAlorum et al., 2021; Perry et al., 2015; Vlachakis et al., 2020) have also been investigated in this field. A short description of each type of sensor follows.

6.2 Types of self-sensing cementitious materials

6.2.1 Structural elements

This category encompasses the majority of cement-based strain sensing applications for both OPC and AAM sensing applications. In this scenario, the structural element and the sensing element refer to the same object. These applications focus primarily on the fabrication of concrete cubes and beams (Abedi et al., 2020; D'Alessandro et al., 2020; Sun et al., 2017).

6.2.2 Embedded cement-based sensors

In regards to embedded cement-based sensors, the sensor and the structural element refer to two different objects (Han and Ou, 2007). This approach involves embedding a cement-based sensor (typically a small cube or beam) inside a larger cement-based element (such as a larger cube, beam or column), which has not been designed for sensing purposes. The embedded sensor is fabricated beforehand and placed inside the mould of the substrate during casting. Once the new substrate has fully cured (with the sensor embedded), the sensor is able to detect strain variations as it will undergo similar strain changes as the parent substrate. The sensing performance of the embedded sensor as a standalone object and as an embedded sensor may differ due to the interaction and confined deformation from the concrete element (Ding et al., 2019a; Wang et al., 2018). While adjusting the embedded sensor to match the properties of the substrate is not essential, mismatch between the properties of the two elements can cause additional stresses to occur under uniaxial loading (Ding et al., 2019b; Xiao et al., 2011). To the best of the author's knowledge, only OPC based applications have been reported for this application.

6.2.3 Cementitious sensing coatings

Cementitious sensing coatings can be considered as cement-based sensing sheets used primarily for strain sensing rather than damage localization. Instead of adhering a manufactured sheet onto a surface, an overlay with sensing properties is applied onto an existing structure. The overlay is able to detect strain in the substrate from strain transferring from one element to the other. Strain transfer and thus the sensing

performance of these coatings is governed by the degree of adhesion between the two materials. Higher strain transmission can be achieved with a stronger bond (Gerber et al., 2018). Higher sensing performance can also be achieved in cement-based sensing overlays with low thickness (Baeza et al., 2013).

Table 6.1 presents a comparison between sensing cementitious coatings, embedded cement-based sensors and sensing sheets. Compared to other types of cementitious sensing materials, coatings can provide multiple advantages. The primary focus of sensing coating is to monitor existing infrastructure. As a result, rather than constructing structural members with sensing capabilities, coatings can be applied onto designated areas for monitoring purposes while using less material and reducing costs. Furthermore, compared to embedded sensors, coatings provide a simpler means of installation for both existing and new infrastructure. Their field of application is also wider as they can be applied onto steel structures (Temuujin et al., 2011) and pavements (Alanazi et al., 2016) if tailored accordingly. Lastly sensing coatings can also provide flexibility in terms of monitoring as apart from strain sensing, they can be applied onto larger areas with relative ease and used for damage detection.

Table 6.1 – Comparison between 'supportive' sensing elements.

	Sensing coating	Embedded sensor	Sensing sheet
Material	Cementitious	Cementitious	Carbon/Epoxy/Plastic
Fabrication sequence	After parenting substrate	Before parenting substrate	After parenting substrate
Substrate	Concrete/pavement/steel	Concrete/pavement	Concrete/pavement/steel
Tailoring	Essential	Ideal	No
Application	Strain/damage	Strain/damage	Damage
Additional functions	Nonstructural repair	–	Coating
Bond	Chemical/mechanical	Embedded	Epoxy

The importance of material preparation is crucial in sensing overlays. As mentioned in Chapter 4 & 5, if coatings are not properly tailored, this can result in high levels of shrinkage which could lead to either delamination or cracks. This in turn can compromise

the sensing integrity of the coatings. Compared to the aforementioned sensing elements, cementitious sensing overlays have not been investigated in great depth. In this chapter the following experimental investigation is carried out:

- The strain sensing of AAM patches under compression, tension and 4-point bending is explored.
- Repeatability issues of AAM patches are addressed.
- The strain sensing performance of AAM patches is characterized.
- Parameters affecting strain sensing are pointed out recommendations for this technology are made.

6.3 Methodology

The following sections outline the experimental procedure followed to fabricate AAM coatings and investigate their strain sensing performance. Material fabrication (Mix design 2) and mixing sequence were based on the methodology outlined in Chapter 3.

As mentioned in Section 2.3.3 the loading rate, temperature and humidity impact the strain sensing performance of AAM binders. In OPC applications it is common to dry the samples prior to testing to remove the excess water in the matrix to avoid polarization and increase sensing performance (Dong et al., 2019; Hong et al., 2018; Siad et al., 2018). For AAM, water has been speculated to be necessary to facilitate ion migration. Completely dry AAM samples have been stated to be incapable of showcasing a sensing response (Lamuta et al., 2016). Therefore, drying samples is not a common practice in AAM sensing. Considering the above the following considerations were made in the experimental investigation:

- Loading rate was kept constant.
- Experiments were conducted in a testing environment with stable temperature and humidity.
- Samples were not dried and were wrapped in plastic film to avoid liquid evaporation from the sample over the course of the tests.

Even if these precautions are taken though, the sensing response of AAM can present great variability. Very high sensitivities – gauge factors between 1000-2000 (Lamuta et al., 2017; Ma et al., 2020) and at the same time much lower sensitivities – gauge factors between 10-60 (D'Alessandro et al., 2020; Saafi et al., 2014) have both been reported for filler free applications (as a reminder, filler free refers applications refer to binders that do not employ electrically conductive filler e.g. carbon fiber).

6.3.1 Substrate preparation

AAM patches were printed onto concrete and glass fiber reinforced plastic (GFRP) substrates following the methodology presented in Chapter 4. Prior to printing the surfaces were required to be properly prepared to ensure adhesion with the printed patches.

6.3.1.1 Concrete substrates

The concrete substrates that were used in this chapter were 100 mm cubes, 50 mm cubes and 40 mm × 40 mm × 200 mm single reinforced beams of the same concrete mix design presented in Table 4.2. A single steel rod with 6 mm thickness was used as reinforcement for the beams. AAM chemically bond with OPC concrete as the calcium ions in the substrate are able to charge balance the aluminium ions in the AAM binder. (Pacheco-Torgal et al., 2008). The substrates were prepared following the surface preparation procedure presented in Section 4.2.4.5.

6.3.1.2 Glass fiber reinforced plastic sheets

GFRP sheets were cut into suitable tensile testing pieces. The dimensions of the GFRP substrates are presented in Figure 6.1. The material properties as provided by the manufacturer are displayed in Table 6.2. GFRP was selected as it is a nonconductive material and presents a linear stress-strain response in the loading range investigated in this chapter (Zhang et al., 2018). While a steel substrate is a more traditional route to tensile testing, complete electrical insulation between a steel substrate and an AAM layer is difficult to achieve. Current flow in a steel test piece (and indeed the grips of the tensile tester and the load cell) would make these part of the sensing system. AAM and GFRP sheets present poor adhesion compatibility, therefore sand was epoxied onto the 'neck' of the tester (area between A × W as portrayed in Figure 6.1) in which the patches were to

be deposited. This allowed the AAM patches to mechanically interlock with the sand and was achieve an adequate bond with the GFRP sheets[23]. The sand-epoxy layer was kept thin (2 mm – 3 mm) to avoid as much strain loss as possible.

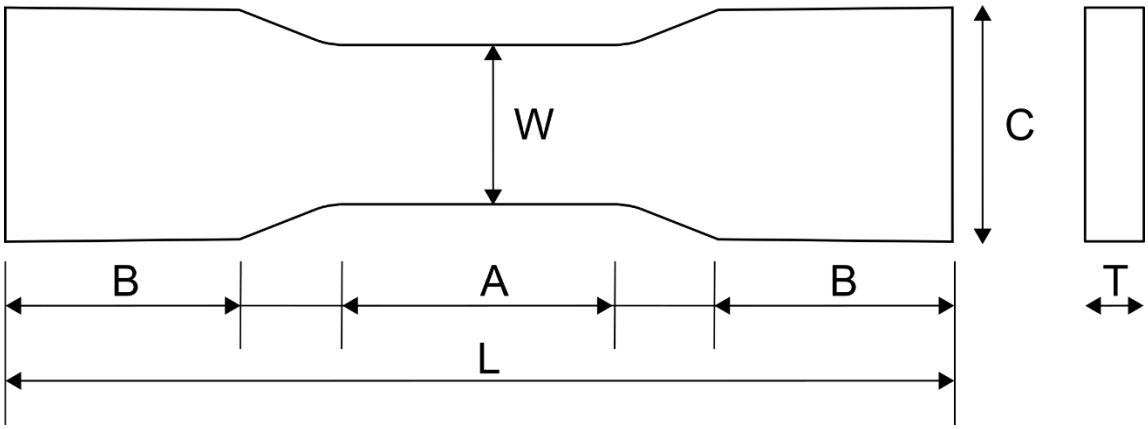

Figure 6.1 – Schematic drawing of glass reinforced fiber plastic tensile tester piece.

Where: A=60 mm, B=50 mm, C=50 mm, L=200 mm, T=8 mm and W=35 mm.

Table 6.2 – Specifications of glass reinforced fiber sheet as provided by manufacturer.

Modulus of elasticity	Tensile strength	Elongation	Density
5.5 GPa	160 MPa	3.5-5%	1.35 g/cm^3

6.3.2 3D printing and data preparation

3D printing and data preparation in the chapter were based on the procedures outlined in the Chapters 4 and 5. With that in mind, the following data files were prepared:

- Square patch: 90 mm × 90 mm for 100 mm concrete cubes
- Square patch: 45 mm × 45 mm for 50 mm concrete cubes
- Rectangular patch: 35 mm × 50 mm for GFRP and concrete beams.

Each patch consisted of two layers, a single perimeter and was printed with 100% rectilinear density. The print speed was set at 30 mm/s and the layer height was 0.66 mm. The following considerations were made when printing on each individual substrate:

[23] The purpose of this approach is to showcase the sensing capability of AAM rather than presenting the compatibility between AAM and GFRP.

Concrete cubes: Patches were extruded while avoiding printing close to the edges. This was to ensure that strain applied to the patch occurred solely from load transferring from the concrete cube rather than being directly loaded from the testing apparatus.

GFRP: Patches were printed onto the 'neck' of the specimen, within regions A × W, as displayed in Figure 6.1 to ensure that maximum tensile strain was being detected.

Concrete beams: The patches were printed in the region where maximum displacement occurs according to bending theory for a rectangular beam under 4-point bending. An illustration of the position of the patches in relation to the 4-point bending setup is presented in Figure 6.2.

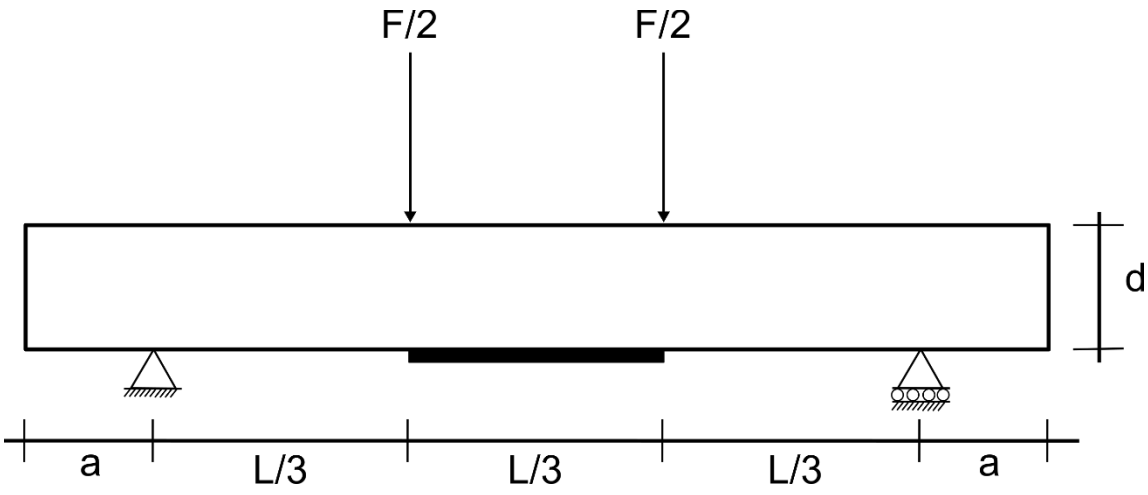

Figure 6.2 – Patch placement and 4-point bending setup.

Where L=150 mm, a=25 mm and d=40 mm.

6.3.3 Electrodes and curing

Once each patch was extruded onto the substrates mentioned in Section 6.3.1, stainless steel electrodes were inserted according to the Van der Pauw (VDP) configuration (van der Pauw, 1958). As the VDP method is able to provide average measurements, this can also reduce the effects of potential uneven stress distributions in the substrate and thus eliminate any sort of localized behavior. In this chapter, stainless steel tape was used as probes instead of wires as in Chapter 5. Tape allowed greater contact with the impedance analyzer's connecting clips thus preventing potential slippage during testing. Moreover, as larger patches were printed for strain interrogation compared to

temperature sensing, there was greater distance between electrodes. This reduced the risk of tensile stresses developing from the tape such that would affect the structural integrity of the patch.

Literature suggests that both heat cured (Saafi et al., 2018) and ambient cured (D'Alessandro et al., 2020) binders can be used in strain sensing applications. Therefore, once the electrodes were inserted, the samples were stored in sealed containers and two curing regimes were followed:

- Cured in an oven at 40 ^{o}C for 24h to accelerate alkaline activation and then transferred to an environmental chamber at 17 ^{o}C until testing.
- Cured in an environmental chamber at 17 ^{o}C for at least 28 days until testing.

6.3.4 Electrode configuration

Electrode connection is critical when using the VDP method as it will have a direct impact on the electrical response of the samples (Yao et al., 2017). Under compression and tension, the probes were connected such that the applied voltage and measured current were parallel to the applied load. This will allow the proper interpretation of the sensing results following the current understanding of self-sensing materials. Figure 6.3a displays the typical electrode configuration for compression and tension. Voltage was applied across electrodes 1 and 4 and the current was measured across electrodes 2 and 3. This electrode orientation was denoted as 'Layout 1'.

Under compression a second layout orientation, denoted as 'Layout 2' was investigated in which the voltage and current were both perpendicular to the applied load. Figure 6.3b displays electrode layout 2 in which voltage is applied across electrodes 1 and 2 and the current is measured across 3 and 4.

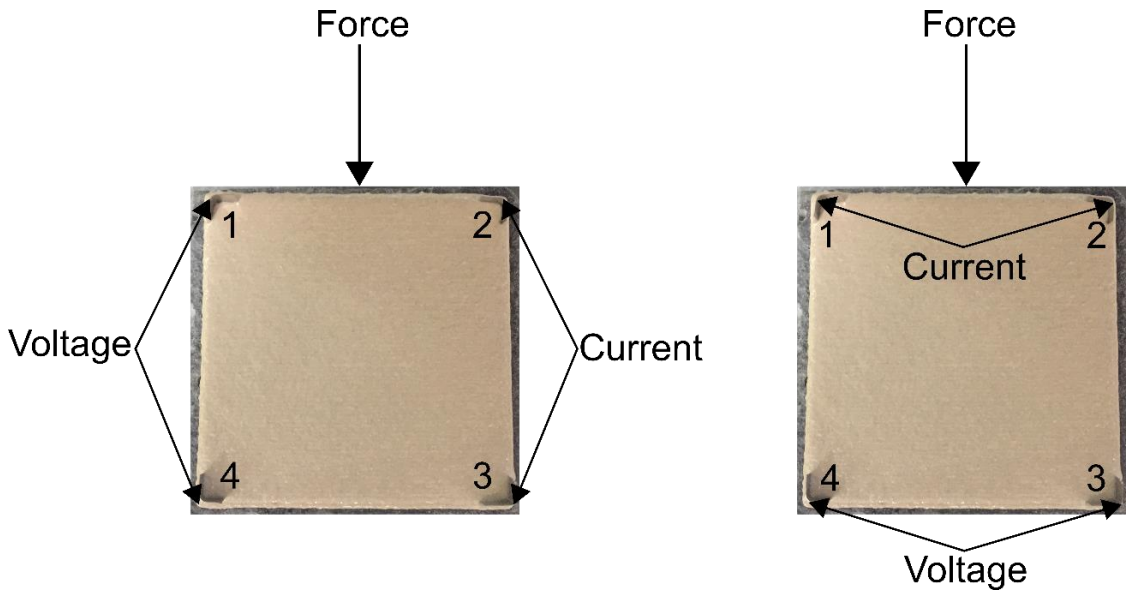

(a)

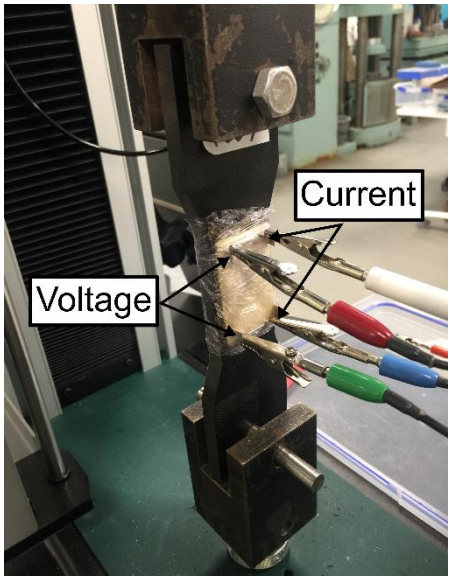

(b)

Figure 6.3 – Electrode orientation of patches a) under compression, layout 1 voltage and current are parallel to applied force (left), layout 2 voltage and current are perpendicular to applied force (right) b) under tension, voltage and current are parallel to applied force.

Figure 6.4 presents the electrode connection for patches printed onto concrete beams. Under 4-point bending, the voltage and measured current were applied across the longer dimension of the patch. This was to ensure that the measurement followed the maximum deformation of the beam under 4-point bending.

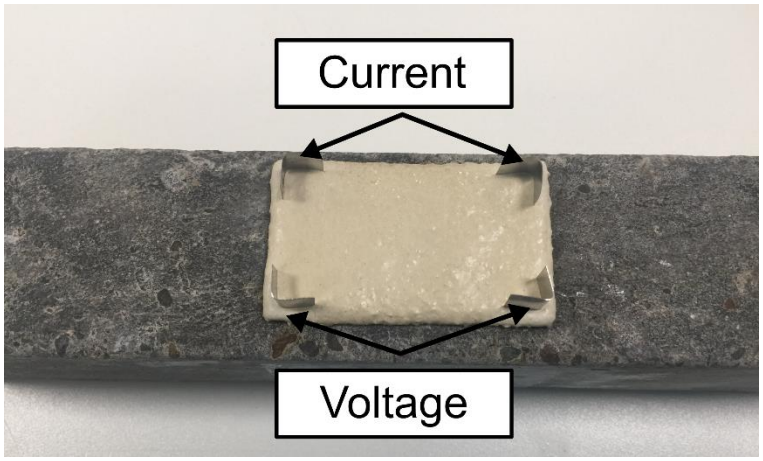

Figure 6.4 – Electrode arrangement for patches printed on concrete beams. Voltage and current were applied on the longer dimension of the patch.

6.3.5 Loading schemes and data acquisition

Prior to testing, the samples were wrapped in a thin plastic film to reduce moisture fluctuations during testing. The samples were also removed from the plastic containers and were placed in the same vicinity as the loading cell for at least 12h before testing to allow for greater stabilization. Due to the prolonged time of the strain sensing tests, the temperature of the testing area was measured with an external temperature and humidity sensor to ensure a constant testing environment. The mechanical tests conducted in this chapter are portrayed in Figure 6.5.

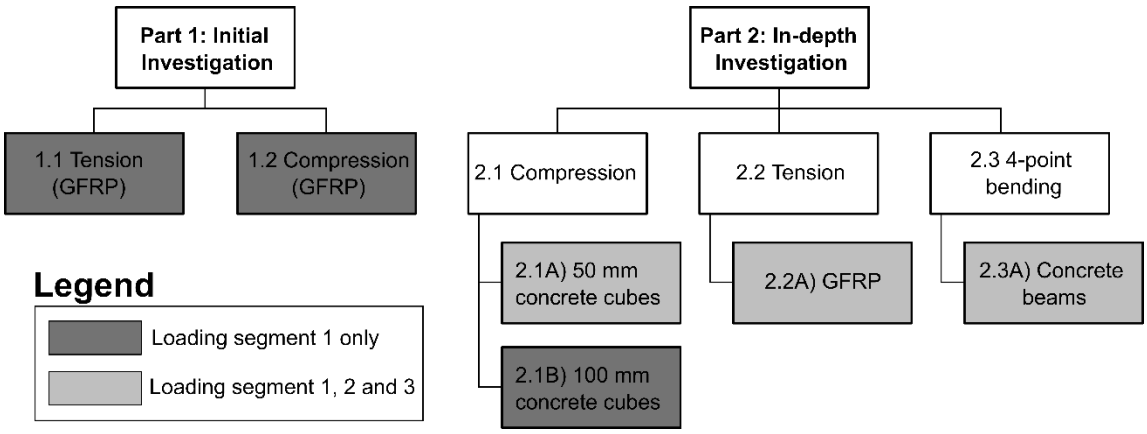

Figure 6.5 – Diagram of mechanical tests conducted.

6.3.5.1 Displacement controlled load cell

Sample sets 1.1, 1.2, 2.1A), 2.2A and 2.3A (see Figure 6.5) were tested using a universal load cell with a loading capacity of 25 kN and displacement accuracy of 0.001 mm. For compression testing, insulating layers were placed between the loading plates and the sample to avoid electrical interference. Under 4-point bending insulation was achieved by attaching electrical tape at the points of contact between the machine and concrete beam. As the GFRP sheet is nonconductive, electrical insulation was not required. The displacement rate applied in all tests was 0.3 mm/min.

As can be seen in Figure 6.5, strain sensing investigation was divided into two parts: the initial investigation (part 1) and the in-depth investigation (part 2). In part 1 compression and tension were investigated in GFRP sheets for loading segment 1 (see Section 6.3.5.1.1). In part 2 compression, tension and 4-point bending were investigated in separate substrates for loading segment 1,2 and 3 (see Sections 6.3.5.1.1, 6.3.5.1.2 and 6.3.5.1.3 respectively). Tension was investigated in GFRP sheets, 4-point bending in concrete beams and compression in 50 mm concrete cubes.

The same loading scheme was applied for sample sets 2.1A), 2.2A) and 2.3A). The loads were applied via displacement control and were kept low to avoid excessive damage to the patches and to the bond between the substrates to allow reversible and repeatable sensing. A small preload was applied to the samples to eliminate any nonlinearity issues that commonly occur at low loads (Galao et al., 2014). The loading scheme was broken

down into three sequential segments, Segment 1, Segment 2 and Segment 3. An explanation of each loading pattern follows.

6.3.5.1.1 Segment 1

A qualitative representation of the loading pattern followed in Segment 1 is presented in Figure 6.6. The samples were loaded in 5-step increments and then unloaded in 5-step increments. This sequence was regarded as one cycle. The load cell paused at each load for 1 minute to allow the data analyser (Gamry Interface 1000) to acquire the necessary data. During each load, the analyser ran in potentiostatic mode in which the impedance of the samples was measured by applying 10 mV voltage for frequencies between 1000 Hz and 10 kHz. Three measurements were acquired for each load and an average value for each frequency was able to be extracted. Segment 1 consisted of 6 cycles. The loads applied for each substrate follow:

- Compression (50 mm cube), four-point bending and tension: 0 – 0.10 mm – 0 with a step of 0.02 mm.
- Tension: 0 – 0.04 mm – 0 with a step of 0.008 mm.

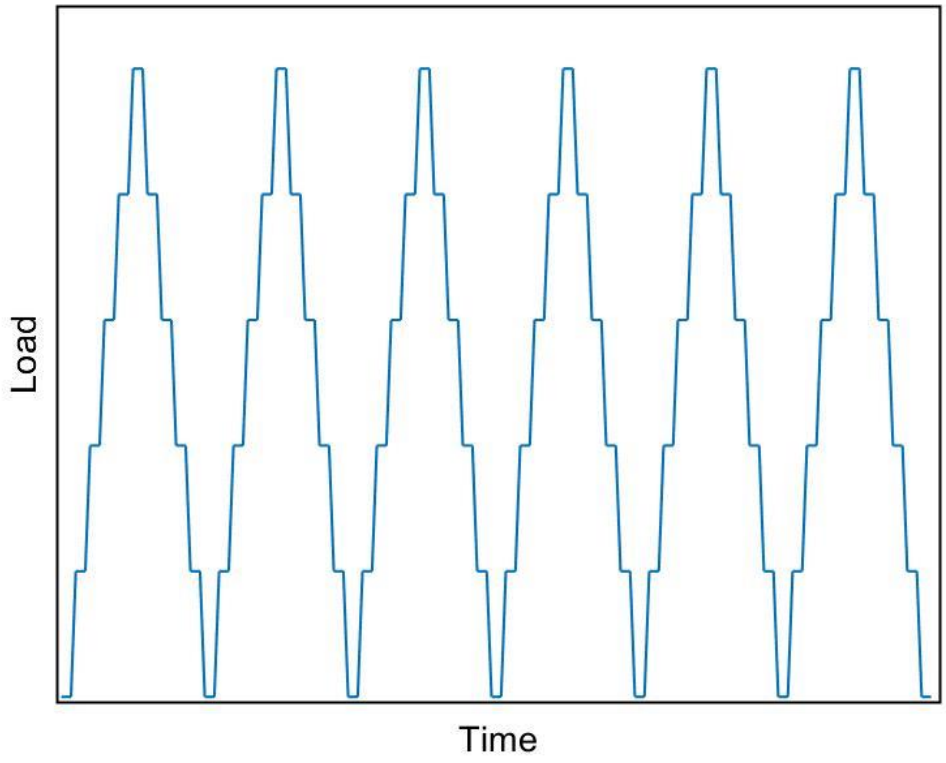

Figure 6.6 – Qualitative representation of step loading pattern of patches for six cycles.

6.3.5.1.2 Segment 2

A qualitative representation of loading in Segment 2 is displayed in Figure 6.7. The maximum displacement for each substrate mentioned in Segment 1 was cyclically applied for 40 cycles. In this investigation, the impedance analyser logged data at a single frequency mode at 5 kHz.

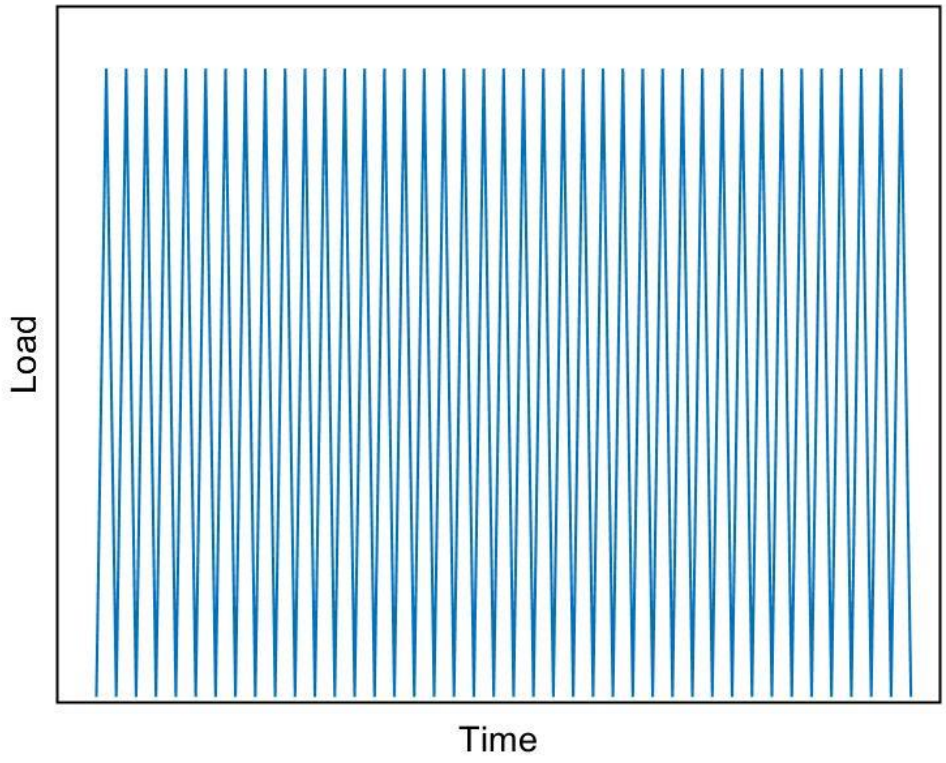

Figure 6.7 – Qualitative representation of cyclic loading pattern of samples for 40 cycles.

6.3.5.1.3 Segment 3

The loading pattern and electrical application followed in Segment 1 is repeated for this loading segment.

6.3.5.2 Loading schemes and data acquisition for force controlled loading cell

Patches printed on 100 mm cubes (sample set 2.1B)) were tested using a force controlled hydraulic compression tester with a loading capacity of 500 kN and 2 kN accuracy. The load measurements in this case were verified with a separate load cell. Two nonconductive plates were placed between the sample and loadings plates for insulation.

The loading pattern and data acquisition in this application is based on loading Segment 1 mentioned in 6.3.5.1. The main difference in this application is the magnitude of the applied load and the total number of cycles. The load patterns and their applications are presented below. All loads were applied with a step of 10 kN.

- Strain sensing, loading scheme similar to Segment 1: 0 – 50kN – 0 for 6 cycles.
- Electrode effects: 0 – 40kN – 0 for 3 cycles.
- Adhesion effects: 0 – 100 kN – 0 for 3 cycles; 0 – 70 kN – 0 for 1 cycle.

6.3.6 Sensing response

The strain sensing capabilities of the samples were measured using the gauge factor Equation (6.1) for the displacement-controlled tests. The strain for the 50 mm cubes and GFRP sheets was calculated using Equation (6.2). The strain for the concrete beams under 4-point bending was calculated using Equation (6.3).

$$GF = (Z_i - Z_0)/Z_0/\varepsilon, \tag{6.1}$$

where Z_0 = impedance at start of the test, Z_i = impedance after a given strain change, and ε = applied strain change.

$$\varepsilon = \frac{\Delta L}{L} \tag{6.2}$$

Where: ΔL=displacement acquired from loading apparatus; L=length of sample.

$$\varepsilon = \frac{12\delta h}{\left(3L^2 - 4a^2\right)} \tag{6.3}$$

Where: δ=deflection acquired from loading apparatus; h=height of beam; L=length of beam; a=distance between support and load point.

The stress sensing coefficient Equation (6.4) was calculated for the force-controlled tests. Stress was calculated via Equation (6.5).

$$SSC = (M_i - M_0)/M_0/\sigma \tag{6.4}$$

where σ = applied stress.

$$\sigma = \frac{F}{A} \tag{6.5}$$

Where: F=applied force, A=cross-sectional area.

In samples where repeatability was not achieved in loading Segment 3, the sensing performance was evaluated using only the cycles that showcased repeatability. If a constant change in impedance was not able to be achieved at all, the sensing performance was evaluated taking into account only last load cycle. The number of cycles considered for assessing the sensing performance for each application will be clearly stated.

6.4 Results and discussion

6.4.1 Sensing response

Heat cured samples were initially tested under compressive strain testing. Under these circumstances, the samples did not showcase a response to the applied load. This behavior was initially not expected as heat cured AAM binders have been used in sensing applications before (Lamuta et al., 2017; Saafi et al., 2018). Considering that dry samples have been stated to not showcase a response under load (Lamuta et al., 2016), it can be speculated that water was driven out of the samples during curing and thus a better means of sealing is required. As shown in Chapter 5, the bond strength is not significantly influenced by the curing method. Taking this into consideration, heat cured samples were not investigated and ambient curing is used for the remainder of this thesis.

6.4.1.1 Initial sensing response of printed AAM coatings

Figure 6.8 displays the change in impedance over time for sample set 1.1 and 1.2. The reader is referred to Figure 6.5 for a recap of how sample sets are defined. The change in impedance aligned the expected behavior of AAM in both loading directions; the impedance increased in tension and decreased in compression (see Section 2.3.3). Under both loading directions, repeatability and reversibility issues were evident. The impedance of the sample at zero load increased upon each load cycle. In order to properly assess the sensing performance of the patches a repeatable sensing performance is required. Therefore, additional load cycles were applied the samples as this is able to lead to more consistent behavior (Deng et al., 2019). Tension was assessed through GFRP sheets and

in 4-point bending of concrete beams in Sections 6.4.1.3 and 6.4.1.4 respectively. Compression was further investigated in concrete cubes in Section 6.4.1.2.

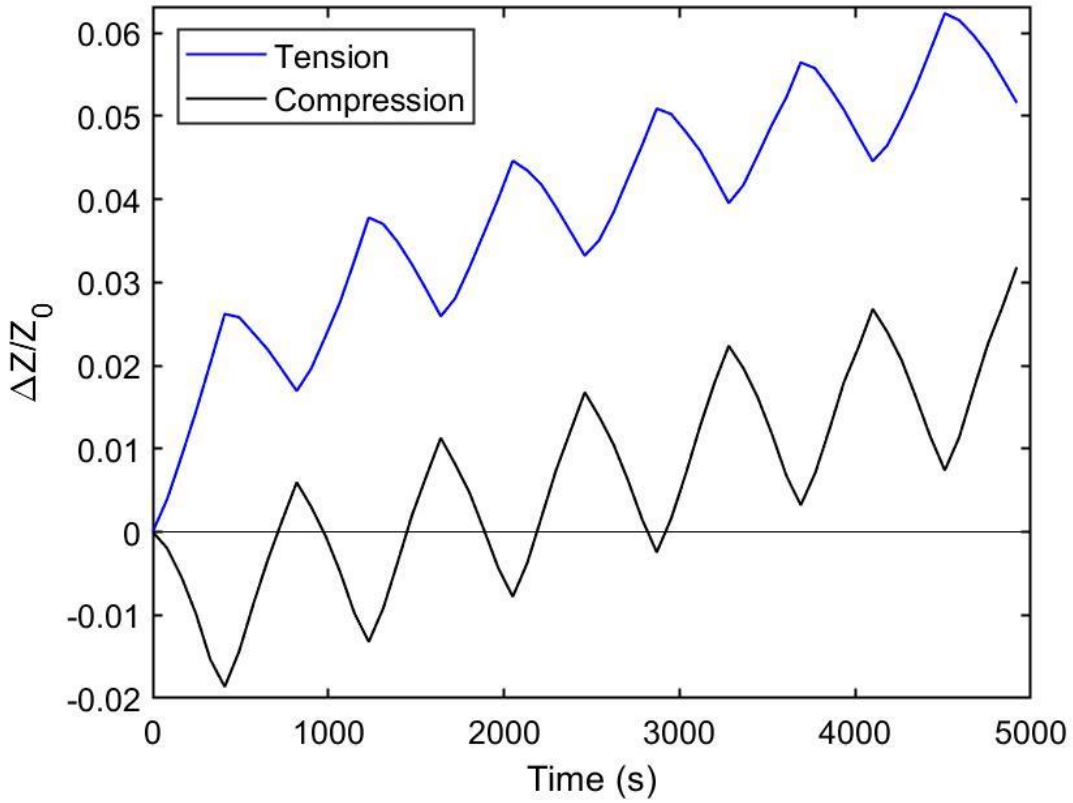

Figure 6.8 – Compression and tensile behavior of patches printed on GFRP sheets under loading Segment 1.

6.4.1.2 Compression

6.4.1.2.1 50 mm cubes

Figure 6.9 presents the sensing response of sample set 2.1A) under compression for loading Segment 1 and Segment 3. Similar to the GFRP sheets it can be seen that repeatability issues were evident for the first loading segment. These repeatability issues can be explained by minor damage in the patch. Another factor that must be considered in sensing patches is that apart from changes in the microstructure of the patch, stresses develop at the interface between the substrate and the overlay upon each cycle. As a result, changes in the bond between the samples will also impact sensing performance. After undergoing loading Segment 2 the patch was reexamined in Segment 3. It can be seen that

the sensing performance is able to reach stability within this loading segment. Compared to standalone sensing objects, it can be speculated that a higher number of cycles is required in patches as the sensing behavior is influenced by the patch, substrate and bond between the two. This phenomenon is similar in embedded sensors in which the sensors require multiple cycles to conform to the parenting substrate (Sun et al., 2014).

Nonlinear behavior can be detected at early loading stages and near the peak of the maximum load applied. At high strain values this behavior could indicate that the total load applied is exceeding the elastic region of the patch. Nonlinear behavior is quite common at low loads (Rovnaník et al., 2019a; Sun et al., 2014). This may indicate that a higher preload was required.

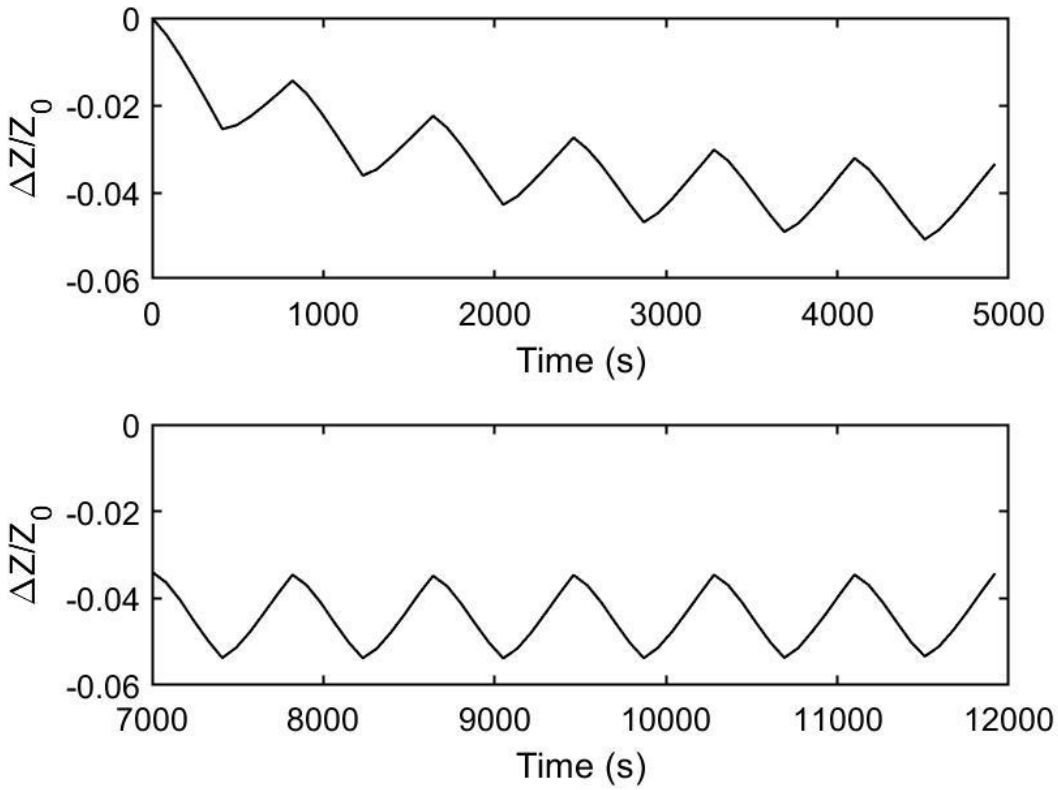

Figure 6.9 – Sensing response of patch printed on 50 mm cube under compression for loading: (top) Segment 1 (cycles 1-6) and (bottom) loading Segment 3 (cycles 47-52).

Figure 6.10 presents the change in impedance as a function of applied displacement for all six load cycles in Segment 3 for the sample presented in Figure 6.9. It can be seen that

despite the multiple loading cycles, the patches showcased hysteresis in upward and downward loading. This is quite common in filler free samples compared to binders with conductive additives (D'Alessandro et al., 2020).

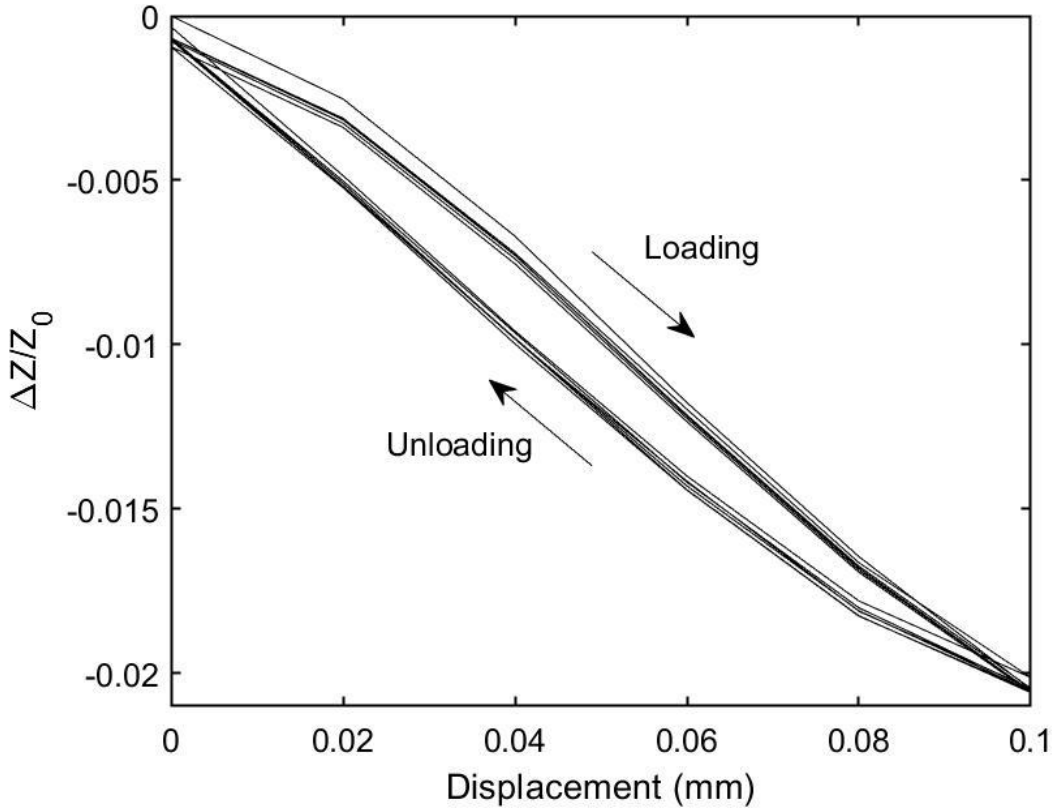

Figure 6.10 – Hysteresis plot for one patch under compression for all six loading cycles of loading Segment 3.

Figure 6.11 displays the average fractional change in impedance against applied strain for all six load cycles in Segment 3, the error bars are calculated using the standard deviation of the three impedance measurements for each strain point for 6 total load cycles. The gauge factor was calculated via the slope of the plot. The GF for this sample was measured as 10. The change in impedance is not zero for zero strain due to slight offsets of the patch's impedance at the start of each load cycle. The average gauge factor for 2 samples under compression was measured as 8.59±1.55.

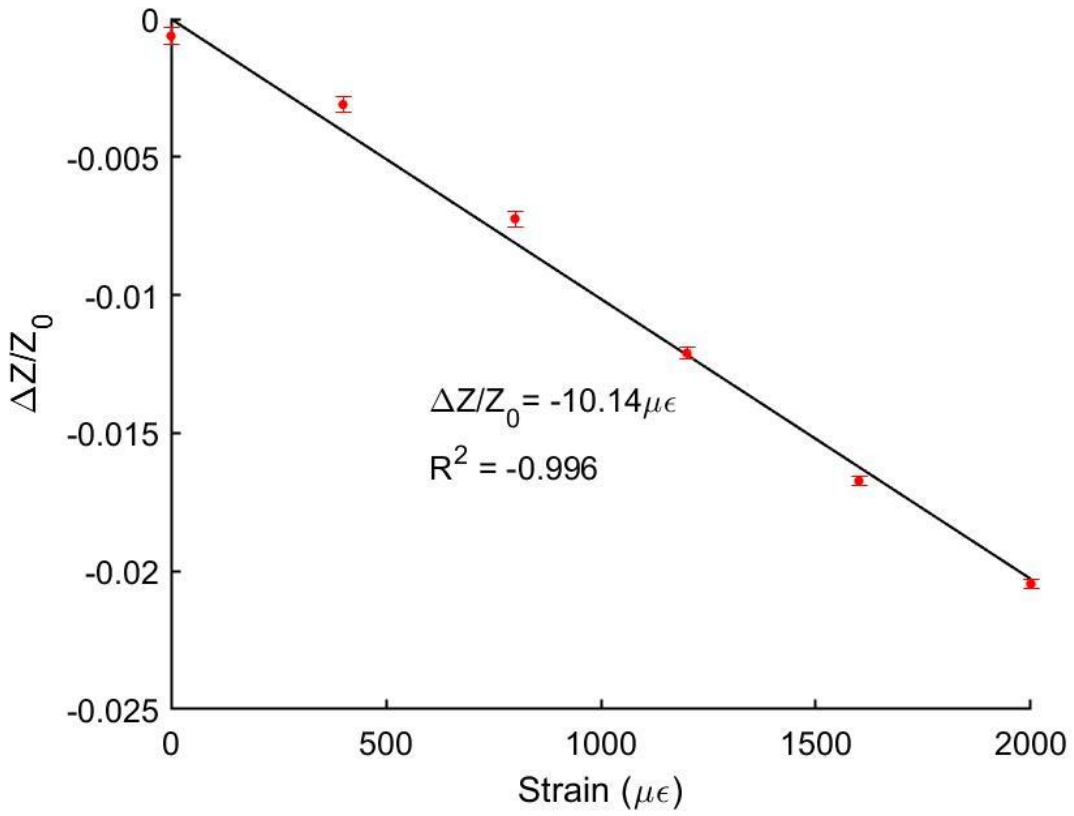

Figure 6.11 – Average fractional change in impedance versus strain for patches under compression for six load cycles in segment 3. Error bars represent standard deviation of six load cycles with three impedance measurements per cycle for one sample.

6.4.1.2.2 100 mm cubes

The compressive strain response of larger concrete cubes was also investigated. Figure 6.12 presents the electrical response of sample set 2.2B) under compressive load (0-5 MPa) for 6 load cycles. The change in impedance remained fairly constant in this application. As displacement measurements were not able to be acquired with this loading apparatus, the stress sensitivity coefficient was used to characterize the sensing performance of the patches. Figure 6.13 presents the change in impedance vs the applied stress. The average sensing performance of 3 samples for this configuration was measured as 0.033 ±0.008 MPa^{-1}. When converting the GF in Figure 6.11 to SSC, the average sensing performance is 0.014 MPa^{-1}. A greater sensing capability can be observed for the larger concrete substrates.

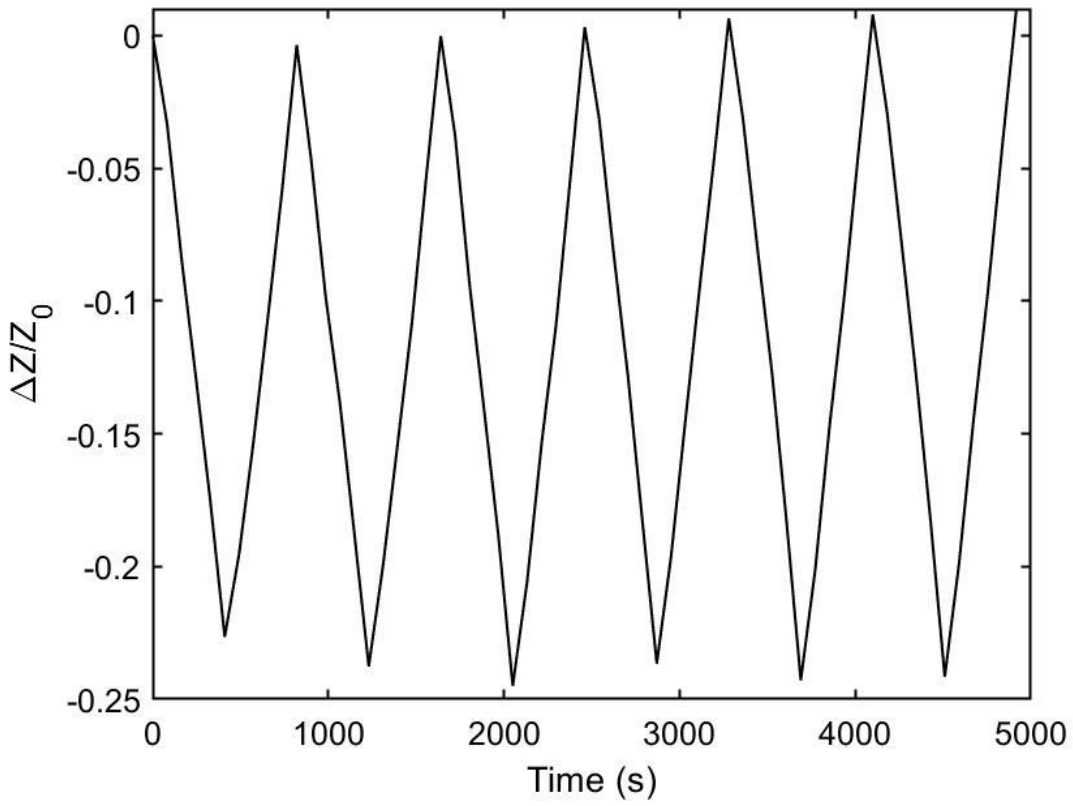

Figure 6.12 ─ Fractional change in impedance versus time for patches printed on 100 mm cubes.

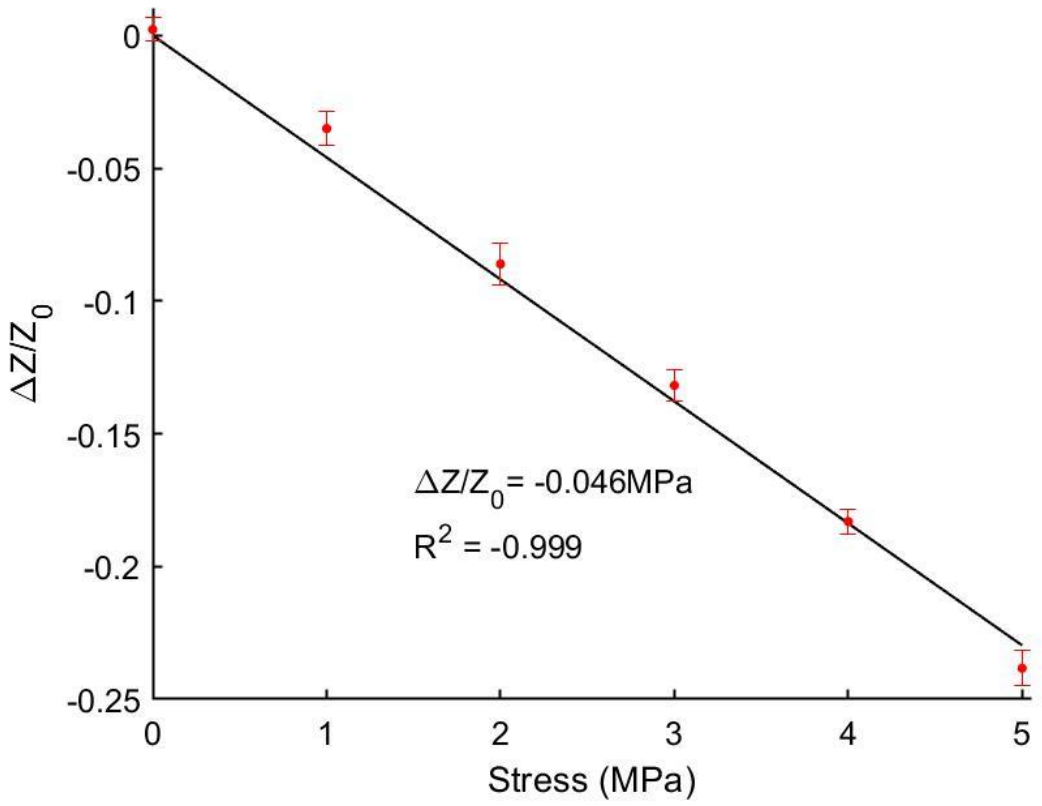

Figure 6.13 – Average fractional change in impedance versus applied stress for 100 mm concrete cubes for 6 load cycles. Error bars represent standard deviation of six load cycles with three impedance measurements per cycle for one sample.

6.4.1.2.3 Adhesion effects

Adhesion plays a significant role in sensing coatings. While the patch may remain intact, poor adhesion that can occur due to delamination which may decrease strain transfer from the substrate to the sensing patch.

Figure 6.14 presents a patch that displays slight delamination at the corners. Figure 6.15 presents the change in impedance of the referred sample incrementally loaded up to 10 MPa and then incrementally unloaded for three load cycles. The sensing response of this sample differed compared to samples presented in Figure 6.12. The change in impedance at the beginning of each cycle initially increased which is opposite to what is expected in compression. The sample was initially required to be loaded up to 4 MPa in order for it to start behaving in an expected manner. Upon subsequent load cycles though,

this point shifted to 5 MPa and 7 MPa for cycles 2 & 3 respectively. The patch also presented reversibility issues as the impedance continued decreasing (instead of increasing) once the load was removed. A significant amount of the applied load was required to be removed in order for the sample to begin behaving in a reversible manner. For the three load cycles, the point in which reversibility could be detected was at 9 MPa, 5 MPa & 5 MPa of the unloading phase of each cycle. While a linear-like behavior could be detected within the regions the patch presented an expected behavior under compression, these regions cannot be easily defined due to reversibility issues presented in the patch. Furthermore, the change in electrical properties compared to applied load is relatively low when compared to a fully bonded sample. As a result, samples that present slight adhesion issues cannot be reliably used in sensing applications.

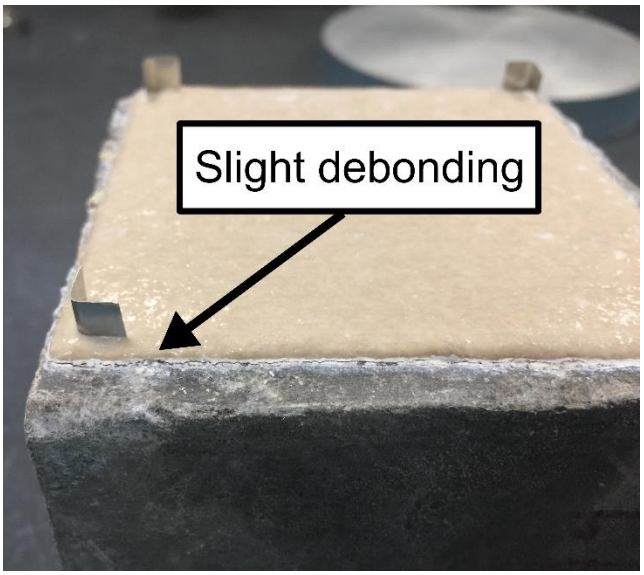

Figure 6.14 – Slightly debonded patch printed on concrete cube.

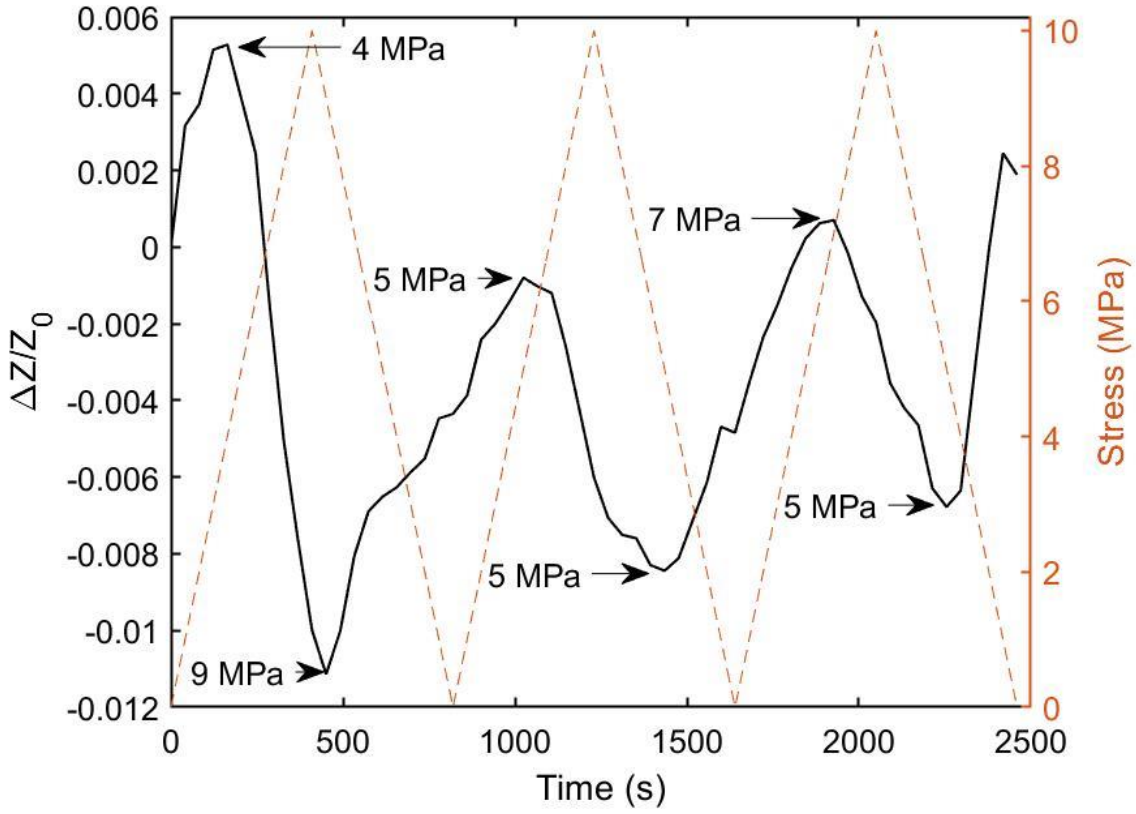

Figure 6.15 – Fractional change in impedance versus time for one slightly debonded patch printed on 100 mm concrete cube.

Samples that present major debonding issues do not showcase a strain sensing response. Figure 6.16 displays the sensing response for such samples. One of the disadvantages of sensing coatings is failure may not always be evident. As shown in this example, load is being applied to the substrate but the patch is not able to indicate any external interference due to delamination.

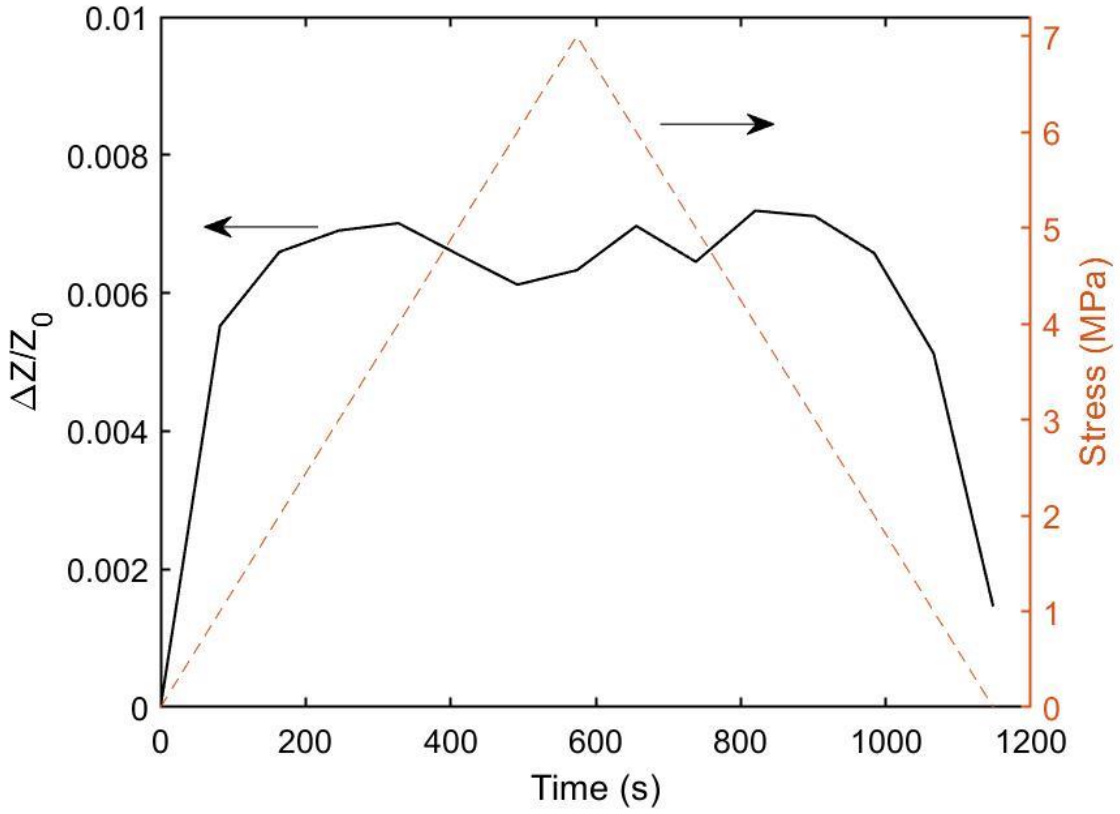

Figure 6.16 – Fractional change in impedance against time for one sample with clear debonding for loads up to 7 MPa.

6.4.1.2.4 Electrode configuration

Regardless of the electrode configuration (conventional serial layout or van der Pauw) the orientation of the electrodes in relation to the applied load is significant in sensing applications. To give an example, in a self-sensing AAM investigation conducted by Bi et al. (2017) the electrodes were placed on opposite faces of the cube-shaped specimen. When testing, this resulted in the current and voltage being perpendicular to the applied load, rather than parallel. Once the load was applied, the resistance of the binder increased instead of decreasing which is considered the norm in compression. It was stated by the authors that this increase occurred due to formation of cracks which led to the hinderance of ion migration in the matrix. While this is a justifiable answer, what also needs to be taken into account is that the electrode orientation was in the transverse direction of the applied load rather than the longitudinal. Due to the Poisson effect, the

transverse direction of the cube is in tension. Therefore, it can be speculated that the electrodes were measuring the tensile behavior of the sample in which an increase in resistance would be anticipated[24].

In this investigation, the electrodes were connected using the Layout 2 configuration as specified in Section 6.3.4. In this layout, the applied voltage and measured current were perpendicular to the applied load. As can be seen in Figure 6.17, even though the sample is under compression, the impedance increased as the current is flowing in the tensile direction. For this investigation the maximum stress applied was 4 MPa and was only tested for 3 cycles as this configuration led to measurement errors. For the 3 load cycles, the maximum change in impedance remained fairly constant. Figure 6.18 presents the fractional change in impedance versus the applied stress. The average sensing performance for this configuration was measured as 0.014 MPa^{-1}. This value is lower than the compressive strain response of the patches.

[24] This conclusion is drawn assuming the authors of the respective study fully insulated the testing specimens.

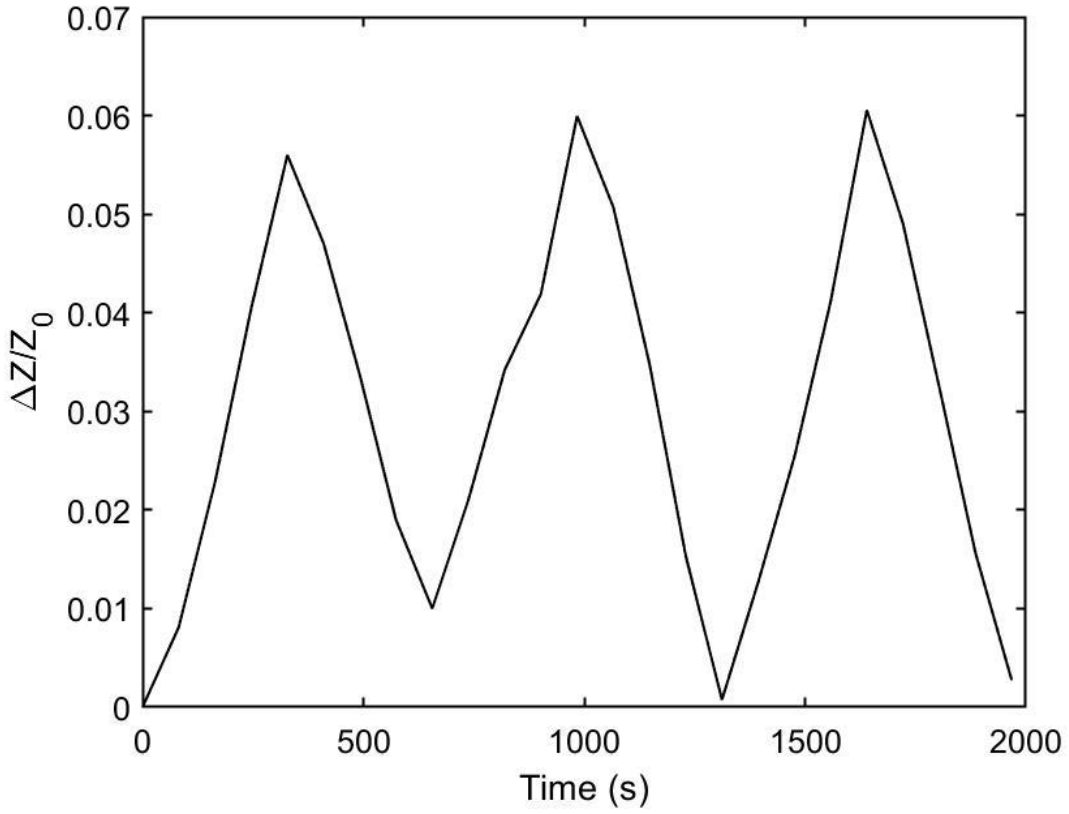

Figure 6.17 – Fractional change in impedance under compression for samples employing electrode layout 2.

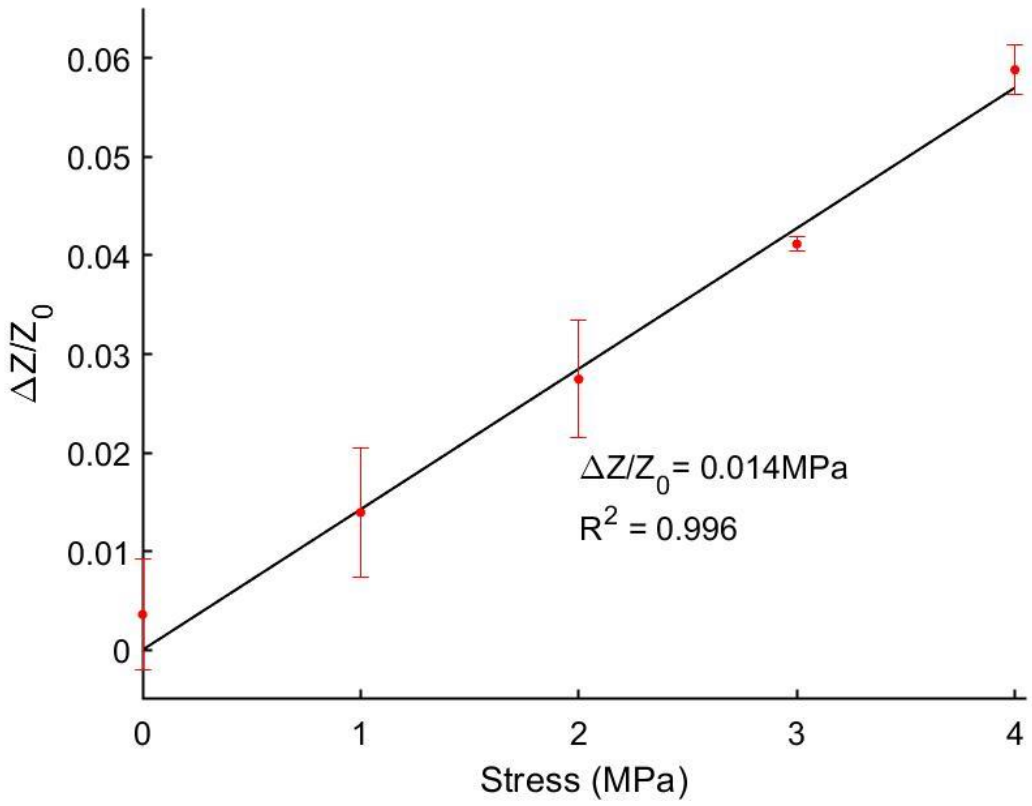

Figure 6.18 – Average fractional change in impedance versus applied stress for samples for 3 load cycles while using electrode layout 2. Error bars represent standard deviation of six load cycles with three impedance measurements per cycle for one sample.

Studies that focus on the electrode configuration are not that frequent. Liu et al. (2018) conducted a compressive strain investigation on OPC binders while employing an electrode layout similar to the VDP method (4 electrodes were placed at the corners of the sample but only two probes were connected during testing). Despite the electrode orientation (parallel or perpendicular to the applied load), all configurations led to a decrease in resistance. It was stated by the authors that changes in the volume of the sample play a key role in the electrical properties in self-sensing cementitious materials. Similarly, in a study conducted by Wen and Chung (2000) it was stated that the microstructural changes in both compression and tension have a similar effect on the electrical properties of the material. Therefore, despite the Poisson effect on the specimen, the changes in electrical properties in both the transverse and longitudinal directions are expected to follow the change in resistance in relation to the primary stress axis.

The literature available is quite limited and a decisive conclusion cannot be made. The study conducted in this thesis is based on overlays rather than structural objects and thus direct parallels cannot be easily drawn. For this investigation the electrical response of Layout 2 followed the expected change in regards to the Poisson effect. The VDP electrode configuration was used in this investigation which allows for a greater coverage of the surface when compared to serial arrangements. It can be speculated that the larger coverage and average measurement provided by the VDP method compared to the serial arrangement allows for more accurate sensing of overall element behaviour, as it eliminates any localized effects on the electrical response. This subject does, however, warrant further investigation in future work.

6.4.1.3 Tension

Figure 6.19 presents the tensile behavior for sample set 2.2A) for loading Segment 1 and 3. Similar to Figure 6.9, these samples presented repeatability issues in loading Segment 1. Upon being subjected to multiple cycles, it can be seen that the sensing performance of the patches stabilizes.

Similar to compression, a nonlinear response can be detected at low strain values for tension. Likewise this can be avoided by increasing the preload of the sample. However, greater attention is required to avoid damaging the sample due to the inherently weaker tensile behavior of cementitious materials.

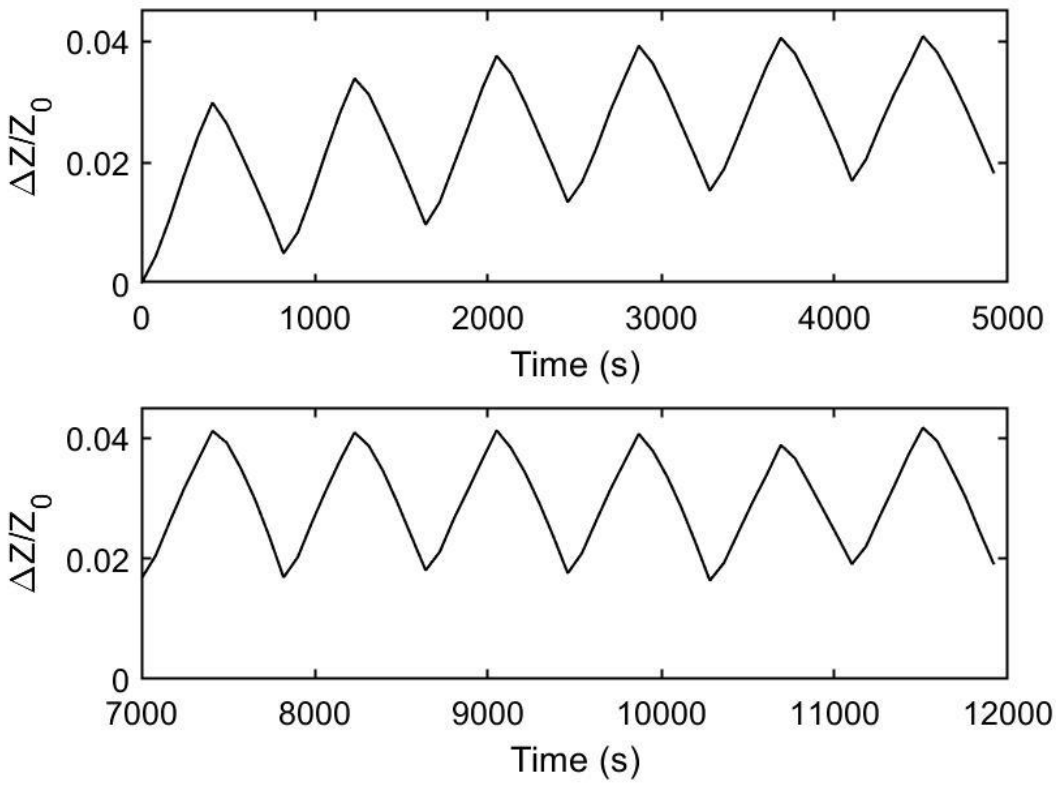

Figure 6.19 – Sensing response of patch printed on GFRP sheet under tension for (top) loading Segment 1 (cycles 1-6) and (bottom) loading Segment 3 (cycles 47-52).

Figure 6.20 presents the change in impedance in regards to the applied displacement. Similar to compression, hysteresis between loading and unloading can be observed in the sample. This phenomenon in cementitious strain sensing is not well understood and is usually countered with incorporating sufficient doses of conductive filler (D'Alessandro et al., 2020; Wang et al., 2018). In other sensing applications outside of cementitious materials hysteresis has been found to be dependent on the pre-strain applied (De Focatiis et al., 2012). It can be hypothesized that the weakened interface upon each cycle may also contribute to higher degree of hysteresis. Overall this area of study requires greater investigation.

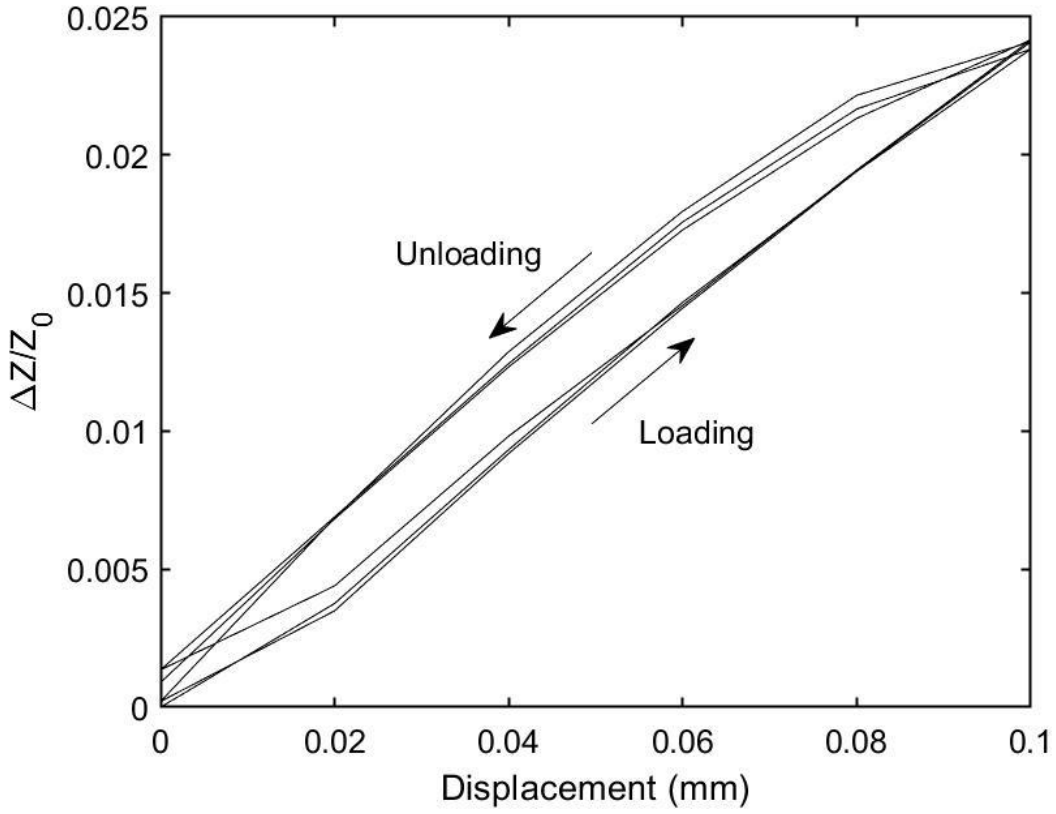

Figure 6.20 – Typical hysteresis plot of fractional change in impedance versus displacement for 3 load cycles under tension for one patch printed on GFRP sheets.

Figure 6.21 presents the average fractional change in impedance of a patch against tensile strain for the GFRP sample depicted in Figure 6.20 for 3 load cycles. The average GF under tension for 5 samples was calculated as 38.4±21.6. While repeatability in the same sample can be detected, the maximum sensing performance between samples presented great variability. This could be in part due to the manner in which adhesion between the AAM overlay and the GFRP sheet was achieved. Inconsistencies in the sand-epoxy layer could result in different thicknesses which in turn could impact strain transfer from the GFRP sheet to the patch. The sensing performance of the patches is comparable to GFs reported in other filler free AAM applications under tension (Saafi et al., 2014).

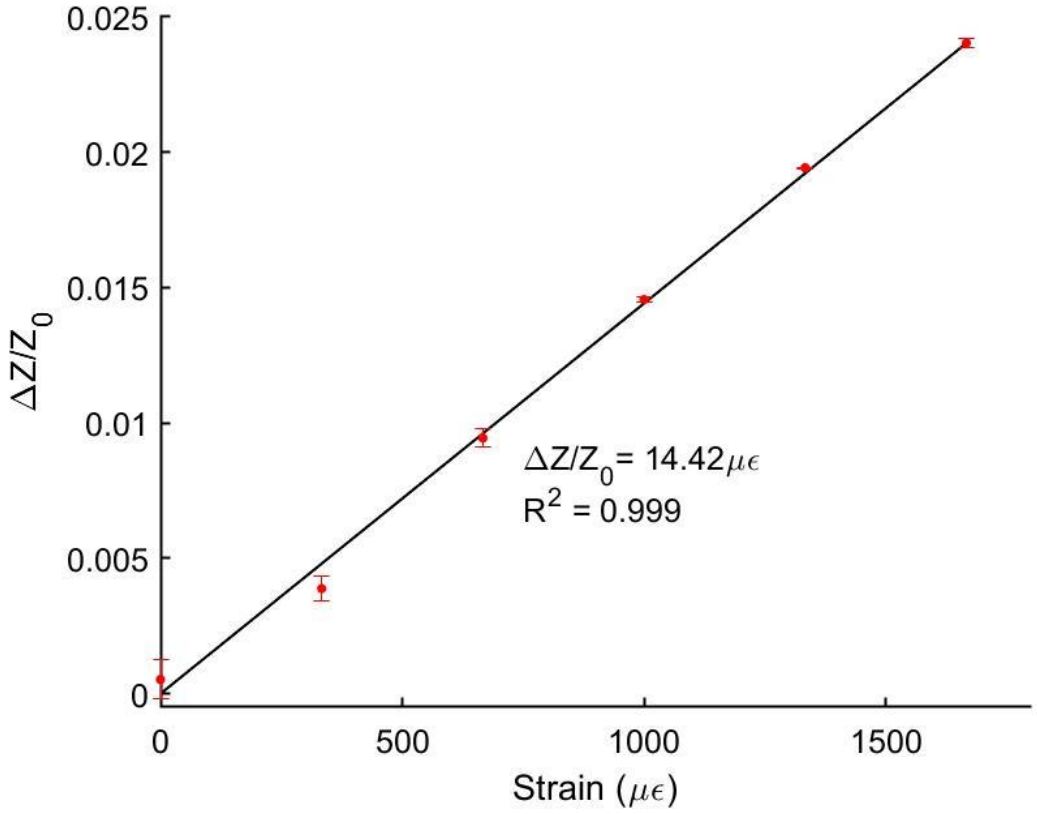

Figure 6.21 – Average fractional change in impedance versus tensile strain for patch printed on GFRP sheet for 3 load cycles. Error bars represent standard deviation of six load cycles with three impedance measurements per cycle for one sample.

Samples that exceeded the loading limits presented in Section 6.3.5 resulted in nonlinear and nonrepeatable behavior. Figure 6.22 displays the sensing response of patches under high tensile strain[25]. The response under these conditions was nonlinear as depicted in (Yoo et al., 2018a). Applying high loads compromised the structural integrity of the patches which apart from poor sensing capabilities also led to cracks and debonding.

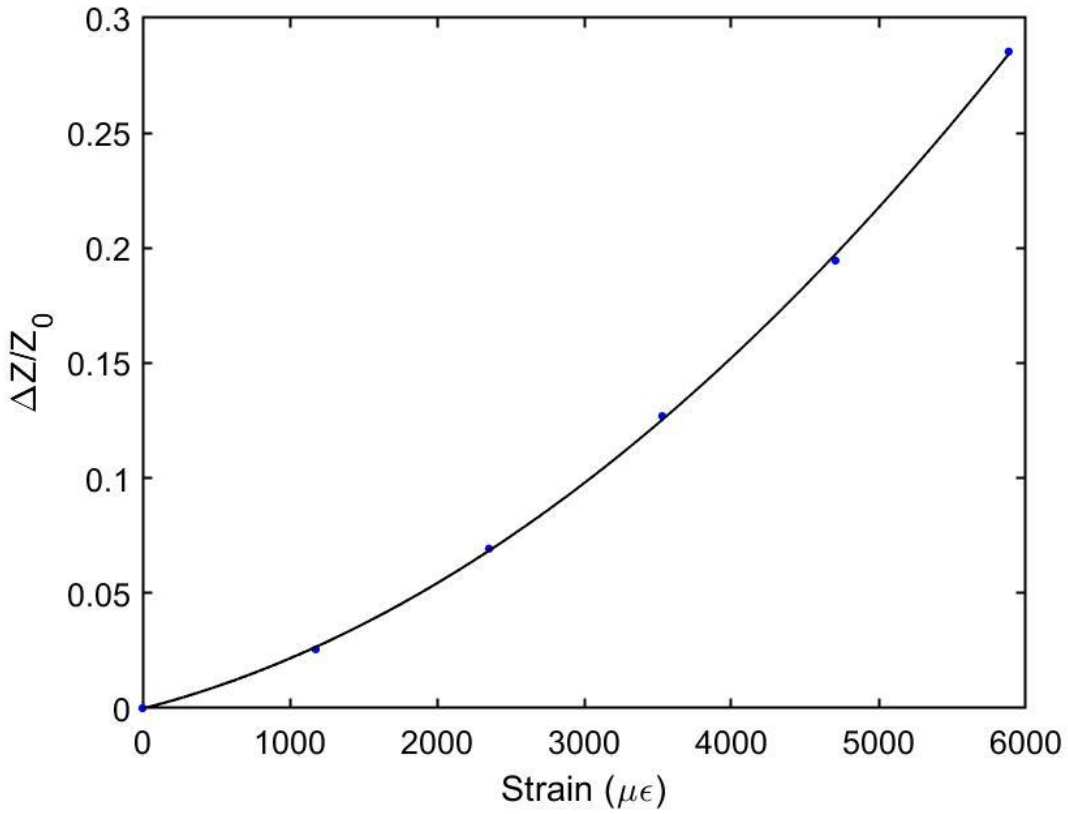

Figure 6.22 – Nonlinear sensing response of one patch printed on GFRP sheet under high loads under tensile strain.

6.4.1.4 4-point bending

Figure 6.23 presents the sensing behavior of sample set 2.3A) for loading Segments 1 & 3. Contrary to tension and compression, the sensing performance of the samples did not stabilize under this loading scheme as an increase in the initial impedance

[25] Applying close to 6000 με to a plain AAM sample will most likely lead to material failure at an earlier load. It can be speculated that low strain transfer occurs due to the presence of the glue and sand that were used to achieve adequate adhesion with the GFRP sheet. This phenomenon is similar to that found in sensing sheets (Gerber et al., 2018). If a greater bond was achieved, the patch would experience a larger portion of the applied load.

upon each load cycle can be viewed. 4-point bending also led to frequent debonding of the patches under loading. Both these occurrences have been speculated to occur due to weakening of the bond upon each loading cycle due to fatigue and differential curvature of the substrate and the patch (Turatsinze et al., 2011).

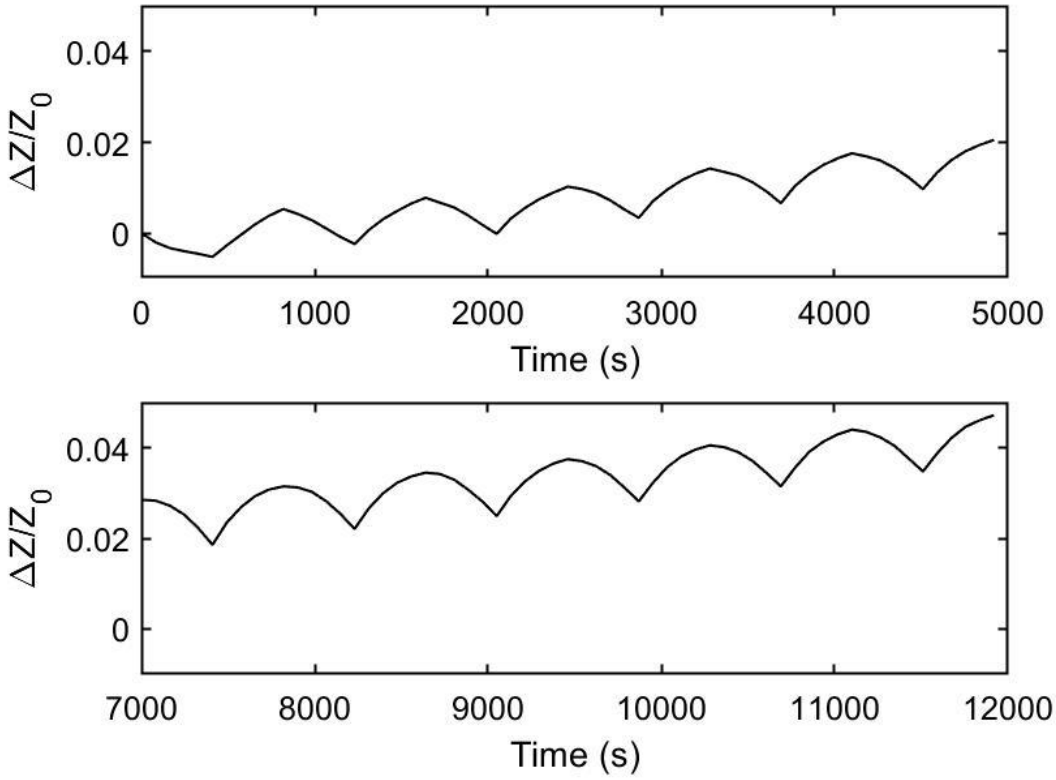

Figure 6.23 – Sensing response of patch printed on concrete beam under 4-point bending for (top) loading Segment 1 (cycles 1-6) and (bottom) loading Segment 3 (cycles 47-52).

As mentioned in Section 6.3.2 the patches for this investigation were printed between the two load points to ensure a constant strain following the behavior of beams under 4-point bending. The patches were also situated on the bottom face of the beam rather than the lateral face to ensure the patch was completely in tension to avoid any irregular behavior due to the measurement of simultaneous compression and tension in the sample. Taking these factors into account, the impedance of the sample was initially expected to increase. Despite this hypothesis, the impedance of the sample decreased as load was applied.

The impedance response of AAM under flexural loading is quite conflicted in the literature, being reported to both increase (Saafi et al., 2014) and decrease (Rovnaník et al., 2019b). In the current setup, the author of this thesis posits that the reason for the decrease in impedance during 4-point bending is that part of the electrical current flows through the concrete substrate during impedance measurement. As the load increases, deflection of the beam presents a larger cross-sectional area for the current to flow between two points. This means more current can flow, and this would lead to a decrease in impedance.

The sensing performance of the patches under 4-point bending was relatively difficult to characterize due to their variable and nonrepeatable behavior. In regards to the sample depicted in Figure 6.23, while the strain response was nonlinear, linear regions can be detected. As a result, the sensing performance was determined using only the linear region of the last cycle (therefore the first two loading points were removed).

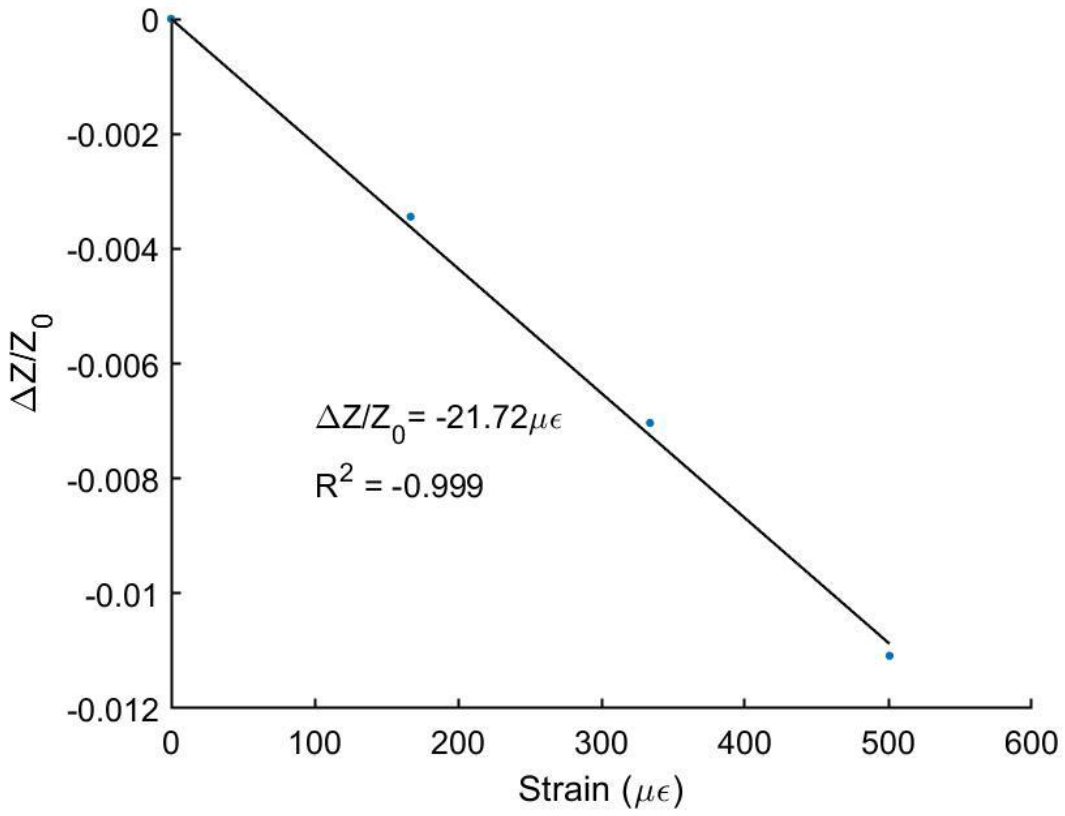

Figure 6.24 – Fractional change in impedance versus applied strain under linear region for one patch under 4-point bending for last load cycle of Segment 3.

The gauge factor for the last load cycle was calculated as 21.7, as can be seen in Figure 6.24.

In certain load trials, linear regions were not able to be detected. In this scenario the sensing response was characterized using a second-degree polynomial equation. Figure 6.25 presents an example of samples with nonlinear sensing behavior for all load points for one load cycle. In this situation though it can be seen that the maximum change in impedance is lower (0.009) for higher applied strain (830 με) compared to Figure 6.24 (maximum change in impedance 0.011 for 500 με). This difference could be a result of poorer adhesion in the former sample. Overall, accurately investigating beams under 4-point bending is currently a limitation of the technology presented in this thesis. Compared to compression and tension, this sensing approach was not as successful. Apart from better adhesion, different patch placement may be required to avoid excessive

damage in adhesion to allow repeatable sensing. These issues can be addressed in future work.

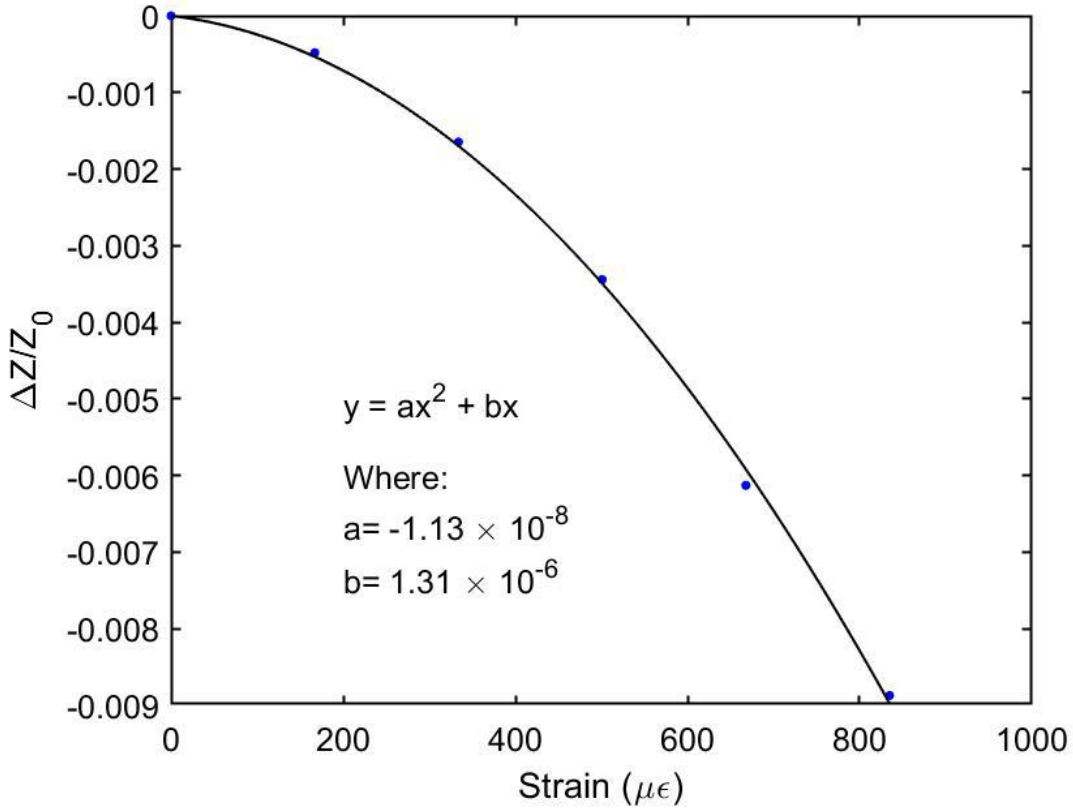

Figure 6.25 – Nonlinear response of one patch printed on a concrete beam under 4-point bending for one load cycle.

6.4.2 Strain sensing evaluation

6.4.2.1 Sensing performance

The AAM patches investigated were able to showcase sensing capabilities without relying on the use of conductive filler. This reiterates the benefits of employing AAM in sensing applications. The sensing performance of the sensing coatings examined in this chapter is presented in Table 6.3. The coatings were able to present the expected behavior under tension and compression e.g. increase in impedance in tension and decrease in impedance in compression. The response for this loading type was characterized as a linear behavior in terms of the applied strain or stress with high coefficients of determination. The sensing performance in tension (38.4±21.6) was comparable to GFs

reported in other filler free AAM applications under tension (D'Alessandro et al., 2020; Saafi et al., 2014). The sensing performance of the patches under compression (8.59±1.55) was lower compared to filler free applications reported by other authors where GFs range between 20-65 (D'Alessandro et al., 2020; Rovnaník et al., 2019c; Saafi et al., 2014). It can be speculated that the bond between the samples affects the strain sensing capacity. Overall as mentioned in Chapter 4 & 5, adhesion between the printed overlays and the concrete cubes was relatively low (0.6 MPa). This could be in part due to the low the roughness index achieved with wire brushing. It can be inferred that by employing a more effective means of surface preparation such as sandblasting can not only increase adhesion but also the sensing performance as well.

Table 6.3 – Sensing performance of AAM coatings.

Loading type	Sensing performance	Repeatability
Compression (50 mm cubes)	8.59±1.55	Good
Compression (100 mm cubes)	0.033 ±0.008 MPa^{-1}	Good
Tension	38.4±21.6	Good
4-point bending	21.7	Poor

In regards to 4-point bending the sensing performance of the patches was again quite low when compared with other applications. The GF calculated in this study was 21.7 with poor repeatability. Studies on the GF on general flexural loading (3-point and 4-point) have ranged between 150-1100 (Bi et al., 2017; Rovnaník et al., 2019b). Considering the frequent debonding of samples and the variable response presented (both linear and nonlinear) in 4-point bending it can be inferred that greater material preparation for the coatings and concrete surface preparation is required. Incorporating conductive filler can increase the gauge factor and the repeatability of the samples (D'Alessandro et al., 2020; Deng et al., 2019; Ma et al., 2020; Rovnaník et al., 2019a).

One of the main drawbacks of AAM sensors absent of conductive filler is their variable sensing behavior between samples. As mentioned in Section 2.3.3.4 reported gauge factors for such applications have ranged between 20 – 2000 without a detailed explanation (D'Alessandro et al., 2020; Lamuta et al., 2017; Ma et al., 2020; Saafi et al., 2014). While studies on ion exchange and ion conductivity in AAM have been carried out

(Biondi et al., 2020; Lamuta et al., 2016; Skorina, 2014) this concept is not understood to the extent where sensing performance of AAM binders can be reliably predicted. As the main form of conduction is ionic conduction, it can be hypothesized that one means of increasing sensing performance could be achieved by increasing the alkali ions (Na^+ and K^+) in the AAM matrix. However, as strain sensing is influenced by numerous factors, such claims cannot be easily made. Overall, despite the research that has been carried out, further investigation is required in this field to better comprehend this concept.

6.4.2.2 Limitations of experimental setup

An important point to mention is that the displacement values used in the displacement-controlled tests were obtained from the sensor in the load cell of the testing apparatus rather than with the use of external sensors. This obviously induces certain limitations in the investigation carried out. The displacement that is applied and the actual displacement experienced in the substrates most likely differs. Under compression testing, the applied displacement is distributed throughout the loading plates, the insulation plates and the concrete substrate. Similarly, in tensile testing the displacement is applied to the GFRP sheet which is then transferred to the layer of epoxy and sand before reaching the AAM patch. As a result, the actual displacement in the substrates will be affected by potential contact issues and strain transfer between the aforementioned components. This assumption can be verified by comparing the results of sample sets 2.1 A) and 2.1 B) (50 mm and 100 mm concrete cubes respectively). The SSC of the 100 mm cubes can be converted into GF by using the stress-strain relationship $\sigma=\varepsilon E$. Assuming a modulus of elasticity for concrete between 20 – 30 GPa, this would lead to a GF between 660-990 for the average SSC. The GF for the 50 mm cubes though was calculated as 8.59. These results differ by two orders of magnitude. Looking at these results through a different lens, the SSC of the 50 mm concrete cubes was calculated as 0.014 MPa^{-1}. This value is within the same order of magnitude as the SSC of the 100 mm samples, 0.033 MPa^{-1}. In addition, by assessing the stress-strain plot acquired from the load cell the modulus of elasticity of the concrete cubes was calculated as 0.65 GPa. This is much smaller compared to conventional values for concrete. This further supports the claim that the displacement

that is applied to the concrete substrate is lower and is likely affected by the experimental setup.

For this thesis the GF was calculated using the nominal displacement values from the load cell. We acknowledge that this is an issue, however this is currently a limitation of the current setup that cannot be overcome. It should also be mentioned that the displacement applied to substrate and the displacement that is experienced in the patch may also differ as strain transfer is governed by the bond between the two materials. The displacement that is actually applied to the substrate and the patch can be verified in future work with an additional linear variable differential transformer (LVDT) and/or a strain gauge.

6.4.3 AAM sensors for damage detection

As can be seen in Section 6.4.1, AAM patches require a large number of cycles before a repeatable response can be achieved. This limits immediate deployment as additional calibration steps are required. If repeatable behavior is not achieved this can lead to the incorrect interpretation of sensor's response. Even though mechanical cycling is common practice in achieving repeatability in self-sensing cementitious sensors, an increased number of cycles was required in this application compared to standalone AAM binders (Ma et al., 2020). This could indicate slight damage at the interface between the patch and the substrate upon each load cycle, owing to the low bond strength that was achieved. Apart from sensing performance, it can be inferred that improving adhesion may also limit the number of cycles required to achieve sensing repeatability.

Despite the numerous cycles applied, the change in impedance remains within the same order of magnitude. If the patches are damaged during mechanical loading, this will cause an immediate spike in the impedance of the AAM sensor. In this scenario whether repeatability has been achieved or not is of minor importance as the changes due to damage override the changes in cyclic loading. Figure 6.26 depicts the change in impedance for an AAM patch under compression. The sample at first displayed the expected response of AAM in compression as shown in Section 6.4.1.2. After a few cycles the change in impedance increased dramatically from $\Delta Z/Z_0$=0.01-0.015 to 6-7. This was a clear indication of damage in the patch. Delamination is not considered is it would have

led to the opposite result e.g. no change in impedance as load is applied. In this scenario, the patch entered the ‘damaged’ state of strain sensing as described in Section 2.3.3.1, in which an abrupt change in impedance can be observed. While the patch is no longer able to function as a strain sensor, it was able to immediately detect damage. Once the sample was removed from the testing apparatus this hypothesis was confirmed as cracks were detected on the surface of the patch.

This behavior of printed AAM sensors allows immediate deployment of the current technology and provides new routes for future applications. Furthermore, rather than depositing patches over large areas, these sensors can also be printed over smaller and designated areas of concrete structures for targeted monitoring. This can also allow AAM patches to see applications in the tomography of concrete. Overall, assessing the strain and damage behavior of AAM sensors can provide a greater understanding of these materials for future field and industrial applications.

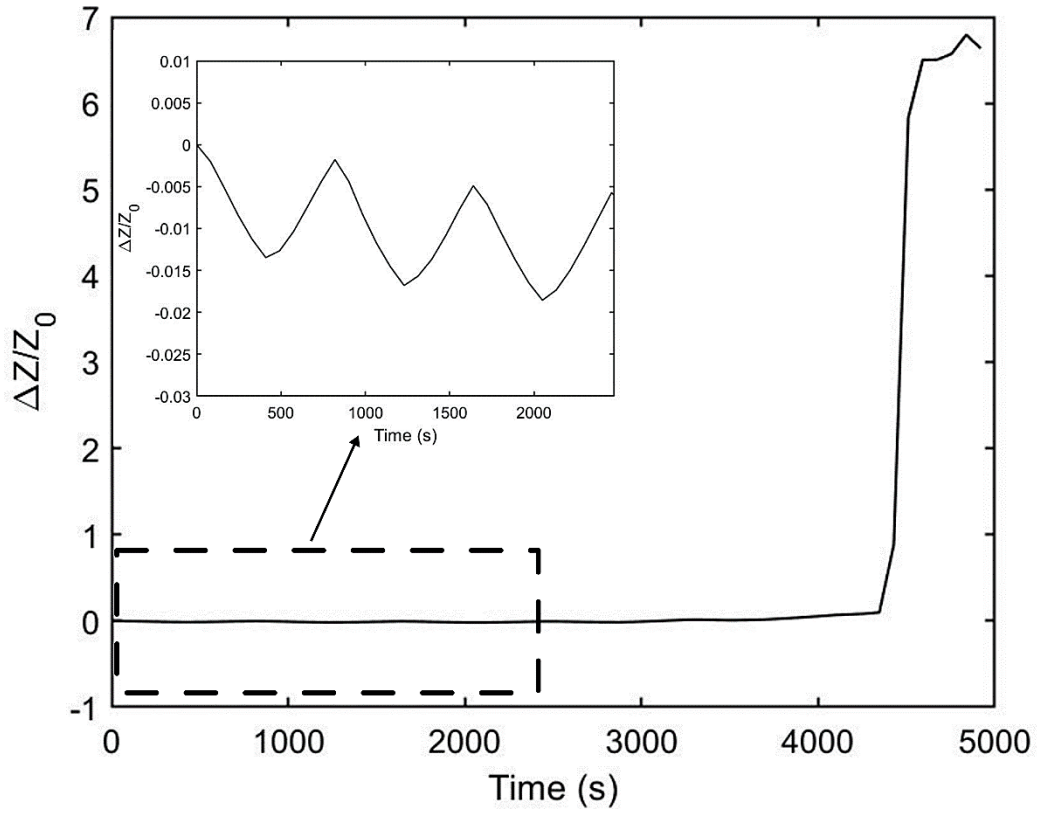

Figure 6.26 – Change in impedance for damaged patch under compression.

6.4.4 3D printing effects on sensing performance

To the best of the author's knowledge, the effect of 3D printing on sensing performance has not been studied. Printed cementitious materials present anisotropic behaviour due to the weakened interface between layers and are thus affected by the direction of the applied load in comparison to the direction of layers (Bong et al., 2019; Panda et al., 2017). In this application, the patches been printed following a 90^{o} crosshatched infill pattern (the first layer is deposited vertically, second layer horizontally). This was done in an attempt to create a more 'uniform' patch in order to minimize the effect of the direction of load in contrast to the filament orientation. As the weakest point of an overlay is usually at the interface between the two materials (Turatsinze et al., 2011) an argument could be made that the orientation of the first layer in association with the direction of load could have a greater impact on the behaviour of the patch. However, the overlay was required to maintain a level of workability to achieve adhesion with the

concrete substrate. This additional workability also promotes greater interlayer adhesion between the extruded filaments compared to stiffer mixes therefore minimizing the printing effects on the patch (Tay et al., 2018). Recent studies have also stated that the rheological properties of a mix play a more important role on the mechanical performance of printed binders rather the printing orientation compared to the applied load (Heras Murcia et al., 2020). It should be pointed out that if the mix design for the patches had poorer workability, apart from potentially introducing anisotropic behavior, this would also comprise adhesion with the concrete substrate (Courard et al., 2014). As a result, stiff mix designs are not ideal in this type of investigation and require greater investigation if employed.

6.5 Conclusions

In this chapter, the strain sensing response of printed AAM coatings onto concrete and glass fiber reinforced plastic sheets under compression, tension and 4-point bending was investigated. The key findings of this chapter are the following:

- Filler-free coatings presented the expected sensing response under compression and tension. The samples showcased linear behavior in regards to the applied loads.
- Sensing coatings require multiple loading cycles before a repeatable response can be achieved.
- Samples presented hysteresis between loading and unloading despite being subjected to multiple load cycles.
- Adhesion plays an important role in sensing overlays. Poorer adhesion can lead to compromised sensing integrity.
- Electrode configuration is critical when employing the van der Pauw electrode configuration.
- Repeatability under 4-point bending was not able to be achieved due to damage of the bond between the two samples. The sensing response was characterized as both linear and nonlinear.
- Damage in the patch can cause sharp spikes in the change in impedance.

Overall, the patches were able to present a repeatable sensing response under compression and tension, however this was compromised under 4-point bending. The repeatability and sensitivity coefficients of the samples can be improved by increasing adhesion with the substrates. Further research in self-sensing coatings includes using additive manufacturing to deposit coatings onto designated areas of substrates for localized sensing and investigating the strain behaviour of patches under biaxial loading and various temperature and moisture conditions. Early results also show that AAM sensors could be used in damage detection applications.

Chapter 7 Deployment methods

In this chapter potential methods of deploying the technology presented in this thesis will be briefly discussed. The focus is primarily on deploying the technology onto precast concrete elements, as the environment of a prefabrication factory couples well with the requirements and limitations of the 3D printing technique employed in this thesis. Methods of improving the deployment are also presented.

7.1 Introduction

Deployment of self-sensing materials is an important aspect in the development of ‘smart’ infrastructure. In its current state, the 3D printing methodology presented in this thesis would be difficult to apply in an onsite construction environment. It is, however, already quite compatible with precast applications as:

- The two-part AAM fabrication method requires additional mixing steps which is better situated in a controlled environment rather than in-situ.
- Precast elements allow more time for surface preparation and proper curing of the printed objects to ensure greater sensing performance.
- Sensing probes can be installed with greater precision.
- Gantry 3D printers which print downwards can be situated in fixed locations.

7.2 Methods of deployment

One of the constraints in deploying extruded elements is the type of printing system employed. Two means of deploying sensing patches will be presented in this section: a gantry 3D printer, and a robotic arm.

7.2.1 Gantry 3D printer

Gantry printing systems can provide an efficient means of printing patches onto precast elements. The allowable size of substrates that could be used is governed by the size of the printing system. The print bed in the printing setup used throughout this thesis is 300 mm × 300 mm. This was able to satisfy the size requirements for the substrates investigated in this project. The largest substrate that was examined in sensing was 100 mm concrete cubes with 90 mm × 90 mm patches. While not electrically interrogated in this work, larger overlays were also printable. Figure 7.1 presents a patch being extruded onto a 200 mm × 200 mm concrete slab.

Figure 7.1 – Patch printed onto 200 mm × 200 mm concrete slab.

Substrates that are larger than the printing bed in one dimension (e.g. a 1000 mm long concrete beam) can also be used in this printing configuration by feeding the substrate through the open sides of the printer. Figure 7.2 presents the printer used in this thesis

extruding a sensing patch onto a 1000 mm beam. This is essentially an upscaled version of the printing process used in Chapter 6[26]. As can be seen the beam must be supported with additional supports, as the frame and bed of the printer could not sustain the weight of the concrete beam. In this configuration, the steps in the z-axis are controlled by the print bed rather than the print head. This prevents multilayer objects from being fabricated as the z-axis is nullified. This poses limitations in the size of the patches that can be extruded as the thickness of the overlays is controlled by the nozzle size and head distance. These limitations are, however, a feature of this particular printer, and a gantry and extruder system could be designed specifically for precast applications.

[26] Larger substrates may require a different electrode configuration than what was used in previous chapters to ensure the current can flow between the electrodes. Detailed consideration of this aspect is outside of the scope of this thesis.

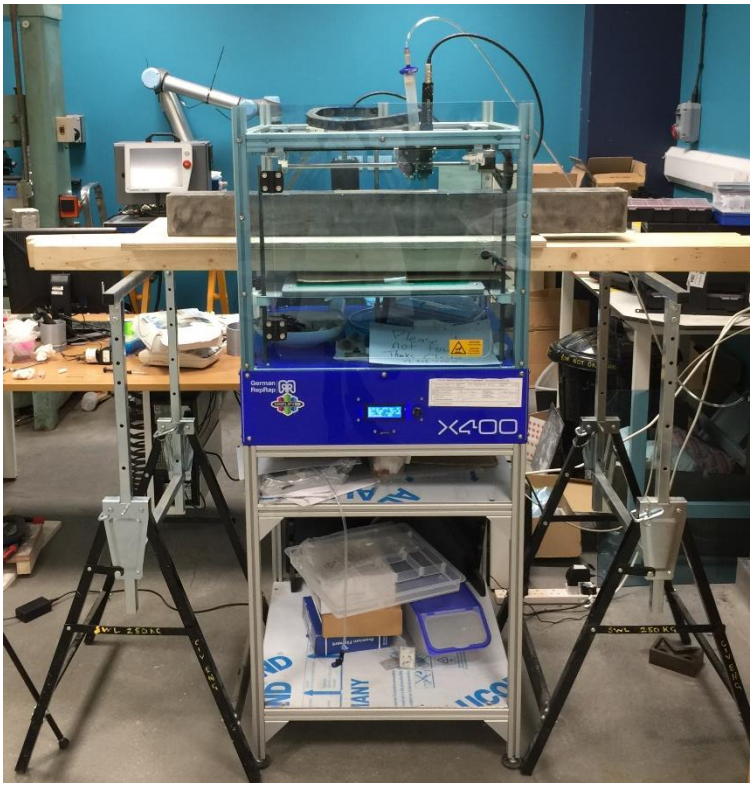

Figure 7.2 – Extrusion of patch onto 1000 mm concrete beam with the use of stationary 3D printer. The walls of the printer were removed and supports were used to accommodate the size and weight requirements of this application.

7.2.2 Robotic arm

Using a six-axis robotic arm could expand the number printing applications that can be achieved. This can replicate the printing process used in this thesis while bypassing size limitations imposed by the size of the printer and substrate. A six-axis robot also enables the extrusion of objects with multiple layers as all print movements are controlled by the print head. In a similar application conducted by the author's research group a sprayer was mounted onto a robotic arm to produce AAM overlays via spraying (McAlorum et al., 2021a). Figure 7.3 presents a picture of the referred setup. The same system can be used for filament printing as well by substituting the sprayer with the cavity dispenser used in this thesis. The use of robotics paves the way for onsite applications, particularly in areas with limited access. Further development would be required to streamline robotic printing methods, and to allow for printing on vertical, curved and overhanging surfaces.

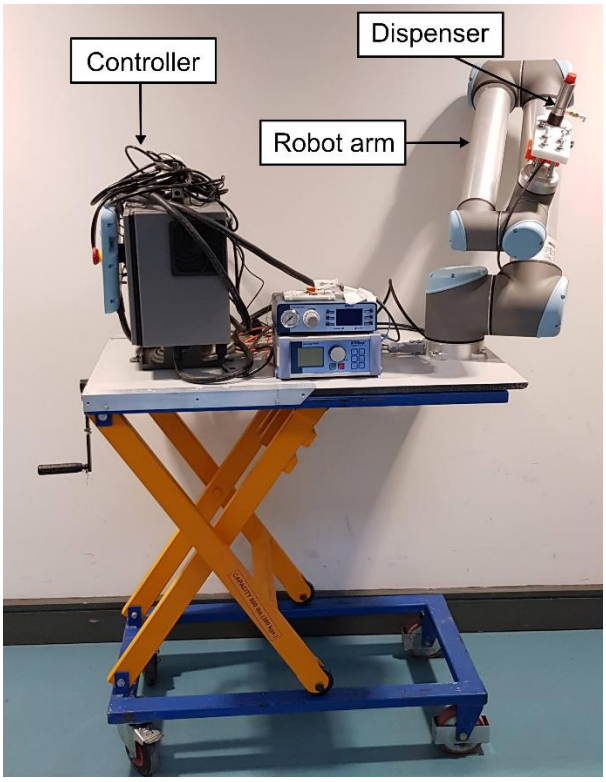

Figure 7.3 – Robotic dispensing system at Civil Automation Group - Photo courtesy of Jack McAlorum.

7.3 Electrode placement

In the work described in this thesis, once a patch was successfully printed onto a substrate, thin stainless steel wires or stainless steel tape were manually inserted in the patches as electrodes. This enabled the interrogation of the sensing patches. A means of improving consistency and allowing a simpler design for electrode placement could involve a prefabricated electrode mould. Apart from greater consistency in electrode placement, this allows a larger variety of electrodes to be used that would otherwise present installation issues. Such electrodes include carbon fiber tow (carbon fiber filaments that are woven into fabric).

7.4 Sensing interrogation

Sensing interrogation was carried out with a commercial electrical impedance analyzer. While this is able to present rich datasets, these systems are expensive and operate from mains power. Currently low-cost impedance analyzers are being developed within the author's group at the University of Strathclyde (McAlorum et al., 2021b). These

interrogators are able to replicate the functionality of commercial systems within 5.2% of error. This allows a more efficient means of monitoring patches particularly when multiple elements are being deployed. Moreover, while data transmission was conducted via cable connections in this thesis, data can also be wirelessly transmitted to avoid connection complexities. Lastly, additional reference sensors will be required when sensing patches are installed for temperature and humidity compensation.

7.5 Conclusions

In this chapter a brief overview of the challenges and opportunities facing the deployment of current system are presented. The sensing patches presented in this thesis are, for now, aimed at precast applications due to the Gantry-like methodology followed throughout this thesis. Deployment of sensing patches can be improved by upscaling to robotic deployment methods, by employing lower cost and wireless interrogation systems, and by using moulds for more consistent electrode placement.

Chapter 8 Conclusions and future work

This chapter provides a synopsis on printing alkali activated sensors for concrete structures. An overview of the thesis is presented, the significant findings are pointed out and avenues for future work in this field are proposed

8.1 Conclusions

In this thesis cementitious patches were printed onto substrates as a new means of combining the structural health monitoring & maintenance of concrete infrastructure. The PhD has enabled:

- The automated extrusion of overlays onto concrete substrates and glass fiber reinforced plastic sheets.
- Temperature and strain characterization of filler-free alkali activated material patches.

This thesis began with a literature review introducing alkali activated materials (AAM), AAM as self-sensing materials and 3D printing cementitious materials. A general overview on the theory and background behind AAM is initially provided. The current understanding of AAM as strain, temperature and moisture sensors along with reported applications follows. While AAM are ideal candidates for self-sensing materials they are relatively under-researched when compared to ordinary Portland cement (OPC) binders.

Lastly, literature on 3D printing cementitious materials is presented. The printing process and printing requirements for cementitious mixes are depicted. Common printing terminology, printing configurations and intricacies in cementitious printing are also outlined.

Chapter 3 provides experimental results on the mechanical properties of AAM. It was found that ambient cured metakaolin AAM binders are able to achieve adequate strength at 28 days (compressive strength – 34 MPa and flexural strength – 3.3 MPa) with the majority of strength being reached after 7 days of curing.

The development of 3D printed overlays for concrete substrates follows. Current guidelines in 3D printing cementitious materials do not cover the requirements that must be considered for the extrusion of coatings. In this thesis the existing printing guidelines were expanded to accommodate the needs for this application. The requirements defined for sensing patches are the following: extrudability, buildability (degree of buildability), printability window, adhesion and conductivity/sensing capability. Extrudability and printability window are intrinsically linked as they are able to define whether and how long a mix can be extruded respectively. Buildability is associated with the degree an object can achieve its intended shape without major deformation. As overlays are much thinner than structural materials the buildability requirements for this application are much lower than in conventional cementitious applications. The patches must also be able to achieve adequate adhesion with the substrate to ensure proper functionality. This requires proper surface preparation and filler to increase adhesion between the two elements. Lastly, as these patches are intended for sensing applications they must be electrically conductive and be able to showcase temperature and strain sensing response. Due to their chemical microstructure these properties are innately fulfilled.

The temperature sensing capability of these patches was investigated between 10 ^{o}C – 30 ^{o}C – 10 ^{o}C for two cycles. The patches were able to present the expected change in electrical properties of AAM under these circumstances. Increasing temperature accelerates the movement of ions in the AAM matrix thus led to lower impedance. Similarly, ions move slower at lower temperatures which resulted in the impedance

increasing. The change in impedance in response to temperature change was characterized as an exponential equation. Furthermore it was also determined that frequency played a minor role in the sensing response of the samples. Between the two temperature cycles the patches presented a resolution of 0.1 °C and a repeatability of 0.3 °C.

Following temperature sensing, the strain sensing response of the overlays was investigated. The samples were tested under compression, tension and 4-point bending. The experimental results confirmed that AAM can be used in strain sensing applications without relying on the use of conductive filler. The response of the patches in compression and tension was according to the behavior outlined in the sensing review. Impedance decreased in compression and increased in tension. Similar to temperature sensing this behavior is attributed to the movement of the ions in the matrix. As the sample is compressed the distances ions must travel is shortened which results in lower impedance. Analogously these distances increase as tension is applied to the sample which increases impedance. The samples required multiple load cycles before a repeatable response could be achieved. The change in impedance in regards to the applied strain displayed a linear relationship. The gauge factor was calculated as 8.59±1.55 in compression and 38.4±21.6 in tension. Poor adhesion between the patch and the substrate led to compromised sensing performance. Damage in the patch resulted in an abrupt increase in the sample's impedance. Furthermore, the direction the electrical properties are being measured compared to the applied load influences electrical measurements despite the type of load being applied to the substrate. Compared to compression and tension, patches under 4-point bending presented sensing issues. Frequent delamination of patches occurred which could be a direct result of the difference in mechanical response between the two elements. Repeatability was not able to be achieved despite samples being subjected to multiple load cycles. In turn this led to difficulties in the characterization of their electrical performance in which both linear and nonlinear responses were detected.

In Chapter 7, potential means of deployment of sensing patches is presented. The manner in which the technology in this thesis is developed is more suitable for precast elements. The AAM fabrication and printing setup are better situated in a controlled environment

rather than onsite applications. The development of sensing patches can be easily upscaled to larger sized applications based on work that is currently being developed within the author's research group.

8.2 Future work

3D printing self-sensing overlays is a novel multidisciplinary field of study. The experiments conducted in this thesis were therefore naturally limited by available time and equipment. Recommendations on future work in this area of study follow.

8.2.1 Understanding sensing performance

Despite the research that has been carried out in AAM sensing, the mechanisms behind the changes in electrical impedance are not fully understood. Large differences in investigations have been reported which makes predicting the performance of these sensors quite difficult. The variance in results could be attributed to additional effects that are not always accounted for in the evaluation of these sensors. Such factors include geometry, molecular composition, degree of saturation and testing environment (temperature and humidity), and variations in the substrate. These parameters must be taken into greater consideration to allow for the accurate characterization and design of these sensors.

8.2.2 Improving sensing performance

In this thesis the temperature and strain sensing performance of AAM patches was characterized, however, potential means of improving the sensing response were not assessed. In regards to strain sensing, the adhesion investigation conducted suggests that the sensing performance of the patches can be improved by increasing the bond strength between the patch and the substrate. This could be achieved by increasing the surface roughness of the substrate, incorporating additional filler to enhance adhesion or by applying bonding agents. Once a higher bond is achieved, the overall impact adhesion plays on sensing could be investigated. This would involve assessing patches of different bond strengths and determining the strain transferred from the substrate to the patch with the use of strain sensors. A correlation between bond strength and sensing response (gauge

factor) could then be drawn. This will provide greater insight on the utility of cement-based overlays as strain sensors.

When it pertains to temperature sensing, the patches can initially be assessed for a larger temperature range to imitate temperature conditions in site applications, with a safety factor. Moreover, it is rather unclear if adhesion will impact the temperature response to the same degree as strain sensing. As stated in Chapter 2 temperature sensing is affected by moisture content and by the chemical composition of the binder. In this scenario it would be more fitting to focus on these parameters to improve temperature sensing response.

8.2.3 Sensor size and placement

In this thesis, patches were printed onto the entire surface of concrete cubes and onto areas where maximum strain was expected in concrete beams and glass reinforced fiber sheets. Replicating this in larger structures though may not be feasible. As a result strategic deployment of patches would be required for more effective monitoring. To provide an example, smaller patches or even objects containing few ‘filaments’ can be extruded for temperature sensing applications. This will allow for quicker stabilization of the sensor and require overall less printing setup (e.g. less surface preparation for substrates and shorter printing duration). Moreover, similar to the tensile and 4-point bending investigation, patches can be printed in critical areas of larger structures for targeted strain sensing.

8.2.4 Additional sensing applications

In this thesis, temperature and strain sensing were assessed separately. It is likely that multiple effects may simultaneously occur in field and industrial applications. Therefore, a better understanding on how AAM respond under multiple measurands is necessary. The combined effects of sensing though should not be limited to these measurands alone. How sensors behave under different temperature, strain, moisture and loading conditions should be better understood to allow proper functionality and interpretation of the response of these materials.

One of the drawbacks of employing AAM patches as strain sensors is the high number of cycles required to reach a repeatable sensing response. Preliminary results of this thesis show that AAM patches could also be used for damage detection. Whether sensing repeatability is achieved in this scenario is of minor importance as the change in impedance is instantaneous and of greater magnitude compared to the impedance shifts between loading cycles. This allows for immediate deployment of this technology by-passing the current limitations presented in strain sensing. Moreover, by focusing on damage detection, smaller patches can be deployed over large spans in structures for distributed monitoring rather than relying on a single patch to monitor an entire surface. While the fabrication of such patches is relatively straightforward, additional electrodes and data processing will be required to deliver a distributed measurement system.

8.2.5 Improving sensor fabrication

While the technology presented in this thesis is suitable for precast elements, simplifying the fabrication of sensing patches is greatly beneficial nonetheless. This can improve repeatability of the sensors while at the same time broadening potential applications. A first step in improving this system would be by converting AAM fabrication from the two-part mixing method to the one-part method. This change is advantageous as the same end-product can be achieved by reducing the number of steps required in mixing while also minimizing prior knowledge in the chemical background of AAM.

A further step that can be taken to simplify the design process is to use small pins as electrodes rather than tape or wires. This can minimize the impact the sensing probes have on patches (e.g. cracks) while also avoiding instalment issues such as electrodes falling out. In turn the pins can be inserted with the use of prefabricated moulds for consistent spacing. The probes could then be extended by soldering wires to fit application needs. This features a more consistent technique in electrode placement by eliminating any potential electrode effects during testing.

8.2.6 3D printing

In this project, the printing requirements were based on existing guidelines and were expanded where necessary. These were made based on author's judgement and need for an expanded set of design guidelines to deliver the printed sensors. The same application though may be approached differently by other researchers based on equally viable methods. As printing applications progress it will be relatively difficult to keep track of how printing could be approached primarily by new researchers entering this field. Guidelines on printing setups, developing mixes and assessing their properties should be developed to allow for greater unification of existing applications. This will provide a strong foundation for 3D printing applications going forward. Furthermore, printable mixes should be classified according to their application. This can avoid confusion and misconceptions in the scientific community that all mixes must adhere to the same set of rules to the same degree.

8.2.7 Field and industrial application

Despite the research that has been carried out field applications in self-sensing materials are very limited. Rather than being confined solely to laboratory applications, these materials should also be tested in field and industrial environments. This will also allow better understanding of how these materials behave under realistic site conditions. Even failure would provide useful information on how the development of these materials should continue going forward. In order for sensing patches presented in this thesis to be deployed in field and industrial applications the following steps must be taken.

8.2.7.1 Upgrading printing system

In its current state this technology can only be used in precast elements of limited size. Upscaling from a gantry printer to an autonomous robotic system will by-pass the size limitations imposed by the current printing setup. This will provide greater flexibility in the patches than can be printed and allow for the extrusion of additional layers to cover any potential inconsistencies in larger and/or field applications.

8.2.7.2 Data interrogation and acquisition

Data acquisition and processing is an important feature in sensing applications. In this thesis data were acquired with the use of a commercial impedance analyzer which were then analyzed after the completion of testing. This process though should be more user-friendly for applications outside the lab. Currently, commercial interrogators are not suitable for onsite applications due to their high costs. Low-cost interrogation systems that can be easily deployed with low power requirements should be used instead. Furthermore, a more automated system of data acquisition and analysis is required for the assessment of real time occurrences. This can be achieved by wireless transmission of data and through the development of software that is automatically able to process data and provide information on the condition of the structure the patch is monitoring.

8.2.7.3 Material properties

While the mechanical properties of the patches in this thesis were examined, not all tests were carried out according to existing standards. Certain experiments were also adjusted to meet material and equipment limitations while others were not considered due to the nature of the investigation involved. As a result, reevaluation and additional tests will be required to be carried according to existing repair standards. In all, the recommendations made are in hope that this technology will provide an additional solution to structural health monitoring applications in the future.

Appendix

A.1 Calculation of molar ratios

The steps for calculating the molar ratios of alkali activated materials (AAM) in this thesis are outlined below.

1. Calculation of mass of total solids and liquids.
2. Calculation of mass of each constituent in solids and liquids.
3. Calculation of Si, Al and Na in precursor.
4. Calculation of Si, Na in sodium silicate and sodium hydroxide.
5. Calculation of Si/Al, Na/Al ratios in AAM binder.

The molar and molecular weight of typical chemical compounds found in constituents for AAM formulation used in this thesis are displayed in Table A.1.

Table A.1 – Molar and molecular weight of typical chemical compounds and elements found in constituents for AAM formulation used in this thesis.

Chemical compound or element	Molecular/molar weight
SiO_2	60.0843 g/mol
Na_2O	61.97894 g/mol
K_2O	94.2 g/mol
Al_2O_3	101.961276 g/mol
H_2O	18.01528 g/mol
Si	28.085 g/mol
Na	22.98977 g/mol
K	39.0983 g/mol
Al	26.981538 g/mol

A.1.1 Step 1

Calculations begin by assuming 100g of liquid and determining the total solid content via the solid-liquid ratio (s/l) used in each application (A.1).

$$\text{Solids} = \frac{s}{l} \times 100\text{g} \tag{A.1}$$

A.1.2 Step 2

The percentage of each constituent in the solids and liquids is calculated e.g. percentage of metakaolin in precursor or sodium silicate in alkaline activator (A.2).

$$\text{Mass of constituent} = \text{percentage of constituent} \times \text{mass of solid or liquid} \quad \text{(A.2)}$$

A.1.3 Step 3

The percentage of SiO_2, Al_2O_3, Na_2O and Si, Al and Na respectively in each constituent in the precursor is calculated (A.3)(A.4)(A.5). An example of SiO_2 in metakaolin is provided.

$$\text{mass of } SiO_2 \text{ in metakaolin} = \frac{SiO_2\ \%\ \text{in metakaolin} \times \text{mass of metakaolin}}{100} \quad \text{(A.3)}$$

$$\text{Moles of } SiO_2 = \frac{\text{mass}(SiO_2)\ \text{in metakaolin}}{\text{molecular weight of } SiO_2} \quad \text{(A.4)}$$

$$\text{Mass of Si} = \text{moles of } SiO_2 \times \text{molar weight of Si}; \quad \text{(A.5)}$$

A.1.4 Step 4

The same process as outlined in Step 3 is followed for the sodium silicate in the alkaline activator. When it pertains to the sodium hydroxide (NaOH) a different procedure is followed (A.6)(A.7)(A.8)(A.9).

$$\text{Volume of NaOH} = \frac{\text{mass of NaOH}}{\text{density of NaOH}} \quad \text{(A.6)}$$

$$\text{Moles of NaOH} = \frac{\text{Molarity of NaOH}}{1000} \times \text{volume of NaOH} \quad \text{(A.7)}$$

$$\text{Moles of } Na_2O^{*} = \frac{\text{moles of NaOH}}{2} \quad \text{(A.8)}$$

*From $2NaOH + H_2O = Na_2O + 2H_2O$

$$\text{Mass of Na} = 2 \times \text{moles of } Na_2O \times \text{molar weight of Na} \quad \text{(A.9)}$$

A.1.5 Step 5

The molar ratios for the AAM binder are calculated by dividing the sum of the mass of the desired elements (A.10). An example for Si/Al is provided.

$$\text{Si/Al} = \Sigma(\text{mass of Si})/\Sigma(\text{mass of Al}) \quad \text{(A.10)}$$

A.2 3D Printing

In this thesis, printing was investigated primarily on a trial-and-error basis. Various mix designs were tested prior to the mix design in Chapter 4. Figure A.1 and Figure A.2 present the effect mixes with high liquid content (solid-liquid ratio=0.8) had on the printed objects. As can be seen, this led to mixes with large air bubbles and patches with rounded corners indicating low print quality and were not considered suitable for printing.

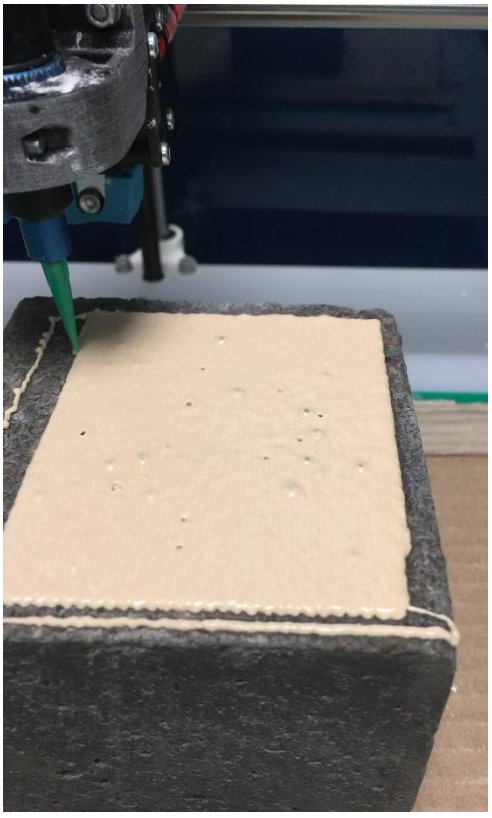

Figure A.1 – Extrudability issues due to high liquid mix.

Figure A.2 – Patches with rounded corners due to high liquid content.

Extrudability and the printability window of mixes were assessed by printing straight lines. In certain cases poor extrudability was a result of the paste solidifying in the dispenser due to the generation of heat in prolonged printing sessions, Figure A.3. In printing applications where a large time delay took place between layers due to large surfaces and/or low print speed, drying effects at the interface were observed, Figure A.4. While this is more prominent in full-width printing, as such the delay time and print speed were adjusted accordingly to avoid potential interlayer adhesion issues in the patches.

Figure A.3 – Solidification of alkali activated mix inside dispenser.

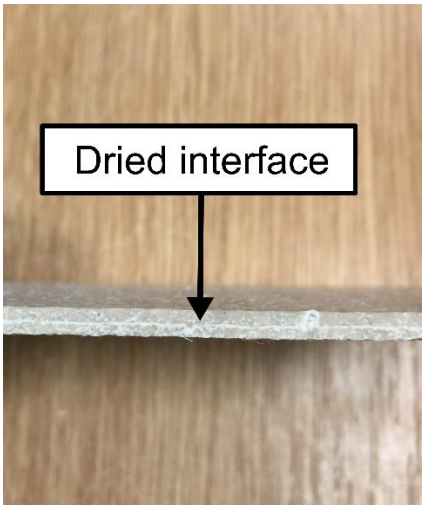

Figure A.4 – Dried interface due to prolong delay time between layers.

As mentioned in Chapter 4, the bond strength of the printed patches was relatively low (0.6 MPa) compared to other studies. The low strength was attributed in part due to the low roughness index achieved with wire brushing. In certain cases wire brushing was unable to provide adequately roughened surfaces. This led to weak adhesion which resulted in delamination of patches during coring of the samples for adhesion testing, Figure A.5. This reiterates the need for a more effective surface preparation technique.

Figure A.5 – Delamination of patch during coring for adhesion tests.

A.3 Repeatability of sensor

In temperature sensing the AAM patches were tested under two temperature cycles. The response of the patch at a given point was calculated as $R=Z_{mod}/Z_{mod,0}$. The repeatability of the sensor for both cycles was assessed by the following process, (A.11).

$$R_{repeatability} = \sqrt{\frac{\sum_{i=1}^{p}(m_i - 1)\, {s_i}^2}{\left(\sum_{i=1}^{p} m_i\right) - p}} \tag{A.11}$$

Where: m_i=number of cycles, p=number of points, s_i=standard deviation (A.12)

$$s = \sqrt{\frac{\sum_{i=1}^{m}(R_i - R_{mean})^2}{m - 1}} \tag{A.12}$$

Where R_i is the response for all the cycles.

A.4 Strain sensing of alkali activated overlays

In order to ensure a constant testing environment during strain testing, the temperature and humidity were measured with an external sensor. As can be seen in Figure A.6 the temperature and humidity conditions in the lab were stable at 21 ^{o}C and 35% relative humidity during standard working hours.

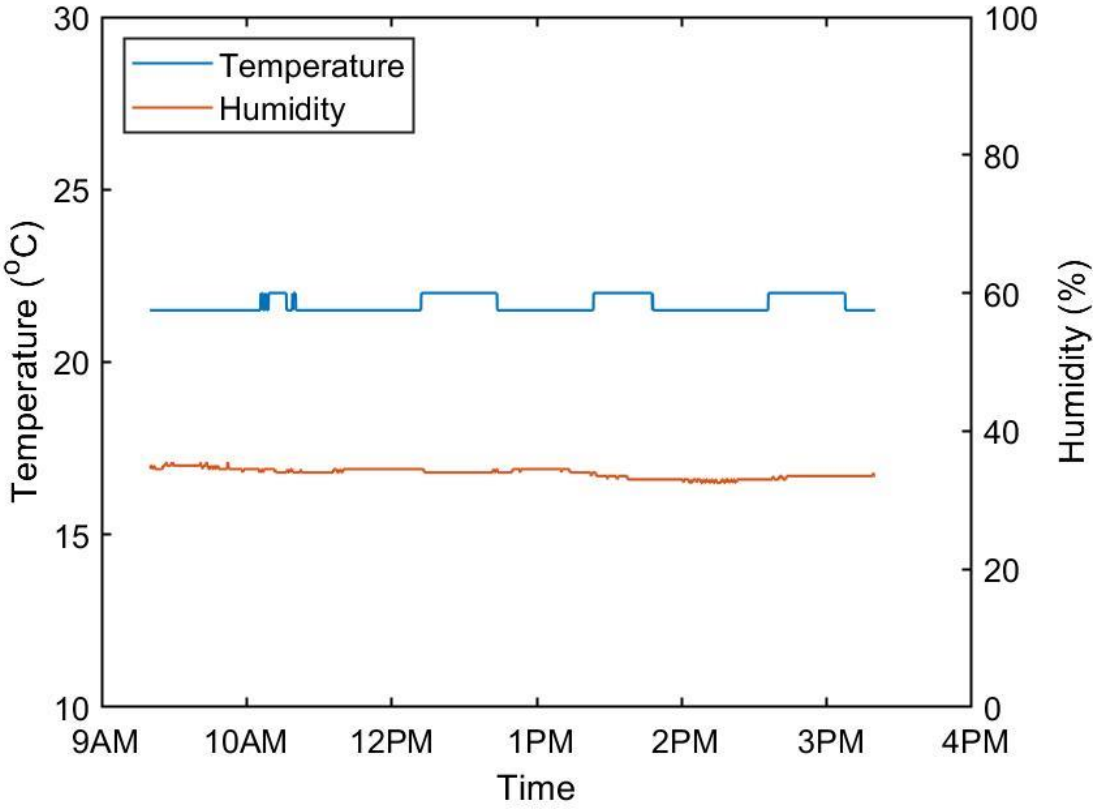

Figure A.6 – Temperature and humidity conditions of testing environment for standard working hours.

In regards to strain sensing, the patches were subjected to 3 loading schemes, Segments 1, 2 and 3. The response of loading segments 1 and 3 is depicted in Chapter 6. Figure A.7 presents the typical response of the change in impedance for patches for loading segment 2.

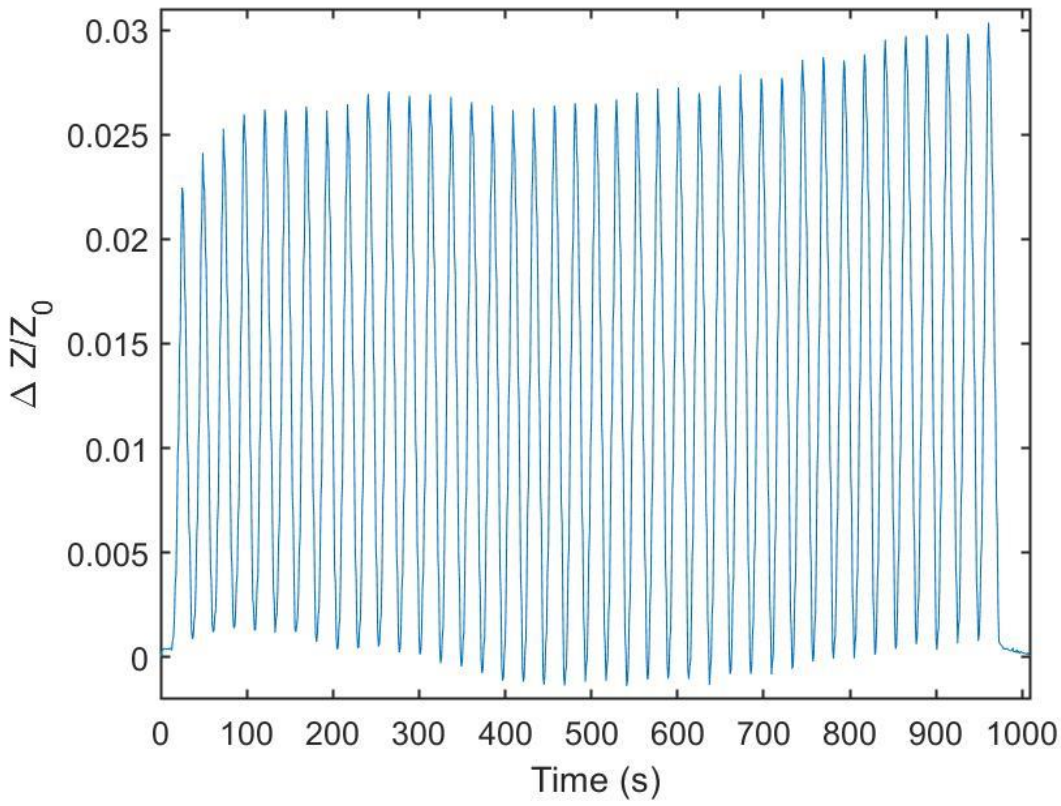

Figure A.7 – Loading segment 2 for patch in tension.

References

Abbasi, S.M., Ahmadi, H., Khalaj, G., Ghasemi, B., 2016. Microstructure and mechanical properties of a metakaolinite-based geopolymer nanocomposite reinforced with carbon nanotubes. Ceram. Int. 42, 15171–15176. https://doi.org/10.1016/j.ceramint.2016.06.080

Abdollahnejad, Z., Mastali, M., Falah, M., Shaad, K.M., Luukkonen, T., Illikainen, M., 2020a. Durability of the Reinforced One-Part Alkali-Activated Slag Mortars with Different Fibers. Waste and Biomass Valorization. https://doi.org/10.1007/s12649-020-00958-x

Abdollahnejad, Z., Mastali, M., Woof, B., Illikainen, M., 2020b. High strength fiber reinforced one-part alkali activated slag/fly ash binders with ceramic aggregates: Microscopic analysis, mechanical properties, drying shrinkage, and freeze-thaw resistance. Constr. Build. Mater. 241, 118129. https://doi.org/10.1016/j.conbuildmat.2020.118129

Abedi, M., Fangueiro, R., Gomes, A.C., 2020. Ultra-Sensitive Affordable Cementitious Composite with High Mechanical and Microstructural Performances by Hybrid CNT/GNP. Materials (Basel). 13, 3484. https://doi.org/10.3390/ma13163484

Aguirre-Guerrero, A.M., Robayo-Salazar, R.A., de Gutiérrez, R.M., 2017. A novel geopolymer application: Coatings to protect reinforced concrete against corrosion. Appl. Clay Sci. 135, 437–446. https://doi.org/10.1016/j.clay.2016.10.029

Aguirre-Guerrero, A.M., Robayo-Salazar, R.A., Mejía de Gutiérrez, R., 2021. Corrosion resistance of alkali-activated binary reinforced concrete based on natural volcanic pozzolan exposed to chlorides. J. Build. Eng. 33, 101593. https://doi.org/10.1016/j.jobe.2020.101593

Al-Dahawi, A., Sarwary, M.H., Öztürk, O., Yildirim, G., Akin, A., Şahmaran, M., Lachemi, M., 2016. Electrical percolation threshold of cementitious composites possessing self-sensing functionality incorporating different carbon-based materials. Smart Mater. Struct. 25. https://doi.org/10.1088/0964-1726/25/10/105005

Alanazi, H., Hu, J., Kim, Y.R., 2019. Effect of slag, silica fume, and metakaolin on properties and performance of alkali-activated fly ash cured at ambient temperature. Constr. Build. Mater. 197, 747–756. https://doi.org/10.1016/j.conbuildmat.2018.11.172

Alanazi, H., Yang, M., Zhang, D., Gao, Z., 2016. Bond strength of PCC pavement repairs using metakaolin-based geopolymer mortar. Cem. Concr. Compos. 65, 75–82. https://doi.org/10.1016/j.cemconcomp.2015.10.009

Albar, A., Chougan, M., Al- Kheetan, M.J., Swash, M.R., Ghaffar, S.H., 2020. Effective extrusion-based 3D printing system design for cementitious-based materials. Results Eng. 6. https://doi.org/10.1016/j.rineng.2020.100135

Albidah, A., Abadel, A., Alrshoudi, F., Altheeb, A., Abbas, H., Al-Salloum, Y., 2020. Bond strength between concrete substrate and metakaolin geopolymer repair mortars at ambient and elevated temperatures. J. Mater. Res. Technol. 9, 10732–10745. https://doi.org/10.1016/j.jmrt.2020.07.092

Albidah, A., Alghannam, M., Abbas, H., Almusallam, T., Al-Salloum, Y., 2021. Characteristics of metakaolin-based geopolymer concrete for different mix design parameters. J. Mater. Res. Technol. 10, 84–98. https://doi.org/10.1016/j.jmrt.2020.11.104

Alghamdi, H., Nair, S.A.O., Neithalath, N., 2019. Insights into material design, extrusion rheology, and properties of 3D-printable alkali-activated fly ash-based binders. Mater. Des. 167, 107634. https://doi.org/10.1016/j.matdes.2019.107634

Alghamdi, H., Neithalath, N., 2019. Synthesis and characterization of 3D-printable geopolymeric foams for thermally efficient building envelope materials. Cem. Concr. Compos. 104, 103377. https://doi.org/10.1016/j.cemconcomp.2019.103377.

Alujas, A., Fernández, R., Quintana, R., Scrivener, K.L., Martirena, F., 2015. Pozzolanic reactivity of low grade kaolinitic clays: Influence of calcination temperature and impact of calcination products on OPC hydration. Appl. Clay Sci. 108, 94–101. https://doi.org/10.1016/j.clay.2015.01.028

Amran, M., Debbarma, S., Ozbakkaloglu, T., 2021. Fly ash-based eco-friendly geopolymer concrete: A critical review of the long-term durability properties. Constr. Build. Mater. 270, 121857. https://doi.org/10.1016/j.conbuildmat.2020.121857

Arabzadeh, A., Ceylan, H., Kim, S., Sassani, A., Gopalakrishnan, K., Mina, M., 2018. Electrically-conductive asphalt mastic: Temperature dependence and heating efficiency. Mater. Des. 157, 303–313. https://doi.org/10.1016/j.matdes.2018.07.059

Archez, J., Texier-mandoki, N., Bourbon, X., Caron, J.F., Rossignol, S., 2021. Shaping of geopolymer composites by 3D printing. J. Build. Eng. 34, 101894. https://doi.org/10.1016/j.jobe.2020.101894

Assi, L.N., Deaver, E., Elbatanouny, M.K., Ziehl, P., 2016. Investigation of early compressive strength of fly ash-based geopolymer concrete. Constr. Build. Mater. 112, 807–815. https://doi.org/10.1016/j.conbuildmat.2016.03.008

Assi, L.N., Carter, K., Deaver, E., Ziehl, P., 2020. Review of availability of source materials for geopolymer/sustainable concrete. J. Clean. Prod. 263, 121477. https://doi.org/10.1016/j.jclepro.2020.121477

ASTM C618-19, 2015. Standard Specification for Coal Fly Ash and Raw or Calcined Natural Pozzolan for Use, Annual Book of ASTM Standards. West Conshohocken, PA. https://doi.org/10.1520/C0618-19.2

Autef, A., Joussein, E., Gasgnier, G., Pronier, S., Sobrados, I., Sanz, J., Rossignol, S., 2013. Role of metakaolin dehydroxylation in geopolymer synthesis. Powder Technol. 250, 33–39. https://doi.org/10.1016/j.powtec.2013.09.022

Avet, F., Snellings, R., Alujas Diaz, A., Ben Haha, M., Scrivener, K., 2016. Development of a new rapid, relevant and reliable (R3) test method to evaluate the pozzolanic reactivity of calcined kaolinitic clays. Cem. Concr. Res. 85, 1–11. https://doi.org/10.1016/j.cemconres.2016.02.015

Awoyera, P., Adesina, A., 2019. A critical review on application of alkali activated slag as a sustainable composite binder. Case Stud. Constr. Mater. 11, e00268. https://doi.org/10.1016/j.cscm.2019.e00268

Aydin, S., Baradan, B., 2012. Mechanical and microstructural properties of heat cured alkali-activated slag mortars. Mater. Des. 35, 374–383. https://doi.org/10.1016/j.matdes.2011.10.005

Azhari, F., Banthia, N., 2012. Cement-based sensors with carbon fibers and carbon nanotubes for piezoresistive sensing. Cem. Concr. Compos. 34, 866–873. https://doi.org/10.1016/j.cemconcomp.2012.04.007

Badogiannis, E., Kakali, G., Tsivilis, S., 2005. Metakaolin as supplementary cementitious material : Optimization of kaolin to metakaolin conversion. J. Therm. Anal. Calorim. 81, 457–462. https://doi.org/10.1007/s10973-005-0806-3

Baeza, F.J., Galao, O., Zornoza, E., Garcés, P., 2013. Multifunctional Cement Composites Strain and Damage Sensors Applied on Reinforced Concrete (RC) Structural Elements 841–855. https://doi.org/10.3390/ma6030841

Baiano, A., 2020. 3D Printed Foods: A Comprehensive Review on Technologies, Nutritional Value, Safety, Consumer Attitude, Regulatory Framework, and Economic and Sustainability Issues, Food Reviews International. Taylor & Francis. https://doi.org/10.1080/87559129.2020.1762091

Bard, A.J., Faulkner, L.R., 2001. Electrochemical Methods: Fundamentals and Applications, 2nd ed. John Wiley & Sons, Inc.

Batista, R.P., Trindade, A.C.C., Borges, P.H.R., Silva, F. de A., 2019. Silica Fume as Precursor in the Development of Sustainable and High-Performance MK-Based Alkali-Activated Materials Reinforced With Short PVA Fibers. Front. Mater. 6, 1–15. https://doi.org/10.3389/fmats.2019.00077

Bature, A.S., Khorami, M., Ganjian, E., Tyrer, M., 2021. Influence of alkali activator type and proportion on strength performance of calcined clay geopolymer mortar. Constr. Build. Mater. 267, 120446. https://doi.org/10.1016/j.conbuildmat.2020.120446

Beer, F.P., Johnston, E.R.J., DeWolf, J.T., Mazurek, D.F., 2009. Mechanics of Materials, 5th ed. McGraw-Hill, New York.

Behera, P., Baheti, V., Militky, J., Naeem, S., 2018. Microstructure and mechanical properties of carbon microfiber reinforced geopolymers at elevated temperatures. Constr. Build. Mater. 160, 733–743. https://doi.org/10.1016/j.conbuildmat.2017.11.109

Bernal, S.A., Rodríguez, E.D., Mejia De Gutiérrez, R., Provis, J.L., Delvasto, S., 2012.

Activation of metakaolin/slag blends using alkaline solutions based on chemically modified silica fume and rice husk ash. Waste and Biomass Valorization 3, 99–108. https://doi.org/10.1007/s12649-011-9093-3

Bernal, S.A., Provis, J.L., 2014. Durability of alkali-activated materials: Progress and perspectives. J. Am. Ceram. Soc. 97, 997–1008. https://doi.org/10.1111/jace.12831

Bernal, S.A., Provis, J.L., Fernández-Jiménez, Ana Krivenko, P. V., Kavalerova, E., Palacios, M., Shi, C., 2014a. Binder Chemistry – High-Calcium Alkali- Activated Materials, in: Provis, J.L., van Deventer, J.S.J. (Eds.), Alkali Activated Materials State-of-the-Art Report, RILEM TC 224-AAM. RILEM, Dordrecht Heidelberg New York London, pp. 59–91. https://doi.org/10.1007/978-94-007-7672-2

Bernal, S.A., Provis, J.L., Myers, R.J., San Nicolas, R., van Deventer, J.S.J., 2014b. Role of carbonates in the chemical evolution of sodium carbonate-activated slag binders. Mater. Struct. Constr. 48, 517–529. https://doi.org/10.1617/s11527-014-0412-6

Bernal, S.A., Rose, V., Provis, J.L., 2014c. The fate of iron in blast furnace slag particles during alkali-activation. Mater. Chem. Phys. 146, 1–5. https://doi.org/10.1016/j.matchemphys.2014.03.017

Bernal, S.A., San Nicolas, R., Myers, R.J., Mejía De Gutiérrez, R., Puertas, F., Van Deventer, J.S.J., Provis, J.L., 2014d. MgO content of slag controls phase evolution and structural changes induced by accelerated carbonation in alkali-activated binders. Cem. Concr. Res. 57, 33–43. https://doi.org/10.1016/j.cemconres.2013.12.003

Bernal, S.A., San Nicolas, R., Van Deventer, J.S.J., Provis, J.L., 2016. Alkali-activated slag cements produced with a blended sodium carbonate/sodium silicate activator. Adv. Cem. Res. 28, 262–273. https://doi.org/10.1680/jadcr.15.00013

Beushausen, H., Bester, N., 2016. The influence of curing on restrained shrinkage cracking of bonded concrete overlays. Cem. Concr. Res. 87, 87–96. https://doi.org/10.1016/j.cemconres.2016.05.007

Bhutta, A., Farooq, M., Banthia, N., 2019. Performance characteristics of micro fiber-reinforced geopolymer mortars for repair. Constr. Build. Mater. 215, 605–612. https://doi.org/10.1016/j.conbuildmat.2019.04.210

Bi, S., Liu, M., Shen, J., Hu, X.M., Zhang, L., 2017. Ultrahigh Self-Sensing Performance of Geopolymer Nanocomposites via Unique Interface Engineering. ACS Appl. Mater. Interfaces 9, 12851–12858. https://doi.org/10.1021/acsami.7b00419

Billong, N., Kinuthia, J., Oti, J., Melo, U.C., 2018. Performance of sodium silicate free geopolymers from metakaolin (MK) and Rice Husk Ash (RHA): Effect on tensile strength and microstructure. Constr. Build. Mater. 189, 307–313. https://doi.org/10.1016/j.conbuildmat.2018.09.001

Biondi, L., Perry, M., Vlachakis, C., Wu, Z., Hamilton, A., McAlorum, J., 2019. Ambient Cured Fly Ash Geopolymer Coatings for Concrete. Materials (Basel). 12, 923. https://doi.org/10.3390/ma12060923

Biondi, L., 2020. Geopolymer-based moisture and chloride sensors for nuclear concrete structures. University of Strathclyde.

Biondi, L., Perry, M., McAlorum, J., Vlachakis, C., Hamilton, A., 2020. Geopolymer-based moisture sensors for reinforced concrete health monitoring. Sensors Actuators, B Chem. 309, 127775. https://doi.org/10.1016/j.snb.2020.127775

Bocullo, V., Vitola, L., Vaiciukyniene, D., Kantautas, A., Bajare, D., 2021. The influence of the SiO2/Na2O ratio on the low calcium alkali activated binder based on fly ash. Mater. Chem. Phys. 258, 123846. https://doi.org/10.1016/j.matchemphys.2020.123846

Borg Costanzi, C., Ahmed, Z.Y., Schipper, H.R., Bos, F.P., Knaack, U., Wolfs, R.J.M., 2018. 3D Printing Concrete on temporary surfaces: The design and fabrication of a concrete shell structure. Autom. Constr. 94, 395–404. https://doi.org/10.1016/j.autcon.2018.06.013

Bong, S.H., Nematollahi, B., Nazari, A., Xia, M., Sanjayan, J., 2019. Method of optimisation for ambient temperature cured sustainable geopolymers for 3D printing construction applications. Materials (Basel). 12, 902. https://doi.org/10.3390/ma12060902

Borges, P.H.R., Bhutta, A., Bavuzo, L.T., Banthia, N., 2017. Effect of SiO2/Al2O3 molar ratio on mechanical behavior and capillary sorption of MK-based alkali-activated composites reinforced with PVA fibers. Mater. Struct. Constr. 50, 1–12. https://doi.org/10.1617/s11527-017-1021-y

Bos, F., Wolfs, R., Ahmed, Z., Salet, T., 2016. Additive manufacturing of concrete in construction: potentials and challenges of 3D concrete printing. Virtual Phys. Prototyp. 11, 209–225. https://doi.org/10.1080/17452759.2016.1209867

Brantervik, K., Berg, A., Niklasson, G.A., Hedberg, B., Nilsson, L.O., 1990. Percolation effects in the electrical conductivity of porous cement mortar. Epl 13, 549–554. https://doi.org/10.1209/0295-5075/13/6/013

British Standards Institution, 1999. Products and systems for the protection and repair of concrete structures - Test methods - Measurement of bond strength by pull-off.

British Standards Institution, 2016. BS EN 196-3:2016 Methods of Testing Cement. Part 3: Determination of Setting Time and Soundness. London.

Buswell, R.A., Silva, W.R.L. De, Jones, S.Z., Dirrenberger, J., 2018. 3D printing using concrete extrusion : A roadmap for research. Cem. Concr. Res. 112, 37–49. https://doi.org/10.1016/j.cemconres.2018.05.006

Cai, J., Li, X., Tan, J., Vandevyvere, B., 2020a. Thermal and compressive behaviors of fly ash and metakaolin-based geopolymer. J. Build. Eng. 30, 101307. https://doi.org/10.1016/j.jobe.2020.101307

Cai, J., Pan, J., Li, X., Tan, J., Li, J., 2020b. Electrical resistivity of fly ash and metakaolin based geopolymers. Constr. Build. Mater. 234, 117868.

https://doi.org/10.1016/j.conbuildmat.2019.117868

Cai, J., Tan, J., Li, X., 2020c. Thermoelectric behaviors of fly ash and metakaolin based geopolymer. Constr. Build. Mater. 237, 117757. https://doi.org/10.1016/j.conbuildmat.2019.117757

Candamano, S., Sgambitterra, E., Lamuta, C., Pagnotta, L., Chakraborty, S., Crea, F., 2019. Graphene nanoplatelets in geopolymeric systems: A new dimension of nanocomposites. Mater. Lett. 236, 550–553. https://doi.org/10.1016/j.matlet.2018.11.022

Cawley, P., 2018. Structural health monitoring : Closing the gap between research and industrial deployment. Struct. Heal. Monit. 175, 1225–1244. https://doi.org/10.1177/1475921717750047

Chang, C., Song, G., Gao, D., Mo, Y.L., 2013. Temperature and mixing effects on electrical resistivity of carbon fiber enhanced concrete. Smart Mater. Struct. 22. https://doi.org/10.1088/0964-1726/22/3/035021

Chaves Figueiredo, S., Romero Rodríguez, C., Ahmed, Z.Y., Bos, D.H., Xu, Y., Salet, T.M., Çopuroğlu, O., Schlangen, E., Bos, F.P., 2019. An approach to develop printable strain hardening cementitious composites. Mater. Des. 169, 107651. https://doi.org/10.1016/j.matdes.2019.107651

Chen, B., Wu, K., Yao, W., 2004. Conductivity of carbon fiber reinforced cement-based composites. Cem. Concr. Compos. 26, 291–297. https://doi.org/10.1016/S0958-9465(02)00138-5

Chen, L., Wang, Z., Wang, Y., Feng, J., 2016. Preparation and properties of alkali activated metakaolin-based geopolymer. Materials (Basel). 9, 1–12. https://doi.org/10.3390/ma9090767

Chen, M., Li, L., Wang, J., Huang, Y., Wang, S., Zhao, P., Lu, L., Cheng, X., 2020. Rheological parameters and building time of 3D printing sulphoaluminate cement paste modified by retarder and diatomite. Constr. Build. Mater. 234. https://doi.org/10.1016/j.conbuildmat.2019.117391

Chen, S., Li, Y., Yan, D., Wu, C., Leventis, N., 2019. Piezoresistive geopolymer enabled by crack-surface coating. Mater. Lett. 255, 1–4. https://doi.org/10.1016/j.matlet.2019.126582

Chen, Y., Li, Z., Figueiredo, S.C., Çopuroğlu, O., Veer, F., Schlangen, E., 2019. Limestone and Calcined Clay-Based Sustainable Cementitious Materials for 3D Concrete Printing: A Fundamental Study of Extrudability and Early-Age Strength Development. Appl. Sci. 9. https://doi.org/10.3390/app9091809

Cheng, H., Lin, K.-L., Cui, R., Hwang, C.-L., Chang, Y.-M., Cheng, T.-W., 2015. The effects of SiO2/Na2O molar ratio on the characteristics of alkali-activated waste catalyst–metakaolin based geopolymers. Constr. Build. Mater. 95, 710–720. https://doi.org/10.1016/J.CONBUILDMAT.2015.07.028

Chi, M., 2012. Effects of dosage of alkali-activated solution and curing conditions on the properties and durability of alkali-activated slag concrete. Constr. Build. Mater. 35, 240–245. https://doi.org/10.1016/j.conbuildmat.2012.04.005

Chiarello, M., Zinno, R., 2005. Electrical conductivity of self-monitoring CFRC. Cem. Concr. Compos. 27, 463–469. https://doi.org/10.1016/j.cemconcomp.2004.09.001

Choo, H., Lim, S., Lee, W., Lee, C., 2016. Compressive strength of one-part alkali activated fly ash using red mud as alkali supplier. Constr. Build. Mater. 125, 21–28. https://doi.org/10.1016/j.conbuildmat.2016.08.015

Chougan, M., Hamidreza Ghaffar, S., Jahanzat, M., Albar, A., Mujaddedi, N., Swash, R., 2020. The influence of nano-additives in strengthening mechanical performance of 3D printed multi-binder geopolymer composites. Constr. Build. Mater. 250, 118928. https://doi.org/10.1016/j.conbuildmat.2020.118928

Chougan, M., Ghaffar, S.H., Sikora, P., Chung, S., Rucinska, T., Stephan, D., Albar, A., Swash, M.R., 2021. Investigation of additive incorporation on rheological , microstructural and mechanical properties of 3D printable alkali-activated materials. Mater. Des. 202, 109574. https://doi.org/10.1016/j.matdes.2021.109574

Chuang, W., Geng-sheng, J., Bing-liang, L., Lei, P., Ying, F., Ni, G., Ke-zhi, L., 2017. Dispersion of carbon fibers and conductivity of carbon fiber-reinforced cement-based composites. Ceram. Int. 43, 15122–15132. https://doi.org/10.1016/j.ceramint.2017.08.041

Chung, D.D.L., 2021. Self-sensing concrete: from resistance-based sensing to capacitance-based sensing. Int. J. Smart Nano Mater. 12, 1–19. https://doi.org/10.1080/19475411.2020.1843560

Chung, D.D.L., 2002. Piezoresistive cement-based materials for strain sensing. J. Intell. Mater. Syst. Struct. 13, 599–609. https://doi.org/10.1106/104538902031861

Coppola, L., Coffetti, D., Crotti, E., Gazzaniga, G., Pastore, T., 2020. The durability of one-part alkali-activated slag-based mortars in different environments. Sustain. 12. https://doi.org/10.3390/SU12093561

Courard, L., Degeimbre, R., 2004. A capillary action test for the investigation of adhesion in repair technology. Can. J. Civ. Eng. 30, 1101–1110. https://doi.org/10.1139/l03-061

Courard, L., 2005. Adhesion of repair systems to concrete : influence of interfacial topography and transport phenomena. Mag. Concr. Res. 57, 273–282. https://doi.org/10.1680/macr.57.5.273.64285

Courard, L., Piotrowski, T., Garbacz, A., 2014. Near-to-surface properties affecting bond strength in concrete repair. Cem. Concr. Compos. 46, 73–80. https://doi.org/10.1016/j.cemconcomp.2013.11.005

Criado, M., Palomo, A., Ferna, A., 2005. Alkali activation of fly ashes . Part 1 : Effect of curing conditions on the carbonation of the reaction products. Fuel 84, 2048–2054.

https://doi.org/10.1016/j.fuel.2005.03.030

Cui, X.M., Zheng, G.J., Han, Y.C., Su, F., Zhou, J., 2008. A study on electrical conductivity of chemosynthetic Al2O3-2SiO2geoploymer materials. J. Power Sources 184, 652–656. https://doi.org/10.1016/j.jpowsour.2008.03.021

D'Alessandro, A., Coffetti, D., Crotti, E., Coppola, L., Meoni, A., Ubertini, F., 2020. Self-Sensing Properties of Green Alkali-Activated Binders with Carbon-Based Nanoinclusions. Sustainabiilityy 12, 9916. https://doi.org/doi.org/10.3390/su12239916

D'Alessandro, A., Rallini, M., Ubertini, F., Materazzi, A.L., Kenny, J.M., 2016. Investigations on scalable fabrication procedures for self-sensing carbon nanotube cement-matrix composites for SHM applications. Cem. Concr. Compos. 65, 200–213. https://doi.org/10.1016/j.cemconcomp.2015.11.001

Dai, X., Aydın, S., Yardimci, M.Y., Lesage, K., Schutter, G. De, 2020. Effects of activator properties and GGBFS/FA ratio on the structural build-up and rheology of AAC. Cem. Concr. Res. 138, 106253. https://doi.org/10.1016/j.cemconres.2020.106253

Dassekpo, J.M., Zha, X., Zhan, J., Ning, J., 2017. The effects of the sequential addition of synthesis parameters on the performance of alkali activated fly ash mortar. Results Phys. 7, 1506–1512. https://doi.org/10.1016/j.rinp.2017.04.019

Davidovits, J., 1989. Geopolymers and geopolymeric materials. J. Therm. Anal. 35, 429–441. https://doi.org/10.1007/BF01904446

Davidovits, J., 1991. Geopolymers: inorganic polymeric new materials. J. Therm. Anal. 37, 1633–1656. https://doi.org/10.1007/BF01912193

Davidovits, J., Huaman, L., Davidovits, R., 2019. Ancient geopolymer in south-American monument. SEM and petrographic evidence. Mater. Lett. 235, 120–124. https://doi.org/10.1016/j.matlet.2018.10.033

De Focatiis, D.S.A., Hull, D., Sanchez-Valencia, A., 2012. Roles of prestrain and hysteresis on piezoresistance in conductive elastomers for strain sensor applications. Plast. Rubber Compos. 41, 301–309. https://doi.org/10.1179/1743289812Y.0000000022

De Vargas, A.S., Dal Molin, D.C.C., Vilela, A.C.F., Silva, F.J. Da, Pavão, B., Veit, H., 2011. The effects of Na2O/SiO2 molar ratio, curing temperature and age on compressive strength, morphology and microstructure of alkali-activated fly ash-based geopolymers. Cem. Concr. Compos. 33, 653–660. https://doi.org/10.1016/j.cemconcomp.2011.03.006

Dehghanpour, H., Yilmaz, K., 2020. Investigation of specimen size, geometry and temperature effects on resistivity of electrically conductive concretes. Constr. Build. Mater. 250, 118864. https://doi.org/10.1016/j.conbuildmat.2020.118864

Demircilioğlu, E., Teomete, E., Schlangen, E., Baeza, F.J., 2019. Temperature and moisture effects on electrical resistance and strain sensitivity of smart concrete.

Constr. Build. Mater. 224, 420–427. https://doi.org/10.1016/j.conbuildmat.2019.07.091

Deng, L., Ma, Y., Hu, J., Yin, S., Ouyang, X., Fu, J., Liu, A., Zhang, Z., 2019. Preparation and piezoresistive properties of carbon fiber-reinforced alkali-activated fly ash/slag mortar. Constr. Build. Mater. 222, 738–749. https://doi.org/10.1016/j.conbuildmat.2019.06.134

Diggs-McGee, B.N., Kreiger, E.L., Kreiger, M.A., Case, M.P., 2019. Print time vs. elapsed time: A temporal analysis of a continuous printing operation for additive constructed concrete. Addit. Manuf. 28, 205–214. https://doi.org/10.1016/j.addma.2019.04.008

Ding, S., Dong, S., Ashour, A., Han, B., 2019a. Development of sensing concrete: Principles, properties and its applications. J. Appl. Phys. 126. https://doi.org/10.1063/1.5128242

Ding, S., Ruan, Y., Yu, X., Han, B., Ni, Y., 2019b. Self-monitoring of smart concrete column incorporating CNT/NCB composite fillers modified cementitious sensors. Constr. Build. Mater. 201, 127–137. https://doi.org/10.1016/j.conbuildmat.2018.12.203

Ding, S., Ruan, Y., Yu, X., Han, B., Ni, Y.Q., 2019c. Self-monitoring of smart concrete column incorporating CNT/NCB composite fillers modified cementitious sensors. Constr. Build. Mater. 201, 127–137. https://doi.org/10.1016/j.conbuildmat.2018.12.203

Dong, B., Qiu, Q., Xiang, J., Huang, C., Sun, H., Xing, F., Liu, W., 2015. Electrochemical impedance interpretation of the carbonation behavior for fly ash – slag – cement materials 93, 933–942. https://doi.org/10.1016/j.conbuildmat.2015.05.066

Dong, W., Li, W., Lu, N., Qu, F., Vessalas, K., Sheng, D., 2019a. Piezoresistive behaviours of cement-based sensor with carbon black subjected to various temperature and water content. Compos. Part B Eng. 178. https://doi.org/10.1016/j.compositesb.2019.107488

Dong, W., Li, W., Tao, Z., Wang, K., 2019b. Piezoresistive properties of cement-based sensors : Review and perspective. Constr. Build. Mater. 203, 146–163. https://doi.org/10.1016/j.conbuildmat.2019.01.081

Downey, A., D'Alessandro, A., Laflamme, S., Ubertini, F., 2018. Smart bricks for strain sensing and crack detection in masonry structures. Smart Mater. Struct. 27. https://doi.org/10.1088/1361-665X/aa98c2

Duxson, P., Provis, J.L., Lukey, G.C., Mallicoat, S.W., Kriven, W.M., Van Deventer, J.S.J., 2005a. Understanding the relationship between geopolymer composition, microstructure and mechanical properties. Colloids Surfaces A Physicochem. Eng. Asp. 269, 47–58. https://doi.org/10.1016/j.colsurfa.2005.06.060

Duxson, P., Provis, J.L., Lukey, G.C., Separovic, F., Van Deventer, J.S.J., 2005b. 29Si NMR study of structural ordering in aluminosilicate geopolymer gels. Langmuir 21,

3028–3036. https://doi.org/10.1021/la047336x

Duxson, P., Fernández-Jiménez, A., Provis, J.L., Lukey, G.C., Palomo, A., Van Deventer, J.S.J., 2007a. Geopolymer technology: The current state of the art. J. Mater. Sci. 42, 2917–2933. https://doi.org/10.1007/s10853-006-0637-z

Duxson, P., Mallicoat, S.W., Lukey, G.C., Kriven, W.M., van Deventer, J.S.J., 2007b. The effect of alkali and Si/Al ratio on the development of mechanical properties of metakaolin-based geopolymers. Colloids Surfaces A Physicochem. Eng. Asp. 292, 8–20. https://doi.org/10.1016/j.colsurfa.2006.05.044

Eaves, S., Gyi, D.E., Gibb, A.G.F., 2016. Building healthy construction workers: Their views on health, wellbeing and better workplace design. Appl. Ergon. 54, 10–18. https://doi.org/10.1016/j.apergo.2015.11.004

El-Sayegh, S., Romdhane, L., Manjikian, S., 2020. A critical review of 3D printing in construction: benefits, challenges, and risks. Arch. Civ. Mech. Eng. 20, 1–25. https://doi.org/10.1007/s43452-020-00038-w

Elahi, M.M.A., Hossain, M.M., Karim, M.R., Zain, M.F.M., Shearer, C., 2020. A review on alkali-activated binders: Materials composition and fresh properties of concrete. Constr. Build. Mater. 260, 119788. https://doi.org/10.1016/j.conbuildmat.2020.119788

Engelhardt, G., 1989. Multinuclear solid-state NMR in silicate and zeolite chemistry. Trends Anal. Chem. 8, 343–347. https://doi.org/10.1016/0165-9936(89)87043-8

Espera, A.H., Dizon, J.R.C., Chen, Q., Advincula, R.C., 2019. 3D-printing and advanced manufacturing for electronics. Prog. Addit. Manuf. 4, 245–267. https://doi.org/10.1007/s40964-019-00077-7

Fan, F., Liu, Z., Xu, G., Peng, H., Cai, C.S., 2018. Mechanical and thermal properties of fly ash based geopolymers. Constr. Build. Mater. 160, 66–81. https://doi.org/10.1016/j.conbuildmat.2017.11.023

Farhan, K.Z., Johari, M.A.M., Demirboğa, R., 2020. Assessment of important parameters involved in the synthesis of geopolymer composites: A review. Constr. Build. Mater. 264. https://doi.org/10.1016/j.conbuildmat.2020.120276

Favier, A., Hot, J., Habert, G., Roussel, N., d'Espinose de Lacaillerie, J.-B., 2014. Flow properties of MK-based geopolymer pastes. A comparative study with standard Portland cement pastes. Soft Matter 10, 1134. https://doi.org/10.1039/c3sm51889b

Feng, S., Xiao, H., Zhang, R., Yang, C., 2020. Bond performance between substrate concrete and repair mortar: Effect of carbon fibre and expansive agent. Constr. Build. Mater. 250, 118830. https://doi.org/10.1016/j.conbuildmat.2020.118830

Fiala, L., Jerman, M., Rovnaník, P., Černý, R., 2017. Basic physical, mechanical and electrical properties of electrically enhanced alkali-activated aluminosilicates. Mater. Tehnol. 51, 1005–1009. https://doi.org/10.17222/mit.2017.051

Fiala, L., Petříková, M., Lin, W.T., Podolka, L., Černý, R., 2019. Self-heating ability of

geopolymers enhanced by carbon black admixtures at different voltage loads. Energies 12. https://doi.org/10.3390/en12214121

Franchin, G., Scanferla, P., Zeffiro, L., Elsayed, H., Baliello, A., Giacomello, G., Pasetto, M., Colombo, P., 2017. Direct ink writing of geopolymeric inks. J. Eur. Ceram. Soc. 37, 2481–2489. https://doi.org/10.1016/j.jeurceramsoc.2017.01.030

Fu, X., Chung, D.D.L., 1996. Self-monitoring of fatigue damage in carbon fiber reinforced cement. Cem. Concr. Res. 26, 15–20.

Funke, K., Banhatti, R.D., 2006. Ionic motion in materials with disordered structures. Solid State Ionics 177, 1551–1557. https://doi.org/10.1016/j.ssi.2005.12.037

Galao, O., Baeza, F.J., Zornoza, E., Garcés, P., 2014. Strain and damage sensing properties on multifunctional cement composites with CNF admixture. Cem. Concr. Compos. 46, 90–98. https://doi.org/10.1016/j.cemconcomp.2013.11.009

Gao, K., Lin, K.L., Wang, D., Hwang, C.L., Shiu, H.S., Chang, Y.M., Cheng, T.W., 2014. Effects SiO2/Na2O molar ratio on mechanical properties and the microstructure of nano-SiO2 metakaolin-based geopolymers. Constr. Build. Mater. 53, 503–510. https://doi.org/10.1016/j.conbuildmat.2013.12.003

Gerber, M., Weaver, C., Aygun, L.E., Verma, N., Sturm, J.C., Glišić, B., 2018. Strain transfer for optimal performance of sensing sheet. Sensors 18, 1–16. https://doi.org/10.3390/s18061907

Ghilan, A., Chiriac, A.P., Nita, L.E., Rusu, A.G., Neamtu, I., Chiriac, V.M., 2020. Trends in 3D Printing Processes for Biomedical Field: Opportunities and Challenges. J. Polym. Environ. 28, 1345–1367. https://doi.org/10.1007/s10924-020-01722-x

Gluth, G.J.G., Arbi, K., Bernal, S.A., Bondar, D., Castel, A., Chithiraputhiran, S., Dehghan, A., Dombrowski-Daube, K., Dubey, A., Ducman, V., Peterson, K., Pipilikaki, P., Valcke, S.L.A., Ye, G., Zuo, Y., Provis, J.L., 2020. RILEM TC 247-DTA round robin test: carbonation and chloride penetration testing of alkali-activated concretes. Mater. Struct. Constr. 53, 1–17. https://doi.org/10.1617/s11527-020-1449-3

Gosselin, C., Duballet, R., Roux, P., Gaudillière, N., Dirrenberger, J., Morel, P., 2016. Large-scale 3D printing of ultra-high performance concrete - a new processing route for architects and builders. Mater. Des. 100, 102–109. https://doi.org/10.1016/j.matdes.2016.03.097

Gu, P., Xie, P., Beaudoin, J.J., Brousseau, R., 1992. A.C. impedance spectroscopy (I): A new equivalent circuit model for hydrated portland cement paste. Cem. Concr. Res. 22, 833–840. https://doi.org/10.1016/0008-8846(92)90107-7

Gu, P., Xie, P., Beaudoin, J.J., Brousseau, R., 1993. A.C. impedance spectroscopy (II): Microstructural characterization of hydrating cement-silica fume systems. Cem. Concr. Res. 23, 157–168. https://doi.org/10.1016/0008-8846(93)90147-2

Gulicovski, J., Nenadovic, S., Kljajevic, L., Mirkovic, M., Nišavic, M., Kragovic, M.,

Stojmenovic, M., 2020. Geopolymer/CeO2 as Solid Electrolyte for IT-SOFC. Polymers (Basel). 12.

Guo, X., Shi, H., Chen, L., Dick, W.A., 2010. Alkali-activated complex binders from class C fly ash and Ca-containing admixtures 173, 480–486. https://doi.org/10.1016/j.jhazmat.2009.08.110

Guo, X., Yang, J., Xiong, G., 2020. Influence of supplementary cementitious materials on rheological properties of 3D printed fly ash based geopolymer. Cem. Concr. Compos. 114, 103820. https://doi.org/10.1016/j.cemconcomp.2020.103820

Habert, G., Ouellet-Plamondon, C., 2016. Recent update on the environmental impact of geopolymers. RILEM Tech. Lett. 1, 17. https://doi.org/10.21809/rilemtechlett.v1.6

Haha, M. Ben, Lothenbach, B., Le Saout, G., Winnefeld, F., 2011. Influence of slag chemistry on the hydration of alkali-activated blast-furnace slag - Part I: Effect of MgO. Cem. Concr. Res. 41, 955–963. https://doi.org/10.1016/j.cemconres.2011.05.002

Hajimohammadi, A., Provis, J.L., Van Deventer, J.S.J., 2010. Effect of alumina release rate on the mechanism of geopolymer gel formation. Chem. Mater. 22, 5199–5208. https://doi.org/10.1021/cm101151n

Hajimohammadi, A., Provis, J.L., Van Deventer, J.S.J., 2011. The effect of silica availability on the mechanism of geopolymerisation. Cem. Concr. Res. 41, 210–216. https://doi.org/10.1016/j.cemconres.2011.02.001

Hajimohammadi, A., van Deventer, J.S.J., 2017. Characterisation of One-Part Geopolymer Binders Made from Fly Ash. Waste and Biomass Valorization 8, 225–233. https://doi.org/10.1007/s12649-016-9582-5

Han, B., Ou, J., 2007. Embedded piezoresistive cement-based stress/strain sensor. Sensors Actuators, A Phys. 138, 294–298. https://doi.org/10.1016/j.sna.2007.05.011

Han, B., Guan, X., Ou, J., 2007. Electrode design, measuring method and data acquisition system of carbon fiber cement paste piezoresistive sensors. Sensors Actuators, A Phys. 135, 360–369. https://doi.org/10.1016/j.sna.2006.08.003

Han, B.G., Han, B.Z., Ou, J.P., 2009. Experimental study on use of nickel powder-filled Portland cement-based composite for fabrication of piezoresistive sensors with high sensitivity. Sensors Actuators, A Phys. 149, 51–55. https://doi.org/10.1016/j.sna.2008.10.001

Han, B., Yu, X., Ou, J., 2010a. Effect of water content on the piezoresistivity of MWNT/cement composites. J. Mater. Sci. 45, 3714–3719. https://doi.org/10.1007/s10853-010-4414-7

Han, B., Zhang, L., Ou, J., 2010b. Influence of water content on conductivity and piezoresistivity of cement-based material with both carbon fiber and carbon black. J. Wuhan Univ. Technol. Mater. Sci. Ed. 25, 147–151. https://doi.org/10.1007/s11595-010-1147-z

Han, B., Zhang, K., Yu, X., Kwon, E., Ou, J., 2012. Electrical characteristics and pressure-sensitive response measurements of carboxyl MWNT/cement composites. Cem. Concr. Compos. 34, 794–800. https://doi.org/10.1016/j.cemconcomp.2012.02.012

Han, B., Zhang, K., Burnham, T., Kwon, E., Yu, X., 2013. Integration and road tests of a self-sensing CNT concrete pavement system for traffic detection. Smart Mater. Struct. 22. https://doi.org/10.1088/0964-1726/22/1/015020

Han, B., Ding, S., Yu, X., 2015. Intrinsic self-sensing concrete and structures: A review. Meas. J. Int. Meas. Confed. 59, 110–128. https://doi.org/10.1016/j.measurement.2014.09.048

Han, B., Wang, Y., Ding, S., Yu, X., Zhang, L., Li, Z., Ou, J., 2017. Self-sensing cementitious composites incorporated with botryoid hybrid nano-carbon materials for smart infrastructures. J. Intell. Mater. Syst. Struct. 28, 699–727. https://doi.org/10.1177/1045389X16657416

Hanjitsuwan, S., Chindaprasirt, P., Pimraksa, K., 2011. Electrical conductivity and dielectric property of fly ash geopolymer pastes. Int. J. Miner. Metall. Mater. 18, 94–99. https://doi.org/10.1007/s12613-011-0406-0

Hanjitsuwan, S., Hunpratub, S., Thongbai, P., Maensiri, S., Sata, V., Chindaprasirt, P., 2014. Effects of NaOH concentrations on physical and electrical properties of high calcium fly ash geopolymer paste. Cem. Concr. Compos. 45, 9–14. https://doi.org/10.1016/j.cemconcomp.2013.09.012

Hansson, I.L.H., Hansson, C.M., 1985. Ion-conduction in cement-based materials. Cem. Concr. Res. 15, 201–212. https://doi.org/10.1016/0008-8846(85)90031-6

He, J., Zhang, G., Hou, S., Cai, C.S., 2011. Geopolymer-Based Smart Adhesives for Infrastructure Health Monitoring: Concept and Feasibility. J. Mater. Civ. Eng. 23, 100–109. https://doi.org/10.1061/(ASCE)MT.1943-5533.0000140

He, P., Wang, M., Fu, S., Jia, D., Yan, S., Yuan, J., Xu, J., Wang, P., Zhou, Y., 2016. Effects of Si/Al ratio on the structure and properties of metakaolin based geopolymer. Ceram. Int. 42, 14416–14422. https://doi.org/10.1016/j.ceramint.2016.06.033

Heras Murcia, D., Genedy, M., Reda Taha, M.M., 2020. Examining the significance of infill printing pattern on the anisotropy of 3D printed concrete. Constr. Build. Mater. 262, 120559. https://doi.org/10.1016/j.conbuildmat.2020.120559

Hong, Y., Li, Z., Qiao, G., Ou, J., Cheng, W., 2018. Pressure sensitivity of multiscale carbon-admixtures–enhanced cement-based composites. Nanomater. Nanotechnol. 8, 1–8. https://doi.org/10.1177/1847980418793529

Hossain, M.A., Zhumabekova, A., Paul, S.C., Kim, J.R., 2020. A review of 3D printing in construction and its impact on the labor market. Sustainability 12, 8492. https://doi.org/10.3390/su12208492

Huseien, G.F., Mirza, J., Ismail, M., Hussin, M.W., 2016. Influence of different curing temperatures and alkali activators on properties of GBFS geopolymer mortars

containing fly ash and palm-oil fuel ash. Constr. Build. Mater. 125, 1229–1240. https://doi.org/10.1016/j.conbuildmat.2016.08.153

Huseien, G.F., Shah, K.W., 2020. Durability and life cycle evaluation of self-compacting concrete containing fly ash as GBFS replacement with alkali activation. Constr. Build. Mater. 235, 117458. https://doi.org/10.1016/j.conbuildmat.2019.117458

Ismail, I., Bernal, S.A., Provis, J.L., San Nicolas, R., Hamdan, S., Van Deventer, J.S.J., 2014. Modification of phase evolution in alkali-activated blast furnace slag by the incorporation of fly ash. Cem. Concr. Compos. 45, 125–135. https://doi.org/10.1016/j.cemconcomp.2013.09.006

Jiao, Z., Wang, Y., Zheng, W., Huang, W., 2018. Effect of Dosage of Alkaline Activator on the Properties of Alkali-Activated Slag Pastes. Adv. Mater. Sci. Eng. 2018, 10–12. https://doi.org/10.1155/2018/8407380

Junaid, M.T., Kayali, O., Khennane, A., Black, J., 2015. A mix design procedure for low calcium alkali activated fly ash-based concretes. Constr. Build. Mater. 79, 301–310. https://doi.org/10.1016/j.conbuildmat.2015.01.048

Juricic, B.B., Galic, M., Marenjak, S., 2021. Review of the Construction Labour Demand and Shortages in the EU. Buildings 11, 17. https://doi.org/10.3390/buildings11010017

Kamseu, E., Beleuk à Moungam, L.M., Cannio, M., Billong, N., Chaysuwan, D., Melo, U.C., Leonelli, C., 2017. Substitution of sodium silicate with rice husk ash-NaOH solution in metakaolin based geopolymer cement concerning reduction in global warming. J. Clean. Prod. 142, 3050–3060. https://doi.org/10.1016/j.jclepro.2016.10.164

Kan, L. li, Lv, J. wei, Duan, B. bei, Wu, M., 2019. Self-healing of Engineered Geopolymer Composites prepared by fly ash and metakaolin. Cem. Concr. Res. 125, 105895. https://doi.org/10.1016/j.cemconres.2019.105895

Kastiukas, G., Ruan, S., Liang, S., Zhou, X., 2020. Development of precast geopolymer concrete via oven and microwave radiation curing with an environmental assessment. J. Clean. Prod. 255, 120290. https://doi.org/10.1016/j.jclepro.2020.120290

Kazemian, A., Yuan, X., Cochran, E., Khoshnevis, B., 2017. Cementitious materials for construction-scale 3D printing: Laboratory testing of fresh printing mixture. Constr. Build. Mater. 145, 639–647. https://doi.org/10.1016/j.conbuildmat.2017.04.015

Kenne Diffo, B.B., Elimbi, A., Cyr, M., Dika Manga, J., Tchakoute Kouamo, H., 2015. Effect of the rate of calcination of kaolin on the properties of metakaolin-based geopolymers. J. Asian Ceram. Soc. 3, 130–138. https://doi.org/10.1016/j.jascer.2014.12.003

Khan, M.N.N., Sarker, P.K., 2020. Effect of waste glass fine aggregate on the strength, durability and high temperature resistance of alkali-activated fly ash and GGBFS blended mortar. Constr. Build. Mater. 263, 120177. https://doi.org/10.1016/j.conbuildmat.2020.120177

Khater, H.M., Abd El Gawaad, H.A., 2016. Characterization of alkali activated geopolymer mortar doped with MWCNT. Constr. Build. Mater. 102, 329–337. https://doi.org/10.1016/j.conbuildmat.2015.10.121

Khan, M.N.N., Kuri, J.C., Sarker, P.K., 2021. Effect of waste glass powder as a partial precursor in ambient cured alkali activated fly ash and fly ash-GGBFS mortars. J. Build. Eng. 34, 101934. https://doi.org/10.1016/j.jobe.2020.101934

Khoshnevis, B., 2004. Automated construction by contour crafting - Related robotics and information technologies. Autom. Constr. 13, 5–19. https://doi.org/10.1016/j.autcon.2003.08.012

Kim, G.M., Yang, B.J., Cho, K.J., Kim, E.M., Lee, H.K., 2017. Influences of CNT dispersion and pore characteristics on the electrical performance of cementitious composites. Compos. Struct. 164, 32–42. https://doi.org/10.1016/j.compstruct.2016.12.049

Kobera, L., Slavík, R., Koloušek, D., Urbanová, M., Kotek, J., Brus, J., 2011. Structural stability of aluminosilicate inorganic polymers: Influence of the preparation procedure. Ceram. - Silikaty 55, 343–354.

Komljenović, M., Tanasijević, G., Džunuzović, N., Provis, J.L., 2020. Immobilization of cesium with alkali-activated blast furnace slag. J. Hazard. Mater. 388. https://doi.org/10.1016/j.jhazmat.2019.121765

Komnitsas, K., Zaharaki, D., Vlachou, A., Bartzas, G., Galetakis, M., 2015. Effect of synthesis parameters on the quality of construction and demolition wastes (CDW) geopolymers. Adv. Powder Technol. 26, 368–376. https://doi.org/10.1016/j.apt.2014.11.012

Kondepudi, K., Subramaniam, K.V.L., 2021. Formulation of alkali-activated fly ash-slag binders for 3D concrete printing. Cem. Concr. Compos. 119, 103983. https://doi.org/10.1016/j.cemconcomp.2021.103983

Kong, Q., Fan, S., Bai, X., Mo, Y.L., Song, G., 2017. A novel embeddable spherical smart aggregate for structural health monitoring: Part I. Fabrication and electrical characterization. Smart Mater. Struct. 26. https://doi.org/10.1088/1361-665X/aa80bc

Konsta-Gdoutos, M.S., Aza, C.A., 2014. Self sensing carbon nanotube (CNT) and nanofiber (CNF) cementitious composites for real time damage assessment in smart structures. Cem. Concr. Compos. 53, 162–169. https://doi.org/10.1016/j.cemconcomp.2014.07.003

Kosson, M., Brown, L., Sanchez, F., 2020. Early-Age Performance of 3D Printed Carbon Nanofiber and Carbon Microfiber Cement Composites. Transp. Res. Rec. 2674, 10–20. https://doi.org/10.1177/0361198120902704

Koutník, P., Soukup, A., Bezucha, P., Šafář, J., Kohout, J., 2020. Low viscosity metakaolinite based geopolymer binders. Constr. Build. Mater. 230. https://doi.org/10.1016/j.conbuildmat.2019.116978

Kramar, S., Šajna, A., Ducman, V., 2016. Assessment of alkali activated mortars based on different precursors with regard to their suitability for concrete repair. Constr. Build. Mater. 124, 937–944. https://doi.org/10.1016/j.conbuildmat.2016.08.018

Krivenko, P., 2017. Why alkaline activation - 60 years of the theory and practice of alkali-activated materials. J. Ceram. Sci. Technol. 8, 323–333. https://doi.org/10.4416/JCST2017-00042

Kruger, J., Cho, S., Zeranka, S., Viljoen, C., van Zijl, G., 2020. 3D concrete printer parameter optimisation for high rate digital construction avoiding plastic collapse. Compos. Part B Eng. 183. https://doi.org/10.1016/j.compositesb.2019.107660

Kubba, Z., Fahim Huseien, G., Sam, A.R.M., Shah, K.W., Asaad, M.A., Ismail, M., Tahir, M.M., Mirza, J., 2018. Impact of curing temperatures and alkaline activators on compressive strength and porosity of ternary blended geopolymer mortars. Case Stud. Constr. Mater. 9, e00205. https://doi.org/10.1016/j.cscm.2018.e00205

Kuenzel, C., Vandeperre, L.J., Donatello, S., Boccaccini, A.R., Cheeseman, C., 2012. Ambient temperature drying shrinkage and cracking in metakaolin-based geopolymers. J. Am. Ceram. Soc. 95, 3270–3277. https://doi.org/10.1111/j.1551-2916.2012.05380.x

Kuenzel, C., Li, L., Vandeperre, L., Boccaccini, A.R., Cheeseman, C.R., 2014. Influence of sand on the mechanical properties of metakaolin geopolymers. Constr. Build. Mater. 66, 442–446. https://doi.org/10.1016/j.conbuildmat.2014.05.058

Kultayeva, S., Ha, J.H., Malik, R., Kim, Y.W., Kim, K.J., 2020. Effects of porosity on electrical and thermal conductivities of porous SiC ceramics. J. Eur. Ceram. Soc. 40, 996–1004. https://doi.org/10.1016/j.jeurceramsoc.2019.11.045

Kusak, I., Lunak, M., 2017. On the effect of addition of carbon nanotubes on the electric conductivity of alkali-activated slag mortars. IOP Conf. Ser. Mater. Sci. Eng. 246, 012044. https://doi.org/10.1088/1757-899X/246/1/012044

Labonnote, N., Rønnquist, A., Manum, B., Rüther, P., 2016. Additive construction: State-of-the-art, challenges and opportunities. Autom. Constr. 72, 347–366. https://doi.org/10.1016/j.autcon.2016.08.026

Lahoti, M., Narang, P., Tan, K.H., Yang, E.H., 2017. Mix design factors and strength prediction of metakaolin-based geopolymer. Ceram. Int. 43, 11433–11441. https://doi.org/10.1016/j.ceramint.2017.06.006

Lamuta, C., Candamano, S., Crea, F., Pagnotta, L., 2016. Direct piezoelectric effect in geopolymeric mortars. Mater. Des. 107, 57–64. https://doi.org/10.1016/j.matdes.2016.05.108

Lamuta, C., Bruno, L., Candamano, S., Pagnotta, L., 2017. Piezoresistive characterization of graphene/metakaolin based geopolymeric mortar composites. MRS Adv. 2, 3773–3779. https://doi.org/10.1557/adv.2017.595

Lasia, A., 2014. Electrochemical Impedance Spectroscopy and its Applications. Springer.

https://doi.org/10.1007/978-1-4614-8933-7

Le, T.T., Austin, S.A., Lim, S., Buswell, R.A., Gibb, A.G.F., Thorpe, T., 2012a. Mix design and fresh properties for high-performance printing concrete. Mater. Struct. Constr. 45, 1221–1232. https://doi.org/10.1617/s11527-012-9828-z

Le, T.T., Austin, S.A., Lim, S., Buswell, R.A., Law, R., Gibb, A.G.F., Thorpe, T., 2012b. Hardened properties of high-performance printing concrete. Cem. Concr. Res. 42, 558–566. https://doi.org/10.1016/j.cemconres.2011.12.003

Lee, S.Y., Le, H.V., Kim, D.J., 2019. Self-stress sensing smart concrete containing fine steel slag aggregates and steel fibers under high compressive stress. Constr. Build. Mater. 220, 149–160. https://doi.org/10.1016/j.conbuildmat.2019.05.197

Leech D.J., Guy, W., Klein, S., 2020. The polychromatic woodburytype—colour tracking in translucent, patterned gelatin/pigment films. Molecules 25. https://doi.org/10.3390/molecules25112468

Li, H., Xiao, H., Ou, J., 2006. Effect of compressive strain on electrical resistivity of carbon black-filled cement-based composites. Cem. Concr. Compos. 28, 824–828. https://doi.org/10.1016/j.cemconcomp.2006.05.004

Li, J., Wee, B., Tay, Y., Lei, J., Yang, E., 2021. Experimental investigation of Seebeck effect in metakaolin-based geopolymer. Constr. Build. Mater. 272, 121615. https://doi.org/10.1016/j.conbuildmat.2020.121615

Li, X., Li, M., 2019. Multifunctional self-sensing and ductile cementitious materials. Cem. Concr. Res. 123, 105714. https://doi.org/10.1016/j.cemconres.2019.03.008

Li, X., Rao, F., Song, S., Corona-Arroyo, M.A., Ortiz-Lara, N., Aguilar-Reyes, E.A., 2018. Effects of aggregates on the mechanical properties and microstructure of geothermal metakaolin-based geopolymers. Results Phys. 11, 267–273. https://doi.org/10.1016/j.rinp.2018.09.018

Li, Z., Hojati, M., Wu, Z., Piasente, J., Ashrafi, N., Duarte, J.P., Nazarian, S., Bilen, S.G., Memari, A.M., Radlinska, A., 2020. Fresh and Hardened Properties of Extrusion-Based 3D-Printed Cementitious Materials: A Review. Sustainability 12, 1–33. https://doi.org/10.3390/su12145628

Liang, K., Zeng, X., Zhou, X., Qu, F., Wang, P., 2017. A new model for the electrical conductivity of cement-based material by considering pore size distribution. Mag. Concr. Res. 69, 1067–1078. https://doi.org/10.1680/jmacr.16.00535

Liew, Y.M., Heah, C.Y., Li, L. yuan, Jaya, N.A., Abdullah, M.M.A.B., Tan, S.J., Hussin, K., 2017. Formation of one-part-mixing geopolymers and geopolymer ceramics from geopolymer powder. Constr. Build. Mater. 156, 9–18. https://doi.org/10.1016/j.conbuildmat.2017.08.110

Lim, S., Buswell, R.A., Le, T.T., Austin, S.A., Gibb, A.G.F., Thorpe, T., 2012. Developments in construction-scale additive manufacturing processes. Autom. Constr. 21, 262–268. https://doi.org/10.1016/j.autcon.2011.06.010

Lim, S., Buswell, R.A., Valentine, P.J., Piker, D., Austin, S.A., De Kestelier, X., 2016. Modelling curved-layered printing paths for fabricating large-scale construction components. Addit. Manuf. 12, 216–230. https://doi.org/10.1016/j.addma.2016.06.004

Liu, J., Li, X., Lu, Y., Bai, X., 2020. Effects of Na/Al ratio on mechanical properties and microstructure of red mud-coal metakaolin geopolymer. Constr. Build. Mater. 263, 120653. https://doi.org/10.1016/j.conbuildmat.2020.120653

Liu, K., Cheng, X., Li, J., Gao, X., Cao, Y., Guo, X., Zhuang, J., Zhang, C., 2019. Effects of microstructure and pore water on electrical conductivity of cement slurry during early hydration. Compos. Part B Eng. 177, 107435. https://doi.org/10.1016/j.compositesb.2019.107435

Liu, Q., Gao, R., Tam, V.W.Y., Li, W., Xiao, J., 2018. Strain monitoring for a bending concrete beam by using piezoresistive cement-based sensors. Constr. Build. Mater. 167, 338–347. https://doi.org/10.1016/j.conbuildmat.2018.02.048

Lloyd, R.R., 2009. Accelerated ageing of geopolymers, in: Provis, J.L., van Deventer, J.S.J. (Eds.), Geopolymers Structure, Processing, Properties and Industrial Applications. Woodhead Publishing Limited, pp. 139–166.

Lo Monte, F., Felicetti, R., Miah, M.J., 2019. The influence of pore pressure on fracture behaviour of Normal-Strength and High-Performance Concretes at high temperature. Cem. Concr. Compos. 104, 103388. https://doi.org/10.1016/j.cemconcomp.2019.103388

Long, W.J., Tao, J.L., Lin, C., Gu, Y. cun, Mei, L., Duan, H.B., Xing, F., 2019. Rheology and buildability of sustainable cement-based composites containing micro-crystalline cellulose for 3D-printing. J. Clean. Prod. 239. https://doi.org/10.1016/j.jclepro.2019.118054

Luan, C., Shi, X., Zhang, K., Utashev, N., Yang, F., Dai, J., Wang, Q., 2020. A mix design method of fly ash geopolymer concrete based on factors analysis. Constr. Build. Mater. 121612. https://doi.org/10.1016/j.conbuildmat.2020.121612

Ma, G., Li, Z., Wang, L., 2018. Printable properties of cementitious material containing copper tailings for extrusion based 3D printing. Constr. Build. Mater. 162, 613–627. https://doi.org/10.1016/j.conbuildmat.2017.12.051

Ma, G., Salman, N.M., Wang, L., Wang, F., 2020. A novel additive mortar leveraging internal curing for enhancing interlayer bonding of cementitious composite for 3D printing. Constr. Build. Mater. 244, 118305. https://doi.org/10.1016/j.conbuildmat.2020.118305

Ma, X., Zhang, Z., Wang, A., 2016. The transition of fly ash-based geopolymer gels into ordered structures and the effect on the compressive strength. Constr. Build. Mater. 104, 25–33. https://doi.org/10.1016/j.conbuildmat.2015.12.049

Ma, Y., Liu, W., Hu, J., Fu, J., Zhang, Z., Wang, H., 2020. Optimization on the piezoresistivity of alkali-activated fly ash/slag mortar by using conductive aggregates

and carbon fibers. Cem. Concr. Compos. 114, 103735. https://doi.org/10.1016/j.cemconcomp.2020.103735

Mabroum, S., Moukannaa, S., El Machi, A., Taha, Y., Benzaazoua, M., Hakkou, R., 2020. Mine wastes based geopolymers: A critical review. Clean. Eng. Technol. 1, 100014. https://doi.org/10.1016/j.clet.2020.100014

Machiels, L., Arnout, L., Jones, P.T., Blanpain, B., Pontikes, Y., 2014. Inorganic polymer cement from fe-silicate glasses: Varying the activating solution to glass ratio. Waste and Biomass Valorization 5, 411–428. https://doi.org/10.1007/s12649-014-9296-5

MacKenzie, K.J.D., Bolton, M.J., 2009. Electrical and mechanical properties of aluminosilicate inorganic polymer composites with carbon nanotubes. J. Mater. Sci. 44, 2851–2857. https://doi.org/10.1007/s10853-009-3377-z

Mahmoodi, O., Siad, H., Lachemi, M., Dadsetan, S., Sahmaran, M., 2020. Optimization of brick waste-based geopolymer binders at ambient temperature and pre-targeted chemical parameters. J. Clean. Prod. 268, 122285. https://doi.org/10.1016/j.jclepro.2020.122285

Manuel, J., Delgado, D., Oyedele, L., Ajayi, A., Akanbi, L., Akinade, O., Bilal, M., Owolabi, H., 2019. Robotics and automated systems in construction : Understanding industry- specific challenges for adoption. J. Build. Eng. 26, 100868. https://doi.org/10.1016/j.jobe.2019.100868

Marchment, T., Sanjayan, J., 2020. Mesh reinforcing method for 3D Concrete Printing. Autom. Constr. 109. https://doi.org/10.1016/j.autcon.2019.102992

Marchment, T., Sanjayan, J., Xia, M., 2019. Method of enhancing interlayer bond strength in construction scale 3D printing with mortar by effective bond area amplification. Mater. Des. 169, 107684. https://doi.org/10.1016/j.matdes.2019.107684

Materazzi, A.L., Ubertini, F., D'Alessandro, A., 2013. Carbon nanotube cement-based transducers for dynamic sensing of strain. Cem. Concr. Compos. 37, 2–11. https://doi.org/10.1016/j.cemconcomp.2012.12.013

McAlorum, J., Perry, M., Vlachakis, C., Biondi, L., Lavoie, B., 2021a. Robotic spray coating of self-sensing metakaolin geopolymer for concrete monitoring. Autom. Constr. 121, 103415. https://doi.org/10.1016/j.autcon.2020.103415

McAlorum, J., Vlachakis, C., Perry, M., 2021b. A low-cost electrical impedance analyser for interrogating self-sensing cement repairs, in: IEEE International Instrumentation and Measurement Technology Conference. IEEE, Glasgow, pp. 1–6.

McCarter, W.J., Brousseau, R., 1990. The A.C. response of hardened cement paste. Cem. Concr. Res. 20, 891–900. https://doi.org/10.1016/0008-8846(90)90051-X

Mechtcherine, V., Nerella, V.N., Will, F., Näther, M., Otto, J., Krause, M., 2019. Large-scale digital concrete construction – CONPrint3D concept for on-site, monolithic 3D-printing. Autom. Constr. 107. https://doi.org/10.1016/j.autcon.2019.102933

Mendes, B.C., Pedroti, L.G., Vieira, C.M.F., Marvila, M., Azevedo, A.R.G., de Carvalho,

J.M.F., Ribeiro, J.C.L., 2021. Application of eco-friendly alternative activators in alkali-activated materials: A review. J. Build. Eng. 35, 102010. https://doi.org/10.1016/j.jobe.2020.102010

Mendoza Reales, O.A., Duda, P., Silva, E.C.C.M., Paiva, M.D.M., Filho, R.D.T., 2019. Nanosilica particles as structural buildup agents for 3D printing with Portland cement pastes. Constr. Build. Mater. 219, 91–100. https://doi.org/10.1016/j.conbuildmat.2019.05.174

Meoni, A., D'Alessandro, A., Ubertini, F., 2020. Characterization of the strain-sensing behavior of smart bricks: A new theoretical model and its application for monitoring of masonry structural elements. Constr. Build. Mater. 250, 118907. https://doi.org/10.1016/j.conbuildmat.2020.118907

Mo, B.H., Zhu, H., Cui, X.M., He, Y., Gong, S.Y., 2014. Effect of curing temperature on geopolymerization of metakaolin-based geopolymers. Appl. Clay Sci. 99, 144–148. https://doi.org/10.1016/j.clay.2014.06.024

Mobasher, N., Bernal, S.A., Provis, J.L., 2016. Structural evolution of an alkali sulfate activated slag cement. J. Nucl. Mater. 468, 97–104. https://doi.org/10.1016/j.jnucmat.2015.11.016

Moeini, M.A., Hosseinpoor, M., Yahia, A., 2020. Effectiveness of the rheometric methods to evaluate the build-up of cementitious mortars used for 3D printing. Constr. Build. Mater. 257, 119551. https://doi.org/10.1016/j.conbuildmat.2020.119551

Mohammad, M., Masad, E., Al-Ghamdi, S.G., 2020. 3D Concrete Printing Sustainability: A Comparative Life Cycle Assessment of Four Construction Method Scenarios. Buildings 10, 245. https://doi.org/10.3390/buildings10120245

Mohseni, E., 2018. Assessment of Na2SiO3 to NaOH ratio impact on the performance of polypropylene fiber-reinforced geopolymer composites. Constr. Build. Mater. 186, 904–911. https://doi.org/10.1016/j.conbuildmat.2018.08.032

Moodi, F., Ramezanianpour, A.A., Safavizadeh, A.S., 2011. Evaluation of the optimal process of thermal activation of kaolins. Sci. Iran. 18, 906–912. https://doi.org/10.1016/j.scient.2011.07.011

Morgan, D.R., 1996. Compatibility of concrete repair materials and systems. Constr. Build. Mater. 10, 57–67. https://doi.org/10.1016/0950-0618(95)00060-7

Muthukrishnan, S., Ramakrishnan, S., Sanjayan, J., 2021. Effect of alkali reactions on the rheology of one-part 3D printable geopolymer concrete. Cem. Concr. Compos. 116, 103899. https://doi.org/10.1016/j.cemconcomp.2020.103899

Muthukrishnan, S., Ramakrishnan, S., Sanjayan, J., 2020. Effect of microwave heating on interlayer bonding and buildability of geopolymer 3D concrete printing. Constr. Build. Mater. 265, 120786. https://doi.org/10.1016/j.conbuildmat.2020.120786

Nair, S.A.O., Alghamdi, H., Arora, A., Mehdipour, I., Sant, G., Neithalath, N., 2019. Linking fresh paste microstructure, rheology and extrusion characteristics of

cementitious binders for 3D printing. J. Am. Ceram. Soc. 102, 3951–3964. https://doi.org/10.1111/jace.16305

Nedeljkovic, M., Li, Z., Ye, G., 2018. Setting, Strength, and Autogenous Shrinkage of Alkali-Activated Fly Ash and Slag Pastes: Effect of Slag Content. Materials (Basel). 11, 2121. https://doi.org/10.3390/ma11112121

Nematollahi, B., Sanjayan, J., Shaikh, F.U.A., 2015. Synthesis of heat and ambient cured one-part geopolymer mixes with different grades of sodium silicate. Ceram. Int. 41, 5696–5704. https://doi.org/10.1016/j.ceramint.2014.12.154

Nematollahi, B., Vijay, P., Sanjayan, J., Nazari, A., Xia, M., Nerella, V.N., Mechtcherine, V., 2018. Effect of polypropylene fibre addition on properties of geopolymers made by 3D printing for digital construction. Materials (Basel). 11. https://doi.org/10.3390/ma11122352

Nerella, V. N., Hempel, S., Mechtcherine, V., 2019. Effects of layer-interface properties on mechanical performance of concrete elements produced by extrusion-based 3D-printing. Constr. Build. Mater. 104, 261–270. https://doi.org/10.1016/j.matdes.2019.107651

Nerella, V.N., Näther, M., Iqbal, A., Butler, M., Mechtcherine, V., 2019. Inline quantification of extrudability of cementitious materials for digital construction. Cem. Concr. Compos. 95, 260–270. https://doi.org/10.1016/j.cemconcomp.2018.09.015

Nerella, V.N., Krause, M., Mechtcherine, V., 2020. Direct printing test for buildability of 3D-printable concrete considering economic viability. Autom. Constr. 109, 102986. https://doi.org/10.1016/j.autcon.2019.102986

Nguyen, A.Q., Klysz, G., Deby, F., Balayssac, J.P., 2017. Evaluation of water content gradient using a new configuration of linear array four-point probe for electrical resistivity measurement. Cem. Concr. Compos. 83, 308–322. https://doi.org/10.1016/j.cemconcomp.2017.07.020

Nuaklong, P., Jongvivatsakul, P., Pothisiri, T., Sata, V., Chindaprasirt, P., 2020. Influence of rice husk ash on mechanical properties and fire resistance of recycled aggregate high-calcium fly ash geopolymer concrete. J. Clean. Prod. 252, 119797. https://doi.org/10.1016/j.jclepro.2019.119797

Nunes, V.A., Borges, P.H.R., Zanotti, C., 2019. Mechanical compatibility and adhesion between alkali-activated repair mortars and Portland cement concrete substrate. Constr. Build. Mater. 215, 569–581. https://doi.org/10.1016/j.conbuildmat.2019.04.189

Ozer, I., Soyer-Uzun, S., 2015. Relations between the structural characteristics and compressive strength in metakaolin based geopolymers with different molar Si/Al ratios. Ceram. Int. 41, 10192–10198. https://doi.org/10.1016/j.ceramint.2015.04.125

Pacheco-Torgal, F., Castro-Gomes, J.P., Jalali, S., 2008. Adhesion characterization of tungsten mine waste geopolymeric binder. Influence of OPC concrete substrate surface treatment. Constr. Build. Mater. 22, 154–161.

https://doi.org/10.1016/j.conbuildmat.2006.10.005

Pacheco-Torgal, F., Moura, D., Ding, Y., Jalali, S., 2011. Composition, strength and workability of alkali-activated metakaolin based mortars. Constr. Build. Mater. 25, 3732–3745. https://doi.org/10.1016/j.conbuildmat.2011.04.017

Padma Kumar, P., Yashonath, S., 2006. Ionic Conduction in the Solid State. ChemInform 37, 135–154. https://doi.org/10.1002/chin.200624229

Palmero, P., Formia, A., Antonaci, P., Brini, S., Tulliani, J.M., 2015. Geopolymer technology for application-oriented dense and lightened materials. Elaboration and characterization. Ceram. Int. 41, 12967–12979. https://doi.org/10.1016/j.ceramint.2015.06.140

Panda, B., Chandra Paul, S., Jen Tan, M., 2017a. Anisotropic mechanical performance of 3D printed fiber reinforced sustainable construction material. Mater. Lett. 209, 146–149. https://doi.org/10.1016/j.matlet.2017.07.123

Panda, B., Paul, S.C., Hui, L.J., Tay, Y.W.D., Tan, M.J., 2017b. Additive manufacturing of geopolymer for sustainable built environment. J. Clean. Prod. 167, 281–288. https://doi.org/10.1016/j.jclepro.2017.08.165

Panda, B., Tan, M.J., 2018. Experimental study on mix proportion and fresh properties of fly ash based geopolymer for 3D concrete printing. Ceram. Int. 44, 10258–10265. https://doi.org/10.1016/j.ceramint.2018.03.031

Panda, B., Paul, S.C., Mohamed, N.A.N., Tay, Y.W.D., Tan, M.J., 2018. Measurement of tensile bond strength of 3D printed geopolymer mortar. Meas. J. Int. Meas. Confed. 113, 108–116. https://doi.org/10.1016/j.measurement.2017.08.051

Panda, B., Tan, M.J., 2019. Rheological behavior of high volume fly ash mixtures containing micro silica for digital construction application. Mater. Lett. 237, 348–351. https://doi.org/10.1016/j.matlet.2018.11.131

Panda, B., Mohamed, N.A.N., Paul, S.C., Singh, G.V.P.B., Tan, M.J., Šavija, B., 2019a. The effect of material fresh properties and process parameters on buildability and interlayer adhesion of 3D printed concrete. Materials (Basel). 12. https://doi.org/10.3390/ma12132149

Panda, B., Ruan, S., Unluer, C., Tan, M.J., 2019b. Improving the 3D printability of high volume fly ash mixtures via the use of nano attapulgite clay. Compos. Part B Eng. 165, 75–83. https://doi.org/10.1016/j.compositesb.2018.11.109

Panda, B., Singh, G.B., Unluer, C., Tan, M.J., 2019c. Synthesis and characterization of one-part geopolymers for extrusion based 3D concrete printing. J. Clean. Prod. 220, 610–619. https://doi.org/10.1016/j.jclepro.2019.02.185

Panda, B., Unluer, C., Tan, M.J., 2019d. Extrusion and rheology characterization of geopolymer nanocomposites used in 3D printing. Compos. Part B Eng. 176. https://doi.org/10.1016/j.compositesb.2019.107290

Panda, B., Ruan, S., Unluer, C., Jen, M., 2020. Investigation of the properties of alkali-

activated slag mixes involving the use of nanoclay and nucleation seeds for 3D printing. Compos. Part B 186, 107826. https://doi.org/10.1016/j.compositesb.2020.107826

Park, S., Park, H.M., Yoon, H.N., Seo, J., Yang, C.-M., Provis, J.L., Yang, B., 2020. Hydration kinetics and products of MgO-activated blast furnace slag. Constr. Build. Mater. 249, 118700. https://doi.org/10.1016/j.conbuildmat.2020.118700

Paul, S.C., Tay, Y.W.D., Panda, B., Tan, M.J., 2018. Fresh and hardened properties of 3D printable cementitious materials for building and construction. Arch. Civ. Mech. Eng. 18, 311–319. https://doi.org/10.1016/j.acme.2017.02.008

Payakaniti, P., Pinitsoontorn, S., Thongbai, P., Amornkitbamrung, V., 2017. Electrical conductivity and compressive strength of carbon fiber reinforced fly ash geopolymeric composites. Constr. Build. Mater. 135, 164–176. https://doi.org/10.1016/j.conbuildmat.2016.12.198

Peng, L., Chan, A.H.S., 2020. Adjusting work conditions to meet the declined health and functional capacity of older construction workers in Hong Kong. Saf. Sci. 127, 104711. https://doi.org/10.1016/j.ssci.2020.104711

Perrot, A., Pierre, A., Vitaloni, S., Picandet, V., 2015. Prediction of lateral form pressure exerted by concrete at low casting rates. Mater. Struct. Constr. 48, 2315–2322. https://doi.org/10.1617/s11527-014-0313-8

Perrot, A., Rangeard, D., Pierre, A., 2016. Structural built-up of cement-based materials used for 3D-printing extrusion techniques. Mater. Struct. Constr. 49, 1213–1220. https://doi.org/10.1617/s11527-015-0571-0

Perry, M., Saafi, M., Fusiek, G., Niewczas, P., 2015. Hybrid optical-fibre/geopolymer sensors for structural health monitoring of concrete structures. Smart Mater. Struct. 24, 045011. https://doi.org/10.1088/0964-1726/24/4/045011

Perry, M., Saafi, M., Fusiek, G., Niewczas, P., 2016. Geopolymeric thermal conductivity sensors for surface-mounting onto concrete structures, in: Environment, Efficiency and Economic Challenges for Concrete. University of Dundee.

Peys, A., White, C.E., Olds, D., Rahier, H., Blanpain, B., Pontikes, Y., 2018. Molecular structure of CaO–FeOx–SiO2 glassy slags and resultant inorganic polymer binders. J. Am. Ceram. Soc. 101, 5846–5857. https://doi.org/10.1111/jace.15880

Peys, A., Douvalis, A.P., Hallet, V., Rahier, H., Blanpain, B., Pontikes, Y., 2019. Inorganic Polymers From CaO-FeOx-SiO2 Slag: The Start of Oxidation of Fe and the Formation of a Mixed Valence Binder. Front. Mater. 6, 1–10. https://doi.org/10.3389/fmats.2019.00212

Pouhet, R., Cyr, M., 2016. Formulation and performance of flash metakaolin geopolymer concretes. Constr. Build. Mater. 120, 150–160. https://doi.org/10.1016/j.conbuildmat.2016.05.061

Pouhet, R., Cyr, M., Bucher, R., 2019. Influence of the initial water content in flash

calcined metakaolin-based geopolymer. Constr. Build. Mater. 201, 421–429. https://doi.org/10.1016/j.conbuildmat.2018.12.201

Pour-Ghaz, M., Isgor, O.B., Ghods, P., 2009. The effect of temperature on the corrosion of steel in concrete. Part 1: Simulated polarization resistance tests and model development. Corros. Sci. 51, 415–425. https://doi.org/10.1016/j.corsci.2008.10.034

Prałat, K., Ciemnicka, J., Koper, A., Buczkowska, K.E., Łoś, P., 2021. Comparison of the thermal properties of geopolymer and modified gypsum. Polymers (Basel). 13, 1–18. https://doi.org/10.3390/polym13081220

Provis, J.L., Duxson, P., van Deventer, J.S.J., Lukey, G.C., 2005a. The role of mathematical modelling and gel chemistry in advancing geopolymer technology. Chem. Eng. Res. Des. 83, 853–860. https://doi.org/10.1205/cherd.04329

Provis, J.L., Duxson, P., Lukey, G.C., Van Deventer, J.S.J., 2005b. Statistical thermodynamic model for Si/Al ordering in amorphous aluminosilicates. Chem. Mater. 17, 2976–2986. https://doi.org/10.1021/cm050219i

Provis, J.L., Lukey, G.C., Van Deventer, J.S.J., 2005c. Do geopolymers actually contain nanocrystalline zeolites? a reexamination of existing results. Chem. Mater. 17, 3075–3085. https://doi.org/10.1021/cm050230i

Provis, J.L., van Deventer, J.S.J., 2007a. Geopolymerisation kinetics. 1. In situ energy-dispersive X-ray diffractometry. Chem. Eng. Sci. 62, 2309–2317. https://doi.org/10.1016/j.ces.2007.01.027

Provis, J.L., van Deventer, J.S.J., 2007b. Geopolymerisation kinetics. 2. Reaction kinetic modelling. Chem. Eng. Sci. 62, 2318–2329. https://doi.org/10.1016/j.ces.2007.01.028

Provis, J.L., Walls, P.A., van Deventer, J.S.J., 2008. Geopolymerisation kinetics. 3. Effects of Cs and Sr salts. Chem. Eng. Sci. 63, 4480–4489. https://doi.org/10.1016/j.ces.2008.06.008

Provis, J.L., 2009. Activating solution chemistry for geopolymers. In: Geopolymers: Structure, processing, properties and industrial applications. Woodhead, Cambridge.

Provis, J.L., Duxson, P., van Deventer, J.S.J., 2010. The role of particle technology in developing sustainable construction materials. Adv. Powder Technol. 21, 2–7. https://doi.org/10.1016/j.apt.2009.10.006

Provis, J.L., 2014a. Geopolymers and other alkali activated materials: Why, how, and what? Mater. Struct. Constr. 47, 11–25. https://doi.org/10.1617/s11527-013-0211-5

Provis, J.L., 2014b. Introduction and Scope, in: Provis, J.L., van Deventer, J.S.J. (Eds.), Alkali Activated Materials State-of-the-Art Report, RILEM TC 224-AAM. RILEM, pp. 1–10. https://doi.org/10.1007/978-94-007-7672-2

Provis, J.L., Bernal, S.A., 2014. Geopolymers and Related Alkali-Activated Materials. Annu. Rev. Mater. Res. 44, 299–327. https://doi.org/10.1146/annurev-matsci-070813-113515

Provis, J.L., Palomo, A., Shi, C., 2015. Advances in understanding alkali-activated materials. Cem. Concr. Res. 78, 110–125. https://doi.org/10.1016/j.cemconres.2015.04.013

Provis, J.L., 2018. Alkali-activated materials. Cem. Concr. Res. 114, 40–48. https://doi.org/10.1016/j.cemconres.2017.02.009

Provis, J.L., Arbi, K., Bernal, S.A., Bondar, D., Buchwald, A., Castel, A., Chithiraputhiran, S., Cyr, M., Dehghan, A., Dombrowski-Daube, K., Dubey, A., Ducman, V., Gluth, G.J.G., Nanukuttan, S., Peterson, K., Puertas, F., van Riessen, A., Torres-Carrasco, M., Ye, G., Zuo, Y., 2019. RILEM TC 247-DTA round robin test: mix design and reproducibility of compressive strength of alkali-activated concretes. Mater. Struct. Constr. 52, 1–13. https://doi.org/10.1617/s11527-019-1396-z

Rahul, A. V., Santhanam, M., Meena, H., Ghani, Z., 2019. 3D printable concrete: Mixture design and test methods. Cem. Concr. Compos. 97, 13–23. https://doi.org/10.1016/j.cemconcomp.2018.12.014

Ranjbar, N., Mehrali, M., Behnia, A., Alengaram, U.J., Jumaat, M.Z., 2014. Compressive strength and microstructural analysis of fly ash/palm oil fuel ash based geopolymer mortar. Mater. Des. 59, 532–539. https://doi.org/10.1016/j.matdes.2014.03.037

Rashad, A.M., 2013. Metakaolin as cementitious material: History, scours, production and composition-A comprehensive overview. Constr. Build. Mater. 41, 303–318. https://doi.org/10.1016/j.conbuildmat.2012.12.001

Ravikumar, D., Neithalath, N., 2013. An electrical impedance investigation into the chloride ion transport resistance of alkali silicate powder activated slag concretes. Cem. Concr. Compos. 44, 58–68. https://doi.org/10.1016/j.cemconcomp.2013.06.002

Riahi, S., Nemati, A., Khodabandeh, A.R., Baghshahi, S., 2020. The effect of mixing molar ratios and sand particles on microstructure and mechanical properties of metakaolin-based geopolymers. Mater. Chem. Phys. 240, 122223. https://doi.org/10.1016/j.matchemphys.2019.122223

Robayo, R.A., Mulford, A., Munera, J., Mejía de Gutiérrez, R., 2016. Alternative cements based on alkali-activated red clay brick waste. Constr. Build. Mater. 128, 163–169. https://doi.org/10.1016/j.conbuildmat.2016.10.023

Rocha, T. da S., Dias, D.P., França, F.C.C., Guerra, R.R. de S., Marques, L.R. da C. de O., 2018. Metakaolin-based geopolymer mortars with different alkaline activators (Na+ and K+). Constr. Build. Mater. 178, 453–461. https://doi.org/10.1016/j.conbuildmat.2018.05.172

Romagnoli, M., Leonelli, C., Kamse, E., Lassinantti Gualtieri, M., 2012. Rheology of geopolymer by DOE approach. Constr. Build. Mater. 36, 251–258. https://doi.org/10.1016/j.conbuildmat.2012.04.122

Roussel, N., 2018. Rheological requirements for printable concretes. Cem. Concr. Res. 112, 76–85. https://doi.org/10.1016/j.cemconres.2018.04.005

Rovnaník, P., 2010. Effect of curing temperature on the development of hard structure of metakaolin-based geopolymer. Constr. Build. Mater. 24, 1176–1183. https://doi.org/10.1016/j.conbuildmat.2009.12.023

Rovnaník, P., Míková, M., Kusák, I., 2017a. Electrical properties of alkali-activated slag mortar with carbon fibres. Mater. Sci. Forum 908 MSF, 100–105. https://doi.org/10.4028/www.scientific.net/MSF.908.100

Rovnaník, P., Šimonová, H., Topolář, L., Keršner, Z., 2017b. Mechanical Fracture Properties of Alkali-Activated Slag with Graphite Filler. Procedia Eng. 190, 43–48. https://doi.org/10.1016/j.proeng.2017.05.305

Rovnaník, P., Kusák, I., Bayer, P., Schmid, P., Fiala, L., 2019a. Electrical and self-sensing properties of alkali-activated slag composite with graphite filler. Materials (Basel). 12, 1–16. https://doi.org/10.3390/ma12101616

Rovnaník, P., Mizerová, C., Kusák, I., Schmid, P., 2019b. Self-sensing properties of alkali-activated slag composite with carbon black during bending test. Solid State Phenom. 296 SSP, 167–172. https://doi.org/10.4028/www.scientific.net/SSP.296.167

Rovnaník, P., Kusák, I., Bayer, P., Schmid, P., Fiala, L., 2019c. Comparison of electrical and self-sensing properties of Portland cement and alkali-activated slag mortars. Cem. Concr. Res. 118, 84–91. https://doi.org/10.1016/j.cemconres.2019.02.009

Saafi, M., Andrew, K., Tang, P.L., McGhon, D., Taylor, S., Rahman, M., Yang, S., Zhou, X., 2013. Multifunctional properties of carbon nanotube/fly ash geopolymeric nanocomposites. Constr. Build. Mater. 49, 46–55. https://doi.org/10.1016/j.conbuildmat.2013.08.007

Saafi, M., Tang, L., Fung, J., Rahman, M., Sillars, F., Liggat, J., Zhou, X., 2014. Graphene/fly ash geopolymeric composites as self-sensing structural materials. Smart Mater. Struct. 23, 065006. https://doi.org/10.1088/0964-1726/23/6/065006

Saafi, M., Tang, L., Fung, J., Rahman, M., Liggat, J., 2015. Enhanced properties of graphene/fly ash geopolymeric composite cement. Cem. Concr. Res. 67, 292–299. https://doi.org/10.1016/j.cemconres.2014.08.011

Saafi, M., Piukovics, G., Ye, J., 2016. Hybrid graphene/geopolymeric cement as a superionic conductor for structural health monitoring applications. Smart Mater. Struct. 25. https://doi.org/10.1088/0964-1726/25/10/105018

Saafi, M., Gullane, A., Huang, B., Sadeghi, H., Ye, J., Sadeghi, F., 2018. Inherently multifunctional geopolymeric cementitious composite as electrical energy storage and self-sensing structural material. Compos. Struct. 201, 766–778. https://doi.org/10.1016/j.compstruct.2018.06.101

Saldarriaga, D.L.C., Montoya, J.A., Tejada, V.M., 2021. Toward Structural Health Monitoring of Civil Structures Based on Self-Sensing Concrete Nanocomposites : A Validation in a Reinforced-Concrete Beam. Int. J. Concr. Struct. Mater. 15. https://doi.org/10.1186/s40069-020-00451-8

Saleem, M., Shameem, M., Hussain, S.E., Maslehuddin, M., 1996. Effect of moisture, chloride and sulphate contamination on the electrical resistivity of Portland cement concrete. Constr. Build. Mater. 10, 209–214. https://doi.org/10.1016/0950-0618(95)00078-X

Salem, T.M., Ragai, S.M., 2001. Electrical conductivity of granulated slag cement kiln dust-silica fume pastes at different porosities. Cem. Concr. Res. 31, 781–787. https://doi.org/10.1016/S0008-8846(01)00461-6

Salet, T.A.M., Ahmed, Z.Y., Bos, F.P., Laagland, H.L.M., 2018. Design of a 3D printed concrete bridge by testing. Virtual Phys. Prototyp. 2759, 1–15. https://doi.org/10.1080/17452759.2018.1476064

Sanjayan, J.G., Nematollahi, B., Xia, M., Marchment, T., 2018. Effect of surface moisture on inter-layer strength of 3D printed concrete. Constr. Build. Mater. 172, 468–475. https://doi.org/10.1016/j.conbuildmat.2018.03.232

Santos, P.M.D., Julio, N.B.S., 2011. Comparison of Methods for Texture Assessment of Concrete Surfaces. ACI Mater. J. 107, 433–440.

Sarkar, M., Dana, K., 2021. Partial replacement of metakaolin with red ceramic waste in geopolymer. Ceram. Int. 47, 3473–3483. https://doi.org/10.1016/j.ceramint.2020.09.191

Sedira, N., Castro-Gomes, J., Magrinho, M., 2018. Red clay brick and tungsten mining waste-based alkali-activated binder: Microstructural and mechanical properties. Constr. Build. Mater. 190, 1034–1048. https://doi.org/10.1016/j.conbuildmat.2018.09.153

Sellami, M., Barre, M., Toumi, M., 2019. Synthesis, thermal properties and electrical conductivity of phosphoric acid-based geopolymer with metakaolin. Appl. Clay Sci. 180, 105192. https://doi.org/10.1016/j.clay.2019.105192

Shah, S.F.A., Chen, B., Oderji, S.Y., Aminul Haque, M., Ahmad, M.R., 2020a. Comparative study on the effect of fiber type and content on the performance of one-part alkali-activated mortar. Constr. Build. Mater. 243, 118221. https://doi.org/10.1016/j.conbuildmat.2020.118221

Shah, S.F.A., Chen, B., Oderji, S.Y., Haque, M.A., Ahmad, M.R., 2020b. Improvement of early strength of fly ash-slag based one-part alkali activated mortar. Constr. Build. Mater. 246, 118533. https://doi.org/10.1016/j.conbuildmat.2020.118533

Siad, H., Lachemi, M., Sahmaran, M., Mesbah, H.A., Hossain, K.A., 2018. Advanced engineered cementitious composites with combined self-sensing and self-healing functionalities. Constr. Build. Mater. 176, 313–322. https://doi.org/10.1016/j.conbuildmat.2018.05.026

Silfwerbrand, J., Beushausen, H., Courard, L., 2011. Bond, in: Bissonnette, B., Courard, Luc, Fowler, D.W., Granju, J.-L. (Eds.), Bonded Cement-Based Material Overlays for the Repair, the Lining or the Strengthening of Slabs or Pavements, RILEM State-of-the-Art Reports 3. Springer, Dordrecht Heidelberg London New York, pp. 51–79.

https://doi.org/10.1007/978-94-007-1239-3

Silva, P. De, Sagoe-Crenstil, K., Sirivivatnanon, V., 2007. Kinetics of geopolymerization: Role of Al2O3 and SiO2. Cem. Concr. Res. 37, 512–518. https://doi.org/10.1016/j.cemconres.2007.01.003

Sisol, M., Kudelas, D., Marcin, M., Holub, T., Varga, P., 2019. Statistical evaluation of mechanical properties of slag based alkali-activated material. Sustain. 11. https://doi.org/10.3390/su11215935

Skorina, T., 2014. Ion exchange in amorphous alkali-activated aluminosilicates: Potassium based geopolymers. Appl. Clay Sci. 87, 205–211. https://doi.org/10.1016/j.clay.2013.11.003

Sobhani, J., Najimi, M., 2013. Electrochemical impedance behavior and transport properties of silica fume contained concrete. Constr. Build. Mater. 47, 910–918. https://doi.org/10.1016/j.conbuildmat.2013.05.010

Soltan, D.G., Li, V.C., 2018. A self-reinforced cementitious composite for building-scale 3D printing. Cem. Concr. Compos. 90, 1–13. https://doi.org/10.1016/j.cemconcomp.2018.03.017

Song, G., 2000. Theoretical analysis of the measurement of polarization resistance in reinforced concrete. Cem. Concr. Compos. 22, 407–415. https://doi.org/10.1016/S0958-9465(00)00040-8

Souza, M.T., Simão, L., Moraes, E.G. De, Senff, L., Renato, J., Pessôa, D.C., Ribeiro, M.J., Oliveira, P.N. De, 2021. Role of temperature in 3D printed geopolymers: evaluating rheology and buildability. Mater. Lett. 293, 129680. https://doi.org/10.1016/j.matlet.2021.129680

Sun, C., Xiang, J., Xu, M., He, Y., Tong, Z., Cui, X., 2020. 3D extrusion free forming of geopolymer composites: Materials modification and processing optimization. J. Clean. Prod. 258, 120986. https://doi.org/10.1016/j.jclepro.2020.120986

Sun, M.Q., Liew, R.J.Y., Zhang, M.H., Li, W., 2014. Development of cement-based strain sensor for health monitoring of ultra high strength concrete. Constr. Build. Mater. 65, 630–637. https://doi.org/10.1016/j.conbuildmat.2014.04.105

Sun, Q., Peng, Y., Cheng, H., Mou, Y., Yang, Z., Liang, D., 2019. Direct ink writing of 3D cavities for direct plated copper ceramic substrates with kaolin suspensions. Ceram. Int. 45, 12535–12543. https://doi.org/10.1016/j.ceramint.2019.03.191

Sun, Q., Peng, Y., Georgolamprou, X., Li, D., Kiebach, R., 2020. Synthesis and characterization of a geopolymer/hexagonal-boron nitride composite for free forming 3D extrusion-based printing. Appl. Clay Sci. 199, 105870. https://doi.org/10.1016/j.clay.2020.105870

Sun, S., Ding, S., Han, B., Dong, S., Yu, X., Zhou, D., Ou, J., 2017a. Multi-layer graphene-engineered cementitious composites with multifunctionality/intelligence. Compos. Part B Eng. 129, 221–232.

https://doi.org/10.1016/j.compositesb.2017.07.063

Sun, S., Han, B., Jiang, S., Yu, X., Wang, Y., Li, H., Ou, J., 2017b. Nano graphite platelets-enabled piezoresistive cementitious composites for structural health monitoring. Constr. Build. Mater. 136, 314–328. https://doi.org/10.1016/j.conbuildmat.2017.01.006

Sun, X., Wang, Q., Wang, H., Chen, L., 2020. Influence of multi-walled nanotubes on the fresh and hardened properties of a 3D printing PVA mortar ink. Constr. Build. Mater. 247, 118590. https://doi.org/10.1016/j.conbuildmat.2020.118590

Sun, Z., Vollpracht, A., 2019. One year geopolymerisation of sodium silicate activated fly ash and metakaolin geopolymers. Cem. Concr. Compos. 95, 98–110. https://doi.org/10.1016/j.cemconcomp.2018.10.014

Suwan, T., Fan, M., 2017. Effect of manufacturing process on the mechanisms and mechanical properties of fly ash-based geopolymer in ambient curing temperature. Mater. Manuf. Process. 32, 461–467. https://doi.org/10.1080/10426914.2016.1198013

Suweni Muntini, M., Ahmadi, H., 2018. Performance of metakaolin geopolymer ceramic for fiber optic temperature sensor. Mater. Today Proc. 5, 15137–15142. https://doi.org/10.1016/j.matpr.2018.04.071

Tan, J., Cai, J., Huang, L., Yang, Q., Mao, M., Li, J., 2020. Feasibility of using microwave curing to enhance the compressive strength of mixed recycled aggregate powder based geopolymer. Constr. Build. Mater. 262, 120897. https://doi.org/10.1016/j.conbuildmat.2020.120897

Tang, S.W., Cai, X.H., He, Z., Zhou, W., Shao, H.Y., Li, Z.J., Wu, T., Chen, E., 2016. The review of pore structure evaluation in cementitious materials by electrical methods. Constr. Build. Mater. 117, 273–284. https://doi.org/10.1016/j.conbuildmat.2016.05.037

Tang, Z., Li, W., Hu, Y., Zhou, J.L., Tam, V.W.Y., 2019. Review on designs and properties of multifunctional alkali-activated materials (AAMs). Constr. Build. Mater. 200, 474–489. https://doi.org/10.1016/j.conbuildmat.2018.12.157

Tay, Y.W.D., Ting, G.H.A., Qian, Y., Panda, B., He, L., Tan, M.J., 2018. Time gap effect on bond strength of 3D-printed concrete. Virtual Phys. Prototyp. 0, 1–10. https://doi.org/10.1080/17452759.2018.1500420

Tay, Y.W.D., Li, M.Y., Tan, M.J., 2019a. Effect of printing parameters in 3D concrete printing: Printing region and support structures. J. Mater. Process. Technol. 271, 261–270. https://doi.org/10.1016/j.jmatprotec.2019.04.007

Tay, Y.W.D., Qian, Y., Tan, M.J., 2019b. Printability region for 3D concrete printing using slump and slump flow test. Compos. Part B Eng. 174. https://doi.org/10.1016/j.compositesb.2019.106968

Temuujin, J., Rickard, W., Lee, M., Van Riessen, A., 2011. Preparation and thermal

properties of fire resistant metakaolin-based geopolymer-type coatings. J. Non. Cryst. Solids 357, 1399–1404. https://doi.org/10.1016/j.jnoncrysol.2010.09.063

Teomete, E., 2016. The effect of temperature and moisture on electrical resistance, strain sensitivity and crack sensitivity of steel fiber reinforced smart cement composite. Smart Mater. Struct. 25. https://doi.org/10.1088/0964-1726/25/7/075024

Tian, Q., Nakama, S., Sasaki, K., 2019. Immobilization of cesium in fly ash-silica fume based geopolymers with different Si/Al molar ratios. Sci. Total Environ. 687, 1127–1137. https://doi.org/10.1016/j.scitotenv.2019.06.095

Tian, Z., Li, Y., Zheng, J., Wang, S., 2019. A state-of-the-art on self-sensing concrete : Materials , fabrication and properties. Compos. Part B 177, 107437. https://doi.org/10.1016/j.compositesb.2019.107437

Tironi, A., Trezza, M.A., Scian, A.N., Irassar, E.F., 2012. Kaolinitic calcined clays: Factors affecting its performance as pozzolans. Constr. Build. Mater. 28, 276–281. https://doi.org/10.1016/j.conbuildmat.2011.08.064

Tironi, A., Trezza, M.A., Scian, A.N., Irassar, E.F., 2013. Assessment of pozzolanic activity of different calcined clays. Cem. Concr. Compos. 37, 319–327. https://doi.org/10.1016/j.cemconcomp.2013.01.002

Turatsinze, A., Beushausen, H., Gagné, R., Granju, J.L., Silfwerbrand, J., Walter, R., 2011. Debonding, in: Bissonnette, B., Courard, L., Fowler, D.W., Granju, J.-L. (Eds.), Bonded Cement-Based Material Overlays for the Repair, the Lining or the Strengthening of Slabs or Pavements. Springer, Dordrecht Heidelberg London New York, pp. 107–139. https://doi.org/10.1007/978-94-007-1239-3

Uysal, M., Al-mashhadani, M.M., Aygörmez, Y., Canpolat, O., 2018. Effect of using colemanite waste and silica fume as partial replacement on the performance of metakaolin-based geopolymer mortars. Constr. Build. Mater. 176, 271–282. https://doi.org/10.1016/j.conbuildmat.2018.05.034

Vaidya, S., Allouche, E.N., 2011. Strain sensing of carbon fiber reinforced geopolymer concrete. Mater. Struct. 44, 1467–1475. https://doi.org/10.1617/s11527-011-9711-3

Valentini, L., Pilehvar, S., Arnhof, M., Kjøniksen, A., 2020. Utilization of urea as an accessible superplasticizer on the moon for lunar geopolymer mixtures. J. Clean. Prod. 247, 119177. https://doi.org/10.1016/j.jclepro.2019.119177

van der Pauw, L.J., 1958. A method of measuring specific resistivity and and Hall effect of discs of arbitrary shape. Philips Res. Reports 13, 1–9.

Van Meurs, N., 1958. Temperature Dependence of the Conductivity of Electrolyte Solutions. Nature 182, 1532–1533. https://doi.org/10.1038/1821532a0

Vasconcelos, E., Fernandes, S., Barroso De Aguiar, J.L., Pacheco-Torgal, F., 2011. Concrete retrofitting using metakaolin geopolymer mortars and CFRP. Constr. Build. Mater. 25, 3213–3221. https://doi.org/10.1016/j.conbuildmat.2011.03.006

Vaysburd, M., Bissonnette, B., Morin, R., 2011. Practice and Quality Assurance, in:

Bissonnette, Benoît, Courard, L., Fowler, D.W., Granju, J.-L. (Eds.), Bonded Cement-Based Material Overlays for the Repair, the Lining or the Strengthening of Slabs or Pavements. Springer, Dordrecht Heidelberg London New York, pp. 157–170. https://doi.org/10.1007/978-94-007-1239-3

Vilaplana, J.L., Baeza, F.J., Galao, O., Zornoza, E., Garcés, P., 2013. Self-sensing properties of alkali activated blast furnace slag (BFS) composites reinforced with carbon fibers. Materials (Basel). 6, 4776–4786. https://doi.org/10.3390/ma6104776

Vilaplana, J.L., Baeza, F.J., Galao, O., Alcocel, E.G., Zornoza, E., Garcés, P., 2016. Mechanical properties of alkali activated blast furnace slag pastes reinforced with carbon fibers. Constr. Build. Mater. 116, 63–71. https://doi.org/10.1016/j.conbuildmat.2016.04.066

Vitola, L., Pundiene, I., Pranckeviciene, J., Bajare, D., 2020. The impact of the amount of water used in activation solution and the initial temperature of paste on the rheological behaviour and structural evolution of metakaolin-based geopolymer pastes. Sustainability 12. https://doi.org/10.3390/su12198216

Vlachakis, C., Perry, M., Biondi, L., Mcalorum, J., 2020. 3D printed temperature-sensing repairs for concrete structures. Addit. Manuf. 34, 101238. https://doi.org/10.1016/j.addma.2020.101238

Vogt, O., Ukrainczyk, N., Ballschmiede, C., Koenders, E., 2019. Reactivity and microstructure of metakaolin based geopolymers: Effect of fly Ash and liquid/solid contents. Materials (Basel). 12, 1–21. https://doi.org/10.3390/ma12213485

Wan, Q., Rao, F., Song, S., 2017a. Reexamining calcination of kaolinite for the synthesis of metakaolin geopolymers - roles of dehydroxylation and recrystallization. J. Non. Cryst. Solids 460, 74–80. https://doi.org/10.1016/j.jnoncrysol.2017.01.024

Wan, Q., Rao, F., Song, S., García, R.E., Estrella, R.M., Patiño, C.L., Zhang, Y., 2017b. Geopolymerization reaction, microstructure and simulation of metakaolin-based geopolymers at extended Si/Al ratios. Cem. Concr. Compos. 79, 45–52. https://doi.org/10.1016/j.cemconcomp.2017.01.014

Wang, A., Zheng, Y., Zhang, Z., Liu, K., Li, Y., Shi, L., Sun, D., 2020. The Durability of Alkali-Activated Materials in Comparison with Ordinary Portland Cements and Concretes: A Review. Engineering 6, 695–706. https://doi.org/10.1016/j.eng.2019.08.019

Wang, G.C., 2016. Ferrous metal production and ferrous slags, in: The Utilization of Slag in Civil Infrastructure Construction. Woodhead Publishing Limited, pp. 9–33.

Wang, W., Dai, H., Wu, S., 2008. Mechanical behavior and electrical property of CFRC-strengthened RC beams under fatigue and monotonic loading 479, 191–196. https://doi.org/10.1016/j.msea.2007.06.046

Wang, X., Wang, Y., Jin, Z., 2002. Electrical conductivity characterization and variation of carbon fiber reinforced cement composite. J. Mater. Sci. 37, 223–227. https://doi.org/10.1023/A:1013107623281

Wang, Y.S., Provis, J.L., Dai, J.G., 2018. Role of soluble aluminum species in the activating solution for synthesis of silico-aluminophosphate geopolymers. Cem. Concr. Compos. 93, 186–195. https://doi.org/10.1016/j.cemconcomp.2018.07.011

Wang, Y., Wang, Y., Han, B., Wan, B., Cai, G., Li, Z., 2018. Strain monitoring of concrete components using embedded carbon nanofibers/epoxy sensors. Constr. Build. Mater. 186, 367–378. https://doi.org/10.1016/j.conbuildmat.2018.07.147

Wang, Y., Wang, Y., Zhang, M., 2020. Effect of sand content on engineering properties of fly ash-slag based strain hardening geopolymer composites. J. Build. Eng. 34, 101951. https://doi.org/10.1016/j.jobe.2020.101951

Wangler, T., Roussel, N., Bos, F.P., Salet, T.A.M., Flatt, R.J., 2019. Digital Concrete: A Review. Cem. Concr. Res. 123, 105780. https://doi.org/10.1016/j.cemconres.2019.105780

Weiss, J.D., 2011. Generalization of the van der Pauw relationship derived from electrostatics. Solid. State. Electron. 62, 123–127. https://doi.org/10.1016/j.sse.2011.04.006

Wen, S., Chung, D.D.L., 2000. Uniaxial compression in carbon fiber reinforced cement, sensed by electrical resistivity measurement in longitudinal and transverse directions. Cem. Concr. Res. 30, 1289–1294. https://doi.org/10.1016/S0008-8846(00)00304-5

Wen, S., Chung, D.D.L., 2001a. Effect of carbon fiber grade on the electrical behavior of carbon fiber reinforced cement. Carbon N. Y. 39, 369–373. https://doi.org/10.1016/S0008-6223(00)00127-5

Wen, S., Chung, D.D.L., 2001b. Electric polarization in carbon fiber-reinforced cement. Cem. Concr. Res. 31, 141–147. https://doi.org/10.1016/S0008-8846(00)00382-3

Wen, S., Chung, D.D.L., 2006. The role of electronic and ionic conduction in the electrical conductivity of carbon fiber reinforced cement. Carbon N. Y. 44, 2130–2138. https://doi.org/10.1016/j.carbon.2006.03.013

Weng, Y., Li, M., Ruan, S., Neng, T., Jen, M., Leong, K., Yeong, O., Qian, S., 2020. Comparative economic , environmental and productivity assessment of a concrete bathroom unit fabricated through 3D printing and a precast approach. J. Clean. Prod. 261, 121245. https://doi.org/10.1016/j.jclepro.2020.121245

Weng, Y., Ruan, S., Li, M., Mo, L., Unluer, C., Tan, M.J., Qian, S., 2019. Feasibility study on sustainable magnesium potassium phosphate cement paste for 3D printing. Constr. Build. Mater. 221, 595–603. https://doi.org/10.1016/j.conbuildmat.2019.05.053

White, C.E., Provis, J.L., Proffen, T., van Deventer, J.S.J., 2012. Molecular Mechanisms Responsible for the Structural ChangesOccurring During Geopolymerization: Multiscale Simulation. AIChE J. 59, 215–228. https://doi.org/10.1002/aic

Winnefeld, F., Gluth, G.J.G., Bernal, S.A., Bignozzi, M.C., Carabba, L., Chithiraputhiran, S., Dehghan, A., Dolenec, S., Dubey, A., Ducman, V., Jin, Y., Peterson, K., Stephan, D., Provis, J.L., 2020. RILEM TC REPORT RILEM TC 247-DTA round robin test :

sulfate resistance , alkali-silica reaction and freeze – thaw resistance of alkali-activated concretes. Mater. Struct. 0. https://doi.org/10.1617/s11527-020-01562-0

Wolfs, R.J.M., Bos, F.P., Salet, T.A.M., 2019. Hardened properties of 3D printed concrete: The influence of process parameters on interlayer adhesion. Cem. Concr. Res. 119, 132–140. https://doi.org/10.1016/j.cemconres.2019.02.017

Wong, C., Yang, E., Yan, X.-T., Gu, D., 2018. Autonomous robots for harsh environments: a holistic overview of current solutions and ongoing challenges. Syst. Sci. Control Eng. 6, 213–219. https://doi.org/10.1080/21642583.2018.1477634

Xia, M., Sanjayan, J.G., 2018. Methods of enhancing strength of geopolymer produced from powder-based 3D printing process. Mater. Lett. 227, 281–283. https://doi.org/10.1016/j.matlet.2018.05.100

Xiao, H., Li, H., Ou, J., 2011. Strain sensing properties of cement-based sensors embedded at various stress zones in a bending concrete beam. Sensors Actuators, A Phys. 167, 581–587. https://doi.org/10.1016/j.sna.2011.03.012

Xu, F., Deng, X., Peng, C., Zhu, J., Chen, J., 2017. Mix design and flexural toughness of PVA fiber reinforced fly ash-geopolymer composites. Constr. Build. Mater. 150, 179–189. https://doi.org/10.1016/j.conbuildmat.2017.05.172

Xu, J., Zhang, D., 2017. Multifunctional structural supercapacitor based on graphene and geopolymer. Electrochim. Acta 224, 105–112. https://doi.org/10.1016/j.electacta.2016.12.045

Xu, J., Zhong, W., Yao, W., 2010. Modeling of conductivity in carbon fiber-reinforced cement-based composite. J. Mater. Sci. 45, 3538–3546. https://doi.org/10.1007/s10853-010-4396-5

Yang, X., Zhu, W., Yang, Q., 2008. The viscosity properties of sodium silicate solutions. J. Solution Chem. 37, 73–83. https://doi.org/10.1007/s10953-007-9214-6

Yao, Y., Duan, X., Luo, J., Liu, T., 2017. Two-probe versus van der Pauw method in studying the piezoresistivity of single-wall carbon nanotube thin films. Nanotechnology 28. https://doi.org/10.1088/1361-6528/aa8585

Yeon, J., Kang, J., Yan, W., 2018. Spall damage repair using 3D printing technology. Autom. Constr. 89, 266–274. https://doi.org/10.1016/j.autcon.2018.02.003

Yoo, D.Y., Kim, S., Lee, S.H., 2018a. Self-sensing capability of ultra-high-performance concrete containing steel fibers and carbon nanotubes under tension. Sensors Actuators A Phys. 276, 125–136. https://doi.org/10.1016/j.sna.2018.04.009

Yoo, D.Y., You, I., Youn, H., Lee, S.J., 2018b. Electrical and piezoresistive properties of cement composites with carbon nanomaterials. J. Compos. Mater. 52, 3325–3340. https://doi.org/10.1177/0021998318764809

Yoo, D.Y., You, I., Lee, S.J., 2018c. Electrical and piezoresistive sensing capacities of cement paste with multi-walled carbon nanotubes. Arch. Civ. Mech. Eng. 18, 371–384. https://doi.org/10.1016/j.acme.2017.09.007

Yoo, D.Y., I., Zi, G., Lee, S., 2019. Effects of carbon nanomaterial type and amount on self-sensing capacity of cement paste. Measurement 134, 750–761. https://doi.org/10.1016/j.measurement.2018.11.024

Yousefi Oderji, S., Chen, B., Ahmad, M.R., Shah, S.F.A., 2019. Fresh and hardened properties of one-part fly ash-based geopolymer binders cured at room temperature: Effect of slag and alkali activators. J. Clean. Prod. 225, 1–10. https://doi.org/10.1016/j.jclepro.2019.03.290

Yu, S., Du, H., Sanjayan, J., 2020. Aggregate-bed 3D concrete printing with cement paste binder. Cem. Concr. Res. 136, 106169. https://doi.org/10.1016/j.cemconres.2020.106169

Yuan, J., He, P., Jia, D., Yang, C., Zhang, Y., Yan, S., Yang, Z., Duan, X., Wang, S., Zhou, Y., 2016. Effect of curing temperature and SiO2/K2O molar ratio on the performance of metakaolin-based geopolymers. Ceram. Int. 42, 16184–16190. https://doi.org/10.1016/j.ceramint.2016.07.139

Yusuf, M.O., Megat Johari, M.A., Ahmad, Z.A., Maslehuddin, M., 2014. Effects of H2O/Na2O molar ratio on the strength of alkaline activated ground slag/ultrafine palm oil fuel ash based concrete. Mater. Struct. Constr. 56, 158–164. https://doi.org/10.1617/s11527-014-0318-3

Zaheer, M., Khan, N., Shaikh, A., Hao, Y., Hao, H., 2016. Synthesis of high strength ambient cured geopolymer composite by using low calcium fly ash. Constr. Build. Mater. 125, 809–820. https://doi.org/10.1016/j.conbuildmat.2016.08.097

Zanotti, C., Borges, P.H.R., Bhutta, A., Banthia, N., 2017. Bond strength between concrete substrate and metakaolin geopolymer repair mortar: Effect of curing regime and PVA fiber reinforcement. Cem. Concr. Compos. 80, 307–316. https://doi.org/10.1016/j.cemconcomp.2016.12.014

Zareiyan, B., Khoshnevis, B., 2017a. Effects of interlocking on interlayer adhesion and strength of structures in 3D printing of concrete. Autom. Constr. 83, 212–221. https://doi.org/10.1016/j.autcon.2017.08.019

Zareiyan, B., Khoshnevis, B., 2017b. Interlayer adhesion and strength of structures in Contour Crafting - Effects of aggregate size, extrusion rate, and layer thickness. Autom. Constr. 81, 112–121. https://doi.org/10.1016/j.autcon.2017.06.013

Zeng, S., Wang, J., Lake, M., 2016. Characterization of mechanical and electric properties of geopolymers synthesized using four locally available fly ashes. Constr. Build. Mater. 121, 386–399. https://doi.org/10.1016/j.conbuildmat.2016.06.011

Zhang, C., Hou, Z., Chen, C., Zhang, Y., Mechtcherine, V., Sun, Z., 2019. Design of 3D printable concrete based on the relationship between flowability of cement paste and optimum aggregate content. Cem. Concr. Compos. 104, 1–10. https://doi.org/10.1016/j.cemconcomp.2019.103406

Zhang, D.W., Wang, D., Lin, X.-Q., Zhang, T., 2018. The study of the structure rebuilding and yield stress of 3D printing geopolymer pastes. Constr. Build. Mater. 184, 575–

580. https://doi.org/10.1016/j.conbuildmat.2018.06.233

Zhang, F., Zhang, L., Liu, M., Mu, C., Liang, Y.N., Hu, X., 2017. Role of alkali cation in compressive strength of metakaolin based geopolymers. Ceram. Int. 43, 3811–3817. https://doi.org/10.1016/j.ceramint.2016.12.034

Zhang, G., Yang, H., Ju, C., Yang, Y., 2020. Novel selection of environment-friendly cementitious materials for winter construction: Alkali-activated slag/Portland cement. J. Clean. Prod. 258, 120592. https://doi.org/10.1016/j.jclepro.2020.120592

Zhang, L., Ding, S., Han, B., Yu, X., Ni, Y.Q., 2019. Effect of water content on the piezoresistive property of smart cement-based materials with carbon nanotube/nanocarbon black composite filler. Compos. Part A Appl. Sci. Manuf. 119, 8–20. https://doi.org/10.1016/j.compositesa.2019.01.010

Zhang, S., Caprani, C.C., Heidarpour, A., 2018. Strain rate studies of pultruded glass fibre reinforced polymer material properties: A literature review. Constr. Build. Mater. 171, 984–1004. https://doi.org/10.1016/j.conbuildmat.2018.03.113

Zhang, X., Li, M., Lim, J.H., Weng, Y., Tay, Y.W.D., Pham, H., Pham, Q.C., 2018. Large-scale 3D printing by a team of mobile robots. Autom. Constr. 95, 98–106. https://doi.org/10.1016/j.autcon.2018.08.004

Zhang, Y.J., He, P.Y., Zhang, Y.X., Chen, H., 2018. A novel electroconductive graphene/fly ash-based geopolymer composite and its photocatalytic performance. Chem. Eng. J. 334, 2459–2466. https://doi.org/10.1016/j.cej.2017.11.171

Zhang, Y., Zhang, Yunsheng, Liu, G., Yang, Y., Wu, M., Pang, B., 2018. Fresh properties of a novel 3D printing concrete ink. Constr. Build. Mater. 174, 263–271. https://doi.org/10.1016/j.conbuildmat.2018.04.115

Zhang, Z., Xiao, Y., Huajun, Z., Yue, C., 2009. Role of water in the synthesis of calcined kaolin-based geopolymer. Appl. Clay Sci. 43, 218–223. https://doi.org/10.1016/j.clay.2008.09.003

Zhang, Z., Wang, H., Provis, J.L., Bullen, F., Reid, A., Zhu, Y., 2012a. Quantitative kinetic and structural analysis of geopolymers. Part 1. The activation of metakaolin with sodium hydroxide. Thermochim. Acta 539, 23–33. https://doi.org/10.1016/J.TCA.2012.03.021

Zhang, Z., Yao, X., Wang, H., 2012b. Potential application of geopolymers as protection coatings for marine concrete III. Field experiment. Appl. Clay Sci. 67–68, 57–60. https://doi.org/10.1016/j.clay.2012.05.008

Zhang, Z., Provis, J.L., Wang, H., Bullen, F., Reid, A., 2013. Quantitative kinetic and structural analysis of geopolymers. Part 2. Thermodynamics of sodium silicate activation of metakaolin. Thermochim. Acta 565, 163–171. https://doi.org/10.1016/J.TCA.2013.01.040

Zhang, Z.H., Zhu, H.J., Zhou, C.H., Wang, H., 2016. Geopolymer from kaolin in China: An overview. Appl. Clay Sci. 119, 31–41. https://doi.org/10.1016/j.clay.2015.04.023

Zhang, Z., Provis, J.L., Ma, X., Reid, A., Wang, H., 2018. Efflorescence and subflorescence induced microstructural and mechanical evolution in fly ash-based geopolymers. Cem. Concr. Compos. 92, 165–177. https://doi.org/10.1016/j.cemconcomp.2018.06.010

Zhao, S., Fan, S., Yang, J., Kitipornchai, S., 2019. A spherical smart aggregate sensor based electro-mechanical impedance method for quantitative damage evaluation of concrete. Struct. Heal. Monit. https://doi.org/10.1177/1475921719888963

Zhong, J., Zhou, G.X., He, P.G., Yang, Z.H., Jia, D.C., 2017. 3D printing strong and conductive geo-polymer nanocomposite structures modified by graphene oxide. Carbon N. Y. 117, 421–426. https://doi.org/10.1016/j.carbon.2017.02.102

Zhou, G.X., Li, C., Zhao, Z., Qi, Y.Z., Yang, Z.H., Jia, D.C., Zhong, J., Zhou, Y., 2020. 3D printing geopolymer nanocomposites structure: Graphene oxide size effects on a reactive matrix. Carbon N. Y. 164, 215–223. https://doi.org/10.1016/j.carbon.2020.02.021

Zhou, J., Ye, G., Schlangen, E., van Breugel, K., 2008. Modelling of stresses and strains in bonded concrete overlays subjected to differential volume changes. Theor. Appl. Fract. Mech. 49, 199–205. https://doi.org/10.1016/j.tafmec.2007.11.006

Zhou, S., Lu, C., Zhu, X., Li, F., 2021. Upcycling of natural volcanic resources for geopolymer: Comparative study on synthesis, reaction mechanism and rheological behavior. Constr. Build. Mater. 268, 121184. https://doi.org/10.1016/j.conbuildmat.2020.121184

Zhou, W., Yan, C., Duan, P., Liu, Y., Zhang, Z., Qiu, X., Li, D., 2016. A comparative study of high- and low-Al2O3 fl y ash based-geopolymers : The role of mix proportion factors and curing temperature. Mater. Des. 95, 63–74. https://doi.org/10.1016/j.matdes.2016.01.084

Zhuang, K., Liu, B., Fang, Y., Guo, Y., Shuai, L., Dong, B., Long, W., Xing, F., 2021. Is electrodeless resistivity method suitable for monitoring the early-age reaction of Na2SiO3-activated slag? Mechanism and application. Constr. Build. Mater. 272, 121719. https://doi.org/10.1016/j.conbuildmat.2020.121719

Zibouche, F., Kerdjoudj, H., de Lacaillerie, J.-B. d'Espinose, Van Damme, H., 2009. Geopolymers from Algerian metakaolin. Influence of secondary minerals. Appl. Clay Sci. 43, 453–458. https://doi.org/10.1016/J.CLAY.2008.11.001

Zulkifly, K., Cheng-yong, H., Yun-ming, L., Mustafa, M., Bakri, A., Shee-ween, O., Suhaimi, M., Khalid, B., 2021. Effect of phosphate addition on room-temperature-cured fly ash-metakaolin blend geopolymers. Constr. Build. Mater. 270, 121486. https://doi.org/10.1016/j.conbuildmat.2020.121486